T-cell interactions with second generation glass-supported lipid bilayers

Edward Blyth Jenkins

Balliol College

Supervisor one: Simon J. Davis
Supervisor two: Christian Eggeling

Thesis submitted for the degree of Doctor of Philosophy

Michaelmas Term, 2020

The work described in this thesis is supported by the Medical Research Council.

Declaration

I hereby declare that except where specific reference is made to the work of others, the contents of this dissertation are original and have not been submitted in whole or in part for consideration for any other degree or qualification in this, or any other university. This dissertation is my own work and contains nothing which is the outcome of work done in collaboration with others, except as specified in the text and in the following:

- Purification of CD43-H6-linker-H6 and CD45RABC-H6-linker-H6 was performed by Heather Brouwer from the Davis group
- Purification of CD58 was performed by Jemma McBride from the Davis Group
- Purification of ICAM-1-H6-linker-H6 was performed by Veronica Chang of the Davis group.
- TIRFM imaging was performed in collaboration with Markus Koerbel from the Klenerman Laboratory, Cambridge. Quantitative analysis of TIRFM data was performed using the 'contact analysis' code written by Markus.
- Calcium release data was analysed using a MATLAB code written by Jane Humphrey from the Klenerman Laboratory, Cambridge.

Abstract

T cells must efficiently scan and discriminate foreign antigen from self. Failure to do so leads to immunodeficiency or autoimmunity. How this process is achieved remains unclear, but recent developments have indicated the topology of the T-cell membrane, and nature of the contact interfaces formed with antigen presenting cells (APCs) may be key. Due to the difficulty of studying cellular contacts, *in vitro* systems that isolate and test specific elements of T cell-APC interface have been essential. One key example is glass-supported lipid bilayers (SLBs) functionalised with foreign antigen and the large adhesive protein ICAM-1 (referred to as 'first generation' SLBs). First generation SLBs have provided unparalleled insight into the spatiotemporal dynamics of key proteins at the T-cell membrane, however, to study the topology of initial membrane contacts, whereby antigen is first detected and discriminated, additional components must be considered. The work described in this thesis sought to establish a novel SLB that builds upon the strong foundation of first generation SLBs by additionally incorporating two key elements of the APC membrane: small adhesion molecules and the glycocalyx (referred to as 'second generation' SLBs). Using second generation SLBs, the results of this thesis addressed the competing effects of adhesion proteins, the glycocalyx, and different antigen density on T-cell contacts, signaling, and antigen discrimination. By visualising the T-cell membrane and exclusion of the glycocalyx on the SLB, small, dynamic membrane protrusions, referred to as microvilli, dominated the contact interface between T cell and SLB. T-cell signaling was rapidly initiated from few microvillar contacts even in the presence of very low densities of antigen, highlighting the sensitive and efficient nature of antigen detection. Finally, antigen discrimination was found critically dependent on the small and constrained geometry of microvillar contacts. In summary, second generation SLBs are a powerful approach to dissect the early events that govern T-cell activation.

Acknowledgements

First, I would like to thank my supervisors Simon Davis and Christian Eggeling for allowing me to be a part of their laboratories. Engaging with members of both laboratories has provided a broader understanding of molecular biology and biophysics, which will be invaluable in my future scientific endeavours. I would particularly like to thank Simon for his scientific guidance, instilling the principle of scientific rigor, and need for a 'clean' presentation slide. I will undoubtedly take the lessons learnt throughout my career with the hope of passing them on myself.

I would like to thank David Klenerman and Steven Lee, as well as the members of their laboratories, for engaging discussions and critical thought on experiments. Having access to such a deep collaboration with these laboratories has not only provided an excellent scientific education, but also friendship, which has made this DPhil a thoroughly enjoyable experience.

The work performed in this thesis was only possible through the support, generosity, and patience of an entire 'village.' I would like to thank Mafalda for her valuable wisdom both in life and science; it's been an honour being 'Junior.' Oliver for his fun chats, relentless help and kind-hearted nature. Mai for always being so cheerful and teaching me her incredible abilities to optimise protocols and make Vietnamese spring rolls; my deepest apologies for only bringing in ¾ of a birthday cake. Jan, Heather and Jemma, for their entertaining chats, sharing their valuable protein production knowledge, and (occasionally) Heather's lab playlists. Rob for teaching me how to put a 'donk on it.' Martin for his calming presence. Matt for sharing his cool scientific ideas with me. Vicky for teaching me how to make bilayers and how to celebrate passing your viva in the most extravagant of ways. Erdinc for his guidance, encouragement, and awesome scientific discussions. I hope your new laboratory flourishes. Falk for being the best example of how to do and present science in the most passionate way. Iztok for his generosity and the lovely collaborative opportunities. Markus for being an amazing scientist who inspires me with his rigor, precision, and technical skill. Working with you has been great fun but introducing me to probably the best pastry in the world (almond pain au

chocolates) was disastrous to my health. Kevin for being an awesome collaborator. I thoroughly enjoyed the hilarious conversations often revolving around science and Squidwards' nose (TITTIS). Anna and Jane for their help and technical prowess as well as providing me with the greatest of gifts; code that works. More broadly I would like to thank members of the WIMM including Craig Waugh and Paul Sopp for their help in sorting cells, Chris Lagerholm and Jana Koth for all their help and problem-solving on the microscopes, and a special thanks to the ladies of the WIMM café who have made my life all the more enjoyable with their fabulous cooking. A large chilli con carne followed by a banoffee pie; must be heaven.

Lastly, I would like to thank my closer friends and family. Alex for the engaging scientific conversations and the occasional stress relieving antics abroad. To Caitlin and Joao, I am blessed that you joined the laboratory and I got to become good friends with you both. Living with you was a pleasure, and I'm going to miss being able to talk about science, general moods, and watching rubbish films like Harry Potter on the regular. To Joao, your intelligence and apt for science leaves me in awe. I hope we remain friends and one day even get to collaborate on projects together, it will have to be T cells though. To Caitlin, you have been such an amazing friend, from the external events, trips abroad, and sampling your amazing cooking skills. Thank you for making my DPhil such a happy experience. To Nicole, thank you for being my best friend, force of encouragement, and grounding my ego and confidence. Your unwavering support has seen me through the worst of times, and I am forever thankful. I hope we remain best friends. People say DPhils are meant to be hard, but they are so incredibly easy with friends like these.

Finally, to my parents, Howard and Alison, my brother William, and sister Samantha, thank you for your undying love, support, and the best advice you can possibly provide a student:

"Just write the damn thesis"

Table of Contents

List of figures

Chapter 1

Chapter 2

Chapter 3

Chapter 4

Chapter 5

Chapter 6

Chapter 7

Abbreviations

ANOVA	Analysis of variance
AP-1	Activator protein 1
APC	Antigen-presenting cell
B2M	Beta-2 microglobulin
BCR	B-cell receptor
CCZ	Close-contact zone
CD	Cluster of differentiation
CDR	Complementarity-determining region
CLIP	Class-II associated invariant chain peptide
CRISPR	clustered randomly interspaced short palindromic repeats
CTLA-4	Cytotoxic T-lymphocyte-associated protein 4
d/p/c SMAC	Distal/peripheral/central supramolecular activation cluster
DAG	Diacylglycerol
DC	Dendritic cell
DTT	Dithiothreitol
ECM	Extracellular matrix
EDTA	Ethylenediaminetetraacetic acid
EGFR	Epidermal growth factor receptor
ER	Endoplasmic reticulum
FACS	Fluorescence-activated cell sorting
FCS	Fetal calf serum
FPLC	Fast protein liquid chromatography
GECI	Genetically encoded calcium indicator
GM-CSF	Granulocyte-macrophage colony-stimulating factor
GPCR	G protein-coupled receptor
GUV	Giant unilamellar vesicle
HLA	Human leukocyte antigen

ICAM	Intercellular adhesion molecule
IgSF	Immunoglobulin superfamily
IL	Interleukin
ILPs	Invadosome-like protrusions
IRM	Interference reflection microscopy
ITAM	Immunoreceptor tyrosine-based activation motif
ITIM	Immunoreceptor tyrosine-based inhibitory motif
J8	$CD4^{-}CD8^{+}$ 1G4-specific TCR Jurkat cell line
K_d	Dissociation constant
KPR	Kinetic proofreading
KS	Kinetic segregation
LAT	Linker for activation of T cells
Lck	Lymphocyte-specific protein tyrosine kinase
LFA-1	Lymphocyte function-associated antigen 1
LLSM	Lattice light sheet microscopy
LN	Lymph node
LRR	Leucine-rich repeat
MHC	Major histocompatibility complex
MoDC	Monocyte-derived dendritic cell
NA	Numerical Aperture
NFAT	Nuclear factor of activated T cells
NF-κB	Nuclear factor kappa-light-chain-enhancer of activated B cells
NiNTA	DGS-NTA(Ni^{2+})
PALM	Photoactivated localization microscopy
PAMP	Pathogen-associated molecular pattern
PBS	Phosphate-buffered saline
PD-1	Programmed cell death protein 1
PDMS	Polydimethylsiloxane

pFCS	Point fluorescence correlation spectroscopy
PKC	Protein kinase C
PLC-γ1	Phospholipase C, gamma 1
PLL	Poly-L-lysine
pMHC	Peptide-complexed major histocompatibility complex
POPC	1-palmitoyl-2-oleoyl-glycero-3-phosphocholine
PRR	Pattern recognition receptor
PRS	Proline-rich sequence
QD	Quantum dot
RAG	Recombination-activating gene
RPMI	Roswell Park Memorial Institute medium
RTE	Recent thymic emigrants
S1P	Sphingosine-1-phosphate
SDM	Spinning-disk microscopy
SEM	Scanning electron microscopy
SFK	Src-family kinase
SH	Src-homology
SLB	Glass-supported lipid bilayer
SMLM	Single-molecule localization microscopy
STORM	Stochastic Optical Reconstruction Microscopy
SUV	Small unilamellar vesicle
TCR	T-cell receptor
TEM	Transmission electron microscopy
TIRFM	Total internal reflection fluorescence microscopy
TLR	Toll-like receptors
TM	Transmembrane
ZAP-70	Zeta-chain association of 70 kDa

Chapter 1 Introduction

1.1 The immune system

1.1.1 Introduction

Microorganisms, including viruses, account for most of the diversity and a large proportion of the biomass on earth [1], [2]. Other organisms had to evolve systems that combat the invasive behaviour of microorganisms, conferring fitness advantages for the host species. This resulted in the generation of the immune system; a defence strategy in a perpetual arms race between host and troublesome microorganisms, found across the entire tree of life. Single-celled prokaryotes, arguably the simplest form of life, counteract bacteriophage infection through restriction-modification induced degradation of non-self DNA, and through adaptive clustered regularly interspaced short palindromic repeat (CRISPR)/Cas systems [3], [4]. Protozoan/colonial eukaryotes possess primitive immune behaviours, capable of phagocytosing and degrading foreign agents [5]. Simple multicellular (metazoan) organisms (i.e. sponges) utilise phagocytosis, and receptor mediated signaling pathways for the release of anti-microbial compounds [6]–[8]. More sophisticated immune defences didn't expand until more complex metazoan life appeared. The transition to multicellularity was dependent on the division of labour, and capabilities for cell-cell contacts. From this context, the immune system burgeoned into an orchestrated network of barriers, cell types, behaviours, secreted proteins, and general and specific cell surface receptors to enact defence in complex metazoan life. Not only has it expanded in diversity and size, so too has its scope. The immune system

pervades the body, collaborating in organ function, general tissue homeostasis and tumour surveillance [9]. Even a vertebrate's choice of breeding partner has been linked to immune components and their association with olfactory cues [10]. Such interconnectedness will surely keep immunologists busy *ad infinitum*.

Crucial to the immune system's effectiveness is that it can discriminate foreign from self. This is achieved by two components: the innate and adaptive immune response. The former, which arose first and forms the first barrier of defence, is composed of cells that perform primitive functions for foreign clearance such as phagocytosis. It discriminates through expression of germline encoded receptors that recognise structurally conserved motifs on pathogens [11]. The latter helps to overcome inefficiencies in innate systems to match the rate of mutations in rapidly dividing pathogens that escape this first line of defence. It is composed of specialist populations of cells referred to as lymphocytes (T and B cells), that can create a memory of previous attacks, and collectively express a vast repertoire of somatically recombined receptors. Each of these receptors can recognise, by chance, specific parts of foreign entities. However, this comes at a significant cost as the response inadvertently creates specificities for self. Extensive quality control processes through lymphocyte development were concurrently evolved [12]. Unfortunately, this process is imperfect as high levels of autoimmunity exist in the human population [13]. A major driver of modern immunology is deciphering the mechanisms by which discrimination is achieved, not only for our intellectual curiosity but also in the hope to manipulate the system for therapeutic gain.

1.1.2 Innate immunity

A defence prototype likely arose at least one billion years ago in unicellular eukaryotes, such as amoebae, which phagocytosed discriminately between 'foreign and self-like' entities [14]. Phagocytosis leads to the degradation of engulfed targets through a flurry of lytic compounds. Additional defences arose in multicellular life such as; (bio)chemical warfare with secreted antimicrobial peptides; cell-mediated killing with directed degranulation of destructive enzymes; and physical barriers formed from the epidermis and mucosal membranes. Put forward by Charles Janeway Jr. in 1989, the decision-making process of phagocytosis, and innate immune responses in general, is dependent on germline encoded pattern recognition receptors (PRRs) that detect structurally conserved and distinct pathogen associated molecular patterns (PAMPs; [11]). PAMP recognition leads to integrated signaling pathways that result in the expression of immune pro-inflammatory cytokines and interferons that drive the innate defences. Chemokines are also produced and recruit additional immune cells to the site of infection. The diversity of receptors and defence mechanisms in this system can achieve effective immunity within minutes to hours of invasion [15].

There are six protein families of PRRs that can be broadly stratified into surface membrane bound, intracellular, or soluble. The Toll-like receptors (TLRs) are the most extensively studied family and was discovered in 1997 based on homology to Drosophila melanogaster Toll protein [16]. To date, there are 10 human TLRs expressed on all cells of the innate immune system, T and B cells of the adaptive immune system and even on

non-immune epithelial and endothelial cells. Other families include the C-type lectin receptors, nucleotide binding domain, leucine-rich repeat-containing receptors, RIG-I-like receptors, AIM2-like receptors, and OAS-like receptors [17]. Extracellular PRRs recognise a range of PAMPs derived from bacterial and fungal cell surface composition (e.g. lipopolysaccharides, lipoproteins and peptidoglycans). Intracellular PRRs recognise viral and bacterial nucleic acid. Soluble PRRs target microbial cell surfaces, aiding phagocytosis. PRRs confer a powerful defence system as their targets are conserved across microbial species and attempts to mutate these targets for escape purposes typically result in diminished fitness. However, it is not possible for PRRs to cover all pathogens, and additional failures of this system result from high infectious load, and immune escape mechanisms (e.g. targeted downregulation of antimicrobial production in immune cells). Regardless, infectious agents must still run the gauntlet of the adaptive immune response.

1.1.3 Adaptive Immunity

A defining feature of the adaptive immune system is that it expands and utilises only a subset of immune cells best suited to dealing with the pathogenic threat, as opposed to spread equally across a range of lymphocytes equally equipped to respond. This is achieved by a clonally diverse set of lymphocytes each expressing a unique antigen-specific receptor. This form of adaptive/acquired immunity first arose approximately 500 million years ago around the appearance of jawless vertebrates [18]. These organisms contain lymphocytes that each express a unique variable lymphocyte receptor (VLR), which is composed of modular and recombinatorial leucine rich repeat domains,

combined via a gene conversion mechanism [19]. Jawed fish achieve adaptive immunity through a clonally diverse set of lymphocytes each uniquely expressing a somatically recombined antigen receptor [20]. The mechanism for somatic recombination is hypothesised to have occurred evolutionarily via the insertion of recombination-activating gene (RAG)-encoding transposons (RAG transposon hypothesis) into an immunoglobulin superfamily (IgSF) member in combination with whole genome duplication events [21]. This has given rise to the three distinct antigen recognition receptors: T-cell receptor (TCR, similar to VLR-A and VLR-C), B-cell receptor (BCR, similar to VLR-B) and major histocompatibility complex (MHC).

Another key aspect of the adaptive immune system is that it provides both a cellular and humoral response. This is achieved by two major lymphocytes: T cells (express TCR) and B cells (expresses BCR). The TCR recognises processed antigens (8-20aa protein fragments) complexed with MHC class I, presented at the surface of all nucleated cells, or MHC class II, expressed on specialised antigen presenting cells (APCs; [22]). APCs include macrophages, dendritic cells (DCs) and B cells. Recognition of cognate antigen by the TCR results in T cell activation, leading to T-cell mediated cytotoxicity or the production of immunomodulatory agents such as cytokines and chemokines. B cells recognise unprocessed antigens presented in solution or on the surface of follicular dendritic cells. Activated B cells produce antibodies that bind to targets on microorganisms, neutralising their activity, recruiting the complement cascade, and increased phagocytosis. Both cell types can produce self-sustaining cells that retain memory of previous infections.

1.1.4 Diversity in the adaptive immune response

Creation of the TCR and BCR repertoire occurs during development of T and B cells in the thymus and bone marrow, respectively. In response to developmental cues such as secreted cytokines (e.g. IL-7) individual cells stochastically rearrange and imprecisely recombine specific gene segments to encoding a novel receptor with unique specificity [23]. The resulting new gene is made up of four segments, the variable (V), diversity (D), joining (J) and constant (C) regions [24]. V(D)J recombination is instigated by V(D)J recombinase, which recognises conserved recombination signal sequences (haptamer-12 or 23bp spacer-nonamer sequence consensus) adjacent to each V, D and J segments. Additional variability from V(D)J recombination is derived from the random addition or removal of nucleotides where VDJ segments are fused together [25]. It is also generated from the multimeric structure of TCR and BCR. For example, the TCR is composed of both TCRα and TCRβ. TCRα and TCRβ are formed from VJ and V(D)J recombination, respectively. Different chain pairings can occur, increasing diversity. Similarly, the BCR pairs two heavy and two light chains, with the light and heavy chain being produced by VJ and V(D)J recombination, respectively. Unlike the TCR, the BCR has an additional mechanism for diversification as it can undergo somatic hypermutation during B-cell activation. Here the variable regions (antigen recognition domain) are randomly mutated to potentially generate higher affinity clones for a stronger immune response via selection in the B cell follicle.

There are 10^{11}-10^{12} T cells in the body [26]. The estimates of potential TCR diversity (10^{15}-10^{20}) suggest an individual will only express a fraction of the potential repertoire, understandably, as 10^{15} T cells would increase our weight 500kg [27], [28]. Previous estimates of actual diversity within the adult human circulation (10^{8}; 10^{9} for BCR) were based on all possible pairing between 10^{6} TCRβ chains and 25 unique TCRα chains [29], [30]. Although the large diversity clearly future proofs the immune defence, the real advantage of this diversity maybe gained from the 'personalised repertoire' of the individual in a population [31]. This allows for a distribution of immunity that ensures highly resistant individuals exist within the population for each microbe. Each TCR may also recognise 10^{6} different antigens with varying degrees of affinity, bolstering functional diversity to 10^{14} [27], [32], [425].

1.1.5 Antigen presentation to T cells

For the TCR to function it requires recognition of antigenic peptides complexed with MHC class I and II protein (**Figure 1.1**). MHC class I and II are recognised by T cells that express the CD8 ($CD8^{+}$ T cells) or CD4 ($CD4^{+}$ T cells) co-receptors, respectively. Each MHC protein can present a range of peptides (10^{6}-10^{12}) depending on the chemical properties and geometry of the peptide binding groove [33], [34]. MHC class I likely has a lower repertoire because its binding cleft only accommodates 8-10aa peptide fragments resulting from steric structural limitations. Conversely, MHC class II binds 13-25aa with a core 9-11aa in the binding groove, and the remainder emerging from the open-ended binding pocket. Peptides for MHC class I are from self and viral particles created in the

cytoplasm. The exact source of peptide fragments for MHC class I isn't fully understood, although it may stem from 'retired' proteins or defective ribosomal products degraded by the proteasome in a ubiquitin-dependent manner [35], [36]. MHC class I is a trimer composed of a heavy-α chain, which forms the peptide binding groove, β-2-microglobulin (β_2M), and the peptide. These proteins assemble in the endoplasmic reticulum (ER) lumen [37]. Peptides are moved into the ER by the transporter associated with antigen processing complex. ER peptidases and chaperones help process and stabilise the α and β_2M components until a suitably high affinity peptide is loaded. Conversely, MHC class II antigens come from the phagocytosis and subsequent degradation of extracellular pathogens through the endolysosomal pathway [38]. This protein is also a trimer composed of an α and β chain, which combined form the peptide binding interface. The α and β chain are folded in the ER with a specialist chaperone called the invariant chain (Ii) attached at the peptide binding groove to block self-loading during transport to the endosomal compartment. Once arrived, Ii is cleaved by cathepsin proteases into a short peptide fragment, which remains attached at the binding interface and is referred to as the Ii-associated invariant chain peptide (CLIP). CLIP acts as a placeholder for a high-affinity cognate peptide.

MHC Class I antigens may also be derived from exogenous sources through 'cross-presentation' [39]. Cross-presentation either occurs by loading of MHC class I in the endolysosomal pathway (similar to class II), or through transfer of antigens through the endosome-cytosol pathway mediated by the ER-associated degradation pathway, which otherwise allows the traditional MHC class I antigen complex processing to occur.

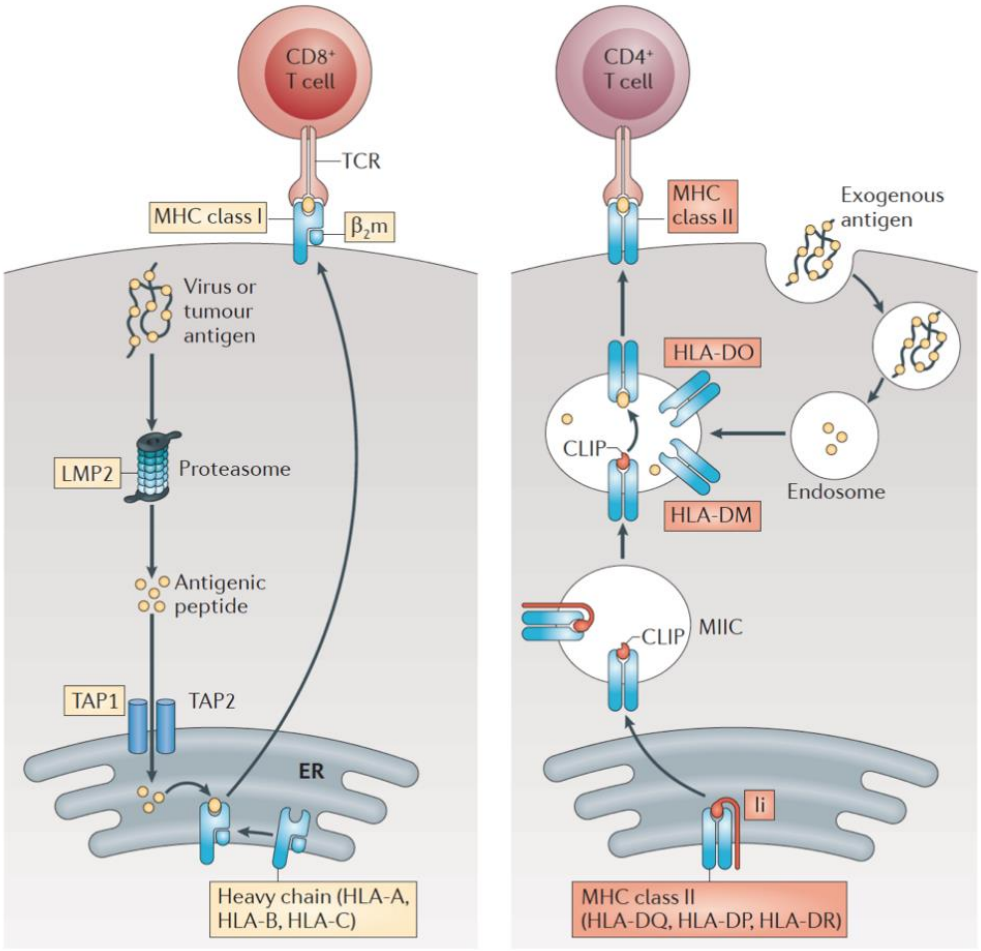

Figure 1.1. **MHC class I and II antigen presentation**. MHC class I protein presents viral or tumour antigens derived from proteasomal degradation within the cytoplasm. Antigens are passed into the ER via the TAP complex and loaded into MHC before trafficking to the surface. MHC class II protein presents exogenous antigens, derived from proteins degraded through the endo-lysosomal pathway. MHC class II is folded in the ER in the presence of the 'surrogate' peptide called the invariant chain (Ii) that attaches to the peptide binding groove. Once in the endosome Ii is cleaved leaving a small peptide remaining in the binding groove (CLIP). CLIP is eventually replaced by antigens from the endolyosome, and the complex is trafficked to the surface. Image taken and adapted from [40].

1.2 Life of a T cell

1.2.1 Introduction

T cells are derived from bone marrow progenitors and migrate to the thymus to undergo maturation and quality control. From the thymus, naïve T cells migrate and cycle between the blood and secondary lymphoid organs (i.e. lymph nodes, (LN) spleen, and tonsils). For the rest of their lifetime their purpose is to perform surveillance activities, persistently and efficiently scanning for foreign peptides loaded into MHC protein (referred to as pMHC from hereon). Upon recognition of their cognate pMHC, T cells rapidly proliferate and change their transcriptional profiles, differentiating into a range of specialised subsets each with shared and unique effector properties. Their terminal state of activation largely depends on the context and environment in which they are activated. After activation, they migrate from lymph nodes into the periphery, typically localising to the most intense sites of infection, or stay to increase other immune cell efforts.

1.2.2 Maturation and selection of T cells

T cell progenitors (prothymocytes) are drawn to the thymus by chemoattractants secreted by resident thymic epithelial cells (TECs). These cells first arrive as double negative (DN) for CD4 and CD8 co-receptors. Upon migration of cells to the cortex of the thymus, DN cells express a prototype TCR composed of a V(D)J recombined TCRβ paired with an invariant pre-TCRα chain. The pre-TCRα serves as a surrogate to test

correct rearrangement of the TCRβ gene. Pairing between the pre-TCRα and TCRβ chains ensures pre-TCR surface expression and signaling can occur, terminating TCRβ chain rearrangement through downregulation of *Rag1/2*. This mechanism of allelic exclusion ensures each T cell clone expresses a single well-folded TCRβ chain. Failure to produce a functional TCRβ chain from either allele results in elimination by apoptosis. This is the first stage in quality control, referred to as β-selection. Pre-TCR expression enables DN progression to the $CD4^{+}CD8^{+}$ double-positive (DP) stage, where rearrangement of the TCRα chain begins. Successful rearrangement of TCRα results in expression of a functional TCR$\alpha\beta$ complex at the surface [41].

DP cells are then subject to 'positive selection' where ineffective recognition of self-antigens presented by cortical TECs (cTECs) leads to cell death through lack of signaling and neglect. Low affinity TCR-antigen interaction appears optimal for positive selection. For MHC class I antigen presentation, cTECs express the unique subunit β5t in their proteasome, suggesting they display a unique set of self-peptides for selection. cTECs are also equipped with specialist endo-lysosomal protein degradation machinery, i.e. cathepsin L and thymus-specific serine protease (TSSP), to produce self peptides for MHC class II [41]. As humans only express 12-14 MHC alleles (out of >27,000 variants, IPD-IMGT/HLA Database Release 3.41.0), positive selection likely confers specificity to the TCR repertoire for these MHC. Selection depends on interaction between MHC and complementarity-determining region 1 (CDR1) and CDR2 of the TCR, which form binding interfaces independent of peptide. Whether this interaction is germline encoded

or dependent only upon ad hoc selection from the TCR repertoire remains an open debate [42].

Cells that pass positive selection stop TCRα gene rearrangement and downregulate either CD4 or CD8 to become $CD4^{-}CD8^{+}$ or $CD4^{+}CD8^{-}$ single positive (SP) T cells [41]. SP cells migrate to the LN medulla in a CCR7 chemokine-dependent fashion, where they undergo 'negative selection' through interaction with medulla TECs (mTECs), hematopoietic DCs and macrophages. mTECs express greater than 85% of genes in the genome (referred to as promiscuous gene expression (PGE)), allowing for a near complete display of self and tissue-restricted antigens. This library of antigen is expressed collectively as individual mTECs only expresses a fraction of the repertoire at a time. PGE is driven by the transcription factor autoimmune regulator (AIRE; [43], [44]). AIRE contains several distinct domains involved in nuclear transport, DNA binding, E3 ubiquitin ligase activity, transcriptional regulation, and formation of multimeric transcriptional complexes that regulate the expression of proteins that are normally found in the peripheral tissue [45]. These proteins are broken down and presented as self-antigens. Strong affinity for self-antigen results in death by apoptosis of T cells, thus selecting for the TCR repertoire which has low capacity for recognition of self. Upon passage of negative selection, T cells enter the peripheral circulation as naïve T cells. As ~10% of thymocytes make it through positive and negative selection, this severe energetic cost is a testament to the protection and therefore fitness advantage the adaptive immune system provides [46]–[48].

This selection process means that the ability to discriminate antigens is borne from a developmental process where self-recognition, albeit weakly, is essential for survival of T cells. It appears that each T cell must discriminate a narrow affinity window between self and agonist in the periphery. Self-peptide recognition by the TCR may be beneficial as it provides 'tonic' sub-threshold signals that maintain T cells in a primed but non-activated state [49]. This is supported by self antigen maintaining T-cell sensitivity to foreign antigen, and the partial phosphorylation of the TCR complex in the presence of self-antigens [50]–[54].

1.2.3 T-cell trafficking

Exit from the thymus is dependent on the recognition of sphingosine-1-phosphate (S1P) by the S1P receptor upregulated on SP thymocytes [55]. An S1P gradient is set up by pericytes and DCs surrounding blood vessels, eventually leading recent thymic emigrants (RTEs) to enter the peripheral T-cell pool in the blood stream. RTEs are thought to have a post-thymic maturation over a period of three-weeks and can be (partially) characterised by CD31 (PECAM-1) expression [56]. T cells (RTEs and other T-cell populations) spend 30-minutes in the blood when moving between lymph nodes, with efficient entry into LNs depending on the expression of the homing receptor CD62L (L-selectin; [57], [58]). L-selectin ligands are commonly expressed on high endothelial venules (HEVs), which are specialised blood vessels that control entry of immune cells into LNs. Upon entering the HEVs, T cells experience an adhesion cascade that slows their passage through the vessel until they arrest and undergo transendothelial

migration from the lumen of the HEV into the LN. This is referred to as diapedesis or extravasation and takes approximately 15-minutes for a cell to pass into the LN [59], [60]. Once in the LN, the chemokine receptor CCR7 (recognises CCL19 and CCL21) and adhesion proteins called integrins aid migration and retention of T-cells. The time it takes to pass through the LN back into the blood (i.e. the egress time) is 12-24 hours depending on cell type, status of the microenvironment, and whether a T cell finds antigen [61]. As with RTEs moving out of the thymus, LN egress is also dependent on gradients of S1P. A balancing act between chemokine and integrin retention, and S1P exit signals therefore governs the egress time for a cell. The need to traffic around the body stems from the limited frequency of each T-cell clonotype. With only a few thousand cells of a given specificity, and with 500-600 lymph nodes in the body, cells must circulate widely to find antigen [62].

1.2.4 T cells in the lymph node

LNs provide highly organised structures that aid antigen recognition. Key to the organisation and architecture of LNs are stromal cells such as fibroblastic reticular cells (FCRs), lymphatic endothelial cells, and blood endothelial cells. FRCs form 3D networks that regulate LN size [63]. They are closely entwined with, and produce, extracellular matrix (ECM) components such as collagen, laminin, fibronectin and chemokines. T cells directly interact and migrate along the FRC-ECM network, which may allow increased interaction with APCs such as DCs [59], [64]**.** Migration along FRC networks is mediated by chemokines and integrins such as lymphocyte function associated-1 (LFA-1),

although integrin activity is not a strict requirement. Of note, the importance of integrins in leukocyte function may have been overestimated because *in vitro* studies require 'two-dimensional' migration whereas leukocytes migrate in three dimensions *in vivo* [426]. DCs are normally present within the peripheral tissue, found at interfaces between the body and environment such as skin or mucosal layers. Their long dendritic spines sample their environments for pathogens. Upon recognition of a microbe by PRRs, DCs downregulate tissue retention receptors, upregulate CCR7, and migrate towards LNs. FRC secretion of CCL21 aids migration and retention of both T cells and DCs via CCR7. Therefore, the FRC network within LNs serve as facilitators for T cells by providing a physical location for T cells and DCs to encounter one another [65].

Each DC in the LN can engage 500-5000 naïve T cells per hour, whereas each T-cell spends 1-5 minutes per DC, scanning 10-60 DCs per hour [61], [66], [67]. The migration of T cells and their process for scanning multiple DCs within the LN appears to resemble a 'guided random-walk', where cells exhibit random motility patterns, but are overall directed along the FRC network chemokine gradient [64], [68], [69]. As the frequency of naïve T cells specific for a given antigen is relatively low (10^3-10^4 per individual human), and because T cells have no knowledge about the location of their antigen, the best strategy is likely one that allows equal scanning opportunity to all cells i.e. a random walk. However, a T cell will likely adapt its strategy on a continuum between explorative (i.e. random walk) and intense localised search behaviour dependent on the cues it receives [70]**.** For example, strong antigens induce full motility arrest at the presenting

DC, whereas weak antigens promote only a partial deceleration in motility, presumably to increase localised scanning [71].

1.2.5 T-cell signaling

T-cell signaling begins with increased net phosphorylation of the TCR by the kinase Lck. This leads to recruitment of another kinase, ZAP-70, to phosphorylated immunotyrosine activation motifs (ITAMs). ITAMs have a conserved consensus sequence of YxxI/Lx_{6-12}YxxI/L, which is phosphorylated on the tyrosine (Y) residue by Src-family kinases (SFK; Src, Yes, Fyn, Fgr, Lck, Blk and Lyn). ZAP-70 binds to phosphorylated tyrosines via its tandem SH2 domains. ZAP-70 normally resides in the cytoplasm in an autoinhibited state. Recruited ZAP-70 is activated via phosphorylation of tyrosine residue Y319 by Lck, which stabilises its active conformation by providing a docking site for Lck SH2 domains, and by trans-autophosphorylation of its activation loop at Y493 [72], [73]. Activated ZAP-70 then goes on to phosphorylate linker for activation of T cells (LAT). Through phosphorylation of its nine tyrosine residues, LAT acts as a multivalent scaffold for the creation of sub-micron-micron sized signaling complexes. It achieves this through recruiting adapter proteins (e.g. Grb2 and Gads) that further recruit proteins such as SOS1 and SLP-76, each with their own multivalent interactions, allowing crosslinking of all the components into a large cluster. This cluster recruits downstream mediators of signaling that lead to calcium release, cytoskeletal remodelling, and activation of transcription factors that reconfigure the phenotype of the T cell (**Figure 1.2**).

A key downstream signaling mediator is intracellular calcium release. From TCR triggering to calcium release takes ~6-7s [74]. It occurs via LAT recruitment of phospholipase C γ1 (PLCγ1), which cleaves phosphatidylinositol 4, 5-bisphosphate (PIP_2) into inositol 1, 4, 5-triphosphate (IP_3) and diacylglycerol (DAG). IP_3 is free to diffuse in the cytoplasm and binds its receptor IP_3R located on the ER, causing the transient release of calcium into the cytoplasm. The concentration of calcium in the cytoplasm is 0.05-0.1μM whereas in the ER it is 300-1000μM [75], [76]. Intracellular calcium release leads to activation of calcium release-activated calcium channels, that help to sustain the calcium signal. This activates the phosphatase calcineurin, which de-phosphorylates the transcription factor nuclear factor of activated T cells (NFAT) allowing its translocation into the nucleus. Sustained calcium signaling is essential for this process (**Figure 1.2**).

1.2.6 The immune synapse

Strong signals will cause cell arrest and spreading directed towards the location where antigen was first detected. This will eventually lead to the formation of the immune synapse, a large contact interface between a T-cell and APC with an area of 50-100μm^2, characterised by extensive reorganisation of surface proteins into specific domains based on protein binding energies, density and height [77]–[79]. The immune synapse organisation was first described by Kupfer and colleagues looking at fixed T cell-B cell interactions, which showed a distinctive bull's-eye pattern with pMHC at the centre of the contact interface, surrounding by a ring of intercellular adhesion molecule-1 (ICAM-

1; [80]). These separate domains were referred to as supramolecular activation clusters (SMACs), with small molecules like pMHC occupying the central SMAC (cSMAC) and larger integrins such as ICAM-1 in the peripheral SMAC (pSMAC). A third distal SMAC (dSMAC) was described for large non-adhesive proteins like CD45 and CD43 [80], [81].

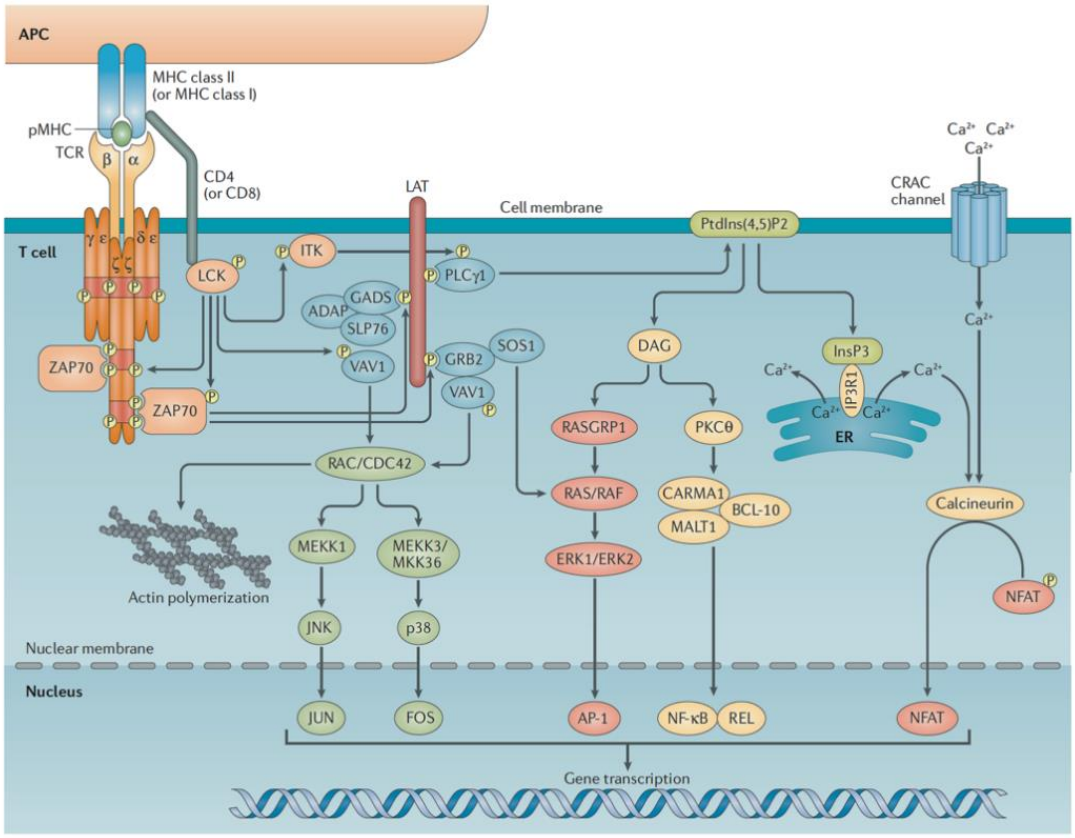

Figure 1.2. **TCR signaling network.** Upon recognition of agonist pMHC the TCR is stably phosphorylated by Lck. This recruits the kinase ZAP-70, which phosphorylates LAT. LAT behaves as a signaling hub forming large 0.5-1μm diameter protein clusters that recruits components associated with actin remodelling agents (GTPases, VAV1, Arp2/3 complex), and downstream signaling (SOS1, PLCγ1). These proteins act to alter the cells morphology, in favour of making additional close contacts directed at the location of the initial signal and activate transcription factors that alter the cells phenotype (NFAT, NFkB and AP-1). More details are provided in the main text. Stable TCR phosphorylation takes 2s. The time for calcium release takes 6-7s. The time for visible NFAT-translocation into the nucleus is 5-15 minutes. The time taken for transcriptional changes is 12-72 hours. Image taken and adapted from [77].

Using supported-lipid bilayers (SLBs; discussed in **Section 1.5.**1) functionalised with pMHC and ICAM-1, the Dustin group studied the dynamics of formation [83]. Here pMHC (TCR) would centripetally migrate towards the centre of contact interface, forming the SMAC over a period of five-ten minutes. Importantly, active signaling (as seen by activated kinase recruitment) precedes mature synapse formation, occurring predominantly in the pSMAC and largely ablated in the cSMAC (**Figure 1.3**; [84]). Similar findings were found using T cell-SLB experiments like that just described [85], [86]. These studies shifted the focus of the immune synapse away from being key to sustained signaling and activation, and instead it appears its main functions are TCR downregulation (dependent on signal strength) and directed secretion of cytotoxic granules by $CD8^+$ T cells [26], [78], [87], [88]. Recently, cytotoxic granules have been found in multiprotein 'supramolecular attack particle' complexes, which may provide a more concentrated or directed 'hit' on target cells [89].

1.2.7 TCR microclusters and microsynapses

Studying cells *in vitro*, synapse formation was found to be preceded by microclusters of CD3ζ and CD4, which coincided with onset of signaling (**Krummel & Davis, 2000**). On antibody-functionalised glass and SLBs, these 'TCR microclusters' have been found enriched for key signaling, coreceptor and cytoskeletal components (e.g. Lck, ZAP-70, LAT, CD4/CD8, CD28, CD2, actin, dynein), excluded CD45, and appeared within seconds of T-cell contact [85], [86], [90]–[94]. How TCR microclusters form, and whether

their formation is essential for signaling and activation seems unclear (discussed in **Chapter 8**).

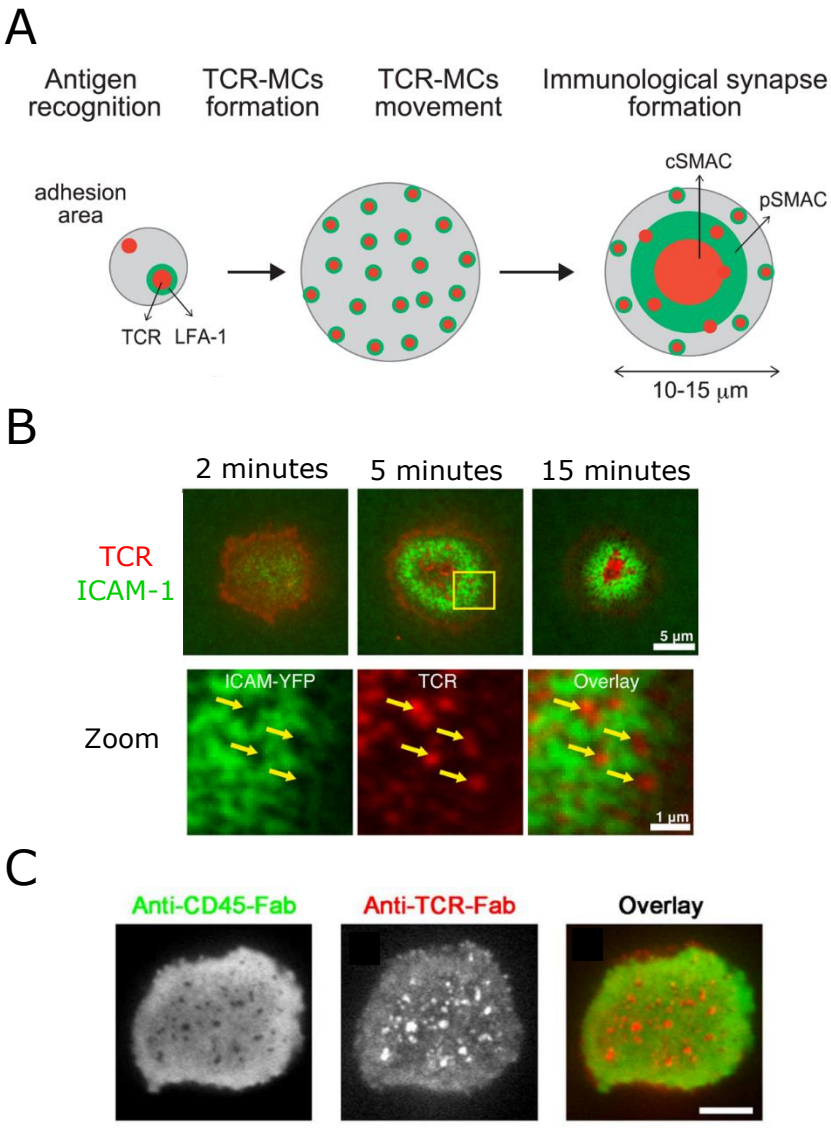

Figure 1.3. **TCR microclusters and synapse formation.** (A) Cartoon of a T cell recognising antigen on an APC, leading to the formation of TCR microclusters (red) that centripetally migrate towards the centre of the large contact interface to form the SMAC (taken and adapted from [102]). (B) Experimental data of T cells interacting with SLB functionalised with ICAM-1 and pMHC. Shows TCR microclusters (red) surrounded by ICAM-1 rings (green) that eventually result in the SMAC formation (taken and adapted from [95]). (C) CD45 (green) exclusion from TCR microclusters (red; taken and adapted from [85]).

TCR microclusters were found to mimic the large immune synapse on a smaller spatiotemporal scale, with each cluster bordered by integrins and focal adhesion molecules [96], [97]. Interestingly, formation of large symmetrical synapses is not wholly required for activation, as T-cells can become activated by integrating signals over more transient, mobile and asymmetric interactions with APCs (referred to as 'kinapses;' [98]–[100]). In addition, large synapse formation has typically been characterised between T cells and B cells but is frequently not seen between T cells and DCs, which instead form multifocal contacts [101]. It may be that microsynapses are a common mode of interaction and activation for T cells. It should be noted that even cytotoxic granule release has been seen from the tips of smaller pseudopodia structures on CD8 T cells, arguing against a need for symmetrical contacts for cell-mediated killing [102].

1.2.8 T-cell activation

Activation requires either sustained signaling, through the formation of symmetric, large and stable immune synapses, or integrated signaling across many productive interactions with APCs through asymmetric, transient and small kinapses [98]–[100]. The latter may be possible through some degree of hysteresis from nuclear transcription factors (e.g. NFAT), whereby productive signaling quickly leads to transcription factor accumulation in the nucleus, combined with significant lag time for transcription factor depletion from the nucleus upon loss of productive signaling [103]. Kinapses appear the more common form of activation in naïve T cells, whereas synapses are found in memory cells [104]. However, the TCR alone is insufficient to drive full activation, as cells require

secondary signals from co-stimulatory surface proteins such as CD28, which binds CD80/86 on DCs (the 'two-signal' model of T-cell activation). Without co-stimulation T-cell activation leads to a form of peripheral tolerance, such as clonal anergy, whereby T-cells become desensitised to antigen [105]–[107]. Mature APCs (ones that have encountered pathogens) upregulate co-stimulatory molecules and therefore have the capacity to provide all necessary signals for T-cell activation.

1.2.9 T-cell subsets

T cells are broadly divided into two subsets: $CD4^+$ helper T cells (Th) or $CD8^+$ cytotoxic T cells. The former orchestrates the immune response through immunomodulatory receptors and cytokines. The latter mediates target cell killing through the directed release of cytotoxic granules (containing perforin and granzyme) that puncture and annihilate targets. Differentiation of T cells into different subsets within these two groups during activation is dependent on the activity of a range of transcription factors that genetically predispose the cells towards distinct fates. The context of the immune response (i.e. types of cytokines in the microenvironment), in combination with antigen recognition, is responsible for shifting cell fates down distinct avenues. Th cells can differentiate into Th1, Th2, Th9, Th17, Th22, regulatory T cells (Tregs) and follicular helper T cells, each characterised by their own cytokine profiles and specialist functions. Broadly speaking Th1, Th2 and Th17 produce cytokines for enhancing immune response against intracellular, helminth, and extracellular pathogens, respectively. Tregs have a role in dampening immune responses through the production of anti-inflammatory

cytokines. Follicular helper T cells are specialised in supporting B-cell activation in LNs [108].

Cytotoxic T cells can be divided into short-lived effector and long-lived memory cells. The former requires the cytokine IL-2 and quickly die after resolution of an infection, whereas the latter will form in the absence of IL-2 and persist for years to allow more efficient responses upon re-infection [109]. It has been estimated that cytotoxic T cells can perform 19 cell divisions within a week after activation, creating 524,288 cells to fight an infection [110]. After activation, T-cells will either remain in the lymphatic system to further enhance the immune response, or downregulate CCR7 and upregulate CXCR3 to traffic into the peripheral tissue to perform their effector functions.

1.3 How do T cells scan for antigen?

Naïve T cells scan for antigen in the lymph node. T cells migrate through the LN utilising special membrane structures to increase the efficiency of their scanning process. These structures are actin-rich, dynamic membrane protrusions, referred to as either microvilli or invadosome-like protrusions (ILPs), which create close contacts with target surfaces allowing interaction of pMHC and TCR. The mechanics of antigen detection are tuned by many factors, the most relevant being the antigen density and affinity, the glycocalyx, adhesion proteins and co-stimulators/inhibitors on mature DCs.

1.3.1 The glycocalyx

Critical to the process of antigen scanning are the dimensions of the relevant proteins. The TCR and pMHC are both ~7.5nm in height. Close membrane contacts (~15nm) must form between T cells and DCs to allow for antigen scanning. However, both cells are coated in a negatively charged glycocalyx (e.g. CD45 and CD43) that acts as a steric and repulsive barrier to contact formation [111]–[115]. The 'height' of CD45 ranges from 21.5-40nm, dependent on the isoform expressed, and CD43 is ~41nm [116], [117]. In the absence of any force, and because of their glycosylation, these proteins are unlikely to interdigitate between cells, thus making the gap between T cell and DC membranes 50-100nm apart. Modelling of crowded protein environments has suggested that even membrane contacts 40nm apart would be unlikely to make 15nm contacts passively by thermally driven membrane fluctuations, even when adjusting for membrane rigidity [79]. In addition, spontaneous segregation of CD45 from a 100nm diameter circle was estimated to take 10^9s (31.7 years; [118]). Using simplified and thermodynamically equilibrated *in vitro* systems, passive binding of short receptor-ligands could only be seen at 20 minutes in the presence of CD45 [119]. Experimental systems have yet to directly measure the kinetics of antigen detection in the context of a glycocalyx present on opposing surfaces. This is addressed using live cells in **Chapters 4 and 5** of this thesis. As T cells spend 1-5-minutes scanning each DC, previous studies support the need for an active process to drive close membrane contacts and efficient scanning in the presence of a glycocalyx [61].

1.3.2 Membrane topology

Active formation of close contacts has been related to the membrane topology of T cells [120]–[122]. Two overlapping membrane structures have been described: ILPs and microvilli. ILPs were first described for memory/effector T-cells interacting with endothelial monolayers [120]. They appeared as 0.2-1μm contacts based on LFA-1 exclusion rings enriched with actin at the centre. Using transmission electron microscopy, the protrusions had an average diameter of 340nm and extended between 0.1-2μm, with an average depth of 480nm into the endothelial layer. Similarly, microvilli have been shown to be 100-500nm diameter and 300-1000nm long membrane protrusions surrounding the cell [122]–[124]. Like ILPs, microvilli are also actin-rich structures, but were additionally found to be highly dynamic, remodelling themselves on the scale of minutes, migrating at speeds of 5μm/min, and capable of covering 95% of the T-cell surface in ~1-minute [122]. As the glycocalyx can extend from 50-500nm (depending on cell type) it appears the dimensions and parameters of microvilli/ILP activity are well suited to overcoming this barrier to scan for antigen (**Figure 1.4**). In accordance, stabilised ILP contacts were found enriched in TCR signaling components (i.e. ZAP-70 and protein kinase C) and formed prior to calcium release following antigen detection [121]. Treatment of memory T cells with latrunculin, known to disrupt the actin cytoskeleton (and therefore membrane topology), ablated calcium signaling [121]. As treated cells could still signal with antibody treatment, this suggests membrane protrusions were essential for overcoming the barrier function of the glycocalyx to detect antigen presented on the endothelial cells. Regarding microvilli, TCR signaling machinery was found enriched on microvilli, and increased ZAP-70 recruitment has

been observed in membrane areas in contact with antibody-labelled glass [123], [125], [126].

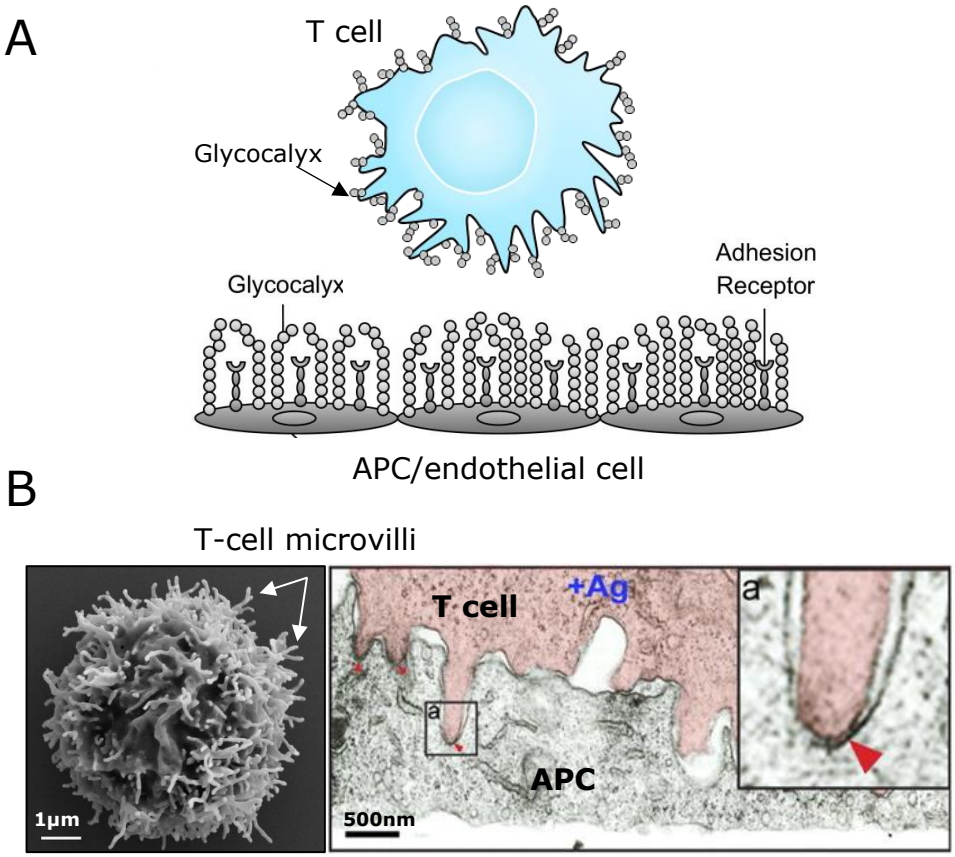

Figure 1.4. **Overcoming the glycocalyx barrier to scan for antigen.** (A) The glycocalyx surrounding cells increases the degree of crowdedness at the surface, acting as a barrier to close contact formation. T cells must overcome the glycocalyx barrier in both endothelial cells (~500nm in height) and APCs (~50nm in height). Image taken and adapted from [120]. (B) T-cell microvilli (left; SEM image, white arrows) and ILP (right; transmission electron microscopy image of T cell and APC) structures are likely responsible for antigen scanning by penetrating through the glycocalyx barrier to make close contacts. Images are taken and adapted from [114] (left) and [121] (right).

Interestingly, the glycocalyx and morphology of cells appears to be linked. Increased glycocalyx expression in human embryonic kidney cells resulted in a transition from sinuous to point-like contacts with glass [116]. A more extensive analysis in epithelial cells showed that increased glycocalyx dramatically enhanced the number of finger-like membrane protrusions surrounding cells through entropic forces [113]. These lines of evidence point to morphology changes as a cellular adaptation to the difficulty of making cell-cell contacts imposed by the glycocalyx. It was proposed that the appearance of the CD45-glycocalx element in the evolution of primitive lymphoid cells may have given rise to contact-sensitive, molecular-segregation-based receptor signaling [116].

1.3.3 Adhesion molecules

Although membrane topology is likely essential for TCR/pMHC interaction, cell adhesion molecules (CAMs) are likely the dominant factor stabilising contacts to aid scanning of individual APC surfaces. Most relevant to early antigen scanning of APCs are members of the integrin and IgSF proteins. The key integrin on the T-cell surface is lymphocyte function-associated antigen 1 (LFA-1). LFA-1 binds ICAM1-5 and junction adhesion molecule-1. ICAM-1 is the highest affinity and best studied of the ligands. [128], [129]. LFA-1 and ICAM-1 are found on both naïve T cells and DCs, although LFA-1 is more prevalent on T cells, and ICAM-1 higher on mature DCs [130]. LFA-1 (and all other integrins) is an alpha (CD11α) and beta (CD18) heterodimer, with the globular 'headpiece' binding domain for ICAM-1 formed from both chains. LFA-1 is found in a

bent low-affinity conformation in the resting state of T cells (headpiece <5nm from the membrane). LFA-1 is regulated by 'inside-out' signaling, whereby chemokine, TCR, and TLR mediated signals alter the activity of intracellular proteins (e.g. talin and kindlin) that bridge the cytoplasmic tail of the alpha and beta chains of LFA-1 and the cytoskeleton [131]. Their association destabilises the transmembrane regions of LFA-1, allowing structural rearrangement to an open, extended and higher-affinity form. The transition from closed to open results in an affinity shift from 1mM to 100nM (K_d; 10,000x change) and a height change from <5nm to 20-25nm [132], [133]. The function of LFA-1 has mostly been attributed to T-cell homing to the LN, and activation through stabilising large contact interfaces between cells [78], [134], [135]. LFA-1 has been shown to provide increased adhesion, allowing for more efficient TCR-pMHC engagement, and supposedly co-stimulatory signals to T cells, lowering the threshold for activation. Without LFA-1, cells required 10-100x more antigen to achieve the same response [136]. The role of LFA-1 in antigen scanning is less clear, given it requires inside-out signaling, although could conceivably exist primed medium-high affinity state that allows for adhesive contacts with ICAM-1 (~40nm across membranes) as a result of extensive chemokine signals throughout the LN.

A more appropriate adhesion protein for antigen scanning under resting conditions would be one that doesn't require signaling dependent conformational changes, has a reasonably low affinity, and is enriched in microvilli. This would ensure scanning independent of cell state, stabilise contacts sufficiently without preventing further migration, and likely be involved in initial interactions, respectively. For these reasons

the IgSF member CD2 is a good candidate. CD2 is a small (~7.5nm) adhesion protein that binds CD58 (also an IgSF member;~7.5nm on the DC surface) with a weak 3D K_d of 20μM and 2D K_d of 1-8 molecules/μm^2 [137]–[139]. The dimensions of the CD2/ligand interaction therefore match that of the TCR-pMHC (~15nm). In accordance, CD2-CD58 can be found spatially segregated from ~40nm LFA-1-ICAM-1 complexes in the immune synapse and initially co-localised with TCR [92], [140], [141]. CD58 is found on all immune cells, particularly upregulated on matured DCs, and expressed on non-haemopoietic cells (fibroblasts, endothelia and epithelia), indicating the importance of CD2-CD58 interactions in both the LN and peripheral tissue. CD2 has a 117aa cytoplasmic tail with five proline rich repeat domains, allowing its association with actin binding proteins (e.g. CD2-associated protein and CD2 cytoplasmic tail binding protein 2) and signaling molecules (e.g. the kinases Lck and Fyn). These protein associations could allow for cytoskeletal changes that alter antigen scanning dynamics. CD2 has been found to lower the threshold for T-cell activation particularly under low antigen conditions presumably through increased adhesion and enhanced antigen scanning [142]. Furthermore, CD2 was recently found enriched at microvilli [126]. All these findings point towards CD2 being intricately tied to the process of antigen scanning. As the role of microvilli in antigen detection has only recently gained attention, the CD2/CD58 interaction (and LFA-1/ICAM-1) remains poorly characterised in this context. This will be addressed in **Chapters 6 and 7** of the thesis.

1.3.4 Co-stimulatory/inhibitory molecules

There are many co-stimulatory and inhibitory receptors that can be found on the T-cell surface, most of which are minimally expressed and upregulated after naïve T-cell activation. Co-stimulatory molecules include CD27, CD28, CD134 (OX40), CD137 (4-1BB), and CD278 (ICOS). Naïve T cells predominantly express CD27 and CD28 [143], [144]. Inhibitory proteins include CTLA-4, PD-1, TIM-3, LAIR-1, VISTA, CD272 (BTLA), CD160, LAG-3, and TIGIT. LAIR-1, BTLA and VISTA are expressed on naïve T cells [145]–[149]. Co-stimulatory and inhibitory molecules are known to have distinct pathways, but also alter the threshold for signal induction in the presence of antigen. This is because the cytoplasmic domains of these receptors have either stimulatory ITAMs or inhibitory immunotyrosine inhibitory motifs (ITIMs). ITAMs recruit SH2 domain (binds phosphorylated tyrosines)-containing kinases e.g. ZAP-70 and SYK, leading to downstream signaling and activation. ITIMs recruit SH2-domain containing lipid or protein tyrosine phosphatases e.g. SHIP-1 and SHP1-2. Their increased recruitment to the membrane leads to de-phosphorylation of kinases (e.g. Lck and ZAP-70) and antigen and co-stimulatory receptors resulting in decreased down-stream signaling and activation [150]–[152]. Through these mechanisms, it is possible these receptors collectively tune the migration and scanning rates of T cells in the LN. In support, they typically have small dimensions, which likely allows them to co-localise with the TCR in close contacts [152]–[156], [424]. Similar findings have been shown for activating and inhibitory receptors of NK cells, which based on their small sizes, likely colocalise to the same areas of contact interfaces with target cells [427]. PD-1 has been found to co-localise with the TCR during immune synapse formation and could reduce

the fraction of cells exhibiting early signaling events, causing a three-fold increase in the number of antigens required to achieve the same response [152], [157]. In another study, CTLA-4 expression led to more transient interactions with DCs, increased T-cell motility, and reduced overall T-cell activation *in vitro* and *in vivo* [158]. Although the role of other co-stimulatory/inhibitory receptors on antigen scanning kinetics have not been addressed (particularly those expressed on naïve T cells) they could conceivably alter the kinetics of antigen detection like PD-1 and CTLA-4.

1.4 How do T cells discriminate foreign from self?

Whether a T cell responds to antigen will depend on its affinity and/or off-rate. Assuming those parameters meet required thresholds, signal transduction will occur. Although most of the key players have been described in this process, quantitative treatments of how the relevant surface and intracellular proteins integrate to derive overall activation outcomes are still required. Most importantly, how pMHC binding creates signals in the cell in the first instance is still not answered.

1.4.1 TCR triggering machinery

How pMHC results in phosphorylation of the TCR (referred to as TCR triggering) is an enigma, with several models proposed all of which are dependent on altering the balance between kinase and phosphatase activity on the TCR. Prior to discussing the

models, it is important to understand the key players in TCR triggering and the resting state of these components on the T-cell surface.

TCR

Both the TCRα and TCRβ chains are composed of a variable domain, generated through V(D)J recombination, and constant domain, which includes membrane-proximal connecting peptide (CP), a transmembrane region (TM) and very short cytoplasmic tails (5-6aa) with no enzymatic activity. To allow signaling, the TCR is found in an octameric complex composed of the extracellular antigen binding (TCR$\alpha\beta$) and intracellular signaling (CD247 (TCR zeta/ζ) homodimer, and CD3$\delta\varepsilon$ and CD3$\gamma\varepsilon$ heterodimer) subunits. CD3$\gamma\delta\varepsilon$ are composed of an extracellular immunoglobulin domain, short membrane-proximal CP, TM and intracellular domain, whereas ζ has a short extracellular sequence, a TM and intracellular domain. Signaling is dependent on kinase recruitment (i.e. Lck and ZAP-70) to the ITAM domains in the CD3 chains, with three found in each ζ and one in the CD3$\gamma\delta\varepsilon$ chains for a total of ten ITAMs per TCR. The first complete cryo-electron microscopy image of the TCR-CD3 complex (without the intracellular domains or ligand) was recently obtained, providing key insights into the complexes assembly, and confirmed the 1:1:1:1 (TCR$\alpha\beta$:CD3$\delta\varepsilon$:CD3$\gamma\varepsilon$:$\zeta\zeta$) stoichiometry of the TCR-CD3 complex [159]. Despite this achievement, the resting state of the TCR on the membrane remains controversial. For example, the intracellular domains were excluded from the cryo-EM image due to their high degree of freedom, which means it remains unclear on how the intracellular domains exist in the resting state. This is

important to solve to provide clarity on the mechanism of TCR triggering (discussed below).

The overall receptor valency (i.e. monomer vs oligomer) of the TCR has largely, but only recently, been resolved [160]–[167]. Previously, most evidence for the TCR being in a pre-clustered state was derived from experimental setups and analyses prone to imaging artefacts that heavily biased results towards the receptor being clustered [168]–[170]. Considering more recent biophysical image analysis, the monomeric state appears to be settled [166], [167]. Lastly, several reports have indicated the TCR is enriched at microvilli tips relative to the cell body, which would fit in principle with these membrane structures being key to antigen scanning and detection [123], [126].

Lck

Lck is the key kinase involved in TCR triggering. Lck contains five domains: an N-terminus Src-homology 4 domain (SH4), which contains a glycine for myristoylation and CxC motif for dual and labile palmitoylation, helping anchor Lck to the plasma membrane [171]. Mutation of any of the lipid modification sites prevents trafficking to the membrane. Next to this is the unique zinc clasp domain (CxxC) which non-covalently links Lck to the coreceptors CD4 and CD8 (CxCP sequence) through coordination of a zinc ion. The dissociation constant is 400nM and 800nM for CD4 and CD8, respectively [172]. This domain is connected to the SH3 domain, which recognises proline-rich sequences (PRS). Through this domain Lck is claimed to associate with the

PRS in the adhesion protein CD2 and adapter protein LAT [173], [423]. The SH2 domain importantly allows interaction with phosphorylated tyrosine residues such as those on the ITAM domains of the TCR. Lastly, the C-terminus contains the SH1 domain with an active tyrosine kinase catalytic domain. Lck contains two key tyrosine residues involved in regulating its activity. The first is C-terminal Y505, which is phosphorylated by another kinase Csk [174]. Although Csk may play a role in setting thresholds for TCR triggering (by tuning the pool of active Lck) and overall T-cell activation, it is unlikely to play a role in the triggering event itself as it is hard to envision how TCR-pMHC interaction could translate into altered Csk activity. Regardless, Csk phosphorylation of this site results in Lck adopting a closed conformation as it binds its own SH2 domain (**Figure 1.5;** [175]). The closed conformation is further supported by the PRS in the linker region (between SH2 and SH1) and the SH3 domain [73]. However, de-phosphorylation of this site (producing an open conformation) is not sufficient for Lck activity, which further requires phosphorylation of Y394. This provides an indispensable stabilisation of the catalytic residues in the catalytic domain of Lck and is achieved by autophosphorylation [73], [176], [177]. De-phosphorylation of Y505 and Y394 is mediated by CD45, SHP-1 and several other protein tyrosine phosphatases [178], [179]. In the resting state of a cell up to 40% of Lck was claimed to be constitutively active [180]. Free-Lck (not associated with a coreceptor) may provide the initial trigger because of its higher mobility and Y394 phosphorylation state [181], [182].

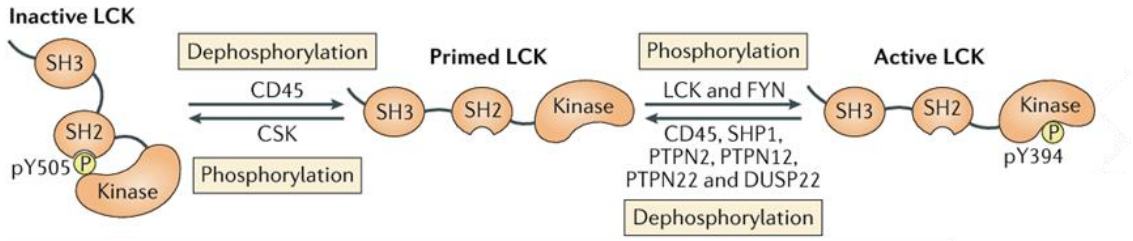

Figure 1.5. **TCR triggering machinery.** Cartoon of Lck regulation. Inactive Lck occurs by phosphorylation of tyrosine residue Y505 by Csk. This results in Lck adopting a close conformation through binding its own SH2 domain. CD45 dephosphorylates this site putting Lck into a primed state. The open conformation is not enough for activity and Lck still requires phosphorylation of tyrosine residue Y394, which stabilises its catalytic domain. This is done by trans-autophosphorylation (or by the kinase Fyn). CD45 (among other) phosphatase inactivates Lck. Image taken from [82].

Coreceptors (CD4 and CD8)

CD4 and CD8 coreceptors are known to enhance T-cell activation as much as 30-100-fold. However, their role in TCR triggering is not so clear as both receptors are dispensable for triggering and bind extraordinarily weakly to the membrane proximal regions of MHC class I and II, respectively [183]–[186]. CD8 is composed predominantly of disulphide linked CD8α and CD8β chain heterodimers (although CD8$\alpha\alpha$ homodimers are present at the surface on specialist subsets of cells), each with a TM domain and an intracellular domain. Only CD8α associates with Lck. The extracellular region is composed of an Ig-like domain linked to the TM by a long flexible stalk, 'sitting' at a height of 10nm from the membrane. Both CD8$\alpha\beta$ and CD8$\alpha\alpha$ are thought to bind MHC class I with a low 3D affinity of 100-200μM [187], [188]. CD4 is of a similar height, with the extracellular made of four Ig-like domains, linked to a TM, and cytoplasmic domain. Crystals of the CD4-TCR-pMHC assembly show that CD4 binds MHC class II

at an angle of 65° relative to the T-cell surface, creating a V-shape complex between all the components [189]. It binds MHC class II with the weakest measured interaction to date, with a 3D affinity of >2.5mM (measurements above this are not possible based on current methods) and a 2D affinity of 4800 molecules/μm^2 (the number of molecules required to achieve 50% binding). Modelling showed that this weak interaction could only provide a 3x increase in signaling relative to random collisions of free-Lck with the TCR [186]. Based on these findings the coreceptors do not increase Lck association with the TCR. Rather a two-step model for coreceptor engagement seems more plausible wherein Lck first phosphorylates the TCR. This is followed by further recruitment of coreceptor-Lck complexes to the TCR-pMHC interaction through the SH2 domain of Lck binding the now phosphorylated tyrosine of the CD3 ITAMs [187], [190], [191]. Binding both the phosphorylated tyrosine on the inside, and MHC on the outside may provide stabilisation of the Lck-coreceptor/MHC/TCR complex, increasing TCR signaling. This is supported by several lines of evidence showing that CD8 recruitment to MHC was abolished when blocking Lck activity, and that CD8 recruitment could still occur when its binding domains for MHC class I were mutated [181], [191]. If this model is true, coreceptor engagement is subsequent to TCR triggering, whereupon it may provide a mechanism of signal amplification. Interestingly, CD4 was recently claimed to be found enriched in microvilli, which would suggest it plays a role in antigen scanning [126]. In this case, the coreceptors may be able to quickly amplify signals once antigens have been detected at microvilli. Despite this, how coreceptors enhance signaling remains largely unknown.

Phosphatase (CD45)

The key phosphatase regulating TCR triggering is CD45. CD45 is a large single-pass transmembrane protein and likely directly involved in the triggering mechanism acting at the very least as a gatekeeper for signaling [192]. CD45 is expressed as different isotypes depending on cell type and differentiation status of a T cell. Isoforms are created by alternative splicing of exons 4, 5 and 6 (corresponding to A, B and C) leading to alterations in the extracellular domain only. The structure is composed of a heavily glycosylated N-terminal mucin-like segment followed by a cysteine-rich domain (d1), three fibronectin domains (d2-d4), a TM region, and tandem protein tyrosine phosphatase domains, with only the membrane-proximal domain being active. d1-d4 are present in all isoforms. CD45RABC (the largest form) can be found on B cells, plasmacytoid dendritic cells, and some subsets of T cells [193], [194]. CD45RA and CD45R0 (the shortest form) are found on naïve and memory T cells, respectively. The height of CD45R0 and CD45RABC ranges from 21.5-40nm. As the protein is rigid, even the smallest isoform will be excluded from areas of TCR-pMHC interaction (~15nm; [116], [119], [195]). CD45 is highly expressed at the T-cell surface with over 100,000 molecules taking up 10% of surface area of the membrane and as a result is likely the dominant phosphatase controlling TCR triggering [115]. However, CD45 has been described as both a positive and negative regulator of T-cell signaling. Deletion of CD45 prevented cells from activating, and when analysing knockout mice, five-fold fewer T cells were isolated from the spleen highlighting a defect in the development of T cells [196], [197]. This can be partially explained by CD45 having specificity for the TCR-CD3

ITAMs, as well as the Lck Y505 and Y394 residues of Lck [77], [192], [198]. Despite this, CD45 showed 20x more activity for CD3ζ ITAMs than Y505 and Y394, supporting its role as the dominant brake on TCR triggering [198].

1.4.2 Models of TCR triggering

Historically, paradigms for receptor triggering come from members of the growth factor receptor (GFR) and G-protein coupled receptor (GPCR) families. The former function by trans-autophosphorylation upon receptor aggregation, whereas the latter is based on conformational changes [199]. In line with the ideas of the time, Janeway first proposed the TCR used a mixture of both [200]. However, application of these models is not entirely appropriate as the TCR contains no enzymatic activity (like EGFRs), pMHC is monomeric and often in limited abundance preventing dimerization, and the TCR is structurally different to GPCRs. An additional model was proposed shortly afterwards, taking into consideration the dimensions of membrane proteins that could be involved [201]. Proteins such as the adhesion protein CD2 and TCR are small (~7.5nm), and close contacts driven by CD2 binding would lead to exclusion of larger proteins such as CD45 (~25-40nm), increasing the half-life of phosphotyrosine residues on the TCR within those exclusion zones. Provided the right peptide was bound, signaling would occur. This was later referred to as the kinetic-segregation (KS) model [202], [203]. For the last 30 years, evidence of varying quality has accumulated in favour of either aggregation, conformational change or KS, with still no definitive answer to the mechanism of triggering (**Figure 1.6**). Answering this question is important because many immunoreceptors share common features with the TCR. Namely, they have no intrinsic

activity, instead containing tyrosine phosphorylation motifs to recruit proteins with enzymatic activity.

Conformational change

The conformational change idea was originally proposed based on 'antagonist peptides' and antibodies against the TCR incapable of eliciting a response in a manner not related to their affinity [200]. However, monomeric agonist pMHC in solution cannot induce signaling, ruling out a GPCR-equivalent mechanism. This is further supported by structural studies analysing the ectodomain of the TCR bound to antibodies, antibody fragments (e.g. fabs) and agonist/antagonist pMHC, which have shown no consistent rearrangements in the V$\alpha\beta$ CDR loops or any other part of the molecule compared to the unbound state [204]–[209]. The small differences at the binding interface are likely just a result of the structurally heterogeneous nature of the variable regions of the TCR. It should be noted that a small and reversible structural rearrangement in the AB loop of the membrane proximal Cα domain was found in one case, although how this rearrangement would be translated to increased kinase recruitment intracellularly remains unclear [210]–[212]. It was proposed that this loop is involved in TCR dimerisation, although experimental evidence for this is largely absent [213]. The recent cryo-EM structure also showed no large conformational changes when docking a previous crystal structure of pMHC-TCR interaction to their TCR [159]. Unfortunately, because they fixed the TCR to ease complex purification it may have disrupted any potential conformational alternatives. A direct comparison of ligand bound and unbound quaternary TCR-CD3 complex is still required to settle this matter.

A conformational change in the CD3ε intracellular domain was reported, where anti-CD3 Fab ligation led to increased recruitment of the kinase Nck to a now exposed PRS on CD3 [214]. Using a nuclear magnetic resonance structure and *in vivo* Förster resonance energy transfer-based assay another group showed that the basic residues of CD3ε associated with acidic lipids in the inner leaflet of the membrane, and mutating these basic residues disrupted association [215]. Similar findings exist for CD3ζ [216], [217]. The model for triggering suggests the CD3 intracellular domains form a 'safety-catch', with ITAM domains embedded into the inner leaflet of the membrane, only accessible when forces applied to the TCR tangentially or normal to the membrane induce its release [218]. However, these models were inconsistent with the effects of the treatment of T cells with the phosphatase inhibitor pervanadate, or a Csk inhibitor (which negatively regulates Lck), both of which lead to *de novo* signaling by the TCR [192], [219]. Furthermore, by creating large close contact zones through signaling-deficient adhesion molecules, a high proportion of cells can trigger in the complete absence of ligand [116]. These lines of evidence argue against the mechanosensory/conformational change model because the receptor should have remained inaccessible to Lck.

Aggregation model

Clustering of the TCR would lead to a local increase in Lck substrate, increasing the likelihood of downstream signaling. Data in support of aggregation is mostly derived

from non-physiological sources of TCR engagement. This includes antibody crosslinking, as well as pre-dimerisation and tetramerization of pMHC to crosslink the TCR [220]–[222]. As agonist pMHC is often in low abundance, has a low affinity, and is found as monomers on APC surfaces, it seems rather unlikely that even two productive TCR-pMHC interactions would occur within proximity of each other [223]–[225]. Weaker self-pMHC could be co-opted into making TCR aggregates (dimers) through the coreceptor, as proposed in the pseudodimer model, but coreceptor-pMHC interaction is very weak and the coreceptors are dispensable for triggering [176]–[179], [226]. In addition, the TCR can trigger and activate to a single pMHC (and even in the absence of ligand), which makes it difficult to envisage how aggregation is necessary for triggering [116], [227]–[229].

Kinetic-segregation model

The 'kinetic-segregation' (KS) model for receptor triggering proposes that TCR-pMHC binding occurs in small adhesion-mediated close contacts of T cell-APC membranes (~15nm). These close contacts lead to the lateral segregation of large inhibitory phosphatases (e.g. CD45; ~25-40 nm) away from the TCR. This is proposed to perturb the phosphatase/kinase balance between CD45 and Lck in favour of the latter resulting in a net increase in TCR-CD3 phosphorylation [201], [203]. The quantitative model for this assumes that if TCR can stay within this segregation zone for a threshold dwell time (determined by pMHC density and affinity) triggering will be achieved [124]. There are several lines of evidence in favour of the model: (1) CD45 segregation has been observed in close contacts, prior to signaling, TCR microclusters, and the immune synapse formed

by T cells or reconstituted cellular systems interacting with model membranes or APCs [85], [116], [119], [124], [230], [231]; (2) a loss of triggering through extending or shortening of the TCR ligand or CD45, respectively [116], [232]–[234]; (3) attaching large extracellular domains to Lck, causes a reduction in signaling [116]; (4) soluble monomers are incapable of triggering the TCR yet their surface-bound counterpart can [225]; (5) treatment with the drug pervanadate (blocks phosphatases non-specifically) leads to phosphorylation of the TCR [219], [235]; (6) the CD45 crystal structure shows that it is large and rigid supporting its passive exclusion within pMHC-TCR sized membrane gaps [116]; (7) CD45 is one of the most abundant membrane proteins, occupying as much as 10% of the surface area, with 2-3 CD45 per TCR [115]; (8) CD45 preferentially dephosphorylates the TCR over Lck [198]; and (9) the TCR is capable of being triggered in the complete absence of ligand, correlating with the degree of CD45 exclusion [116], [124]. This last point is especially important as ligand-centric models (conformational change and aggregation) fail to explain this observation.

Key criticisms for the KS model are that: (1) confusingly, CD45 appears to act as both a negative and positive regulator on T-cell triggering, whereby CD45 is required to help activate Lck by removing phosphate groups of Y505, preventing Lck from adopting a closed and inactive conformation [428]. This point may recently have been addressed by showing that CD45 acts as a 'signaling gatekeeper,' establishing the thresholds for triggering and activation by tuning the size of the active Lck pool, whilst also acting directly on the TCR to filter our weak signaling events [192]. (2) TCR triggering and downstream signaling has been seen in the absence of substantial CD45 exclusion on the

T-cell membrane using TIRFM in combination with supported lipid bilayers containing elongated monomeric ligands for the TCR [400]. However, exclusion of CD45 is likely to be difficult to observe from small initial contacts when considering the membrane topology and axial resolution of TIRFM. More advanced imaging analysis may be required to address this fully. In addition, CD45 must be imaged in the context of physiological contacts e.g. in the presence of small adhesion molecules like CD58, which likely enhance CD45 exclusion prior to TCR signaling [141]. Lastly, (3) CD45 exclusion has yet to be observed from early contacts (i.e. the contacts prior to antigen detection) made within a cell-cell context, although imaging cell-cell contact interfaces are starting to occur using more advanced microscopy techniques [122].

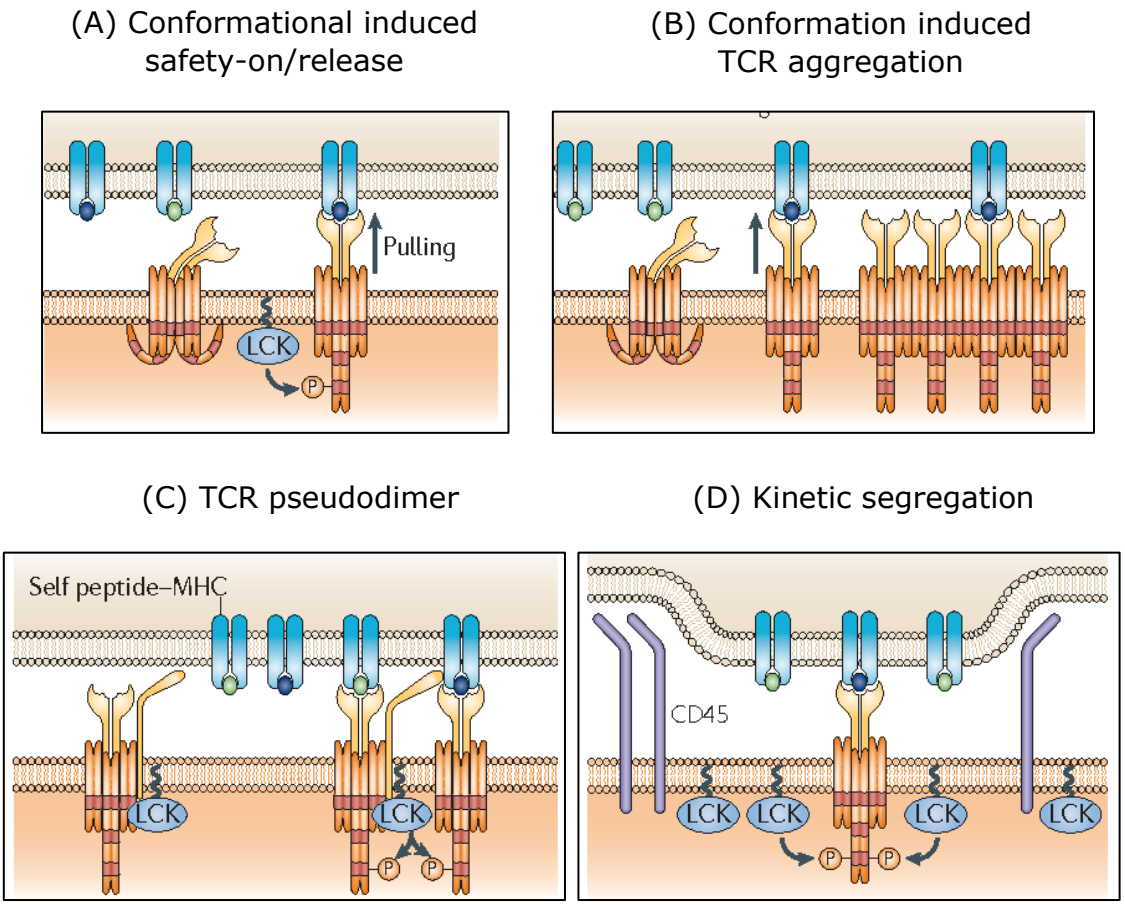

Figure 1.6. **Models of TCR triggering.** (A) Safety-on/release model suggests the ITAMs on the cytoplasmic domains of the TCR-CD3 are sequestered from Lck based on association of the intracellular domains with charged lipid species. Pulling forces (tangential or normal to membrane plane) cause dissociation of the intracellular domains, allowing access to Lck. This is also referred to as the piston-like model. Only pMHC of high enough affinity will bind long enough to allow the open conformation to persist long enough for triggering. (B) Another conformational change-based model whereby pulling forces alter the TCR structure to induce dimerisation, thus increasing the local Lck concentration at the ITAMs resulting in triggering. (C) Pseudodimer model suggests that rare high affinity pMHC lead to TCR dimers by co-opting weak/self pMHC-TCR interactions via the CD4/CD8 co-receptors. (D) The kinetic segregation model suggests that disruption of the kinase-phosphatase balance results in TCR triggering. This is achieved through segregation of large phosphatases from the small pMHC-TCR interactions. Image taken and adapted from [231]

1.4.3 Antigen discrimination by the TCR

The TCR is highly sensitive and specific, capable of responding to a single foreign antigen amongst 10^5-10^6 self-peptides per APC [229]. How the TCR achieves this sensitivity and discriminates foreign antigen from self so effectively has long been a matter of debate. Key is recognising the important biophysical parameters that govern the TCR-pMHC interaction, and how this relates to the mechanism of TCR triggering.

Sensitivity

TCR sensitivity may be achieved through several structural and functional mechanisms to amplify the signal from rare events. For example, the TCR has 10 ITAMs. This is distinct from other immune receptors, with the next highest being six, based on CD3ζζ homodimers pairing with other receptors (e.g. FcγRIIIa, NKp46 and NKp30), although most contain only one or two. More ITAMs were found to enhance the likelihood (i.e. potency), but not the magnitude, of signaling in T cells suggesting sensitivity of receptors is proportional to ITAM number [237]. Multiple ITAMs can also support the recruitment of possibly six ZAP-70 molecules to a single TCR, which are likely to be stabilised by their tandem SH2 domains, producing remarkably high levels of kinase activity [238].

Functionally, high sensitivity to a single antigen could be achieved by a 'serial rebinding' model [239]. As T cells can recognise a single antigen, and due to fast binding kinetics of the TCR (~0.1-10s bond lifetimes), a single foreign antigen could effectively bind and trigger multiple TCRs within proximity to each other [229], [238], [240]–[242]. This may

be plausible as the TCR was claimed to be enriched at microvillar tips, increasing the local concentration of TCR within close contacts scanning for antigen [123], [126]. CD2-mediated close contacts could stabilise microvilli to allow serial triggering of multiple TCRs within a contact. Mathematical modelling supports that serial triggering can occur, but it remains unclear whether it is necessary for activation [243], [244]. For it to be necessary, each TCR must show limited capacity for signaling, otherwise a single strong interaction would be enough to activate the cell. Limited capacity may derive from silencing of TCR bound to MHC via recruitment of ubiquitination pathway components to phosphorylated ITAMs [245]. A recent report found that limited signaling occurred at supra-physiological bond lifetimes (~60s) suggesting that serial triggering is important to the process of activation [246]. Furthermore, TCR-pMHC binding events that were close in both time and space, could be integrated to induce NFAT translocation into the nucleus of T cells [247].

Specificity

Another key property of the TCR is its specificity. The TCR recognises antigen with low affinity (1-100μM Kd) and is capable of discriminating antigens differing by a single amino acid [248]. As the difference in antigen affinity between foreign and self could be small (in one case a 5x increase in off-rate could abolish signaling) clearly the TCR must have a way to amplify small differences in affinity such that it is highly specific [249], [250]. Models proposed to explain specificity include kinetic proofreading (KPR) and although it has been argued that a segregation-based theory of signaling provides relatively high levels of discrimination, obviating a strict requirement for KPR [124].

Kinetic proofreading (KPR) and extensions of KPR

KPR was first invoked to explain the specificity to which the genetic code is followed during protein synthesis [251]. It was later applied to antigen discrimination in T cells [252]. KPR suggests that a small change in a TCR-pMHC half-life can be amplified to achieve high specificity with low error rates. In the original calculations, a 10-fold affinity change could result in >7500-fold difference in activation across six steps. This is achieved by a threshold dwell time for pMHC engagement. This dwell time is created through a series of biochemical steps, that are quickly reversed to the initial state upon removal of pMHC. Biochemical steps may include initial phosphorylation of the TCR, recruitment of Lck-coreceptor complexes, recruitment of ZAP-70, and the many steps between that and calcium release. A key prediction of KPR is that half-life of bound antigen correlates with T-cell activation, which was found to be the case in several studies [206], [247], [250], [253]–[257]. In contrast, other experiments showed antigens with short binding times could still activate cells [258]–[260]. This discrepancy may be reconciled if antigens rebind the same TCR after dissociation, integrating the total bond lifetime from multiple binding events dependent on fast binding kinetics to prevent diffusion away from the TCR ('confinement time model'; [258], [261]. Rather than binding the same TCR, binding different TCR within spatiotemporal proximity could also achieve a 'pseudo slow off-rate' if signaling hubs downstream of the TCR are shared by triggered TCR in proximity. This would require hubs to show some degree of hysteresis. However, integrating signals across rebinding the same or different TCR is at odds with kinetic proofreading, which assumes complete and immediate reversal of the

signaling upon dissociation of pMHC to maintain specificity. Whether this assumption is true across all stages of T-cell signaling is unclear. Although KPR is sufficient to explain high specificity, it sacrifices sensitivity [262]. Additional/modified models are therefore required to explain all the quirks of T-cell responsiveness.

KS model

Recently, Fernandes et al. (2019) established a KS based mathematical treatment whereby TCR dwell time within small microvilli close contact induced CD45 exclusion zones governs antigen discrimination (**Figure 1.7;** [124]). This model was established to relate the biophysical parameters of TCR-pMHC interaction with the observation that TCR triggering could occur independent of ligand, dependent on large areas of CD45 exclusion [116]. The model suggests antigen discrimination must occur in size regulated contacts to prevent loss of antigen specificity. For example, a two-fold increase in contact diameter (and therefore CD45 exclusion zone) from 400 to 800nm resulted in a thousand-fold probability of TCR triggering, independent of antigen. Using known binding kinetics of agonist pMHC, the model could predict their potencies with high accuracy, suggesting TCR diffusion (altered by pMHC affinity and density) and geometry of microvilli contact zones are enough to explain the specificity of the TCR. Although the KS model argues against a need for KPR (as high specificity is set purely by TCR dwell time in the contacts), KS, serial triggering and KPR-based signaling are not mutually exclusive, as KS may just represent the first significant threshold in the process of antigen

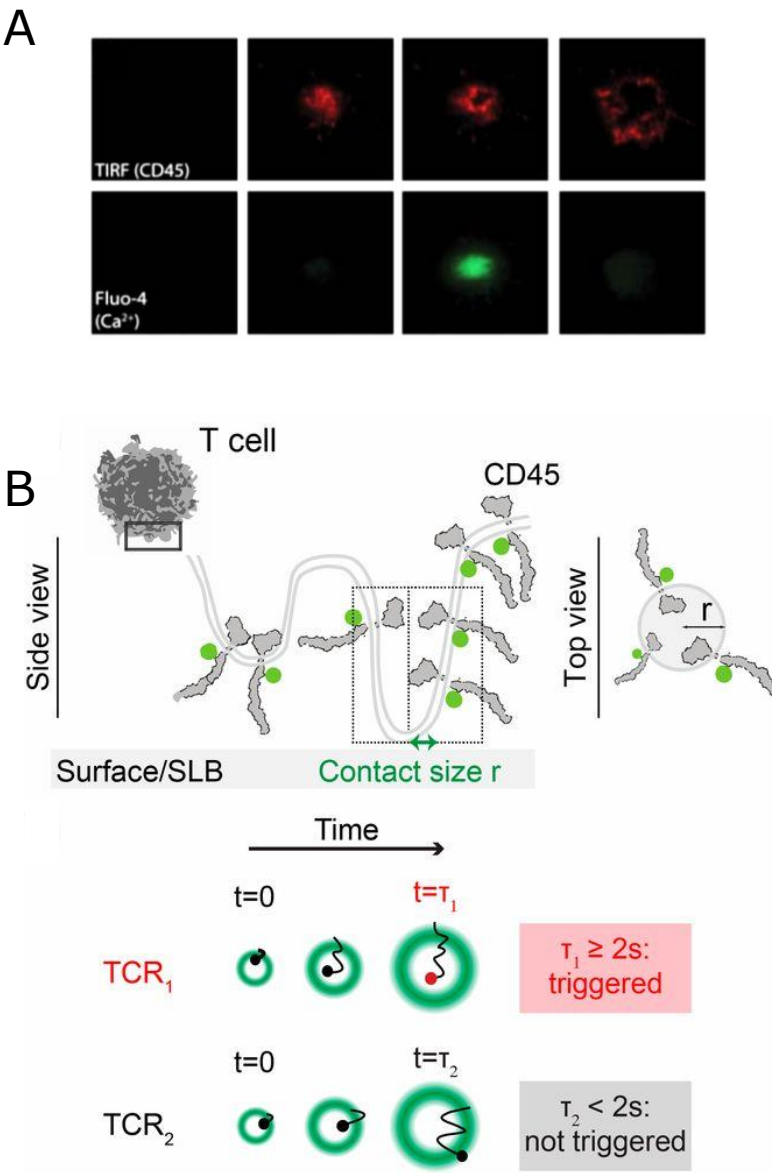

Figure 1.7. **Quantitative treatment of the KS model.** (A) TIRF imaging of T cells with fluorescently labelled CD45 and a calcium dye, dropped onto surfaces containing only small non-signaling adhesion proteins. CD45 segregation coincides with TCR-dependent calcium release in a ligand-independent manner. (B) Model for TCR triggering based on TCR dwell time within CD45 exclusion zones. If a TCR spend more than or equal to 2s within a CD45 exclusion zone the TCR will trigger. If it exits within 2s it will not trigger. The size of the contact, which alters the CD45/Lck balance, and the diffusion of the TCR, altered by pMHC density and affinity, will tune the time taken to respond, and the probability of reaching the temporal threshold, respectively. Figure taken and adapted from [115].

discrimination. This may be apparent at low ligand densities as the KS model achieves a 100-fold difference in TCR triggering probability with ligands differing 10-fold in affinity when presenting 100 antigens per APC [124]. Despite this, as the KS model only requires one step, the lower specificity is traded for a much higher level of sensitivity and therefore, perhaps, better reflects the sensitive and specific nature of the T-cell response. However, it is important that these predictions are tested in a ligand-dependent context (addressed in **Chapter 7**).

1.5 Studying T-cell-APC contacts

Although the key players in T-cell signaling and activation have been identified, a quantitative framework for the molecular events that take place between T-cell antigen scanning to synapse/kinapse formation remains elusive. Imaging *in vivo* forms the gold-standard for understanding T-cell contacts, however, it is very difficult to obtain molecular information in this setting, and most studies only obtain data relating to T-cell migration and trafficking. Analysis of the molecular events that take place between cell-cell interactions needs higher spatiotemporal resolution in highly controlled systems to provide any clarity. Despite recent advances, dissecting protein interactions between cells *in vitro* remains challenging because of opposing membrane topologies, receptor-ligand diversity, converging/diverging signaling networks, lipid heterogeneities, and the effects of the underlying cytoskeleton. Therefore, it is no surprise that over the last 40 years model *in vitro* systems with modifiable complexity have been, and will continue to be, essential for imaging live-cell contact interfaces. These systems include simplified

2D surfaces such as glass, glass-polymer surfaces, and supported lipid-bilayers (SLBs). Importantly, all are amenable to imaging techniques such as confocal, total internal reflection fluorescence microscopy (TIRFM) and super-resolution imaging.

1.5.1 Systems to study T cell-APC interaction

Glass surfaces

Glass surfaces provide an efficient method for imaging T-cell contacts. Glass is functionalised via adsorption of purified proteins or more commonly (and commercially available) antibodies against the surface protein of interest. This allows control over the density and variety of proteins to be studied. For example, coating glass with anti-CD3 (occasionally with ICAM-1) surfaces have proven useful for examining the composition of TCR microclusters and co-localisation of key T-cell signaling molecules in live T cells [92], [263], [264]. Glass surfaces are still used to image TCR microclusters and the actin cytoskeleton in live cells using TIRFM, or TCR valency in fixed cells using super resolution imaging [104], [123], [270], [271], [125], [165], [231], [265]–[269]. However, these experiments come with several caveats: (1) There is no way to control for spacing and orientation of proteins that adsorb to the glass surface. This could result in proteins stochastically being found in clusters; (2) proteins bound to glass are static. This simplifies tracking individual components of TCR microclusters, but the dynamics of contacts cannot be addressed. (3) antibodies (more commonly used) bind with typically non-physiological affinities and because they are bivalent, artificially cluster proteins. For example, anti-CD3 can lead to erroneous conclusions regarding the effect of the valency of the TCR. It also provides a potent stimulatory signal to T cells, and thus T-cell

responses may not be representative of what occurs in nature as their bona fide ligand is monomeric, monovalent and low affinity; (4) the glass surface is 10^5-10^6-fold stiffer than the membrane of cells. This is important because surface stiffness has been shown to affect T-cell activation.

Polymer surfaces

The stiffness of cell membranes is 0.1-1kPa whereas glass is 100GPa. Polyacrylamide (PA) or polydimethylxilosane (PDMS) can be used to tune surface stiffness to the physiological range, overcoming the rigid limitation of glass surfaces [272]. This is done by altering the amount of a crosslinking agent and curing temperature/time during preparation. Atomic force microscopy is used later to measure surface stiffness. These surfaces are functionalised by passive adsorption of antibodies/proteins, or by using biotin-streptavidin conjugation e.g. by incorporating streptavidin-acrylamide into the surface and later adding biotinylated proteins [273], [274]. Using lithography, PDMS surfaces can be endowed with topological complexity. For example, 1μm diameter x 1-5μm long micropillars functionalised with pMHC/anti-CD3 and ICAM-1 were created to study the tole of the T-cell cytoskeleton and membrane protrusions [102], [275]. Soft PA surfaces have also been modified to contain fluorescent beads, which can be used to measure forces created by T cells based on their displacement within the gel [270]. Despite their unique benefits, as with glass, proteins are static on these surfaces.

Glass-supported lipid bilayers (SLBs)

A powerful and established tool to study the molecular events at the T-cell surface is the glass supported lipid bilayers (SLBs), with the SLB frequently used as a mimic of an APC (and occasionally T cells). Three methods exist for creating SLBs. First, deposition of lipid monolayers onto hydrophilic surfaces from air-water interfaces can be used. A lipid bilayer is formed by depositing a second monolayer onto the first (the Langmuir-Blodget method). Second, spin-coating lipids (within a solvent i.e. chloroform/methanol) onto a cleaned surface is also effective. This process results in a dry lipid film that forms a lipid bilayer when resuspended in solution. Finally, vesicle fusion is used. This requires resuspending dried lipid mixes followed by sonication of the subsequently formed multi-unilamellar vesicles to produce small unilamellar vesicles (SUVs). Provided SUVs are added at high enough density they fuse to surfaces, such as glass, producing a lipid bilayer. SLBs can be functionalised by attaching purified GPI-anchored proteins or through producing proteins with modified tags that allow non-covalent (e.g. biotin-streptavidin) or metal chelation-based (e.g. his-tag-nickelated lipid) conjugation to modified lipids [276]. Regardless of attachment method, SLBs allow diffusion within a fluid two-dimensional plane. SLBs provide control over both the variety and density of proteins presented, thus proving a flexible system for studying all cell types. Unlike with glass, site specific attachment of proteins to the SLB ensures the protein is in the correct orientation. SLBs are especially amenable to TIRF microscopy, super-resolution imaging and biophysical imaging techniques (e.g. point fluorescence correlation spectroscopy (pFCS) and fluorescence recovery after photobleaching to study protein organisation and dynamics in T cells (pFCS is discussed below). However, as the separation of the

glass and lipid bilayer is only a 1-2nm hydration layer, only the extracellular domains, or intracellular domains of proteins are used due to the influence of the underlying glass support on protein diffusion. In addition, as SLBs are only ~5nm thick, cells will still experience the stiffness of the underlying glass substrate. However, previous workers have succeeded in preparing SLBs on PDMS surfaces, thus providing a method to maintain physiological surface stiffness and protein diffusion [277].

3D surfaces

The principles of 2D SLBs can be converted to 3D through the creation of giant unilamellar vesicles (GUVs) or glass/silica beads coated with SLBs [79], [119], [278], [279]. The former are commonly made through 'electroformation.' This involves coating (platinum) electrodes with a dry film of lipids, placing them into an aqueous environment (e.g. a high concentration of sucrose) and passing a current running through it. SLB-beads are formed by mixing liposome containing solution with beads. Both can be functionalised with proteins using similar bioconjugation methods for SLBs. GUVs have the added advantage of being a free-standing membrane and therefore have a more physiologically-relevant surface stiffness and deformability. They also are of comparable sizes to cells, which may better reflect the limited contact interface area that T cells experience. Although most imaging methods used on SLBs are applicable to live T cell-GUV/SLB-bead interactions, they cannot be used with TIRFM, which requires a 2D interface. Instead they are better for studying the activation of T cells and late-stage synapses with 3D imaging [278]. Nonetheless, TIRFM was used to image GUVs interacting with SLBs to study passive reorganisation of key T-cell surface proteins [119].

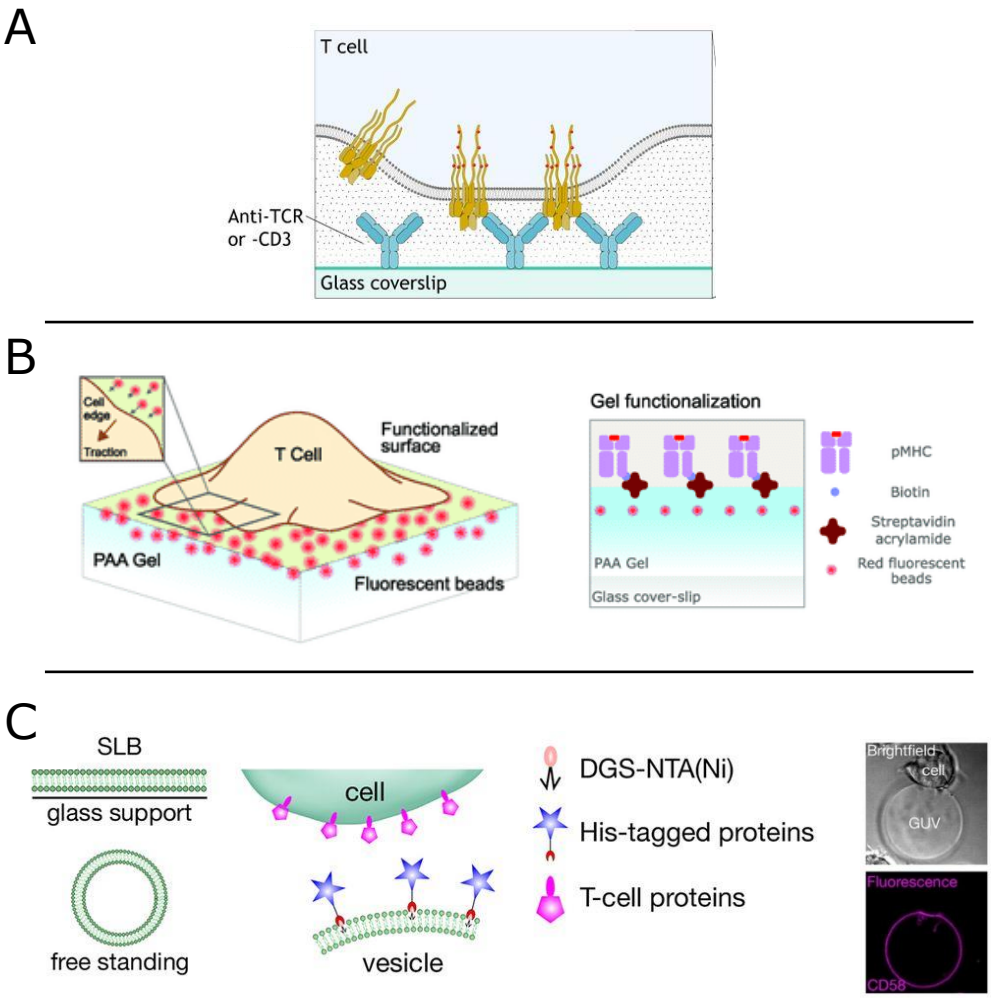

Figure 1.8. **Surfaces to image T-cell contacts.** (A) Glass surface functionalised with antibody. Advantage: efficient and cheap. Disadvantage: this setup artificially immobilises and crosslinks proteins of interest. Glass has a surface x10^6 stiffer than an APC membrane and is a metric known to affect T-cell activation. Image adapted from [272]. (B) Polymer surfaces (polyacrylamide, PAA) functionalised either by passive adsorption (not shown) or through biotin-streptavidin conjugation. Advantage: Can tune surface stiffness and has increased functionality for measuring force and influence of environmental topology on T-cell migration (not shown). Disadvantage: proteins are static so cannot be used to study dynamic contacts. Image adapted from [260]. (C) Glass-supported lipid bilayer (SLB) and free-standing membranes (GUVs) functionalised using biotin-streptavidin or nickel-his-tag conjugation. Advantage: proteins can diffuse in 2D plane. Disadvantage (SLB): has the same stiffness as glass. Disadvantage (GUV): can't be used with TIRFM. Image adapted from [272]. All surfaces have quantitative control over ligand density and variety presented to cells. All (except GUVs) are compatible with advanced imaging techniques such as confocal microscopy, TIRFM, and super resolution imaging.

1.5.2 Imaging techniques for T cell-APC interfaces

Epifluorescence

A variety of approaches exist for imaging T-cell contacts with model surfaces. One basic imaging technique is epifluorescence, which relies on exciting fluorophores and collecting their emission through the same objective lens. This technique led to the discovery of the immune synapse between T-cells and B cells [80]. The light sources are separated through dichroic mirrors, which allow passage of light with wavelengths above a cut off value and reflecting those below it. Excitation filters are used to select for a narrow band of light for illumination coming from a generic light source. This allows imaging of fluorescently tagged proteins within a cell, achieving a lateral (x-y) resolution of 200-300nm, but unfortunately a poor axial (z) resolution because emissions across the whole cell are collected when imaging a specific z-plane. In order to improve this, it is necessary to use lasers that provide monochromatic light sources, methods for filtering out-of-focus light (confocal), or illuminating only a portion of the sample at a time (TIRFM and super resolution).

Confocal microscopy

There are two main types of confocal microscopy: laser scanning (LSM) and spinning-disk (SDM). Both types use a monochromatic laser source and decrease out-of-focus light using pinholes. This leads to an increased signal/noise and axial resolution, but also results in a loss of signal intensity, although this can be compensated for by increased laser power. In LSM, a laser beam is passed through a pinhole aperture directed onto an objective which focuses the light into a single point on the specimen. The focused beam

is scanned across the sample to build up an image. Emitted light is passed back through the objective towards a second pinhole that is placed in a conjugated plane to the focus point (hence confocal microscope). This second pinhole blocks out-of-focus light above and below the focal plane, so that only light of 0.5-1μm in depth is taken from a given z-plane, unlike epifluorescence, which detects light across the whole sample. LSM allows higher axial resolution and is ideal for producing 3D images of cells. However, given the need to scan across the sample, temporal resolution is poor. Using SDM can mitigate this but requires sensitive cameras due to reduced transmission of light to the sample. SDM uses an expanded laser beam passing through two aligned disks, one containing a micro-lens and the second containing pinholes. An electric motor rotates the disks at high speed creating an array of focused light to scan the sample at multiple positions simultaneously. Not only does this provide high temporal resolution but also reduced phototoxicity and photobleaching to samples.

TIRFM

TIRFM provides high signal/noise and axial (z) resolution when imaging contact interfaces as it only produces a fluorescence excitation 100nm from the bottom of the cover-slip surface. This differs from epifluorescence (and to a lesser extent confocal imaging), which excites fluorophores within a large area of the cell resulting in high background fluorescence when imaging a specific z-plane. As a result, TIRFM can achieve 2000x lower background signal than in epifluorescence [280]. TIRFM relies on the principle of total internal reflection. When monochromatic light passes through an interface with different refraction indexes (e.g. at an air/water boundary) it will either

refract (pass through to the second medium but at a different angle to the incident light) or reflect. Whether refraction or reflection occurs depends on the angle of the incident light and the difference in refractive index between two mediums. TIRF requires the second medium to be of a lower refractive index. If the incident light is at a sufficiently high angle ('critical angle') the refracted light becomes parallel to the interface. Angles higher than the critical angle results in reflection. Although light doesn't pass into the second medium, it results in the release of electromagnetic radiation of the same frequency as the incident light, which decays exponentially with distance from the medium interface. This is referred to as an evanescent field (wave), and because of its exponential decay it is restricted to exciting fluorophores <100nm above the surface. This property makes TIRFM ideal for experiments with 2D surfaces and has been instrumental in identifying and studying TCR microclusters (discussed below). The drawbacks of TIRFM are that it cannot be used to study different planes of a sample, and that it is still diffraction-limited in lateral resolution (200-300nm). However, this limitation can be overcome when analysing low densities of fluorescently labelled molecules, allowing analysis of single-particle tracking dynamics.

Super resolution microscopy

The main super resolution techniques used to study T cells include single-molecule localization microscopy (SMLM) and lattice-light sheet microscopy (LLSM). SMLM includes photoactivated localisation microscopy (PALM) and stochastic optical reconstruction microscopy (STORM), which both allow the localisation of fluorescent molecules to a lateral resolution of <50nm, breaking the diffraction limit of 200-300nm

from epi/confocal microscopy and TIRFM. These techniques work by illuminating a stochastic array of fluorophores at one time. It requires specialised fluorophores that can be driven to a 'dark' state, with only small populations of fluorophores returning at each point in time. Provided each fluorophore that returns is sufficiently separated in space and time single molecules can be detected. If the cell is imaged for long enough the single particle positions can be reconstructed to produce a super-resolution image of the cell below the 200nm diffraction limit. These techniques have been used to study TCR valency and protein localisation, however they require the sample to be fixed [125], [160], [165], [231]. LLSM relies on creating a sheet of light for illumination (based on another super-resolution technique called structured illumination microscopy (SIM)) perpendicular to the image detector. It allows for quick and gentle exposure to light making it ideal for producing 3D images of live cells. This was recently used to study the dynamics of microvilli on the surface of T cells [122].

1.5.3 First generation glass-supported lipid bilayers

The most common combination of technologies to study T cell biology are SLBs and TIRFM. Although first observed in cell-cell contacts, a seminal Science paper published in 1999 by Dustin and colleagues brought to light the dynamics of the immune synapse between a T cell and APC [83]. They could observe the dynamics using TIRFM in combination with a glass-SLB containing two key proteins: pMHC and ICAM-1 (from here on referred to as first or 1st generation SLBs). For simplicity, it is noted that 1st generation SLBs also include systems which replace pMHC with anti-CD3 antibodies/Fabs. This approach was quickly ushered in as the dominant method for

studying key aspects of T cell-APC interfaces, and for the last 20 years it has yielded unparalleled insight into the composition and spatiotemporal dynamics of key T-cell receptors and signaling molecules (discussed in **Sections 1.3.6 & 1.3.7**; [83], [85], [141], [181], [238], [247], [268], [281]–[285], [86], [286], [287], [88], [89], [91], [94], [96], [97], [122]. Although substantial developments in SLB technology have occurred (e.g. nanostructured SLBs with grids and pillars, glycoprotein mimetics, PEGylation for surface passivation, DNA anchors, and ligands of different size), for the last 20 years the protein composition used in SLBs to study T cells has rarely expanded upon using one/two proteins at a time [327], [400], [417-420]. Furthermore, most studies have predominantly focussed on TCR microcluster analysis and synapse events wherein cells have spread minutes after antigen recognition has already occurred. As a result, this has left a large gap in our knowledge of the events prior to antigen detection where T cells must scan and discriminate between antigens. Although a few recent studies have tried to address this, they still utilise either antibody-coated glass surfaces or 1st generation SLBs, both of which do not accurately reflect the physiological T-cell experience [122], [125]. As discussed in **Section 1.4**, a myriad of factors are likely to alter the mechanics of antigen detection. In order to study the early events in T cell-APC contacts, SLB systems require increased protein complexity than in current use.

In 1st generation SLBs ICAM-1 is used to promote adhesion by binding the integrin LFA-1 on T cells. Although it is a key protein in synapse formation, the role of LFA-1-ICAM-1 interactions in early contacts is unclear. Studies indicate that LFA-1 affinity is only increased upon triggering/activation (inside-out signaling), and that LFA-1 is

concentrated at the cell body, away from microvilli [138], [288], [289]. It may be that LFA-1-ICAM-1 stabilises contacts only once cells identify their cognate pMHC. Combined with the different dimensions of LFA-1-ICAM-1 (30-40nm) vs. the TCR-pMHC complex (~15nm), the TCR is forced to perform both adhesive and antigen-sensing roles. T cells have already evolved a means for adhesion, i.e. the highly expressed protein CD2, that is quite distinct to the LFA-1/ICAM-1 system, especially with respect to its dimensions since the size of CD2-CD58 complexes is comparable to that of the TCR-pMHC complex (~15nm; [201]). This adhesion molecule likely stabilizes microvilli contact and scanning of the surface for ligands by the TCR. This is supported by CD2 enrichment on microvilli and widespread expression of CD58 [126], [290]. Few studies have incorporated this protein into SLBs, but in those that did, CD58 (or similar non-signaling adhesion proteins) studied in isolation formed large adhesive interfaces that led to strong signaling in a ligand-independent yet TCR-dependent manner [116], [124], [141]. Therefore, an SLB that is composed of pMHC, ICAM-1 and CD58 will experience strong stimulation irrespective of antigen. Although incorporation of CD58 is necessary, the loss of specificity means this cannot be a physiologically relevant surface, and therefore insufficient to study early T-cell contacts; additional components are required.

A key surface component thought to reduce overall adhesion, but overlooked in SLB experiments, is the glycocalyx. Depending on cell type, the glycocalyx can extend to 50-500nm out from the membrane, acting as a steric barrier contact formation [291], [292]. On both T cells and APCs this is composed of by the surface proteins CD43 and CD45 [115], [293]. CD43 is single-pass transmembrane protein containing ~80 serine/threonine

residues in its extracellular domain resulting in extensive glycosylation and functionalisation with negatively charged sialic acid residues [294], [295]. These glycan modifications constitute <60% of the mass of CD43. Due to its highly charged surface the protein is thought to stand up straight and was measured ~45nm tall [117]. Similarly, CD45 is a large, rigid and glycosylated single-pass transmembrane protein ranging from 22-40nm in height (isoform dependent; [116]). Given their high surface expression on both the T cell and APC surface, as well as their size, rigidity and negative charge these proteins could induce steric hindrance and charged-based repulsion between the opposing T cell-APC membrane interface, reducing overall adhesion. In accordance, several studies have shown the anti-adhesive properties of CD43 [111], [112], [296], [297]. Both CD43 and CD45 could conceivably block large adhesive interfaces, restoring antigen specificity, and therefore are essential to reconstitute into SLBs alongside CD58.

As mentioned in **Section 1.3.2**, T-cell ILPs/microvilli are suited to overcome the glycocalyx barrier surrounding cells to create close contacts that enable TCR-pMHC engagement [122]–[126], [231], [268]. Recent studies using 1st generation SLBs and antibody-coated glass surfaces have begun to address the characteristics of microvilli contacts, and although informative, studying microvilli is more appropriate in the context of a glycocalyx and adhesion protein for blocking and stabilising such contacts, respectively [122], [125], [231]. There remains much to be explored on the role of ILPs/microvilli in antigen detection. For example, productive signals, although likely, have not been directly shown to occur from ILP/microvilli under the physiological setting of low ligand for the TCR (rather than a high affinity and crosslinking antibody;

[125]). T cells can respond to as little as one pMHC on an APC [229]. Does this happen within ILP/microvilli contacts? As early T-cell signaling events are thought to be analogue in nature, characterising how ILP/microvilli scanning changes in response to differences in signal inputs (i.e. antigen density and affinity) will be informative of how T cells alter their scanning paradigms (i.e. random search vs. intense localised search) in the LN [70]. Lastly, if signaling is indeed initiated at ILP/microvilli, the methods by which the TCR discriminates foreign antigen from self are tied to the molecular events that occur there. Further characterising and imaging the relevant factors and functional outputs derived from ILP/microvilli contacts will help to elucidate the mechanism for antigen discrimination. These questions will be addressed in **Chapter 5-7** of this thesis.

1.6 Aims of the thesis

First generation SLBs have been a powerful tool highlighting how two proteins can drastically alter the behaviour of a T cell. However, as TCR is forced into a dual adhesion and antigen sensing role, and because it neglects the glycocalyx of the APC (and possibly every cell type), this surface is not wholly appropriate to study T-cell contacts. In order to advance our understanding of T cell biology, this thesis proposes to establish a new, more physiological SLB system; second generation SLBs. This system additionally incorporates two key APC membrane components: the small adhesion protein CD58, and the glycocalyx. Using this new setting, I will take advantage of the opportunity to study the competing effects of adhesion proteins, the glycocalyx, and different antigen density on T-cell contacts, signaling and antigen discrimination.

Chapter 2 Methods and Materials

2.1 Cell culture

General

Cell culture was performed in HEPA filtered cell culture cabinets. All media components were bought sterile or 0.22μm filtered before use. Cells were grown at 37°C in 5% $C0_2$. Cell density and viability was monitored with a 1:1 mix of cell culture media and 0.4% Trypan blue. Stained cells were analysed with a Countess II automated cell counter (ThermoFisher). Cells were sent and found negative for mycoplasma testing (Human Immunology Unit, WIMM).

Subculturing cell lines

Suspension cells such as Jurkat T cells and derived cell lines were cultured in RPMI-1640 media supplemented with 10% (v/v) fetal calf serum (FCS), 1% (v/v) HEPES buffer, and 1% (v/v) pen/strep/neo antibiotics (Sigma; complete-RPMI). Cells were maintained between 0.1-1x10^6/ml. PBMCs were kindly donated by members of Professor Graham Ogg's Group (WIMM) and used instantly. For the adherent cell line Human embryonic kidney 293T (HEK-293T), cells were cultured in Dulbecco's Modified Eagle Medium (DMEM) supplemented with 10% (v/v) FCS, 1% (v/v) pen/strep/neo antibiotics (Sigma) and 1% (v/v) glutamine (complete-DMEM). HEK-293Ts were passaged once reaching 80-90% confluency. This was achieved by removing their media, washing in sterile PBS, placing 3ml of 1x Trypsin (Sigma) onto the cells and incubating at 37°C for 5-minutes.

Cells were detached by gently shaking, and 12ml of complete-DMEM was added to inactivate trypsin. The cell suspension was harvested and diluted 1:10 into complete-DMEM in a new flask. This was performed every 72 hours.

HEK plating for lentiviral production

HEK-293T cells were detached and resuspended in fresh complete-DMEM (as above). Cells were counted using Countess II automated cell counted and $1x10^6$ cells were placed into 6-well (Nunc) plates. This was left for two days to achieve 80-90% confluency before transfection of lentiviral production plasmids.

Freezing and thawing cells

For long-term storage, cells were placed in liquid nitrogen tanks. $2\text{-}3x10^6$ cells were centrifuged (1300rpm, 5-minutes, 4°C), resuspended in 1ml of 90% FCS + 10% (v/v) DMSO (Sigma; freezing media), placed in cryovials (Starlab), and transferred to isopropanol-containing freezing containers (Mr. Frosty™ Freezing Container; ThermoFisher). Mr. Frosty was placed at -80°C for several days before transfer to liquid nitrogen tanks. To thaw cells, frozen tubes were placed at 37°C until the content was near defrosted. Thawed cells were transferred to 10ml of fresh complete media, centrifuged (1300rpm, 5-minutes, 4°C), and resuspended in another 5ml of fresh complete media. The next day an additional wash and resuspension step was performed with fresh complete media to increase cell viability.

2.2 Cloning

Overview

Cloning procedures were performed to either insert genes of interest (GOI) into cell lines, CRISPR knockout GOI, or produce proteins. GOI were amplified from cDNA or previously purchased templates (GenWiz or GeneArt Gene Synthesis; ThermoFisher)) using 5′ and 3′ oligonucleotide primers (Merck) in a polymerase chain reaction (PCR). Ordered templates and primers were designed *in silico* using SnapGene to ensure successful cloning. As the primers were designed with restriction enzyme sites, the amplified templates, along with the chosen vector plasmid, were restriction digested, and the now cut GOI was ligated into the cut vector. Newly ligated vector was amplified via transformation of bacteria, isolated from distinct colonies, tested for GOI insertion, and then sent for sequencing to confirm sequence integrity.

Vectors used in thesis

PHR: The pHR vector is a lentiviral vector derived from HIV. It is used in combination with plasmids pMDG and p8.91 to produce replication-incapable lentiviral particles for stable insertion of a GOI into target cell lines. The GOI is flanked by LTR sequences to allow insertion into lentiviral particles and is strongly expressed under the SFFV promoter. The vector confers resistance to ampicillin for selection in bacteria.

PHRi: Same as the PHR vector, however, contains an ecdysone inducible promoter to allow temporal control over GOI expression. The promoter requires the presence of RXR

and FB-ERV nuclear factors, as well as ponasterone to induce expression. Without these components, expression of the GOI is low in the target cell line.

LentiCRISPRv2: A vector designed for stable insertion of CRISPR/Cas9 for gene editing. The vector contains the Streptococcus pyogenes Cas9, and a restriction site for insertion of a 20bp target sequence adjacent to the gRNA scaffold. These sequences are flanked by LTRs allowing packaging into lentiviral particles. The plasmid confers ampicillin resistance for amplification in bacteria, and puromycin resistance for selection in targeted cell lines.

Primer design

Primers were designed with several key rules: 1) 15-60bp in length to reduce aberrant refolding and cost, 2) the 3′ end of each primer ended in a 'GC' clamp to increase specificity, and 3) both 5′ and 3′ primers both had a melting temperature between 55-68°C, which never differed by more than 5°C.

PCR and agarose gel electrophoresis

Each PCR reaction contained 100ng template, 0.5µM of forward and reverse primer each, 200µM dNTPs, 6mM MgSO4, 1xPhusion HF buffer, 0.3µl of Phusion High-Fidelity DNA Polymerase (NEB), and de-ionised water (MQ) for a 20µL total volume. The thermocycler programme was optimised for extension time and annealing temperature according to sequence length of the GOI and Tm of primers used, respectively. PCR products were run on agarose gel for identification of amplification success and

purification. Samples were run on 1% agarose (w/v) in 1x TBE buffer stained with 1xloading DNA gel stain (NEB). HyperLadder 1kb (Bioline) was run alongside samples at 110V for 30-minutes. Correct band sizes were detected using UV irradiation, excised, and purified using a PureLink® Quick Gel Extraction Kit (Invitrogen). DNA was stored in TE buffer at room temperature for immediate use or -20°C otherwise.

Restriction digest and ligation

Purified PCR sequence and vector plasmid were digested using appropriate restriction enzymes (NEB). Optimal buffer was chosen according to Double Digest Finder (NEB) and setup according to the manufacturer's guidelines. Other than the LentiCRISPRv2 plasmids that uses a single BsmBI to clone in gRNA sequences, all other cloning used two different enzymes for directional cloning. All of the GOI templates previously purified from gel electrophoresis were restriction digested, whereas 3µg of vector was cut. Cut samples were either purified directly or run on agarose before purification. DNA was ligated using T4 DNA ligase (NEB) according to manufacturer's guidelines. Ligation mix was left at room temperature for 1 hour and transformed in TOP10 *E. coli* for plasmid propagation.

Designing CRISPR guides

Sequences of genes to be knocked out were taken from Ensembl. Guides were designed and selected for high specificity with minimal off targets using CRISPOR and cross-referenced with CRISPR design feature in Benchling (hg38 reference genome). Several

guides were generated for each gene. Targeted sequences were chosen beyond the ATG start codon and within the first few exons. Oligos were then designed, annealed, and ligated into the LentiCRISPRv2 plasmid using the dual BsmBI sites, as previously described (Addgene plasmid 52961; [298], [299]). The lentiCRISPRV2 plasmid contains the CRISPR target sequence and Cas9 between long terminal repeats (LTRs) allowing production of lentivirus for stable insertion of the target sequence and Cas9.

Plasmid propagation

Using TOP10 cells, 1ng of plasmid DNA or 20µL of ligation mixture, was added to 20µL of competent cells. Cells were placed on ice for 15 minutes, heat-shocked at 42°C for 1 minute, then back on ice for 2 minutes. SOB/LB media was added, and cells placed back at 37°C for 1 hour. Mixture was plated out on LB plates with appropriate antibiotic and incubated at 37°C overnight. Positive colonies were grown in LB with appropriate antibiotic overnight in a 37°C incubator at 225rpm, and subsequently harvested using PureLink HiPure Plasmid Miniprep/Maxiprep Kit (Invitrogen). Purified DNA was collected in TE buffer. DNA purity (260nm/280nm ratio) and concentration was analysed using a NanoDrop™ (ThermoFisher). Plasmids with a purity >1.8 and concentrations above 100ng/µl were sequenced (Source BioScience).

Lentiviral transductions

$1x10^6$ HEKs in complete-DMEM were seeded onto 6-well plates 24 hours prior to addition of plasmids. After 24 hours, 0.5µg of pHR/LentiCRISPRv2-based plasmid were

co-transfected with vectors containing the lentiviral packaging proteins (0.5μg of p8.91 and 0.5μg pMDG). GeneJuice (Novagen) was used to transfect plasmid mixture according to manufacturer's protocol for adherent cells. 48 hours post-transfection, supernatant of the well was collected, filtered (0.22μm), and added to a 6-well plate containing 0.5-1x10^6 of Jurkat cells in 2ml complete-RPMI. 48 hours post infection 4ml complete-RPMI was added. Cells were analysed at least 72 hours post transduction. After 72 hours, CRISPR KO cells were further selected by treating with 1ng/ul puromycin in complete-RPMI for 3 days.

2.3 Phenotypic analysis

Flow cytometry

Cells stained using conjugated mouse anti-human antibodies (BioLegend) against indicated protein. 0.5x10^6 cells were counted, washed in PBS (0.01% NaN_3; PBS azide) then stained at 4°C for 1 hour using 1:100-500 dilution of antibody. Cells were washed x2 in PBS azide, fixed in 2% paraformaldehyde (PFA) and analysed by flow cytometry. For intracellular staining, 1x10^6 cells were washed in PBS azide and fixed in 2% PFA for 15 minutes. Cells were washed in intracellular stain buffer (ICS; 0.5% saponin, 5% FCS in PBS), then stained with 1:100-500 dilution of antibody in ICS buffer for 1 hour at 4°C. Cells were washed x2 with ICS buffer and fixed using 2% PFA. Cells analysed using LSR II, LSRFORTESSA (BD) or Attune NxT (Lifetechnologies). Fluorescent molecules were chosen such that little/no compensation was required. Data was analysed using FlowJo®. Cell sorting was performed by the WIMM FACS facility.

2.4 Protein production

Making protein

HEKs were grown to confluency in a T175 flask, detached, and transferred to a 6320cm^2 Nunc EasyFill Cell Factory with complete-DMEM (5% FCS). Cell factories were gassed with 5% CO_2 and left in a 37 °C incubator room. Once confluent (~3 days later), cells were transfected with 1mg of DNA. To transfect, 1mg of DNA was placed in DMEM, followed by 4mg of linear polyethylenimine (PEI) and left for 10 minutes at room temperature. The old complete-DMEM was removed from the cell factory, the DNA/PEI mix was placed in complete-DMEM (2% FCS) and added to the cell factory. The cell factory was gassed with CO_2 and left in the 37°C incubator room for 1 week before tissue culture supernatant (TCS) was extracted. TCS was centrifuged (2000rpm, 10 minutes) to remove cellular debris, sodium azide added (0.05% w/v) and stored at 4°C until purification.

His-tag protein purification

Proteins were designed with a 6xHis-spacer-6xHis c-terminus to allow nickel bead purification and bilayer insertion. 1.5xTCS volume of PBS azide (0.5M NaCl, pH 8, sodium azide 0.05% w/v) was added to the protein containing TCS. 5ml of Ni-NTA-Agarose (Qiagen) for every 1L of PBS-TCS was added and mixed overnight (4°C) at low speeds using a magnetic flea. Once settled, TCS-PBS-bead mixture was column filtered. Retained beads were washed with 50ml PBS and 10mM imidazole (in 1.5ml fractions) until A280 reading was ~0 to remove non-specific content. Protein was eluted using 250mM imidazole in 0.5ml fractions. Coomassie Staining was used to detect presence of

protein of the right band size in fractions. Positive fractions were pooled and concentrated using 10kDa Amicon filters. Fast purification liquid chromatography (FPLC) was used on concentrated protein to ensure monomeric proteins. This was performed on the AKTA pure Protein Purification System. The purification of monomeric protein was further confirmed by western blot. Proteins were stored at -80°C.

Coomassie

Protein was mixed 1:1 with reducing or non-reducing buffer (Bio-Rad) and then denatured by heating to 95°C for 5-minutes. Denatured protein was analysed on 12% sodium dodecyl sulphate polyacrylamide gel electrophoresis (SDS-PAGE). Proteins samples were run alongside the appropriate protein ladders (Bio-Rad). Gels were placed in Mini-PROTEAN® Tetra Cell (Bio-Rad) and run at 180V in Tris/glycine/SDS-PAGE running buffer until the loading dye in the reducing/non-reducing buffer had run of the gel (0.75-1 hour). For visualisation, gels were stained with Coomassie Blue solution (0.05% (v/v) Coomassie Brilliant Blue, 50% (v/v) methanol, and 10% (v/v) acetic acid), and subsequently de-stained (10% (v/v) acetic acid and 12% (v/v) methanol) to remove background and view protein bands.

Western blot

FPLC fractions of monomeric protein were separated by 12% SDS-PAGE. The Amersham ECL Rainbow Molecular Weight Marker (GE Healthcare Life Sciences) was

used as a protein ladder. Run samples were transferred to nitrocellulose blotting (0.45µm, GE Healthcare) membranes by electroblotting at 100V in ice-cold transfer buffer. Membranes were blocked in PBS containing 0.1% (v/v) Tween 20 (TBS-T) and 1% (w/v) BSA (Sigma) for 4 hours or overnight. Blocked membranes were stained with a 1:2000 dilution of HRP-conjugated primary antibody against 6xhis tag (abcam) in PBS + 1% BSA for 1 hour at 4°C under shaking conditions. Membranes were washed with PBS + Tween 0.05% (v/v) three times every 5-minutes before developing. Immunoblots were developed using ECL or ECL– plus (Amersham Biosciences) and exposed to CLXPosure films (Pierce).

Protein storage and use

Purified monomeric protein was concentrated to 1mg/ml for increased stability. Concentrated protein was then aliquoted into 10 or 100µl aliquots and snap frozen using isopropanol in dry ice and stored at -80°C. 10µl aliquots were for direct use, whereas 100µl was for labelling with organic dyes. In order to use the protein, the frozen tube was thawed at 4°C, centrifuged (13,000rpm, 5-minutes, 4°C) to remove any aggregates formed during the thawing process, re-aliquoted to a fresh tube, and had its concentration measured using a NanoDrop™ (ThermoFisher). After thawing, protein was labelled, re-aliquoted into 10µl and snap frozen, or used and stored at 4°C for two weeks before being discarded.

Protein labelling

Proteins were labelled using Alexa-fluor 488, 555 or 647 Antibody Labelling Kit (ThermoFisher) according to the manufacturer's instructions. Proteins were typically labelled at ≥ 1 dye per molecule.

2.5 Glass-supported lipid bilayers

Glass-supported lipid bilayers (SLBs) were prepared using vesicle fusion. Lipid mixture consisting of 98% (mol%) POPC (Avanti Polar Lipids) and 2% (mol%) DGS-NTA-Ni^{2+} (NiNTA; Avanti Polar Lipids) in chloroform were mixed in a round bottom glass flask and dried under a stream of nitrogen. 2% NiNTA was chosen to minimise unwanted interactions of the lipid with biological material (e.g. non-tag histidine within proteins and negatively charged sugars on cells) whilst allowing physiological densities of multiple his-tagged proteins to be attached to the surface [276]. The dried lipid mix was resuspended in 0.22-⌾m filtered PBS at 1mg/ml, vortexed, and tip sonicated for 30 minutes on ice to produce small unilamellar vesicles (SUVs). Glass coverslips (25 mm, thickness no. 1.5; VWR) were cleaned overnight in 3:1 sulfuric acid/hydrogen peroxide at room temperature, rinsed in MQ water, and plasma cleaned for 1 minute. CultureWell 50-well silicon covers (Grace Bio-Labs) were cut and placed on the washed coverslips (max 4/coverslip). SUVs were added to each well at a final concentration of 0.5 mg/ml (10 µl total volume) and left for 0.5–1 hour at room temperature. Wells were washed by removing and adding 5x5 µl PBS before adding proteins at the desired density. Double His_6 were used to tether the proteins to the lipid bilayer via interaction with NiNTA,

providing more stable binding to SLBs than single His_6 tagged proteins. Protein mixes were incubated with the bilayer for an hour at room temperature and washed in pre-warmed PBS or PBS + 2mM $MgS0_4$ (37°C) 5-10 times immediately before use. Fluorescence correlation spectroscopy (FCS) was used to relate protein concentration to density on the SLB.

2.6 Imaging techniques

Confocal imaging

Imaging was performed on either Zeiss LSM 780 Inverted, or LSM 880 with Airyscan (Carl Zeiss). Fixed cells were imaged using a NA1.4 63x oil immersion objective. Line scan averaging was set to a maximum of 16. Argon 488nm, DPSS 561nm or He-Ne 633nm laser power set at appropriate levels to reduce bleaching and oversaturation. For measurements, the pinhole was set to 1AU and a 488/594/633 MBS was used. In order to gain information on cell spreading and surface contact the confocal was setup to allow interference reflection microscopy (IRM) images. This was setup by choosing an appropriate emission filter that allows incident light reflected from the sample to be detected [300]. Cells were recorded for 1-minute. Images were analysed using Fiji.

Point fluorescence correlation spectroscopy (pFCS)

The Zeiss 780 equipped with a 40x water objective was used for pFCS measurements. Data was acquired on photon counting mode, using a 488/594/633 MBS, and a pinhole

set to 1AU. Excitation was performed with a 633nm He-Ne laser set at 1% power. To calibrate the confocal volume size, 100nM Alexa-647 dye in PBS was used. SLBs were allowed to acclimitise to 37°C before measurements were taken, and the z-axis was tuned to the highest intensity plane before imaging. Measurements were taken for 10s. Data was fitted and processed using both FoCuS_point or PyCorrFit software [301], [302]. pFCS data was exported to Excel to produce graphs in GraphPad Prism. Autocorrelation values G(τ) were fitted to the following equation:

$$G\tau = G0 * G_D(\tau) * G_T(\tau) + O_{ff} \quad (1)$$

The autocorrelation value at a given lag time τ is described by the correlation amplitude G(0) (at τ = 0s), the diffusive processes $G_D(\tau)$, the photophysics $G_T(\tau)$, and correlation offset O_{ff}. The density of protein can be obtained because G0 is inversely related to the average number of particles in the confocal volume ($G(0) = N^{-1}$). To obtain absolute density values the size of the confocal volume must be known. This is obtained from the calibration of free dye in solution. To obtain details on the confocal volume for 2D surfaces the following equation was used:

$$D = \frac{d^2}{8 * \ln * 2 * \tau_D} \quad (2)$$

The equation can be rearranged to identify d, which represents the beam diameter or observation spot size. This is obtained from an assumption of a circular cross-section at the centre and highest intensity region of a laser beam (i.e. a gaussian laser beam; one

with a transverse intensity profile that approximates a gaussian distribution). D is the diffusion coefficient that can be obtained from the literature. The transit time τ_D is the average time taken for a dye to pass through the confocal volume. This is obtained from fitting an autocorrelation plot and taking the decay time. Once the diameter is obtained, the 2D area can be calculated, and therefore the density of labelled and mobile protein on an SLB. The diameter for this setup was ~290nm.

Calcium release assay

Jurkats and derived cell lines were either labelled with Fluo-4 or were stably transduced with a genetically encoded calcium sensor (jGCaMP7s; addgene #104463). For Fluo-4, $1x10^6$ cells were washed x1 in PBS and placed in 1:1 mix of RPMI (no supplements)/2.5mM PBS-probenecid. 25µg/ml of Fluo-4 dye (final concentration; ThermoFisher) was added, and cells left for 15 minutes at room temperature. Cells were washed in pre-warmed (37˚C) PBS-probenecid and resuspended in the same. For the GECI, $0.25\text{-}0.5x10^6$ cells were washed x2 in pre-warmed (37˚C) PBS + 2mM $MgS0_4$, resuspended in the same and incubated for a further 5 minutes at 37˚C. Cells were carefully dropped onto the target surface and imaged using a 10x magnification objective for a larger field of view to simultaneously analyse 100-1000s of cells. Cells were imaged every 1s. Both Fluo-4 and GECI were excited using an argon 488 laser. Data was analysed through Fiji and bespoke MATLAB® scripts.

TIRF imaging

Three-colour live cell imaging of SLB-cell contacts was performed on a bespoke total internal reflection fluorescence (TIRF) microscope (Figure 2.1). The excitation path comprised laser lines of 488 nm (iBeam- SMART, Toptica), 561 nm (LaserBoxx, DPSS, Oxxius), and 641 nm (Obis, Coherent). Each beam was circularly polarized using quarter-wave plates, collimated and expanded. Laser lines were combined using appropriate dichroic mirrors and expanded further to reduce the flat-field variation. The lasers were aligned off-axis at the edge of the objective lens (100 Plan Apo TIRF, NA 1.49 oil-immersion, Nikon Corporation) and focused onto the backfocal plane to achieve TIR illumination. The objective was mounted on an inverted optical microscope (Ti2, Eclipse, Nikon Corporation). The fluorescence emission was collected through the same objective and separated from the excitation light via a dichroic mirror (Di01-R405/488/561/635, Semrock). It was further passed through appropriate filters according to the excitation wavelength, mounted in an automated filter wheel. The fluorescence was expanded (1.5x) and the image formed onto an electron-multiplying charge-couples device (EMCCD, Evolve 512 Delta, Photometrics) with an electron multiplication gain of 250 ADU/photon operating in frame transfer mode. This resulted in an effective pixel size of 106.7 nm.

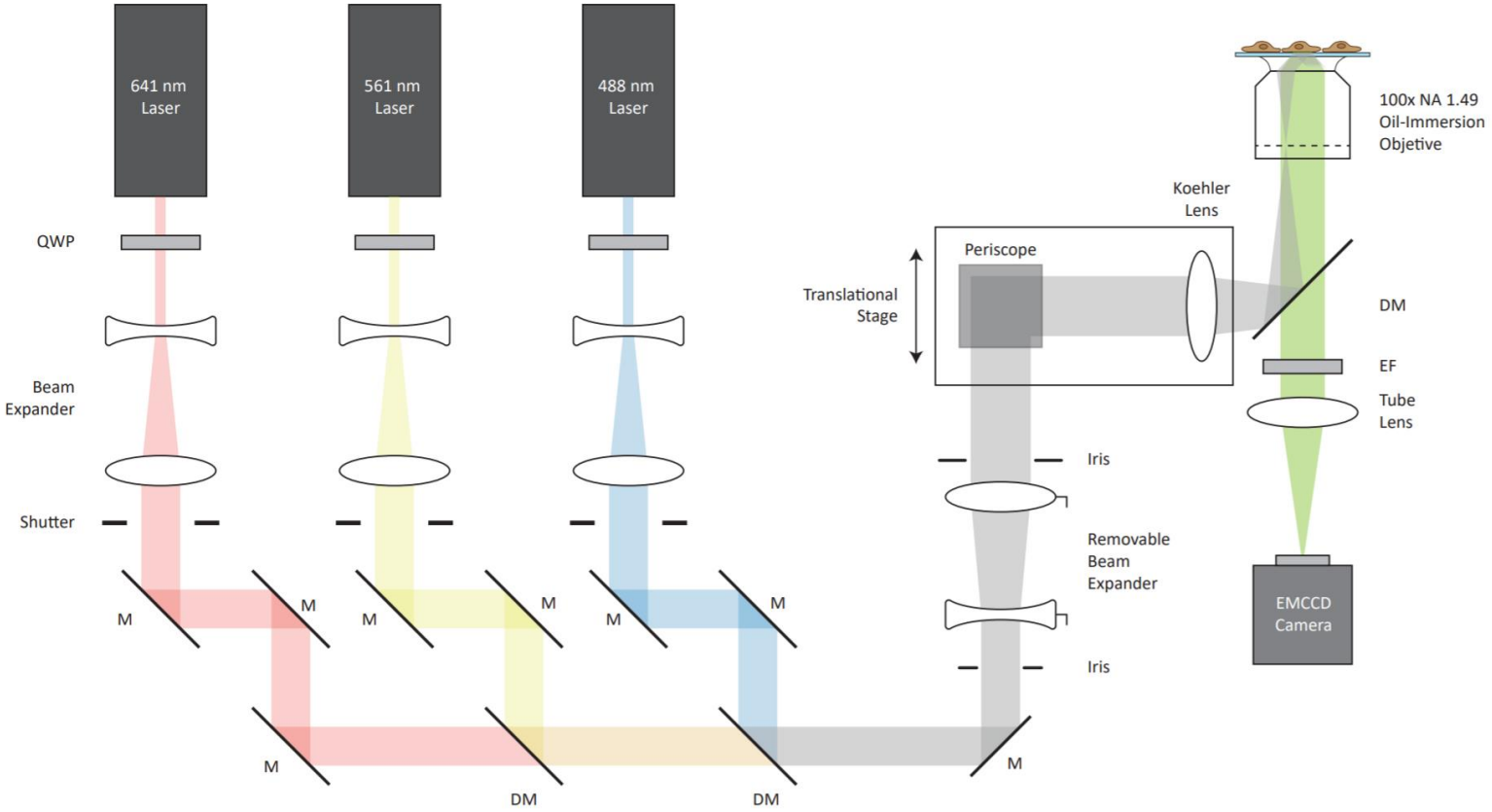

Figure 2.1. **Bespoke TIRF microscope setup**. QWP: Quarter-Wave Plate, M: Mirror, EF: Emission Filter, DM: Dichroic Mirror.

To allow for live cell imaging the microscope was enclosed with an incubator (DigitalPixel) and the temperature maintained at 37 °C. The focus was controlled with the Nikon Perfect Focus System. Image acquisition was automated using the open-source software ©Micro-Manager. Three-colour images were acquired sequentially at 0.5-2 Hz with 100ms exposure time. The laser powers were optimized to reduce bleaching while maximizing signal.

2.7 Image analysis tools

Automated calcium analysis

To facilitate the analysis of calcium responses across hundreds to thousands of cells an automated MATLAB© script was written by collaborators at the University of Cambridge (Jane Humphrey, Department of Chemistry, Klenerman laboratory). The script tracks the movement and fluorescence intensity of the calcium dye (or any fluorescent label) for 100-1000s of individual cells simultaneously. It first removes background, flat field corrects, and Gaussian smooths each video. Local maxima are then identified from the calcium signal, and the maxima from each frame are combined into contiguous tracks using a nearest-neighbour approach. The distance travelled and speed of each cell can be calculated. The time to adhesion is also calculated by a user-set threshold of speed, and when the cells speed drops and stays below this threshold for the remainder of its track a cell is classified as adhered. This was set at 0.2μm/s based on highly adherent interaction of Jurkats with unblocked glass. The mean intensity of the

calcium signal is tracked over time for each cell. The start of a calcium release (i.e. a proxy for TCR triggering events) are identified from a positive rate of increase in calcium signal from an identified background, calculated individually for each cell i.e. the lowest 10% of a cells fluorescence intensity typically derived from the first 30-60s a cell track. To control for any variation in baseline fluorescence levels, thus allowing comparison of calcium responses within and between samples, each calcium intensity trace is normalised by setting the baseline to one. User-set thresholds for identifying triggering events are also set e.g. minimum duration and fold change from baseline for each increase in calcium signal. These criteria were set stringently with a minimum duration of 10s and a fold change from baseline at 3 to remove false-positive increases in fluorescent signal derived from noise or cells landing on top/near each other. These thresholds were set based on comparing the results of automated vs. manual analysis of cell activation from several videos. Cells that showed calcium release within 40s of the start of their measurement track were excluded from the analysis. These cells (typically 5-10% of all cells) landed with a bright calcium signal that then faded over the course of the video. This gave the appearance of an initial calcium spike to the code and were erroneously detected as an activated cell. These cells may represent pre-activated cells derived from charge-based interaction with Eppendorf tubes or from pipetting. Overall, the code provides details on kinetics of movement, cell speed, adhesion, and cell activation as well as more in-depth details such as the strength of the calcium response e.g. height, length and integrated calcium increase. These metrics can be combined providing information about when cells respond relative to adhesion, and the probability of a cell responding based on its time adhered. The code is available on

GitHub and can be found at https://github.com/janehumphrey/calcium. Figures were produced using GraphPad Prism.

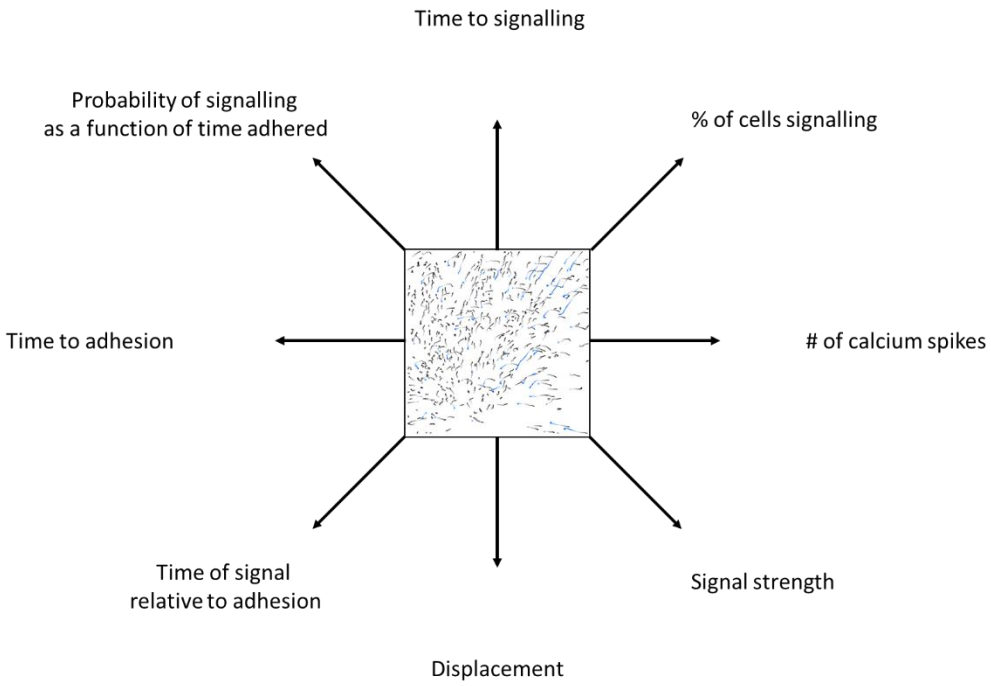

Figure 2.2. **Metrics analysed from automated calcium release analysis**. The analysis is described in the main text. The central box shows single black dots or black/bluelines, with each dot/line representing a single cell. Blue indicates a cell that has displaced more than a threshold distance. Each cell was tracked using the baseline signal from a calcium dye. By tracking both the movement and calcium signal various metrics could be obtained about the behaviour of the cell on the surface, the kinetics of antigen detection, and strength of signaling. The different metrics obtained are indicted surrounding the box.

Automated contact analysis

SLB-Cell Contact Analysis

Imaging data were visualised using the software Fiji (https://imagej.net/Fiji) /cite(doi.org/10.1038/nmeth.2019). Quantitative image analysis was performed with custom-written software in Python (https://www.python.org/)/cite(Numpy:

DOI:10.1109/MCSE.2011.37, Matplotlib: DOI:10.1109/MCSE.2007.55, Pandas: 10.25080/Majora-92bf1922-00a and 10.5281/zenodo.3509134, scikit-image: https://doi.org/10.7717/peerj.453, scipy: https://doi.org/10.1038/s41592-019-0686-2).

Image segmentation

Three-colour TIRF time-lapse images (with dimensions (x,y,t,3)) were used to analyse contact dynamics of SLB interacting T cells. The 641-excitation channel shows the T cell membrane, the 561 channel a protein of the SLB indicating close contact zones (CD43 and/or CD45RABC) and the 488 channel the intracellular calcium levels of the T cell. The cell membrane was used to identify a cell. To reduce noise and an inhomogeneous background a Difference of Gaussian (DoG) filter was applied framewise. A binary mask of the contact zones was created by a global threshold, small objects removed, and holes filled. Image segmentation was done with the Watershed algorithm in (x,y,t) dimensions. T cells interacting with the SLB will adhere to it, keeping their (x,y) position in the images and thus leading to well overlapping masks over t. Using a larger DoG filter on the last frame, cell positions were defined by the detected local maxima, separated by at least the cell radius, and used as seeds for the Watershed segmentation. Disconnected regions were assigned to the closest labelled region, not further than twice the cell radius measured as Euclidean distance in (x,y,t), and assigning them back tracing in time. To analyse CCZs the TIRFM images were first divided by the flat-field. The flat-field was obtained by summing and normalizing a separate image stack, taken before T cells were added to the SLB. A rolling ball filter was applied in (t), followed by a Gaussian filter in (x,y) on the corrected image stack. The Laplacian of the filtered image was calculated using the Sobel operator for partial derivatives. Via hysteresis

thresholding the images were binarized. The two thresholds were defined as $mean(I_{notCZ}) + h \cdot std(I_{notCZ})$, with $h = 2,4$ and I_{notCZ} all pixel intensities of the calculated Laplacian outside of contact zones. CCZs bigger than a minimum size were labelled based on the detected CZs.

Feature extraction and analysis

For each cell the calcium response was measured. The mean fluorescence intensity in a circle centred at the contact zone centroid was calculated for each timepoint. If a contact zones was missing at a timepoint, it was linearly interpolated from the next neighbouring centroids for that cell. The calcium trace was analysed the same way as in the bulk calcium assay to obtain the timepoints of calcium triggering and adhesion. Features for contact zones and close contact zones are based on area and intensity values. Exclusion values were calculated for each frame as $E = 1 - \frac{I_{inside}}{I_{outside}}$, with I_{inside} being the pixel intensities of the flat-field corrected image inside the CCZ masks and $I_{outside}$ being the mean intensity of pixels at the edge of the cell's CZs.

Chapter 3 Creation of a novel $CD8^+$ T-cell line and glass-supported lipid bilayer

3.1 Introduction

First (or 1st) generation SLBs (pMHC and ICAM-1) have been instrumental in understanding of T-cell activation (discussed in S**ection 1.5.3**). However, to better approximate the physiological surface of APCs, and to therefore better understand the key events occurring during antigen scanning, the strong foundations of 1st generation SLBs can be built upon by including small adhesion molecules and the glycocalyx. As these proteins are found on all nucleated cells of haemopoietic origins, new and more complex SLBs that incorporate these components will more faithfully reflect the types of surfaces a T cell will experience in the process of activation [303]–[306]. In addition to a more physiological surface, in order to examine antigen detection in a physiological context it also requires the use of natural ligand (i.e. pMHC) for the TCR. Compared with the difficulties in isolating and expanding primary T-cells, modification of cell lines with specific TCRs offer a very efficient approach for understanding T cell/surface contacts. The key cell line that has been the mainstay for understanding T cell biology is the Jurkats, originally isolated from the peripheral blood of a 14-year old boy with leukemia [307]. Given their extensive use and ease of genetic manipulation, these cells are now well characterised, offering a very good model to study the early events in T-cell activation [308]. The first half of this chapter describes the creation and optimisation

of a novel $CD8^+$ antigen specific cell line derived from Jurkats (referred to as 'J8s') which we have used to allow antigen-dependent experimentation on SLB surfaces. The last half of this chapter describes the preparation of second (or 2^{nd}) generation SLBs.

3.2 Methods

Cloning and CRISPR

For knockout of Jurkat TCRα (TRAV8-4*01), TCRβ (TRBV12-3*01) and CD4 (UniProtKB P01730), guides were designed and selected for high specificity with minimal off targets using Benchling (hg38 reference genome) and CRISPOR. Oligos were then designed, annealed, and ligated into the LentiCRISPRv2 plasmid using the dual BsmBI sites, as previously described (addgene #52961; described in **Section 2.2**). Oligo sequences designed for direct annealing and ligation into LentiCRISPRv2 can be found in Table 3.1.

Knockout target	Exon	Sense	Guide sequence for cloning into LentiCRISPRv2
TCRα	2	Forward	CACCGGTTGCACCTCAGCAGAACCA
		Reverse	AAACTGGTTCTGCTGAGGTGCAACC
TCRβ	2	Forward	CACCGTATCCAGTCACCCCGCCATG
		Reverse	AAACCATGGCGGGGTGACTGGATAC
CD4	2	Forward	CACCGGGCAAGGCCACAATGAACCG
		Reverse	AAACCGGTTCATTGTGGCCTTGCCC
CD4	4	Forward	CACCGGAGGTGCAATTGCTAGTGTT
		Reverse	AAACAACACTAGCAATTGCACCTCC

Table 3.1. **CRISPR guides.** Forward and the corresponding reverse guide sequences were first annealed before ligation. Black sequences are the gRNA sequences whereas purple are base pairs added to allow for direct ligation of the annealed oligos into the BsmBI restriction digested plasmid.

Stable lentiviral insertion

For stable insertion of CD8α (UniProtKB P01732), CD8β (UniProtKB P10966), CD11α (UniProtKB P20701) and CD18 (UniProtKB P05107), the genes were cloned into a pHR plasmid backbone modified with a signal peptide taken from the pOPINVL plasmid. For stable insertion of the genetically encoded calcium indicator (GECI) jGCaMP7s, the sequence was cloned from the parent plasmid (addgene #104463) into the pHR plasmid backbone. Lentiviral particles were produced by lipid nanoparticle transfection into HEK293T cells (GeneJuice, Novagen). Three-seven days after lentiviral transduction, cells with gene/cas9-gRNA insertion were sorted by FACS and/or (for the CRISPR KO specifically) exposed to a puromycin concentration of 1ug/ml in complete media for 3 days. In the case of CD8 and LFA-1, transduced cells were sorted for expression levels comparable to PBMC-purified primary T-cells (donated by Clare Hardman, Ogg group).

Plate-bound calcium release assay

For glass triggering, OKT3 at 1ug/ml (200ul) in PBS was added to glass slides and left overnight at 4°C, washed 10x in PBS and resuspended in 200ul of PBS. $1x10^6$ cells were washed x1 in PBS and placed in 1:1 mix of RPMI (no supplements)/2.5mM PBS-probenecid. Fluo-4 dye was added, and cells left for 15 mins at room temperature. Cells were washed in pre-warmed (37°C) PBS-probenecid and resuspended in the same. To ensure fair comparison to Fluo-4 labelled cells, GECI-containing cells were subject to the same protocol except cells were placed in RPMI (no supplements) for the incubation step and were washed and resuspended in pre-warmed (37°C) PBS (no probenecid). Cells

were then taken to the microscope and left for 5 minutes in the 37˚C incubator prior to use. $5x10^4$ were dropped onto bilayers and recorded immediately. In experiments where only the GECI was tested, the incubation step in RPMI was omitted, and cells were washed x2 in pre-warmed (37˚C) PBS prior to their 5-minute incubation and use. Images were taken at 10x magnification every 1s on a Zeiss 780 Scanning Confocal. Percentage of cells that showed a Ca^{2+} signal and response time distributions were analysed using a bespoke MATLAB® script, as described in **Section 2.7**.

Producing pMHC

cDNA encoding extracellular domain (ECD) of HLA-A2 (residues 25-304, UniProtKB P79603) and beta-2-microglobulin (β2M, residues 21-119, UniProtKB P61769) were ligated into pET28a (+; kanamycin resistant) vector for expression in Rosetta 2 (DE3)pLysS competent *E.coli* (Merck). HLA-A2 gene was modified with a 6xHis-linker-6xHis (H6-linker-H6) at the C-terminus to allow insertion into NiNTA containing SLBs. To make inclusions bodies for separate chain purification: Cells were transformed with 250ng of vector DNA, heat-shocked at 42˚C and plated out on LB agar plates containing kanamycin (50μg/ml) and chloramphenicol (34μg/ml). Single colonies were selected and grown in LB (high salt; 1L de-ionised water contains 10g tryptone, 5g yeast extract, 10g NaCl) with kanamycin (50μg/ml) and chloramphenicol (34μg/ml). This was placed in a 37˚C shaker at 200rpm overnight. Overnight culture was diluted to 0.05 OD600 in 1L LB high salt (+ antibiotics) and grown till 0.6 OD600 (~2 hours). 1μM IPTG (final concentration) was added to induce expression of T7 RNA polymerase under the lacUV5 promoter increasing expression of the HLA-A2/β2M genes. After 4 hours at 37˚C and

200rpm, the culture was centrifuged (4000rpm, 4˚C, 12-minutes) and resuspended in pre-chilled (4˚C) 0.9% NaCl (in MQ water). Pellets were stored at -80˚C until use.

To isolate inclusion bodies, cell pellets were resuspended in 100ml of resuspension buffer (1L MQ water with 50mM Tris-HCl (pH 8.0), 100mM NaCl, and 12.5µg/ml DNase I) and homogenised by magnetic stirring at 4˚C for 30-minutes. Cells in suspension were lysed by being passed through a cell disrupter twice (28Kpsi), washing with MQ water and then resuspension buffer prior to use. Disrupted solution was washed twice by being centrifuged (15,000g, 4˚C, 10-minutes), resuspended in 3ml resuspension buffer and homogenised. After the second wash pellets were resuspended in 1ml with 10ml EDTA/urea denaturation buffer (250ml MQ water with 120.12g urea, 50mM Tris-HCL, 10mM EDTA pH 8.0) and left to incubate at room temperature overnight. Suspension was centrifuged (15,000g, 4˚C, 10-minutes), with the supernatant containing protein of interest in inclusions bodies filtered (0.2µm) and concentrated using an Amicon 10kDa Ultracel-10 membrane (Millipore) to either 15mg/ml (HLA-A2) or 10mg/ml (β2M).

MHC refolding: 1mg gp100 peptide (YLEPGPVTV; Genscript) as well as 15mg HLA-A2-H6-linker-H6 and 6mg β2M inclusion bodies were separately placed into 50ml falcons containing 15ml EDTA/urea denaturation buffer with 150µl 1M DTT. These were incubated at 37-42˚C for 30-minutes to denature the proteins. Proteins were placed sequentially (peptide - β2M - HLA-A2-H6-linker-H6) into 200ml of pre-chilled (4˚C) refold buffer (1L MQ water with 100mM Tris-HCL, 1.2M L-Arginine, 2mM EDTA, 1.14g

cysteamine hydrochloride (added 30-minutes before use) and 0.23 cystamine dihydrochloride (added 30-minutes before use) and magnetically stirred for 20 minutes at 4˚C. This mixture was placed into pre-prepared (boiled in 2% (w/v) sodium bicarbonate and 1mM EDTA pH 8.0) and pre-washed (de-ionised water) 12KDa cellulose membranes for dialysis (Sigma). Dialysis was performed in pre-chilled (4˚C) de-ionised water for four days, placed into fresh de-ionised after day three. After four days, dialysis buffer was exchanged for de-ionised water containing 10mM Tris-HCL pH 8.0 and left at 4˚C overnight. Dialysis membrane content was centrifuged (4000rpm, 4˚C, 20-minutes) to remove aggregate and the supernatant concentrated to between 20-40 A280 values using Amicon 10kDa Ultracel-10 membrane filters (Millipore). Concentrated protein was subject to FPLC.

Protein purification

ICAM-1, CD45RABC, CD58, and CD43 were purified by ion exchange chromatography using nickel beads (described in **Section 2.4**). Monomeric proteins (those just listed and refolded pMHC) were obtained using FPLC with positive fractions tested to be monomeric via coomassie staining. Positive fractions were pooled, concentrated to 1mg/ml in PBS, snap frozen, and stored at -80˚C.

Monocyte-derived dendritic cell creation and surface protein density calculations

Monocyte-derived dendritic cells (moDCs) were produced by isolating human monocytes from PBMCs using a Ficoll gradient and $CD14^+$ $CD16^-$ magnetic bead

isolation kit (Miltenyi). Purified monocytes were grown at $1x10^6$/ml in RPMI 1640 supplemented with 10% (v/v) FCS, 1% (v/v) sodium pyruvate, 1% (v/v) HEPES, 1% (v/v) pen/strep/neo antibiotics (Sigma), 1% (v/v) L-glutamine at 37°C with 5% CO_2. To differentiate monocytes into immature moDCs recombinant human Il-4 (500U/ml) and GM-CSF (800U/ml; both Miltenyi) were added to the media for one week, with fresh media and cytokine mix added on day three of seven. On day 5, spent media was replaced with fresh media containing the cytokines and 1μg/ml of LPS (Sigma) to create mature moDCs. These were analysed by flow cytometry for surface expression of key proteins to place on the SLB. In order to gain estimates of protein density BD Quantibrite PE calibration beads were used to obtain total values for surface proteins. This was done according to the manufacturers protocol. A rough value for their surface area was obtained by using the median diameter for the distribution of mature moDCs from a Countess II automated cell counter. This gave a value of ~10μm, consistent with that measured in the literature [309], [310]. This was converted to surface area using the equation for the surface area of a sphere ($4\pi r^2$).

Creation of 1st and 2nd gen SLBs

2% NiNTA SLBs were produced and proteins incubated on the surface as described in **Section 2.5**. 2nd gen SLBs were made by substituting null pMHC with CD58, CD45 and CD43. 2nd generation SLBs still contained high densities of null pMHC after doing so. To obtain the proteins within the densities ranges consistent with moDCs, different combinations of protein concentrations were tested and analysed using pFCS. To obtain the most accurate readout one protein was labelled with Alexa-647 at a time while the

others were unstained. To obtain the other protein densities for a given set of protein concentrations the Alexa-647 labelled protein was switched to an unstained one at the same concentration, and a previously unstained protein was switched for an Alexa-647 labelled one. For 1st gen SLBs, three separate SLBs were produced to test one concentration set, whereas 2nd gen SLBs required six. This was repeated until the desirable and more physiological protein densities were found. The final concentrations and densities used for 1st and 2nd gen SLBs are shown in **Table 3.2**.

Protein	Concentration (ng/μl)	Concentration (nM)	Density (/μm²)
Agonist pMHC (9V)	0-1	0-20.87	0-100
Null pMHC	11-12 (1-0 agonist)	229.60-250.47	> 2200
ICAM-1	1.2	23.05	400-600

Protein	Concentration (ng/μl)	Concentration (nM)	Density (/μm²)
Agonist pMHC (9V)	0-1	0-20.87	0-100
Null pMHC	9-10 (1-0 agonist)	187.86-208.73	>1700
ICAM-1	1.2	23.05	400-600
CD58	0.5	19.77	200-300
CD45	2.5	37.93	250-350
CD43	1.5	57.87	300-400

Table 3.2. **Concentrations for 1st and 2nd gen SLBs.** Top and bottom table are for 1st and 2nd generation SLBs, respectively.

Point fluorescence correlation spectroscopy (pFCS) measurements

2% NiNTA SLBs containing 1ng/μl Alexa-647 labelled CD58 were tested with pFCS over 1 hour at 37°C. SLBs were made in PBS but then washed and recorded immediately in one of four different media: PBS, PBS + 2mM $MgS0_4$, PBS + 2mM $MgS0_4$ + 1mM CaCl or RPMI (no supplements). Each SLB was measured 3x10s every few minutes in different locations on the SLB to obtain density curves over time.

3.3 Results

3.3.1 Creating an antigen specific CD8$^+$ T-cell line: the J8

For ligand-dependent interaction with the SLB, a Jurkat-based HLA-A2/NY-ESO-1-specific and CD8$^+$ T cell line named 'J8' was established. To create the cells endogenous Jurkat TCRα, TCRβ and CD4 were stably removed using CRISPR-Cas9 lentiviral plasmids, while 1G4-TCRα/β (which recognises tumour antigen derived NY-ESO-1$_{157\text{-}165}$ peptide (ESO-9C) in the context of HLA-A2) and CD8α/β chains were stably introduced using lentiviruses . The strategy for their creation is summarised in **Figure 3.1**. The 1G4-TCR is MHC-class-I restricted and was used because its binding kinetics and potencies to a broad range of peptides have been thoroughly characterised, allowing for quantitative analyses of antigen discrimination [261], [311]. As Jurkats are CD4$^+$, and the 1G4-TCR is class-I restricted, this required the cells to become CD8$^+$. To ensure only antigen specific TCR were present at the surface, CRISPR guide RNAs (gRNA) were first designed targeting the endogenous TCRα (TRAV8-4*01) and TCRβ (TRBV12-3*01) chains. Both chains were separately removed using a single guide targeting exon 2 that was designed to have high on rates and low off target effects. This was achieved using a lentiviral vector for stable insertion of Cas9 and the gRNA (LentiCRISPV2) for each chain. As every chain of the oligomeric TCR-CD3 complex is essential for transport the membrane surface, removal of either the TCRα or TCRβ chain creates difficulties in assessing the removal of the other as the complex will no longer be expressed at the surface. This was overcome by knocking out the endogenous TCRα chain followed by sorting on the CD3$^-$ negative population, and subsequent insertion of the 1G4α chain.

This process was repeated for the endogenous TCRβ and 1G4β chains (**Figure 3.1, first row**). 1G4-TCR specificity was confirmed by staining the cells with tetramerised peptide loaded major histocompatibility complex (pMHC). Tetramers were used owing to the typically low affinity of single pMHC for the TCR (1-100μM K_D). To produce the tetramers, previously purified pMHC loaded with the HLA-A2/NY-ESO/altered-peptide ligand 9V (SLLMWITQV, 7.2μM K_d) was biotinylated via a C-terminus BirA tag on the alpha chain and mixed with Alexa-647 labelled streptavidin at a 1:5 ratio (streptavidin:pMHC). Staining occurred only when both chains were present, which was tested by inserting either the 1G4α or 1G4β chain into a Jurkat cell line with both TCRα and TCRβ knocked out (**Figure 3.1, second row**). CD3 expression after both 1G4α and 1G4β chains were inserted remained comparable to endogenous levels (**Figure 3.2**). A TCR deficient version of the J8s was also created ('$J8^{TCR-}$'), the only difference being that the endogenous TCRα and TCRβ chains were knocked out simultaneously. This was possible as loss of either chain prevents TCR expression. Cells were selected using puromycin and then sorted for the $CD3^-$ population.

Next CD8α/β chains were introduced to ensure heterodimer formation (**Figure 3.1, third row)**. This was necessary because CD8α chains have a propensity to form homodimers in the absence of the CD8β chain [312]. The expression of the CD8αβ heterodimer was then matched with human PBMC-derived $CD8^+$ T cell levels (selected by gating PBMCs on $CD3^+$ then $CD8^+$ cells) to ensure the levels were as physiological as possible. Lastly, CD4 was knocked out using two CRISPR gRNAs targeting exon 2 and 4, with the

negative populations of cells sorted for (**Figure 3.1, fourth row**). This same procedure was then repeated, i.e. CD8 replaced CD4, in J8^{TCR-} cells.

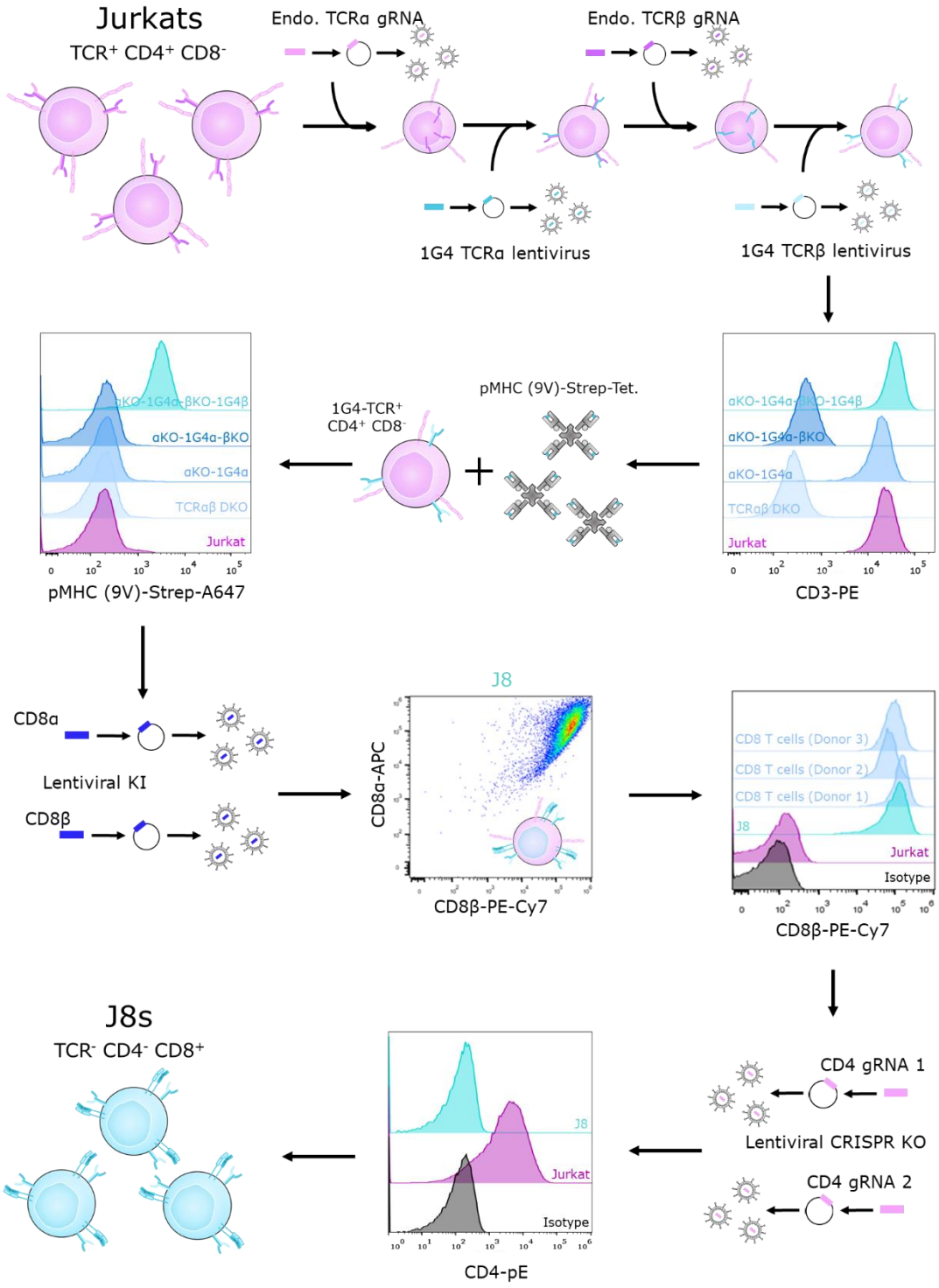

Figure 3.1. **Creating J8s: a 1G4-TCR-specific CD8$^+$ T-cell line.** Jurkats were transduced, alternating between lentivirus containing gRNA-cas9 to knock-out the endogenous TCRα and TCRβ chains, or lentivirus for stable knock-in of the 1G4α and 1G4β TCR chains. This was done to ensure knockout as cells could be sorted on negative CD3 expression for each chain. To confirm specificity in the J8 cells, pMHC (9V, 7.2µM K_d) was biotinylated, tetramerised by Alexa-647 labelled streptavidin, and use to stain the cells. Next, CD8α/β chains were introduced, and confirmed as heterodimers given the propensity for CD8$\alpha\alpha$ homodimers to form in the absence of CD8β. Expression was sorted to match human-PBMC derived CD8$^+$ T cell levels. Lastly, human CD4 was knocked out using gRNA-cas9 containing lentivirus, with cells sorted in bulk on negative CD4 expression without the need for further puromycin treatment.

3.3.2 J8s remains functional in early proximal signaling

J8s were tested for their expression of important surface and proximal signaling proteins as well as their proficiency at proximal signaling compared to the parent cell line (Jurkat). J8 cells exhibited no change from the parental line in their expression of major surface proteins (CD2, LFA-1, and CD45) or intracellular proteins (Lck and ZAP-70) despite extensive CRISPR-based modification indicating that the early signaling of the cells was unlikely to be compromised (**Figure 3.2**).

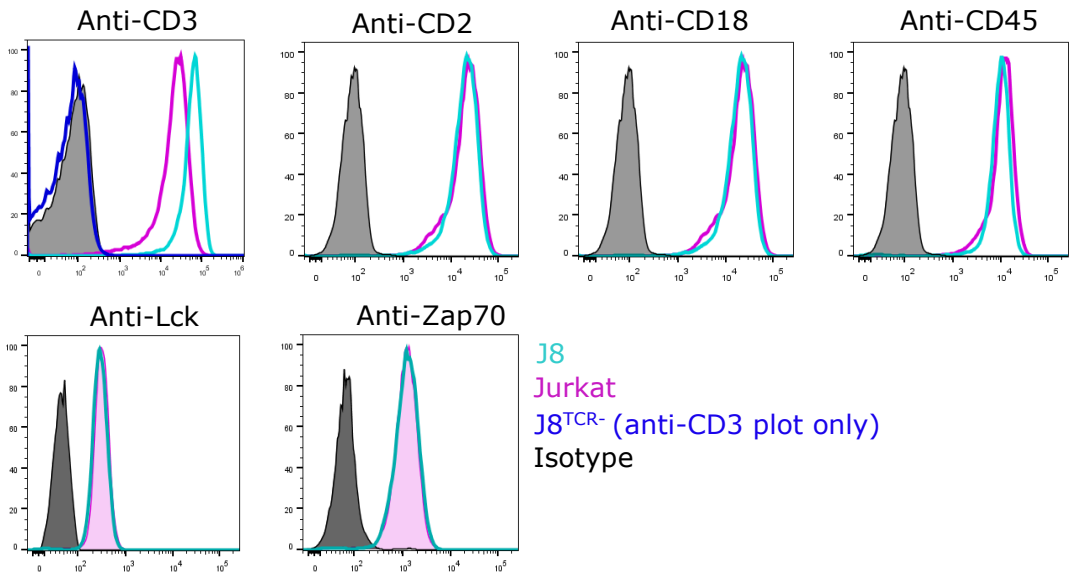

Figure 3.2. **J8s show preserved expression of early signaling proteins.** J8s were compared to Jurkats in their expression of major T cell proteins involved in early signaling by flow cytometry. The cyan, magenta and black lines are the J8s, Jurkats and isotype control, respectively. Anti-CD3 labelling of $J8^{TCR-}$s (dark blue line) was tested to show the loss of TCR-CD3 surface expression. Antibody staining showed there was no/minimal alterations to protein expression.

To support this, J8s were tested against Jurkats for activation by gently placing cells on anti-CD3 (OKT3) coated glass plates. OKT3 binds the CD3ε chain leading to crosslinking of the TCR-CD3 complex, producing signaling. As the focus of this thesis is to understand the initial events that drive T cell activation, cells were monitored only for intracellular calcium release (used interchangeably with 'Ca^{2+} signal' throughout the thesis). Calcium release was used as it occurs as soon as 6-7 seconds downstream of TCR ligation and, in combination with automated analysis, can be used to analyse many cells at the single-cell level simultaneously, allowing for robust statistics [74] **Figure 3.3**). Cells were loaded with Fluo-4, a non-ratiometric green fluorescent calcium binding dye, washed, resuspended in PBS with probenecid and deposited carefully onto wells coated with OKT3 at 37˚C for 10 minutes. Probenecid is required to prevent Fluo-4 leakage from the cytoplasm by inhibiting organic anion exchangers [313]. J8s exhibited no difference in their signaling ability (given as % of cells that show a Ca^{2+} signal) compared to Jurkats (**Figure 3.4**). The $J8^{TCR-}$ cell line was also tested as a negative control to ensure signaling was TCR dependent, and as expected, showed no calcium response (**Figure 3.4**). Overall, this established the J8s as a suitable $CD8^+$ T cell line for studying early signaling events.

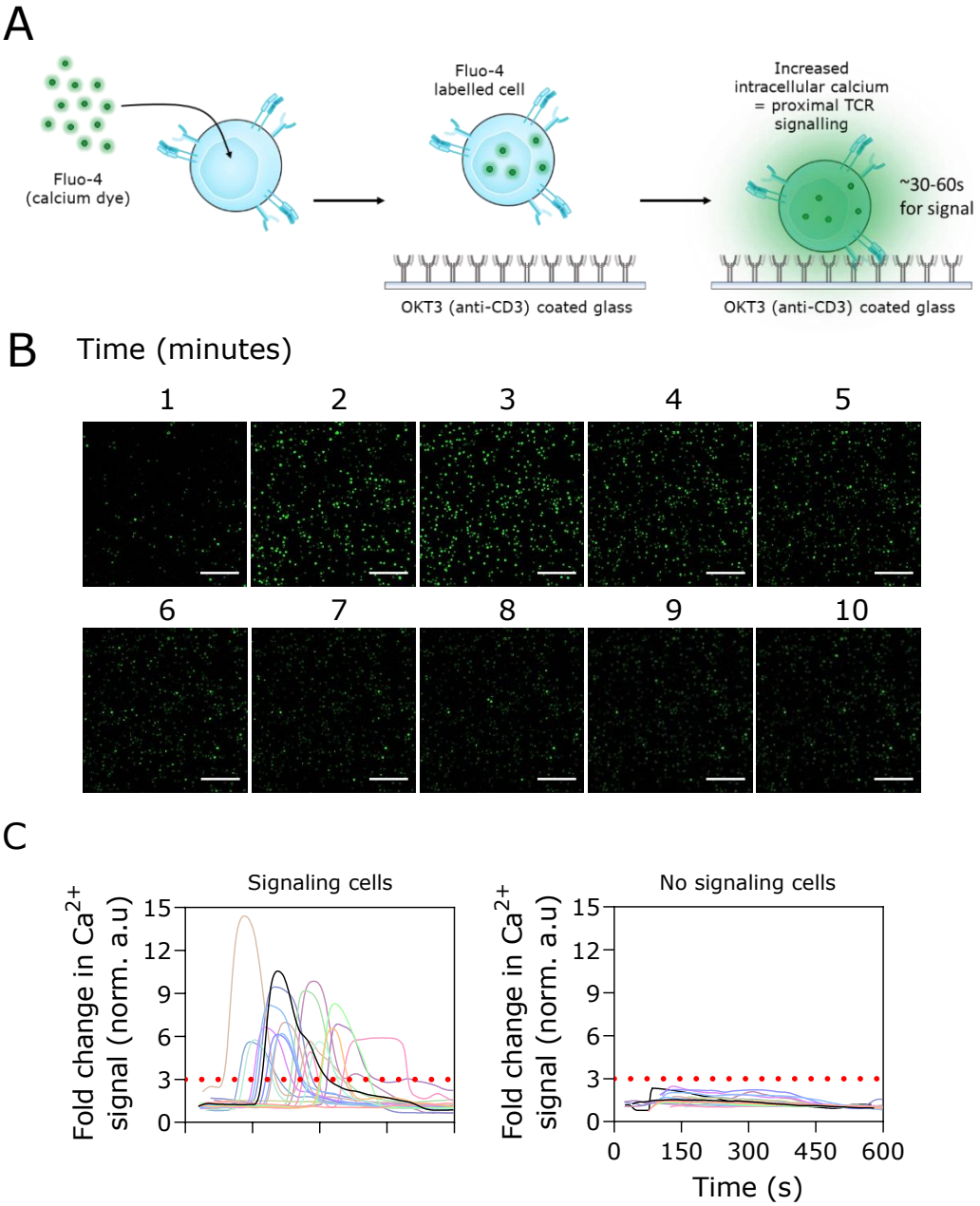

Figure 3.3. **Calcium release assay.** (A) cells are loaded with the chemical calcium dye Fluo-4 and dropped on anti-CD3 (OKT3) coated glass slides. (B) Example of cells landing and signaling as indicated by the bright green circles. Each circle is one cell. Scale bar 200µm. (C) Representative example of 20 cells that Ca^{2+} signal (left plot) and are unresponsive (right plot). Cells are considered responsive if the change in fluorescence signal is at least 3x the background fluorescence signal (described in **Section 2.7**).

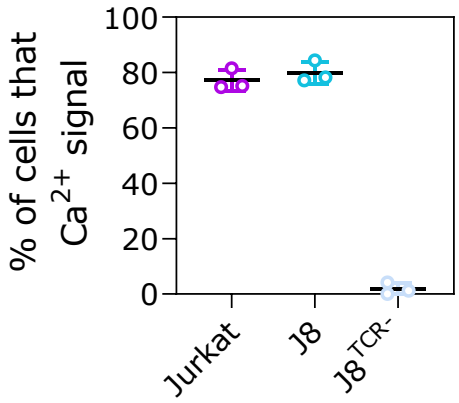

Figure 3.4. **J8s maintain capacity for proximal signaling**. Comparison of cells showing calcium release on OKT3-coated glass. n=300-500 cells for each data point.

3.3.3 Introducing a genetic encoded calcium indicator

As calcium release was a key experiment for the whole of this study, it was beneficial to streamline the experimental setup and analysis. To streamline the assay, the J8s were stably transduced with a genetically encoded calcium indicator (GECI; jGCamp7S; [314]; **Figure 3.5A**) and sorted for low expression to mitigate it's influence as a calcium sink within the cell (**Figure 3.5B**). This was important as intracellular calcium levels have been shown to influence events associated with T cell activation e.g. TCR microcluster formation, cytoskeletal activity, and early TCR signaling [76], [271] [315]. The use of the GECI had two main benefits; 1) it removed the time for dye incubation, limiting the preparation process of the cells to two washes straight from the incubator, and 2) it eliminated the need for toxic agents such as probenecid. An analysis of the responsiveness of cells based on GECI expression level was not performed, however the J8-GECI cells exhibited no change in the expression levels of key surface proteins compared to Jurkats, suggesting that there was no compensation or adaptation (**Figure**

3.5C). Furthermore, J8 cells labelled with Fluo-4 and J8-GECI cells show equal responses on OKT3 surfaces (**Figure 3.5D**).

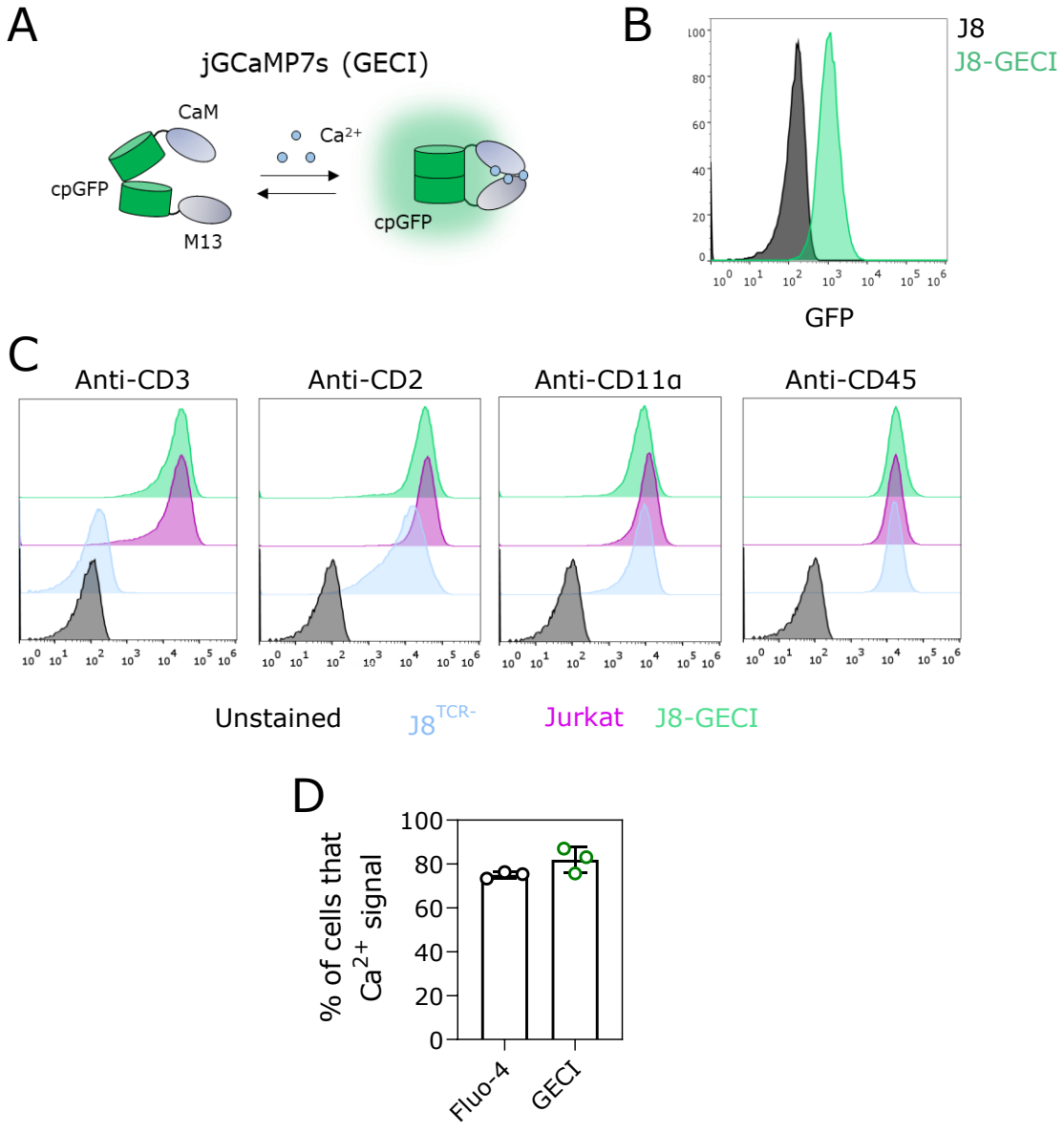

Figure 3.5. **Genetically encoded calcium sensor (GECI) for calcium release assays**. (A) The jGCaMP7s GECI is a circularly permuted GFP (cpGFP) modified with M13 synthetic peptide that binds the calmodulin domain in the presence of calcium. In the absence of calcium, it is in an open and weakly fluorescent conformation. Calcium causes a closing of the cmGFP increasing its ability to fluoresce. (B) The GECI was stably inserted into the J8s by lentiviral transduction and sorted on a low baseline expression (green distribution) that would still be visible above background. (C) J8-GECI surface phenotype remains comparable to Jurkats. (D) Percentage of cells that show a Ca^{2+} signal.

3.3.4 New glass-supported lipid bilayers

Ni^{2+} containing SLBs induce strong adhesion and TCR triggering

With the J8/J8-GECI cell line established, the next task was to build and optimise the 2nd generation SLBs. SLBs were produced by lipid vesicle fusion, which involves incubating vesicles on hydrophilic cleaned glass, which over time undergo adsorption and rupture forming the SLB. The major component of the vesicles is the lipid 1-palmitoyl-2-oleoyl-glycero-3-phosphocholine (POPC), which is a synthetic substitute of phosphatidylcholine, an abundant lipid species in the outer membrane of eukaryotic cells. As POPC is inert, and in order to add proteins to the bilayer, vesicles also contained the lipid DGS-NTA (Ni^{2+}; referred to as NiNTA from hereon). This lipid binds to 4 of the 6 coordination sites of a positively charged nickel ion, leaving the remaining 2 to bind two adjacent histidine residues. This allows attachment of purified proteins containing polyhistidine-tags (e.g. H6 tag) at their N- or C-terminus. H10 or H6-linker-H6 tags are more commonly used, however, to increase the binding stability of proteins to SLBs [316].

Given previous reports on the influence of surface charge causing unspecific T-cell calcium responses and activation, the basic SLBs were first tested for any unwarranted adhesion and signaling in T cells [317], [318]. Calcium responses for the J8-GECI cells were tested on glass, 100% POPC bilayers (referred to as 0% NiNTA SLBs), and functionalised 98% POPC/ 2% NiNTA bilayers (referred to 2% NiNTA SLBs; **Figure 3.6A**). J8-GECI cells with lower TCR expression ($J8^{Low}$-GECI) and no TCR expression

(J8^{TCR-}-GECI) were also compared to test whether signaling was TCR dependent (**Figure 3.6B**). The cells were tracked and analysed for both their kinetics of adhesion to the surface and % of responding cells over 10-minute videos. 'Displacement' tracks for all three cell lines across the three conditions were generated (**Figure 3.6C**). In the analysis, the tracks start out black and become bluer the further the cell becomes displaced over the course of the video. All three cell lines adhered strongly to both glass and 2% NiNTA bilayers (producing black dots) but were incapable of adhering to 0% NiNTA bilayers (series of long black and blue lines). Tracks could be quantified by analysing the time it takes cells to adhere (described in **Section 2.7**). The rate at which cells adhered to the surface was then presented as a cumulative distribution plot of % of adhered cells over time (not shown). The time for 50% of cells to adhere was used for statistical testing. Cells bound strongly to glass as 50% of J8-GECI, J8^{Low}-GECI and J8^{TCR-}-GECI had adhered by 5-18s. This was reversed on 0% NiNTA SLB with 50% of cells taking 1000-8000s to adhere. Adding positive charges to the surface in the form of nickel reintroduced strong adhesion as 2% NiNTA led to comparable results with glass at 8-70s. There were no significant differences between cell lines on each surface, indicating adhesion was TCR (signaling) independent (**Figure 3.6D**).

Using the same videos, the cells were analysed for activation on the different surfaces (**Figure 3.7)**. Calcium responses were dependent on adhesion to the surface as both J8-GECI and J8^{Low}-GECI cells showed calcium responses when placed on glass (22% and 17% of cells respectively) and 2% NiNTA SLBs (25 and 14% of cells, respectively). No/minimal signaling was seen on 0% NiNTA for J8-GECI and J8^{Low}-GECI cells (1% and

2% of cells, respectively). Signaling was almost entirely dependent on the TCR being present as signaling remained below 3% across all surfaces for the J8^{TCR-} cells, despite their strong adhesion to glass and 2% NiNTA. If NiNTA containing SLBs are to be used, unbound nickel sites would need to be blocked sufficiently to prevent artefactual adhesion and signaling.

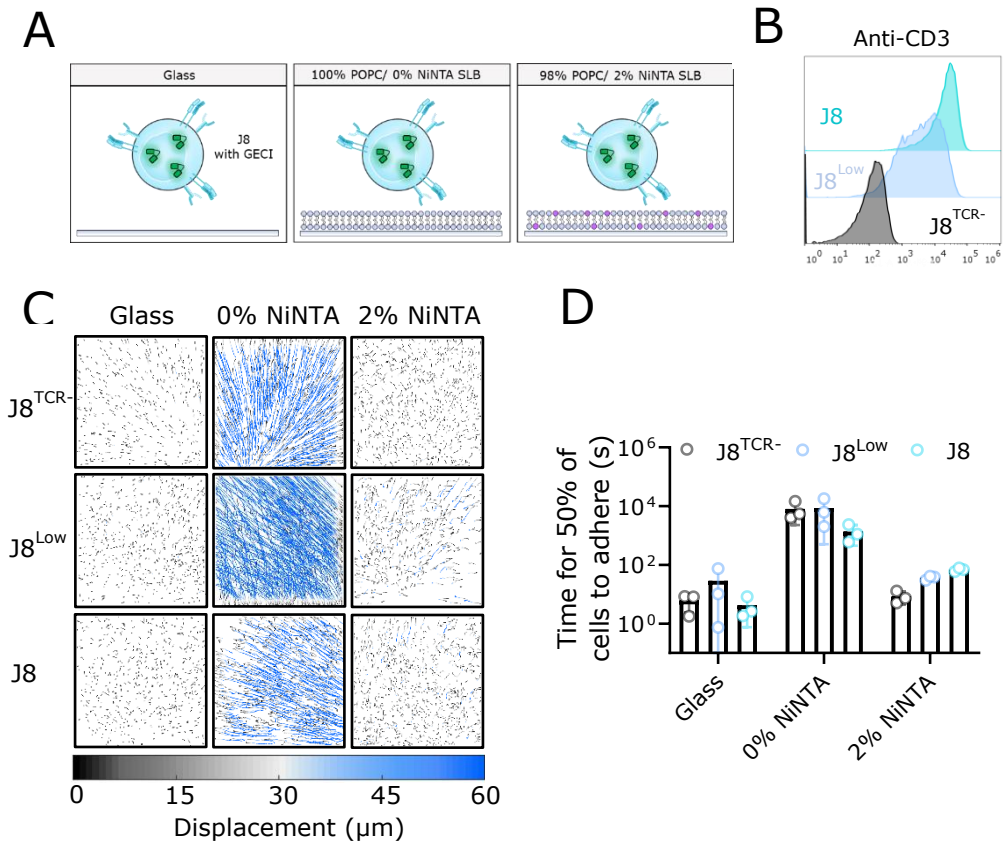

Figure 3.6. **Unspecific T-cell adhesion on glass and 2% NiNTA SLBs.** (A) Cartoon of the J8-GECI cells on the different surfaces tested. Purple spheres indicate nickelated lipids. (B) Flow plots indicating CD3 surface expression. (C) Single cell traces of J8 GECI with no TCR (J8^{TCR-} top row), J8-GECI sorted on low TCR expression (J8^{Low}; middle row) or J8-GECIs (J8; bottom row), on either glass (left column), 0% NiNTA (middle column) or 2% NiNTA bilayers (right column). Each cell was automatically traced over a 10-minute video and coloured from black through to blue dependent on its displacement from 0-60μm i.e. if a cell had moved 60μm its trace would include both a black and blue component. (D) Time for 50% of cells to adhere with s.d. No significance was found between cell lines on each surface when using two-way ANOVA with Sidak multiple comparison test

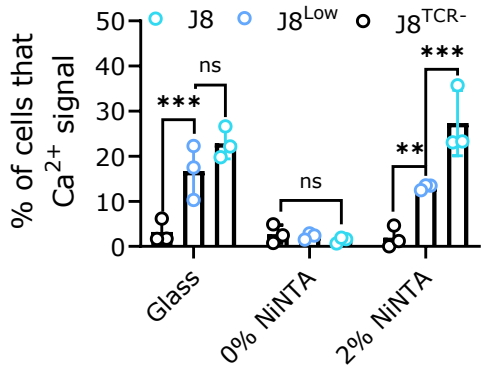

Figure 3.7. **Unspecific T-cell adhesion leads to ligand independent TCR triggering.** % of GECI-containing cells showing calcium release (mean with s.d.). Significance was tested between cell lines on each surface using a two-way ANOVA with Sidak multiple comparison test (shown). The same test was performed to compare different surfaces for each cell line (not shown). For both J8 and $J8^{Low}$ significance (**) was found when comparing glass and 2% NiNTA to 0% NiNTA. No significance was found between surfaces for $J8^{TCR-}$. *** = $p < 0.001$, ** = $p < 0.01$, ns = not significant = $p > 0.05$.

Creating a non-agonist/null pMHC to block unbound Ni^{2+} sites

Bovine serum albumin (BSA) and casein are the most used blocking agents for non-specific protein interactions. BSA has an isoelectric point of 4.8-5.4, and casein 4.4, creating an overall net negative charge on these proteins at a pH of 7. This causes adsorption to either areas of exposed glass or NiNTA on the SLB. However, a different blocking approach was required to allow complete control over the variety and density of proteins presented on the surface to be achieved. This was because all the proteins for the SLBs were made with the same H6-linker-H6 tag for ease and scalability but had the troubling property of competing for nickel sites. This causes difficulties for comparative experiments that involve altering protein composition on the SLB while maintaining the remaining proteins at a given density e.g. when varying the density of agonist pMHC presented. This problem stems from the different kinetics of attachment/detachment of

each protein to nickel in the SLB. Non-agonist pMHC containing gp100 peptide (aa280-288 of glycoprotein 100/premelanosome protein, YLEPGPVTV) loaded into HLA-A2 with a 6xhistidine-linker-6x-histidine (H6-linker-H6) C-terminal tag on the alpha chain (referred to as 'null pMHC' from hereon) was chosen as the blocking agent for two reasons: 1) high densities of null pMHC is more physiologically representative of the 'sea' of irrelevant antigen each T cell is exposed to on an APC, and 2) null pMHC can be readily exchanged for agonist pMHC of differing affinity and density without altering the densities of other proteins. This is because the near identical amino acid composition and therefore physicochemical properties of null and agonist pMHC will lead to similar binding kinetics to free nickel. This meant that SLBs would not require optimisation of all protein densities every time a different density or affinity of pMHC was used, an advantage that BSA or casein do not offer. The blocking null pMHC was produced by refolding purified HLA-A2 in the presence of β2M and the gp100 peptide. The refold gave a yield of 2.4% (of the total protein content) but was observed to be well folded (i.e. the 'correct' size on gel filtration with all components present), pure, and monomeric (**Figure 3.8A-C**).

Measuring null pMHC density to find saturating conditions for free Ni^{2+} site

In order to be certain that nickel sites are blocked sufficiently it is helpful to know the saturating concentration. In addition, it is also helpful to equate the concentration to density to ensure that the physiological densities of a variety of proteins can be simultaneously employed on the same SLB. The range of molecules for a saturating density per μm^2 can be predicted by knowing the area of lipids and the fraction of

molecules of NiNTA. Given that each POPC lipid is ~0.7nm^2 in cross-sectional area (comparable for NiNTA), this equates to 1,428,571 lipid molecules per μm^2 [319]. As only 2% of lipids are NiNTA, there are 28653 free NiNTA molecules per μm^2. With 12 histidine per null pMHC taking up to 6 (two histidine per NiNTA) nickel sites at equilibrium we expect the lower limit for saturation to occur at ~4775 null pMHC molecules per μm^2.

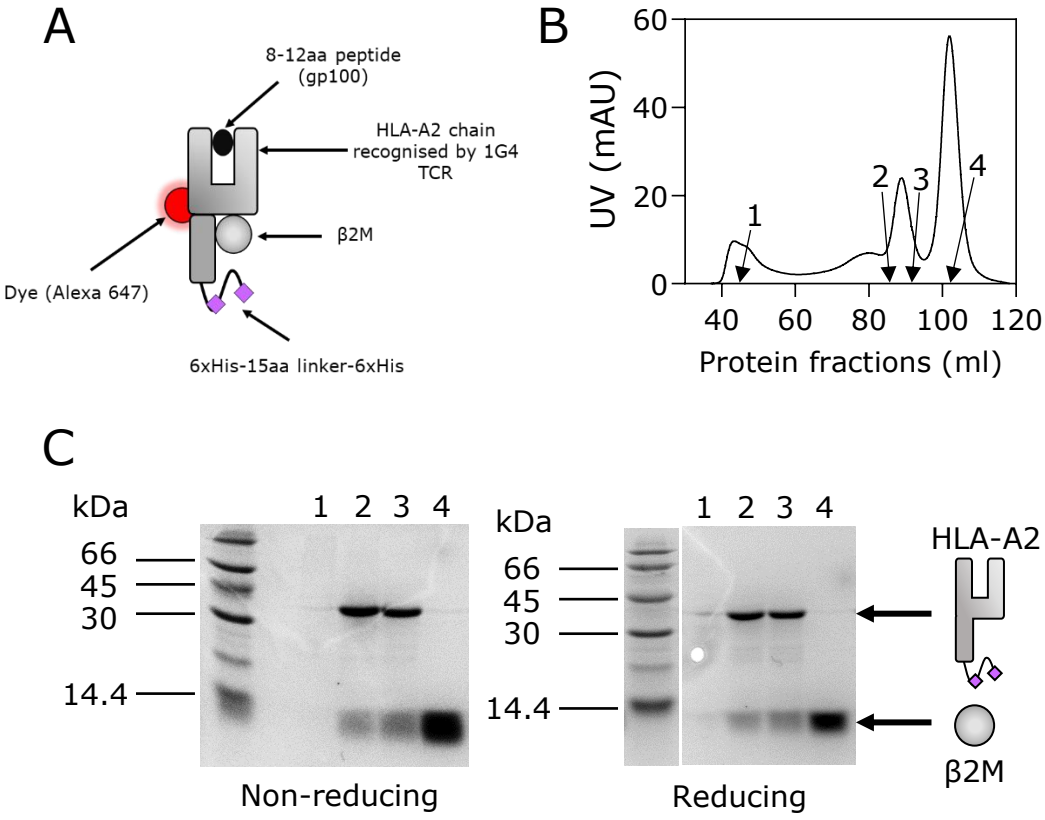

Figure 3.8. **Purification of null pMHC for SLB blocking.** (A) Cartoon representation of the blocking pMHC. Molecular mass of the complex is predicted to be ~48kDa. (B) FPLC plot showing three peaks. From left to right: aggregate, monomeric null pMHC, and excess β2M chain. (C) Left: 12% non-reducing (left) and reducing (right) SDS-PAGE gel (non-reducing) of the FPLC fractions. Lane 1 shows aggregate. Lane 2 and 3 are fractions from the monomeric pMHC peak. Both the HLA-A2 chain (top band, 30-45kDa)) and β2M chain (bottom band, < 14.4 kDa) can be seen. Lane 4 is from the excess β2M peak. The ladder was cropped next to the protein runs in the reducing gel for clarity of band size.

Theoretical saturation values were validated by titrating the concentration of null pMHC and measuring the density using point fluorescence correlation spectroscopy (pFCS; **Figure 3.9**). pFCS records the temporal fluctuations in fluorescence intensity from a small illumination spot (~200-400 nm in diameter in a typical confocal microscope). Fluctuations result from the fluorescent molecules diffusing in and out of this spot. By plotting a temporal autocorrelation of the intensity fluctuations at different lag times it is possible to obtain information that can be used to calculate the density and diffusion rate of particles. Importantly, the density of a protein within the illumination spot is given by the inverse of the y-intercept value (assuming an autocorrelation value of 0 is the baseline). Key to the density calculations is knowing the size of the confocal illumination spot in 2D. This is obtained by putting the diffusion rate of a chosen dye (known from the literature), and the measured transit time of that dye free in solution, into an equation relating these parameters in a 2D plane (**Figure 3.9**). Using this the relationship between concentration and density per μm^2 can be plotted. The concentration titration led to a saturation density of 3994 null pMHC molecules per μm^2 (**Figure 3.10A&B**). This is in line, surprisingly, with the predicted saturation based on each null pMHC utilising all 6 histidine pairs to bind free nickel. The slightly lower value may reflect deviations from the 2% Ni^{2+} occupancy value of the DGS-NTA lipids.

The rate of J8-GECI cell adhesion and activation was also examined for different concentrations of null pMHC. Cells were tested from 0-16ng/μl (0 to ~2500/μm^2). The displacement tracks became longer (i.e. transitioned from black to blue) with increasing

density, reflecting a reduced rate of adhesion (**Figure 3.10C**). At 16 ng/µl of null pMHC, cells no longer adhered to the surface and their rate of adhesion was comparable to that of 0% NiNTA bilayers (**Figure 3.10D**). Cells stopped activating on the surfaces at a level of addition of 12ng/µl (2000/µm²; **Figure 3.10E**). This established a minimum density of proteins at 2500/µm² to prevent signaling artefacts when using 2% NINTA SLBs.

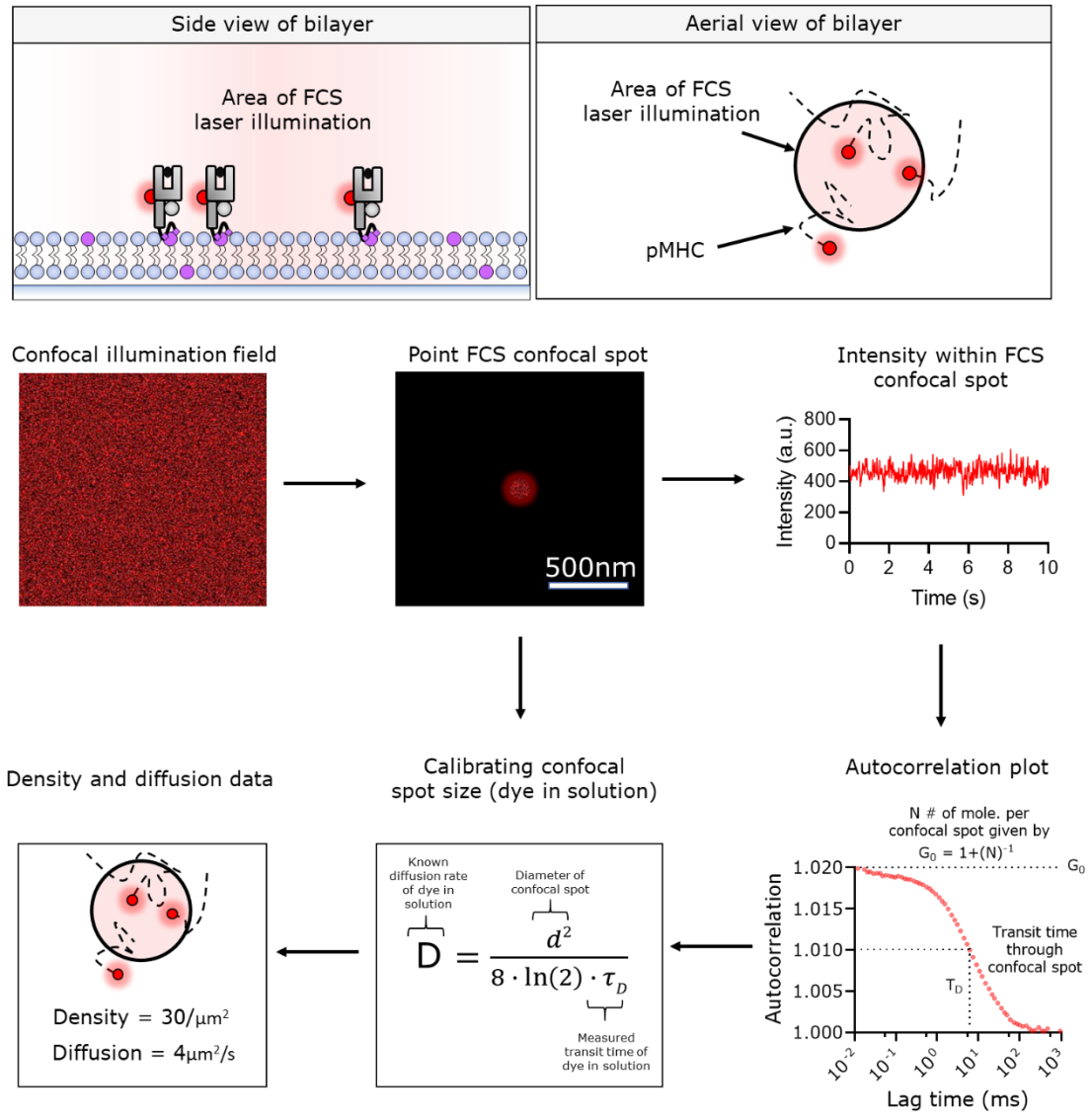

Figure 3.9. **Using pFCS to calculate protein density.** (A) Cartoon representation of fluorophore labelled null pMHC being examined by pFCS. (B) Experimental flow through for obtaining protein density measurements on the SLB by pFCS. Greater details for how to perform pFCS are in the main text and **Section 2.6**

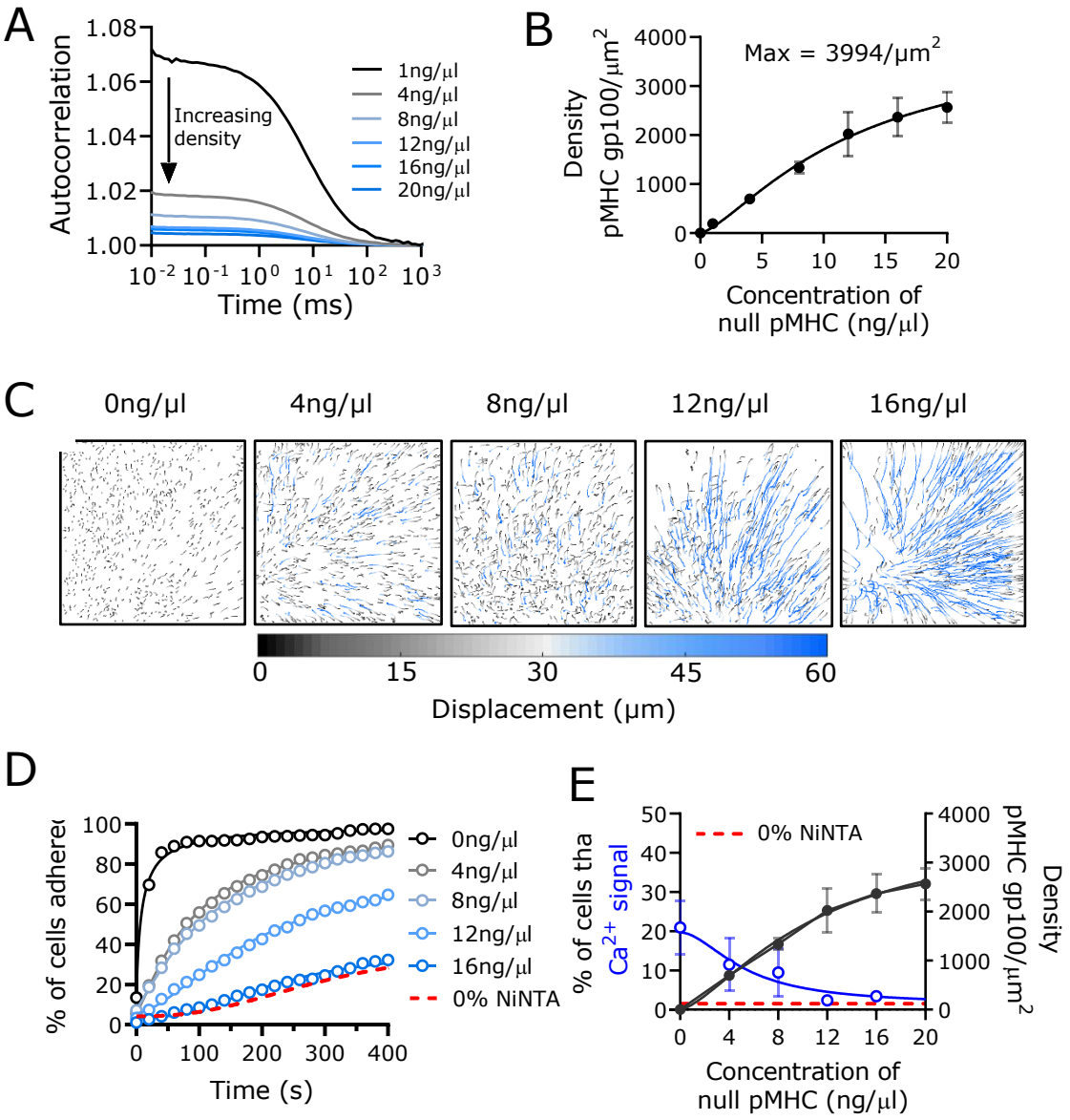

Figure 3.10. **Blocking unspecific adhesion and signaling.** Null pMHC was added to 2% NiNTA SLBs at different concentrations for one hour at room temperature before washing 10x in PBS. Samples were recorded at 37°C. (A) pFCS plots showing decreasing y-intercept with increasing concentration. (B) Concentration vs. density curve derived from pFCS pots in (A). Curve was fit using the [agonist] vs. response curve (four parameters, bottom constraint to 0). (C) Single cell displacement traces of cells on increasing concentrations of blocking pMHC. (D) Representative (N=3, n=150-400 cells) cumulative distribution plots of % of cells adhered vs. time on different concentrations of blocking null pMHC. (E) Plot showing how % of cells that show calcium release anti-correlates with concentration and density of blocking null pMHC.

3.3.5 Creating 2nd generation SLBs

Our 1st generation SLBs contain null pMHC, agonist pMHC (9V) and the adhesion protein ICAM-1. In order to transition to 2nd generation SLBs, null pMHC was substituted for the small adhesion protein CD58 and the glycocalyx components CD43 and CD45 (**Figure 3.11**). Agonist pMHC (9V), ICAM-1, CD58, CD43 and CD45 were all engineered with H6-linker-H6 at their C-terminus, similar to null pMHC, and were purified by nickel-chelation chromatography followed by FPLC (**Figure 3.12**). For agonist pMHC, the altered NY-ESO-1 antigen 9V was used (referred to as agonist pMHC (9V)). This peptide has a 3D equilibrium affinity of 7.2μM K_d. Agonist pMHC (9V) was refolded the same way as the null pMHC. To ensure that the physiological densities of all proteins were used, the densities were first characterised on human primary cells. To achieve this monocyte-derived dendritic cells were purified and tested using a Quantibrite® calibration kit that compares fluorescence PE signal from bound antibodies (assuming 1 dye per antibody) to a series of reference beads with a known number of fluorescent molecules attached (**Figure 3.13A-C**). Membrane area was calculated from a distribution of cell sizes measured from a Countess II automated cell counter. The protein densities are given in **Figure 3.13D**. To achieve densities in the physiological range on the SLB, proteins were added at differing concentrations as a single mix and tested using pFCS. To ensure that the readouts were as accurate as possible, the same dye was labelled on each protein with each confirmed to contain >1 dye/molecule. For each labelled protein tested by pFCS the remaining were unstained. To obtain the density of the remaining proteins, the previously labelled protein was substituted with the unstained equivalent, and a previously unlabelled protein was now

substituted with a labelled version. This meant that three bilayers for 1st generation and six bilayers for 2nd generation SLBs had to be created to obtain densities of each protein for given ratios of mixes of the constituent proteins. This process eventually yielded a mixture ratio giving SLBs with proteins in the physiological range (**Figure 3.14A&B**). This was ratio D and ratio K for 1st and 2nd generation SLBs, respectively. Densities include agonist pMHC (9V) at 50-100 molecules/μm², ICAM-1 at 400-600 molecules/ μm², CD58 at 200-300 molecules/ μm², CD43 at 300-400 molecules/ μm², CD45RABC at 250-350 molecules/ μm² and null pMHC at >1700 molecules/ μm². Both bilayers had free nickel sites blocked sufficiently and comparably as the total protein content of both types of bilayer was ~3000/μm².

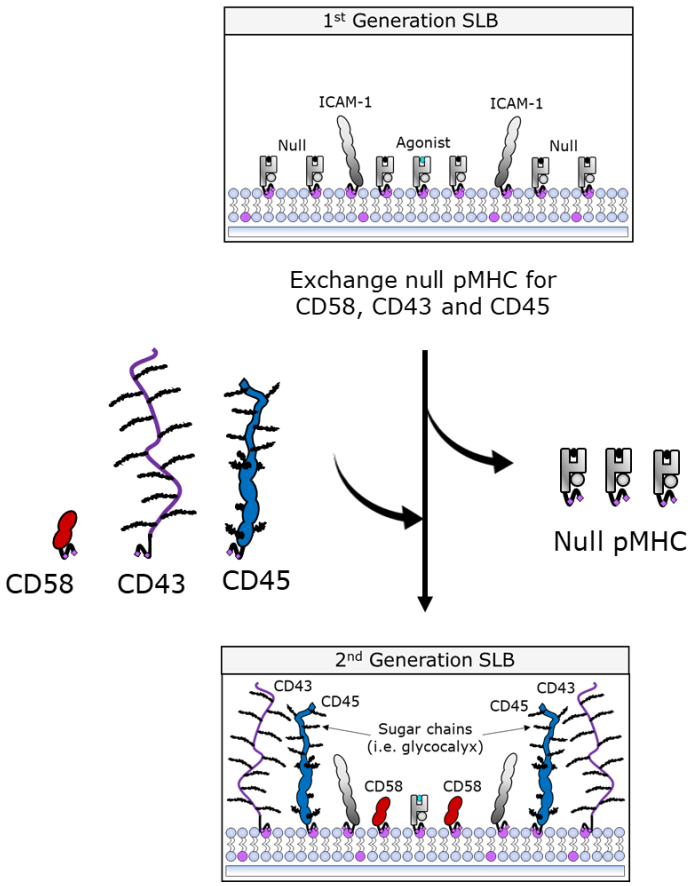

Figure 3.11. **Exchanging null pMHC to build 2nd generation SLBs**. Null pMHC was swapped out with differing concentrations of CD58, CD43 and CD45.

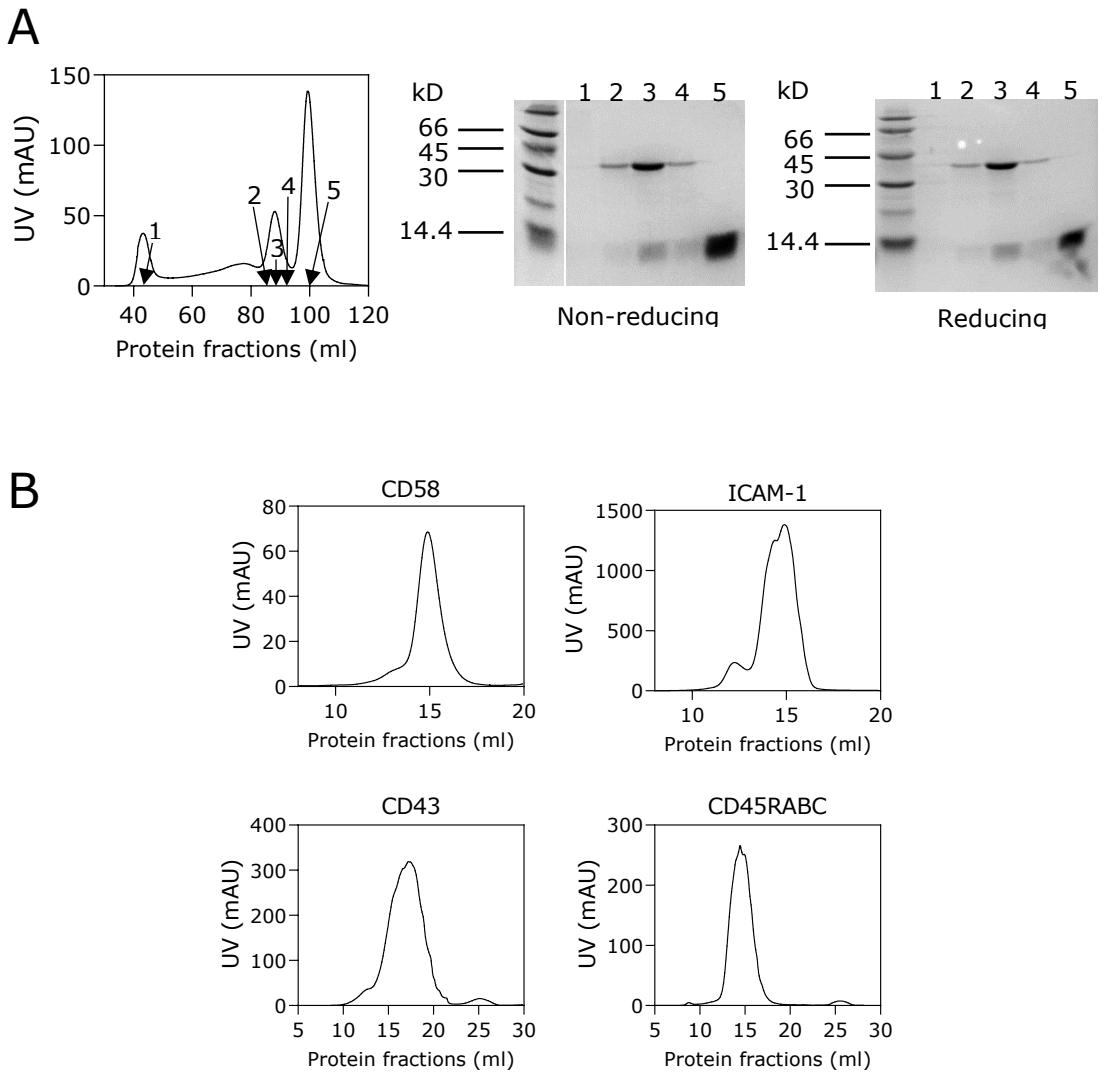

Figure 3.12. **Purification of 1st and 2nd generation proteins.** (A) FPLC and 12% SDS-PAGE (coomassie stain) of agonist pMHC (9V). The FPLC plot and SDS-PAGE gels are similar that shown for null pMHC in **Figure 3.8**. Left: Non-reducing gel SDS-PAGE. The ladder has been cropped next to the protein run. This is also the same ladder for the null pMHC (gp100) in Figure 3.10 as the proteins were purified at the same time and run on the same gel. Right: Reducing gel SDS-PAGE. Lane one on the FPLC and 12% SDS-PAGE corresponds to aggregate. Lanes 2-4 are fractions from the monomeric pMHC peak. Both the HLA-A2 chain (top band, 30-45kDa)) and β2M chain (bottom band, < 14.4 kDa) can be seen. Lane 5 is from the excess β2M peak. (B) FPLC plots for CD58, ICAM-1, CD43 and CD45RABC all with H6-linker-H6 at their C-terminus.

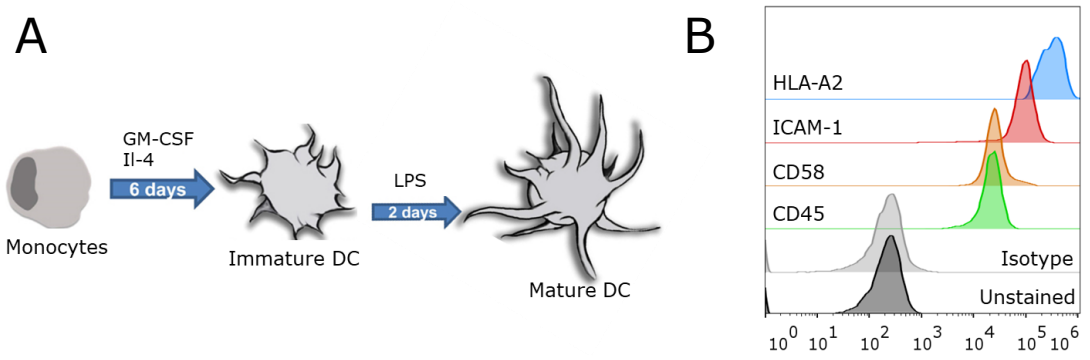

C

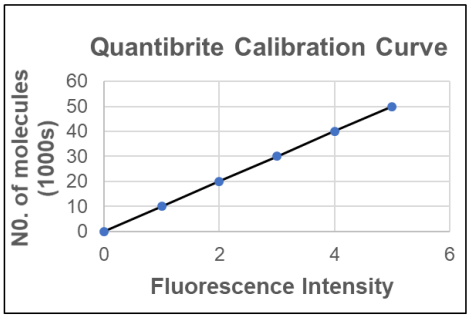

D

Donor A	Total Proteins (000s)	Protein Density (μm^2)
HLA-A2	380-850	1200-2700
ICAM-1	100-310	330-1000
CD58	30-120	95-380
CD45	30-70	100-220
Donor B		
HLA-A2	0	0
ICAM-1	95-310	300-1000
CD58	35-95	110-300
CD45	30-80	100-250

Figure 3.13. **Obtaining protein densities from moDCs**. (A) Cartoon representation of the production of moDCs. Image taken and adapted from [319]. (B) Flow cytometry data of key proteins for 2nd generation SLBs on moDCs. All were labelled with antibodies directly conjugated to PE to allow use with the Quantibrite PE calibration beads for obtain total surface protein counts. (C) Example of the calibration curve generated from the calibration kit (not actual data). (D) Table of the total protein counts and densities of key proteins on the surface of moDCs. The range given represents two standard deviations below and above the median (calculated using 'robust standard deviation,' FlowJo). Donor B did not stain for HLA-A2 as they did not have this MHC haplotype.

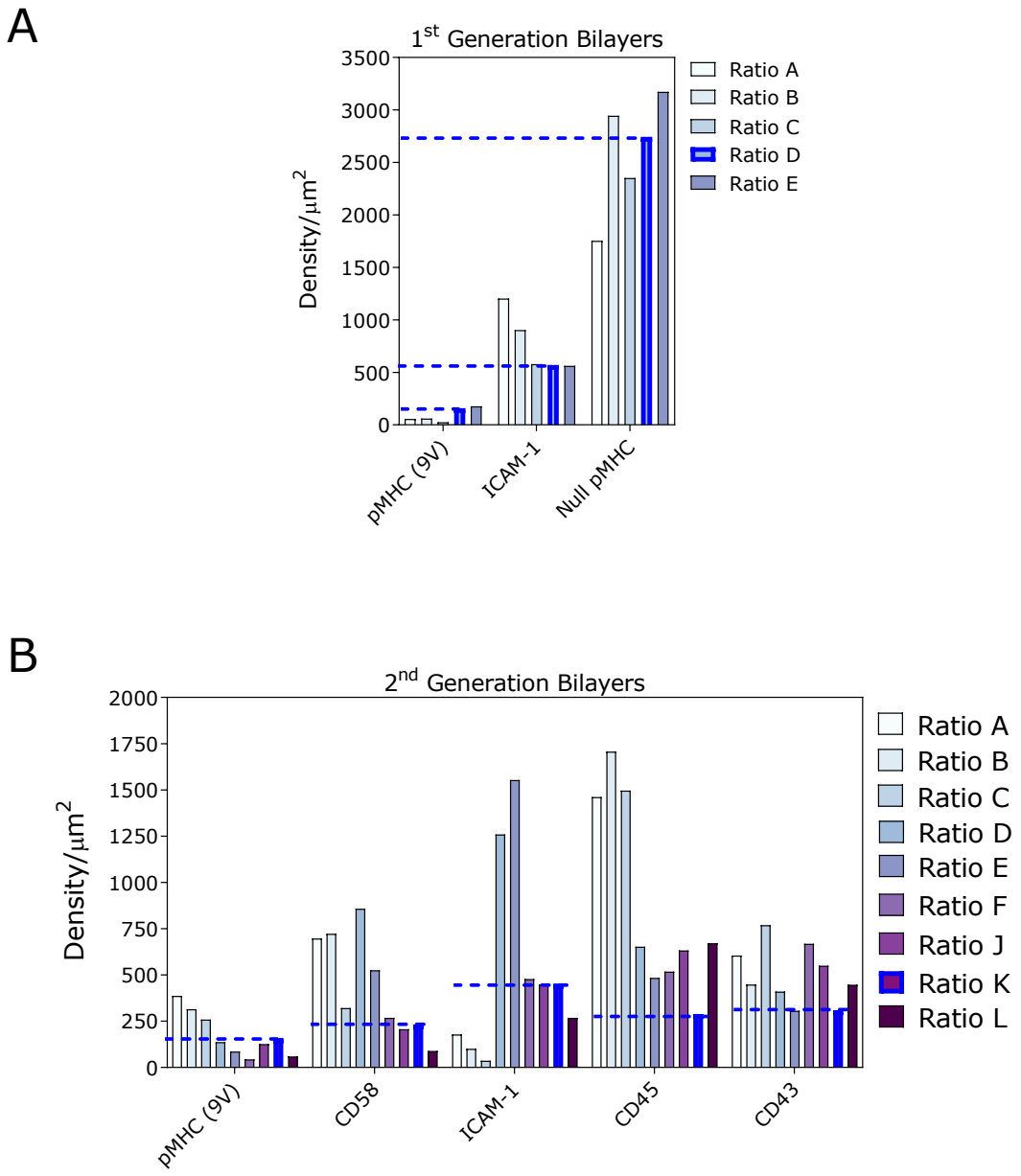

Figure 3.14. **Optimising densities of proteins on 1st and 2nd generation SLBs**. Densities were obtained by pFCS with one protein labelled with Alexa 647 and all other proteins unlabelled. To obtain density readouts for all proteins of a protein mix ratio, the Alexa-647 labelled protein was switched out with the unlabelled equivalent (used at the same concentration), whilst a previously unlabelled version was switched out for an Alexa-647 labelled equivalent. Final concentration ratio used and the corresponding densities of proteins on the SLBs are highlighted in bright blue

3.4 Discussion

The results presented in this chapter describe the creation and optimisation of a novel $CD8^+$ T-cell line expressing the well-characterised 1G4-TCR, specific for the NY-ESO antigen, and the creation of a new more physiological setting for studying T-cell activation than was in wide use previously.

3.4.1 J8s: a model for $CD8^+$ T cells

Several cell lines were created in this chapter: (1) J8, (2) J8-GECI, (3) $J8^{TCR-}$, and (4) $J8^{TCR-}$ GECI cells. To produce the J8 cell line (and variants), single cell cloning was not done, as might be typical in studies involving CRISPR-Cas9 knockout-derived cell lines. Instead, they were sorted in bulk for negative/positive expression of the gene of interest. This was done for efficiency and to minimise issues surrounding introduced 'off-target' mutations. Such mutations may noticeably alter cell function when expanding cells from single clones but are typically hidden in the population of cells. Identifying such mutations would take extensive functional testing or sequencing the genomes of several populations grown from different single cells. As the CRISPR targets were surface proteins, sorting on negative populations through surface antibody staining was very efficient and effective. Clearly, this approach did not disrupt cell responsiveness as the J8s remained comparable to the Jurkat parental cell line in their phenotype and activity on stimulatory surfaces. It should be noted, however, that there are genetic defects in Jurkats leading to the absence of proteins involved in T-cell activation such as the phosphatases PTEN and SHIP, inhibitory receptor CTLA-4 and kinase SYK [321]. These

factors may shift the downstream sequelae of TCR triggering, but clearly are non-essential for initiating signaling as J8-GECI-LFA-1 boosted cells could calcium release in a TCR-specific manner. As J8 cells clearly maintain capacity for membrane-proximal TCR signaling they can be considered to be a suitable model for primary T cells when studying these events. A potential caveat is that the TCR expression of J8 cells was matched to the parental cell line, however, the TCR expression/density may differ from that of primary T cells; an important parameter which may have implications for TCR triggering thresholds [124]. This could be quantified by comparing primary T cells purified from PBMCs and J8s using Quantibrite bead calibrations and measuring the total surface area of primary T cells and J8s using 3D imaging.

3.4.2 Creating second generation SLBs

Non-specific responses of T cells on different surfaces

The J8-GECI cells produced calcium release in a TCR and adhesion-dependent manner on both glass and 2% NiNTA SLBs. Similar effects were found on nonspecific bovine IgG-coated glass or on charged surfaces such as poly-L-lysine (PLL). Both led to TCR-dependent signalling and upregulation of the activation marker CD69 in Jurkats and primary $CD4^+$ T cells [317], [318]. PLL was found to reduce TCR mobility, presumably through electrostatic interactions, and create large flat contacts that resulted in areas of CD45 segregation [317], [318]. Although imaging of TCR and CD45 were not performed in this thesis, it is reasonable to assume a similar effect is occurring on 2% NiNTA given

the strong degree of adhesion and calcium release observed. This underscores the importance of surface and medium choice for experimentation.

Blocking unspecific adhesion using null pMHC

Blocking unbound NiNTA with physiological levels of null pMHC was essential to allow the analysis of ligand-specific responses in the following chapters. Importantly, this blocking agent was not bound or recognised by any proteins on the surface of J8s as cells become increasingly mobile when increasing the density of the null pMHC on the SLB. Evidently, the weak interaction of CD8 with null pMHC (3D K_d ~100-200μM) was not sufficient to drive adhesion of J8 cells to the SLB containing high densities of null pMHC. It may be that auxiliary binding molecules (e.g. small adhesion molecules such as CD58/CD48) are essential for coreceptor/pMHC interaction as has been suggested and shown for CD4 [186], [416].

Additional methods to increase SLB protein variety

When creating 2nd generation SLBs, all proteins were added via a H6-linker-H6 for stable attachment to NiNTA lipids. The key advantage of this approach is that it allows scalability as all surface proteins can theoretically be purified and added to the bilayer in a similar and reproducible manner. However, too many proteins would complicate the tuning of surface densities as all proteins would compete in unpredictable ways for free nickel sites. As a result, increasing complexity beyond 2nd generation SLBs may

prove challenging. One way around this would be to add additional proteins using different conjugation mechanisms. For example, biotin-streptavidin conjugation is a method previously employed for T cell-SLB experiments [122], [268], [322], [323]. A key pitfall with this approach, however, is the potential to artificially cluster biotinylated proteins. Alternatives to nickel-his and biotin-streptavidin include SNAP-Tag or protein-DNA-lipid conjugation [286], [324]. For the former this requires purification of proteins fused to SNAP-Tag and the insertion of commercially available lipids containing SNAP-Tag ligand on the SLB [324]. The latter approach requires conjugation of DNA to site-specific locations on proteins, followed by conjugation of protein-DNA complexes to modified lipid groups on the SLB [286].

Quantifying protein densities

Suitable physiological densities of proteins that formed the 2nd generation SLBs were determined by measuring the levels of proteins on the surface of primary cells using a flow cytometry calibration kit. The values obtained here represent approximate estimates because of the underlying assumption for Quantibrite bead calibrations that each antibody contains one PE molecule attached and that each antibody is in a 1:1 stoichiometry with its target protein. Furthermore, the estimate of surface area by approximating a dendritic cell as a sphere (based on a median 10μm diameter of moDCs in solution) is crude at best, likely overestimating the actual surface density. Another potential issue is that it is now being claimed is that surface proteins are localised relative to membrane topology [123], [126]. This would not be addressed in an average density

calculation using only total protein levels and membrane surface area. Despite these issues, for comparative purpose, it is important that the densities of proteins such as ICAM-1 and CD58 used here match those of previous studies that use SLBs. For example, ICAM-1 has been commonly used at 200-300/μm^2 and CD58 was more recently quantified and used at 200μm^2 [85], [88], [89], [91], [97], [156], [283]. To our knowledge, the density of CD45 has not been characterised on dendritic cells, and so this represents a first estimate. In line with other studies, total CD45 expression was lower than that of other components [325]. CD43 was not tested here, although it is known to be expressed in monocyte-derived dendritic cells, at slightly lower levels than ICAM-1, and at levels comparable to CD58 [325], [326] CD43 density on 2nd generation SLBs was set in accordance with this.

Chapter 4 T-cell activation and synapse formation on second generation SLBs

4.1 Introduction

In the previous chapter, the J8 T-cell line ($CD4^{-}CD8^{+}$ 1G4-TCR specific Jurkat) and second generation SLB (pMHC, ICAM-1, CD58, and CD43 and CD45) were established. The next logical step is to characterise how the J8s behave on second generation SLBs, using the well characterised 1st generation SLBs (pMHC and ICAM-1) as a reference point to distinguish any unique or conserved behaviours. This can be achieved through two approaches: large-scale analysis of T-cell activation through tracking calcium release, and high spatiotemporal imaging of T-cell contact formation using TIRFM. The former technique, in combination with first generation SLBs, has provided key insights into T-cell activation thresholds, kinetics of activation, and adhesion when differing antigen densities and affinities [225], [323], [327]. The latter technique has shown that distinct areas of pMHC-TCR engagement precede calcium release, followed by cell spreading, the appearance of additional pMHC/TCR microclusters and eventual formation of the immune synapse [83], [86], [91]. By combining both techniques, a more complete understanding of T-cell activity can be obtained.

This chapter first describes a methodology for carefully tuning and quantifying the density of agonist pMHC on first and 2nd generation SLB. This is important to allow fair

analysis between the surfaces. Focus then shifts to charactering J8s interaction with these surfaces. By tracking intracellular calcium release for hundreds of cells, any robust differences in metrics such as the rate of adhesion, kinetics of T-cell activation, and magnitude of calcium response can be quantified. This data is then supplemented with TIRFM imaging of pMHC, ICAM-1, the cell membrane and calcium release of J8s with these surfaces.

4.2 Methods

Agonist pMHC (9V) density measurements

Both 1st and 2nd gen SLBs were prepared as described in **Section 3.2**. ICAM-1 and agonist pMHC (9V) were labelled with Alexa 555 and Alexa 647, respectively. All other proteins were unlabelled. In order to alter the density of agonist pMHC, *ceteris paribus*, it was exchanged directly for null pMHC e.g. 0.5ng/μl agonist pMHC and 9.5ng/μl null pMHC becomes 0.1ng/μl agonist pMHC and 9.9ng/μl null pMHC. As the lower limit of detection for pFCS in this setup was ~1 molecule/μm^2, standard curves were produced to extrapolate densities below this. This was achieved by performing a four-point titration of density vs. concentration. The three data points were typically above 1/μm^2 (as measured by pFCS) and were used to extrapolate the 4th lower density by assuming a linear curve between density and concentration that passes through 0,0. This was assumed as the agonist pMHC was directly swapped out for the null pMHC.

Calcium release and synapse formation assay

For each 1st or 2nd generation SLB (using ICAM-1-Alexa 555 and agonist pMHC (9V)-Alexa 647), 0.25-0.5x10^6 J8-GECI-LFA-1 cells were washed x2 in pre-warmed (37˚C) PBS + 2mM $MgS0_4$, resuspended in the same and incubated for a further 5-minutes at 37˚C. SLBs were also washed x10 in pre-warmed (37˚C) PBS + 2mM $MgS0_4$, resuspended in the same, with the glass slides placed in pre-warmed (37˚C) metal chambers. During the 5-minute incubation, pMHC-9V-Alexa 647 on SLBs was subject to 3x10s pFCS measurements using a 40x water objective (NA1.2; with 633nm laser at 1% laser power), to obtain density readouts. The objective was changed to a 10x magnification, and cells were immediately dropped on the SLB and recorded at 1s intervals for 10-minutes (argon 488nm-laser at 10% power). Agonist pMHC density was obtained by fitting autocorrelation plots using both FoCuS point software and PyCorrfit [301], [302]. Cell displacement, time to adhesion, % signaling, time to signaling, and signal strength were analysed using the calcium analysis MATLAB® script described in S**ection 2.7**.

TIRF imaging

1st and 2nd generation SLBs were prepared as above. ICAM-1-Alexa 555 and agonist pMHC-Alexa 647 were used to observe synapse formation in relation to the calcium response of cells. When comparing 1st and 2nd gen SLBs with 0 or low-density agonist pMHC, agonist pMHC (9V) was switched to unstained and the cell membrane was labelled with CellMask® Red. J8-GECI-LFA-1 cells were either washed x2 in pre-

warmed (37˚C) PBS + 2mM $MgS0_4$ and incubated for 5 minutes at 37˚C before use. When staining the cell membrane, cells were placed in RPMI (no supplements) with 1xCellMask® Red for 10 minutes at 37˚C before being washed x3 in pre-warmed (37˚C) PBS + 2mM $MgS0_4$ and resuspended in the same. To correct for unequal TIRFM illumination and/or remove background signal from the SLB (to better observe ligand accumulation), 50 frames (2s interval) of the SLBs were imaged prior to dropping the cells on them. After 5-minutes at 37˚C, cells were gently added to the SLB and imaged at 2s intervals for 10-15 minutes. Videos were processed as described in **Figure 4.1** and further analysed with the contact analysis MATLAB® code described in **Section 2.7**. Videos that were corrected for unequal illumination were used for the contact analysis.

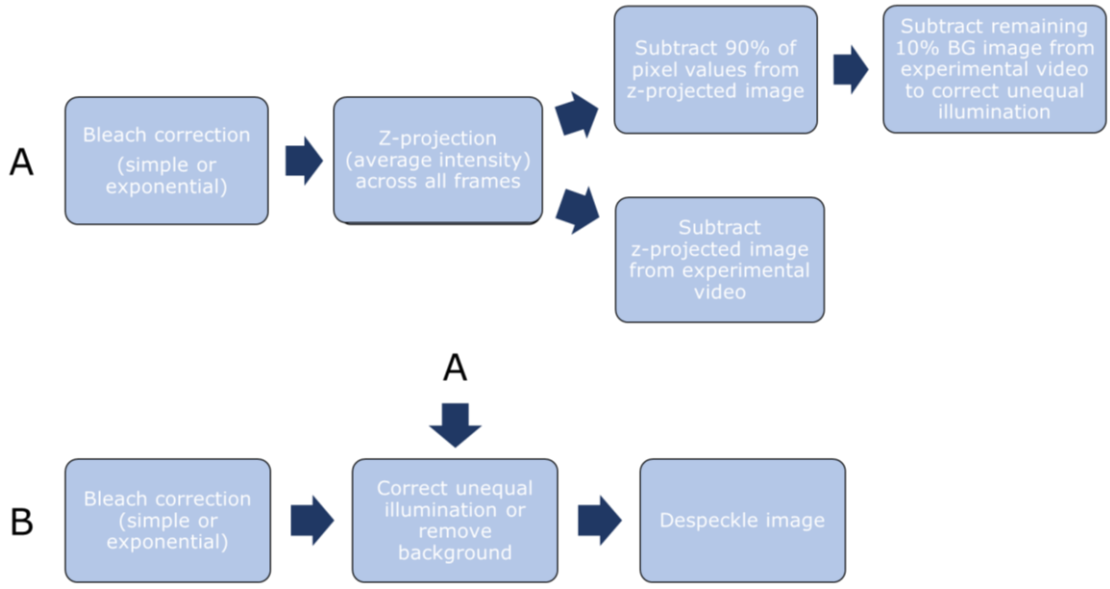

Figure 4.1. **Flow diagram for TIRF image analysis.** Image processing for the background (A) or experimental (B) images of the SLB. (A) Background images are those of the SLB taken before adding cells to the surface. After z-projection, the background images were processed for either correction of unequal TIRFM illumination or for removing all background signal from the experimental video. Images processed in (A) feed into (B) as indicated. BG = background.

4.3. Results

4.3.1 Tuning antigen density on SLBs

From **Chapter 3**, the J8/J8-GECI cell lines were found to have lower LFA-1 expression than primary cells (see **Appendix A**). Boosting LFA-1 expression to physiological levels was important to observe any ICAM-1 accumulation (**Appendix A**). The behaviour and responsiveness of J8-GECI-LFA-1 boosted cells (referred to as J8-GECI-LFA-1 from hereon) was therefore used on 1st and 2nd generation SLBs to understand how T cells behave on these systems. This was done by dropping J8-GECI-LFA-1 cells on 1st or 2nd generation SLBs displaying 0-100 molecules/μm^2 of agonist pMHC (9V) and analysing various metrics using an automated analyses (described in **Section 2.7**) such as their ability to adhere to the surface (**Figure 4.3**), the kinetics of antigen detection (**Figures 4.4-4.6**), and the strength of signaling (**Figures 4.7-4.9**). This was tested over a range of Alexa-647 labelled agonist pMHC densities, measured using pFCS (**Figure 4.2A**). In order to tune the density, null pMHC was exchanged for molar equivalents of agonist pMHC (9V). Due to practical limitations of pFCS at measuring protein density <1/μm^2, lower densities were extrapolated by performing a four-point titration (**Figure 4.2B**). Three measured values, and a point at 0,0, were used to create a linear regression line. This equation for the regression line was used to calculate the extrapolated density value based on the known concentration of protein used. By plotting both measured and extrapolated values, an overall linear regression (passing through 0,0) was produced to provide a guide to the ratio of null and agonist for a desired density of agonist (**Figure 4.3C**). For 1st generation SLBs the regression line was Y=132.6X whereas 2nd generation was Y=185*X (Y is the density and X is the concentration in ng/µl).

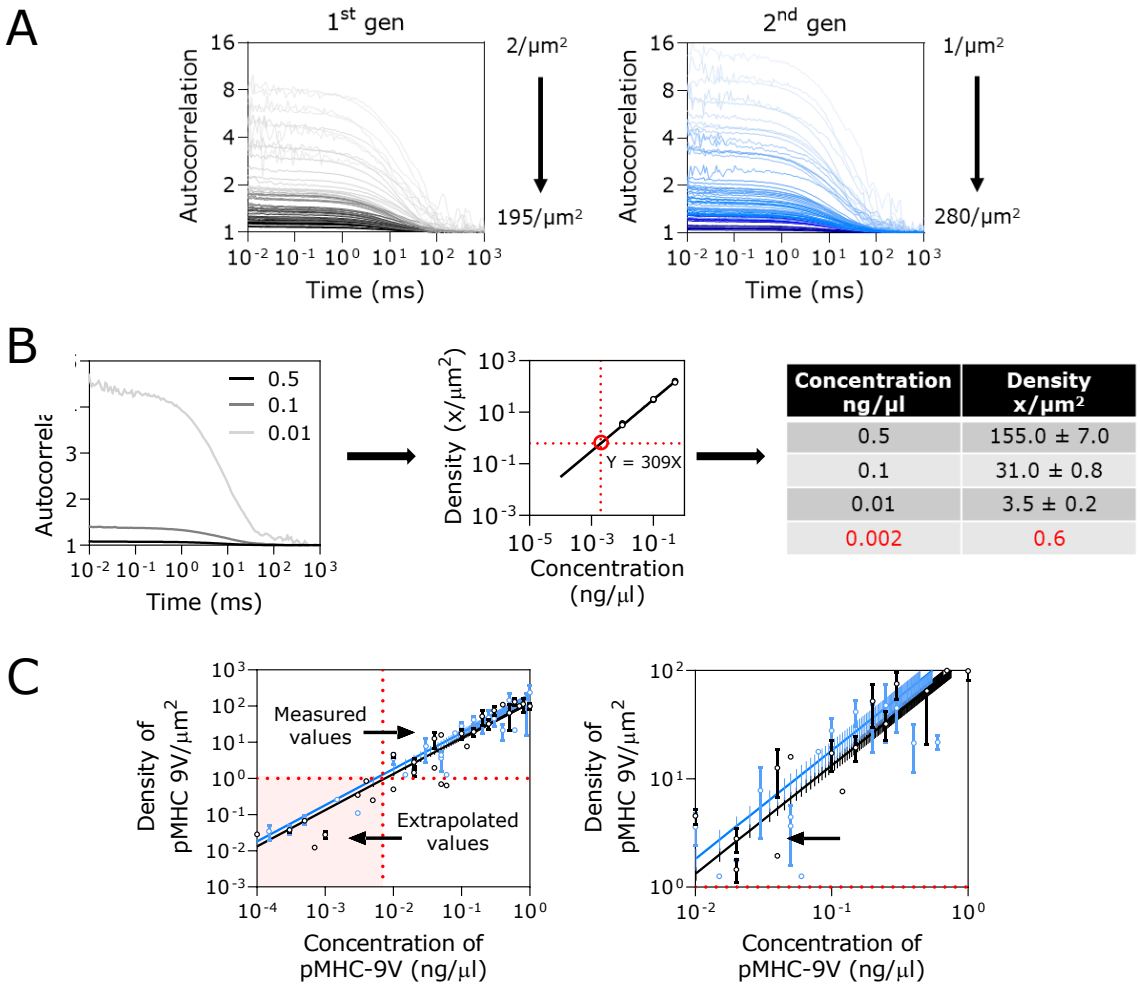

Figure 4.2. **Quantifying the density of agonist pMHC on 1st and 2nd generation SLBs.** 1st and 2nd generation SLBs were setup as described in **Section 3.2** using Alexa-647 labelled agonist pMHC (9V). Agonist pMHC density (molecules/μm²) was measured by pFCS across a range of concentrations, by exchanging out molar equivalents of null pMHC i.e. 10ng/μl null pMHC and 0ng/μl agonist pMHC, becomes 9.5 ng/μl null pMHC and 0.5ng/μl agonist pMHC. (A) pFCS curves showing 75-85 different concentrations of agonist pMHC (9V) on 1st gen (left, black) and 2nd gen (right, blue). Each pFCS curve represents 3x10s recordings on one SLB. (B) Example of a four-point titration to extrapolate agonist pMHC densities below 1 pMHC/μm² from pFCS measurements. Three concentration values were tested and used to produce a regression line that intercepts at 0,0. The equation for the regression line (Y = 309X in this example) was used to extrapolate the lower point (red circle and writing). (C) Left plot showing the relationship between concentration and density for all measured and extrapolated density measurements of pMHC on 1st (black) and 2nd (blue) generation SLBs. Right plot: inset of top right quadrant from left plot. Data points with error bars (s.d.) are concentrations of agonist pMHC (9V) that were used more than once.

4.3.2 Second generation SLBs are less adhesive

The APC glycocalyx is thought to act as a steric barrier, reducing overall adhesion [114]. This can be directly tested by comparing metrics associated with adhesion on 1st and 2nd generation SLBs. Hundreds to thousands of J8-GECI-LFA-1 cells were analysed for both their displacement and time taken to adhere to 1st and 2nd generation SLBs over a range of antigen densities (0-100 molecules/μm^2) measured prior to each experiment. Cells were tracked through the fluorescent intensity of the GECI. Displacement is calculated by tracking the movement of each cell, whereas time to adhesion is dependent on the cells speed of movement. When a cells speed drops and remains below a value of 0.2μm/s until the end of the video it is said to have adhered. By producing a cumulative distribution of adhesion times, the time for 50% of cells to adhere (A_{50}) can be obtained through fitting a dose-response curve.

Analysing 1st generation SLBs first, under null pMHC conditions, J8-GECI-LFA-1 cells showed some mobility in their displacement tracks (**Figure 4.3A**), having a median displacement of ~30μm (**Figure 4.3B**) and an A_{50} of ~100s (**Figure 4.3C)**. To provide context, the A_{50} on glass was ~10s, highlighting how T cells are not stably adhered to 1st generation SLBs instantly under null conditions (taken from **Chapter 3**). Increasing the density of agonist pMHC (9V) to a maximum of 100 molecules/μm^2 showed modest differences in displacement (**Figure 4.3A**) with the median displacement dropping to 20μm (**Figure 4.3B**) and A_{50} to ~30s (**Figure 4.3C**). Given the relatively small differences between null and high densities of agonist pMHC (9V), interactions between ICAM-1

and LFA-1 may still be occurring on null pMHC. Focussing on 2nd generation SLBs, cells appeared visibly more mobile than on first generation SLBs (**Figure 4.3A**). Under null pMHC conditions, cells showed a median displacement of ~70μm (**Figure 4.3B**) with A_{50} of ~300s (**Figure 4.3C**). Cells on 2nd generation SLBs remained considerably more mobile/less adhesive when agonist pMHC (9V) densities were below 1/μm^2. At a density of 10/μm^2 and above, the 1st and 2nd generation SLBs became comparable in terms of adhesion (**Figure 4.3A**). At a maximum of 100 molecules/μm^2, cells had a median displacement of ~25μm (**Figure 4.3B**) and A_{50} of ~50s, similar to 1st generation SLBs (**Figure 4.3C**). These results show that it is harder to adhere to 2nd generation SLBs at low densities of agonist pMHC (9V).

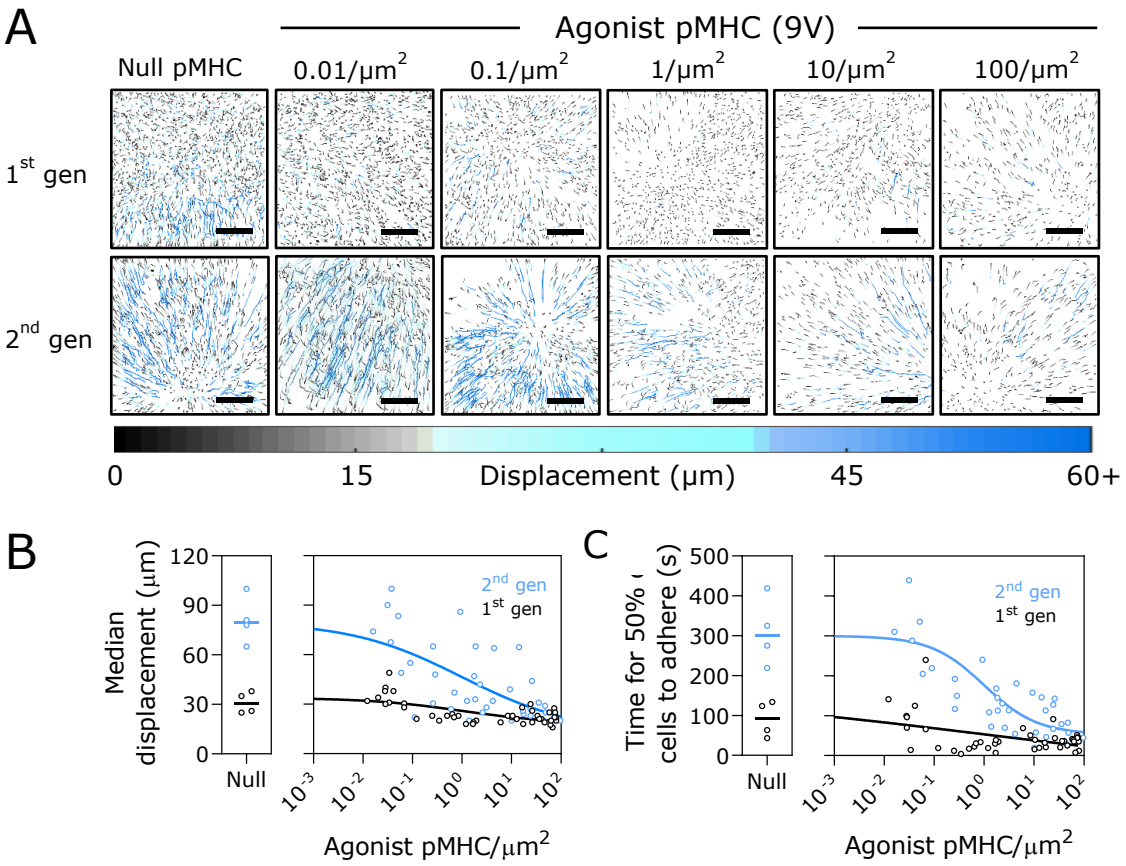

Figure 4.3. **2nd generation SLBs are less adhesive.** J8-GECI-LFA-1 cells were gently deposited on 1st or 2nd generation SLBs with either null pMHC or differing amounts of agonist pMHC (9V). The intracellular calcium signal from the GECI was used to trace the displacement of cells. (A) Displacement tracks of cells on the indicated surface. Each dot/line represents a single cell. Black indicates minimal displacement (<20μm), green represents moderate displacement (20 μm < to <40 μm) and blue indicates high displacement (>40μm). Each cell track can contain black, green and blue components. (B) Median displacement (taken from a distribution of displacement for each SLB (not shown)) plotted against all agonist pMHC densities measured for 1st (black) and 2nd generation SLBs (blue). (C) Time for 50% of cells to adhere for the same experiments shown in (B). Time to adhesion is calculated from when the cell first lands on the surface to when its speed first drops and remains below 0.2μm/s. Time to 50% adhesion were obtained by fitting dose-response curves to cumulative distributions of adhesion times for each SLB (not shown). (C&D) N=38-45 independent SLBs (n=200-500 cells per SLB).

4.3.3 Second generation SLBs alter the kinetics of early T-cell activation at low densities of agonist pMHC (9V).

Using the same samples analysed in **Figure 4.3B&**C, the percentage of J8-GECI-LFA-1 cells that activated was quantified using changes in the fluorescent intensity of the GECI. Only intracellular calcium release was measured here as calcium was not present in the imaging media. A cell is counted as having shown a 'Ca^{2+} signal' if the increase in fluorescent intensity of the GECI becomes three-fold the background fluorescence for each cell and lasts for longer than 10s. Data points for 1st and 2nd generation SLBs were fit to an [Agonist] vs. response curve.

On 1st and 2nd generation SLBs, ~12% and ~25% of cells, respectively, showed a Ca^{2+} signal on null pMHC (**Figure 4.4A**). The half-maximal likelihood of responding (~42.5% of cells showing a Ca^{2+} signal) occurred with an agonist pMHC (9V) density of ~1.0 (1st) and ~2.7 (2nd) molecules/μm^2. The maximum percentage of cells that showed a Ca^{2+} signal first plateaued (~80% of cells) at a density of ~10.6 (1st) and ~6.0 (2nd) molecules/μm^2. The response curves had a Hill coefficient of ~1.0 (1st) and ~4.2 (2nd) indicating that increases in the percentage of cells responding (or probability of a cell responding) from additional pMHC was not cooperative on 1st generation SLBs but was on 2nd generation SLBs. At a density above 10 molecules/μm^2, 1st and 2nd generation SLBs became indistinguishable. This is consistent with metrics associated with adhesion in **Figure 4.3**.

As the percentage of cells that Ca^{2+} signal can be biased by factors such as the time taken for cells to land on the surface (i.e. when they first became visible) as well as the time period chosen for the video or analysis, the kinetics of activation was additionally analysed (**Figure 4.4B&C**). To ease comparison between 1st and 2nd generation SLBs, the time taken for half the maximum percentage of cells that Ca^{2+} signal was quantified ($C_{42.5}$, **Figure 4.4B**). This was measured by fitting response curves (constrained to have a max value of 85% of cells, as this was the highest value obtained) to cumulative distribution plots showing the percentage of cells that Ca^{2+} signal over time (**Figure 4.4B**). For conditions where less than half the cells showed a Ca^{2+} signal, the $C_{42.5}$ was extrapolated from the fit of the response curve (**Figure 4.4B**). With null pMHC, 1st and 2nd generation SLBs had a $C_{42.5}$ of 1000 and 600s, respectively. On both surfaces, the $C_{42.5}$ decreased with increased agonist pMHC density, with a time of ~250s (1st) and ~450s (2nd) at 1 molecule/μm^2, ~110s (1st) and ~150s (2nd) at 10 molecules/μm^2 and ~80s (1st and 2nd) from 20-100molecules/μm^2 (**Figure 4.4C**). These results show that surface composition of SLBs can alter the kinetics of responses at low densities of agonist pMHC (<0.1 molecules/μm^2) but are indifferent at high densities (10< molecules/μm^2).

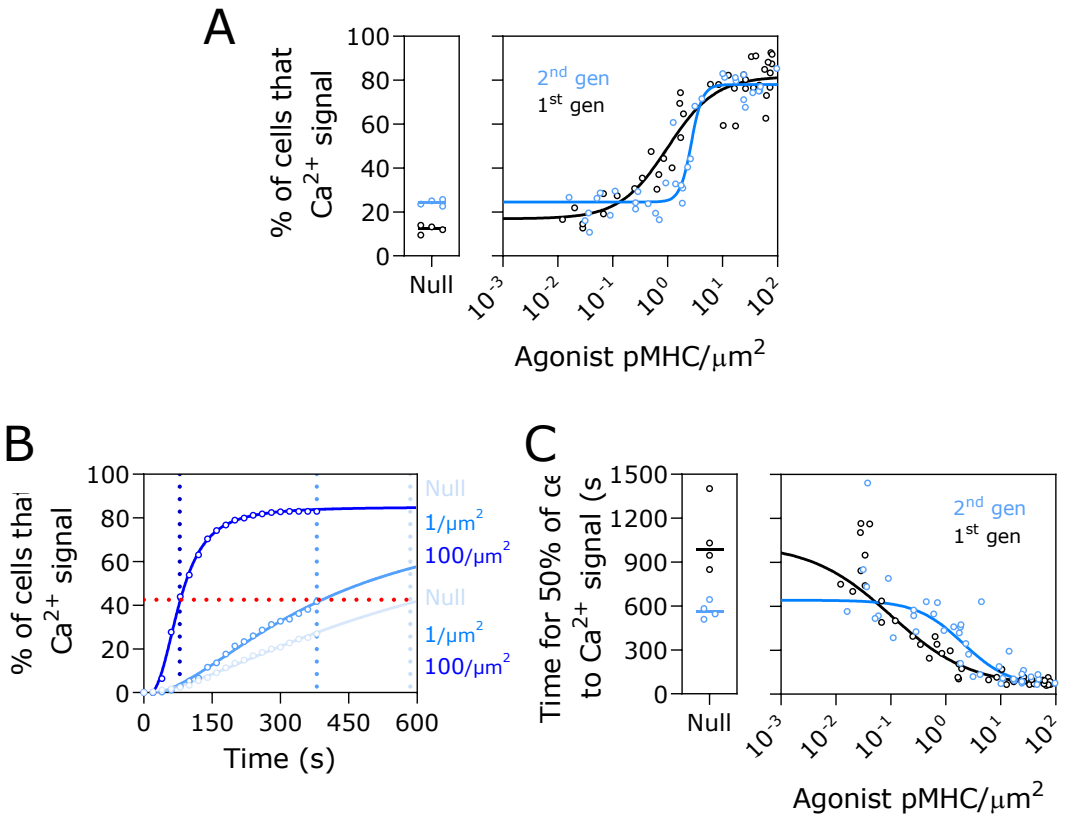

Figure 4.4. **2nd generation SLBs alter the kinetics of early T-cell activation at low, but not high, densities of agonist pMHC (9V).** (A&B) Shows different metrics analysed from the same experimental data in **Figure 4.3**. (A) Percentage of cells that Ca^{2+} signal in a 10-minute video on 1st (black dots) and 2nd (blue dots) generation SLBs. Data points were fit using an [agonist] vs. response curve (four points) in GraphPad Prism. (B) Representative cumulative distribution plots showing the percentage of cells that Ca^{2+} signal on 2nd generation SLBs over time. Three conditions are shown: null, 1 agonist pMHC/μm² and 100 agonist pMHC/μm². Data points were fit using an [agonist] vs. response curve (four points, max constrained to 85%) in GraphPad Prism. Red dashed indicates the half-maximal response (= 42.5% of cells). Blue vertical dashed lines indicate the time taken for the half of the cells to Ca^{2+} signal under the indicated condition. In conditions where cells showed less than 42.5% of cells responding, time for half of the cells to Ca^{2+} signal was extrapolated from the fit line. (C) The time taken for 50% of cells to Ca^{2+} signal (as quantified in (B)) across all SLBs. Data points were fit with an [agonist] vs. response curve (four points) in GraphPad Prism to guide the eye.

Two questions arise from these results: the first, is why cells Ca^{2+} signal on null pMHC? The second is, why J8-GECI-LFA-1 cells were faster to activate on 2nd generation SLBs containing null pMHC or low agonist pMHC (9V) densities, despite these conditions being less adhesive overall? The former is addressed in **Chapter 7**, but briefly it was found adhesion and TCR-dependent. For the latter question, one explanation is that although cells are slower to adhere to 2nd generation SLBs, cells are faster to Ca^{2+} signal once adhered. The total time to Ca^{2+} signal can be considered an equation of time to adhered + time to signal once adhered. This is assuming Ca^{2+} signals are dependent on adhesion (this was found to be the case and is examined more in **Chapter 7**). Based on this, 1st generation SLBs have a quick adhesion time, but are slower to signal once adhered. In contrast, cells on 2nd generation SLBs have a slower adhesion time, owing to the glycocalyx, but a quicker time to signal once adhered, owing to the presence of CD58. The balancing effects of these proteins could give rise to the observed kinetics in **Figure 4.4C**. The time to adhesion has already been quantified in in **Figure 4.3**, highlighting how cells on 2nd generation SLBs tend to be slower. The time signal once adhered was then analysed (**Figure 4.5**). The median of the distribution for each SLB was plotted for ease of comparison. The resulted showed that on null pMHC or low densities of agonist pMHC (9V, < 1 molecules/μm^2), but not high densities of pMHC (>1 molecule/μm^2), J8-GECI-LFA-1 cells showed quicker responses on 2nd generation SLBs (**Figure 4.5**). On null pMHC cells took a median of ~140s vs. ~240s on 1st and 2nd generation SLBs, respectively. This shows that although cells are slower to adhere, they are quicker to signal on 2nd generation SLBs. This may (partially) explain the more switch like response seen in **Figure 4.4A**.

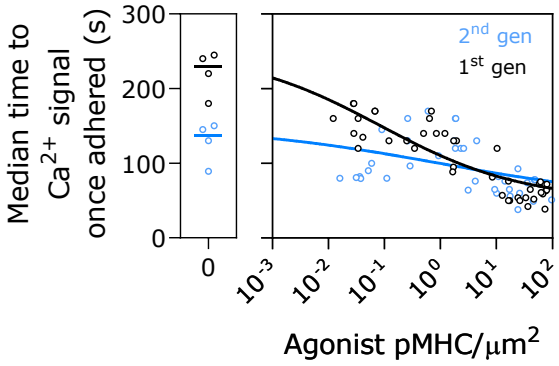

Figure 4.5. **J8-GECI-LFA-1 cells Ca^{2+} signal quicker on 2nd generation SLBs after they have adhered**. Shows the median time for J8-GECI-LFA-1 cells to Ca^{2+} signal once adhered, analysed from the same experimental data in **Figure 4.3**. ~20% of cells across all conditions signalled before adhesion (not shown), but only cells that adhered before signaling were chosen for the analysis. Data points were fit with an [agonist] vs. response curve (four points) in GraphPad Prism to guide the eye. Curves for 1st and 2nd generation SLBs were separately constrained so that the max value was set by the average of the four null pMHC readings

4.3.4 Second generation SLB alter the duration of Ca^{2+} signals at low densities of agonist pMHC (9V).

As cells were quicker to respond on 2nd generation SLBs once adhered, it indicated that the contacts formed may be more stable than on first generation SLBs. This may also influence the quality of the Ca^{2+} signal. For this reason, the next metrics compared between 1st and 2nd generation SLBs were the duration and amplitude of the Ca^{2+} signal. These can be used as a proxy for the quality/strength of stimulation. The duration was calculated using the full width at half-maximum of each Ca^{2+} signal (**Figure 4.6A**). The amplitude was calculated from the maximum fold-change in the normalised calcium intensity (**Figure 4.6B**). As some cells (10-30% depending on SLB condition) showed oscillations in their Ca^{2+} signals (not shown), only the first increase was used for analysis.

The median of the distribution for each SLB was plotted for ease of comparison. On null pMHC, the duration of the response lower on first generation SLBs compared to 2nd generation SLBs (35s vs. 50s). For lower agonist pMHC (9V) densities (0.01-1 molecule/μm²) cells on 1st generation SLBs the median duration remained ~40s with a few experimental outliers at higher values (~60s). At a density of ~10 molecules/μm² this plateaued at ~65s. The median duration of cells on 2nd generation SLBs remained fixed across all agonist pMHC densities at ~65s. Next the magnitude/amplitude of the Ca^{2+} signal was analysed (**Figure 4.6B**). The median amplitude (~6-7) was consistent across both 1st and 2nd generation SLBs on null pMHC and all agonist pMHC densities. These results show the duration, but not the amplitude, is enhanced on 2nd generation SLBs.

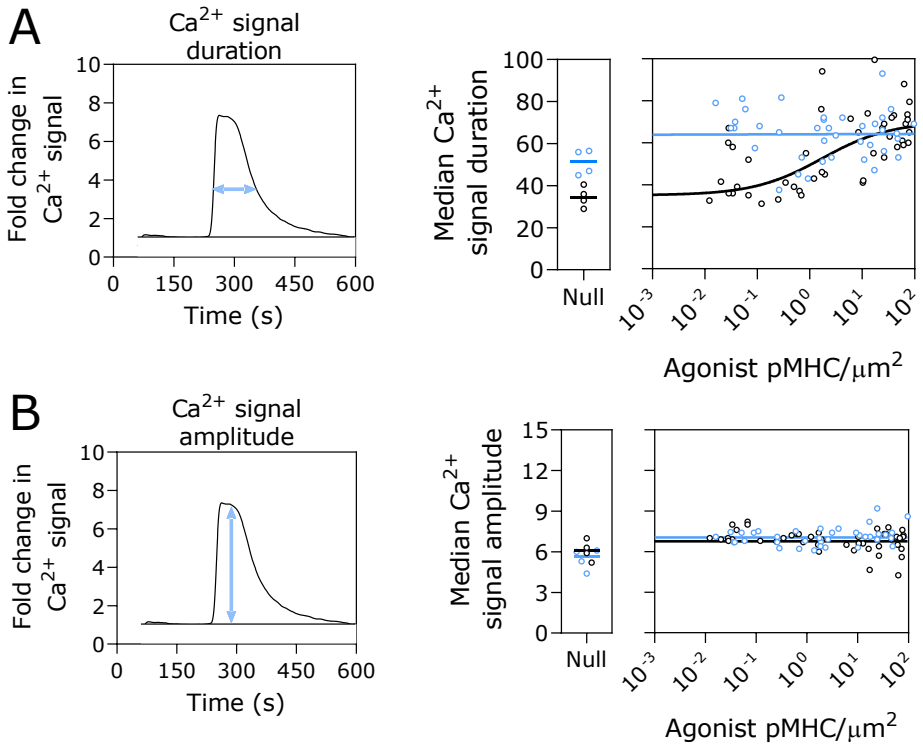

Figure 4.6. **2nd generation SLBs alter the 'strength' of Ca^{2+} signal at low, but not high, densities of agonist pMHC (9V).** Shows the median duration (A) and amplitude (B) for J8-GECI-LFA-1 Ca^{2+} signals across conditions, analysed from the same experimental data in **Figure 4.3**. (A&B) Graphical example of how the duration (A) and amplitude (B) are calculated are shown on the left. Data points were fit with an [agonist] vs. response curve (four points) in GraphPad Prism to guide the eye.

4.3.5 Small T-cell membrane areas are used to probe the SLB surface

Ca^{2+} tracking was useful in obtaining details about the kinetics of adhesion and T-cell activation. To gain insight into the nature of the contacts cells made with 2nd generation SLBs J8-GECI-LFA-1 cells were imaged by TIRFM. Cells were imaged using the GECI and by labelling the cell membrane with CellMask Red. On null pMHC, cells were seen moving across the imaging frame, consistent the increased mobility on 2nd generation SLBs seen in **Figure 4.3**. Whilst moving across the SLB, small (0.25-0.5μm in diameter), distinct areas of CellMask signal (inferred to be cell membrane) could also be seen moving across the imaging frame, as well as in and out of focus (**Figure 4.7A&B**). Given their small and potentially diffraction limited size (TIRF lateral resolution = ~0.25μm), these are likely microvilli probing the surface (**Figure 4.7B**). For cells that didn't stop/adhere to the surface, this continued throughout the video, or until cells moved out the imaging frame. For those that stopped moving/adhered but didn't Ca^{2+} signal, these distinct areas would continue moving in and out of focus beneath the cell (**Figure 4.7C**). Occasionally, some cell membrane areas would remain in view and slowly begin to expand in area. These may represent stably attached contacts. For cells that stopped and showed a Ca^{2+} signal, these distinct membrane areas would expand into a much larger zone before the Ca^{2+} signal occurred (**Figure 4.7D**). These small cell membrane 'puncta' were also seen on 2nd generation SLBs presenting agonist pMHC (9V; **Figure 4.8**). High agonist pMHC (9V) density (50-100 molecules/μm^2) led to a large reduction in the time spent 'probing,' whereby cell adhered to the surface quicker, leading to a shorter time to Ca^{2+} signal and more rapid expansion in the size of the cell membrane (**Figure 4.8**).

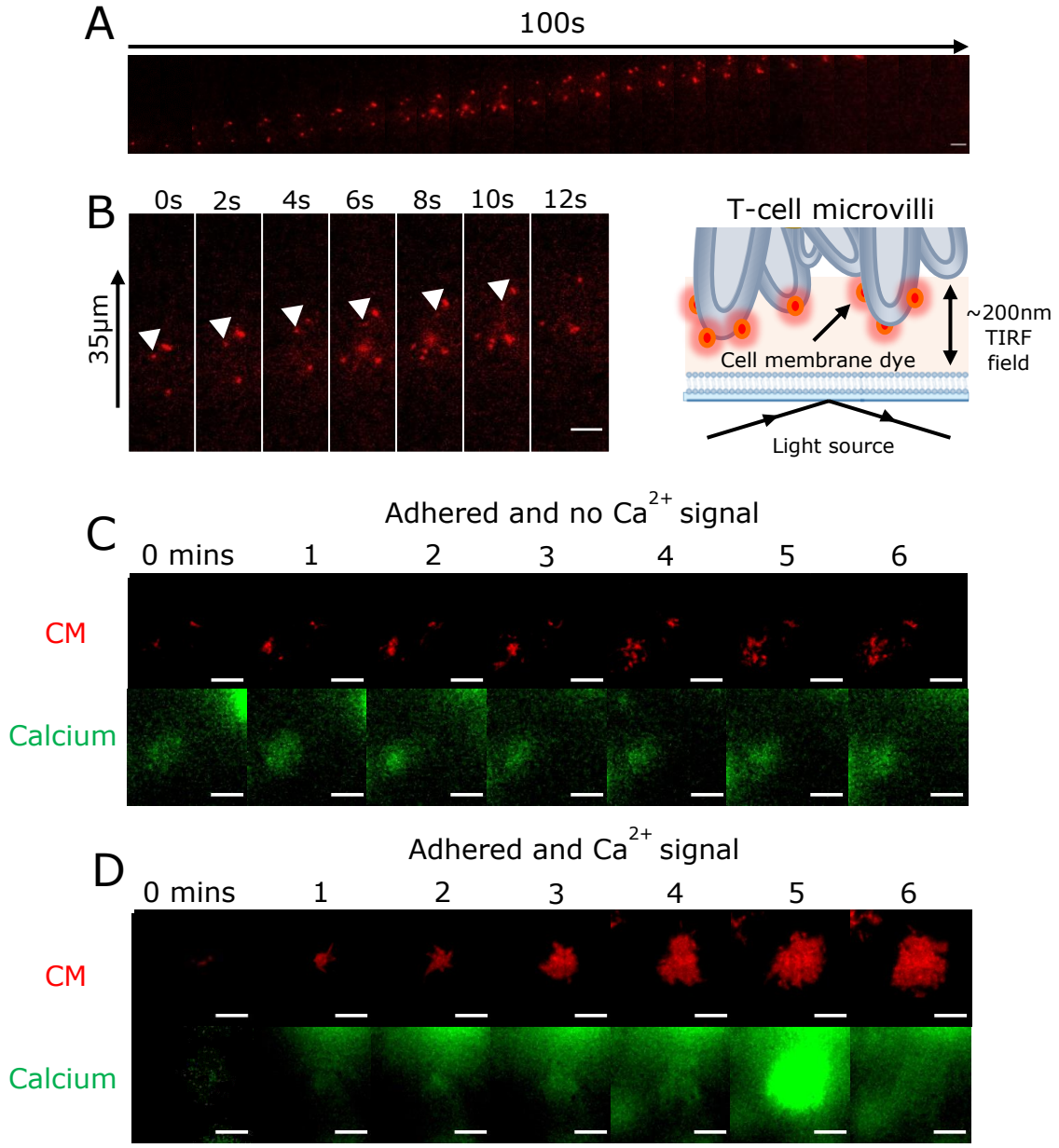

Figure 4.7. **Cells on 2nd generation SLBs (null pMHC) initially probe the surface with small membrane areas.** J8-GECI-LFA-1 cells were imaged on 2nd generation SLBs with null pMHC. Cells were imaged using the GECI (shown in green) and by labelling the cell membrane with CellMask™ Red ('CM,' shown in red). (A) Example of one cell moving over the surface for 100s. Shown are small and distinct areas of cell membrane under the cell that moving across the surface as well as in and out of focus. (B) Digital zoom showing small areas of cell membrane moving in and out of focus (indicated by white arrows). On the right is a cartoon showing the possible cell membrane topology to explain these observations. (C) Example of a cell that has stopped moving over the surface (adhered) but continues to probe with small and distinct areas of cell membrane. These cells did not show a Ca^{2+} signal. (D) Example of a cell that adhered and formed larger contiguous areas of cell membrane. These cells occasionally showed a Ca^{2+} signal. All scale bars are 5µm.

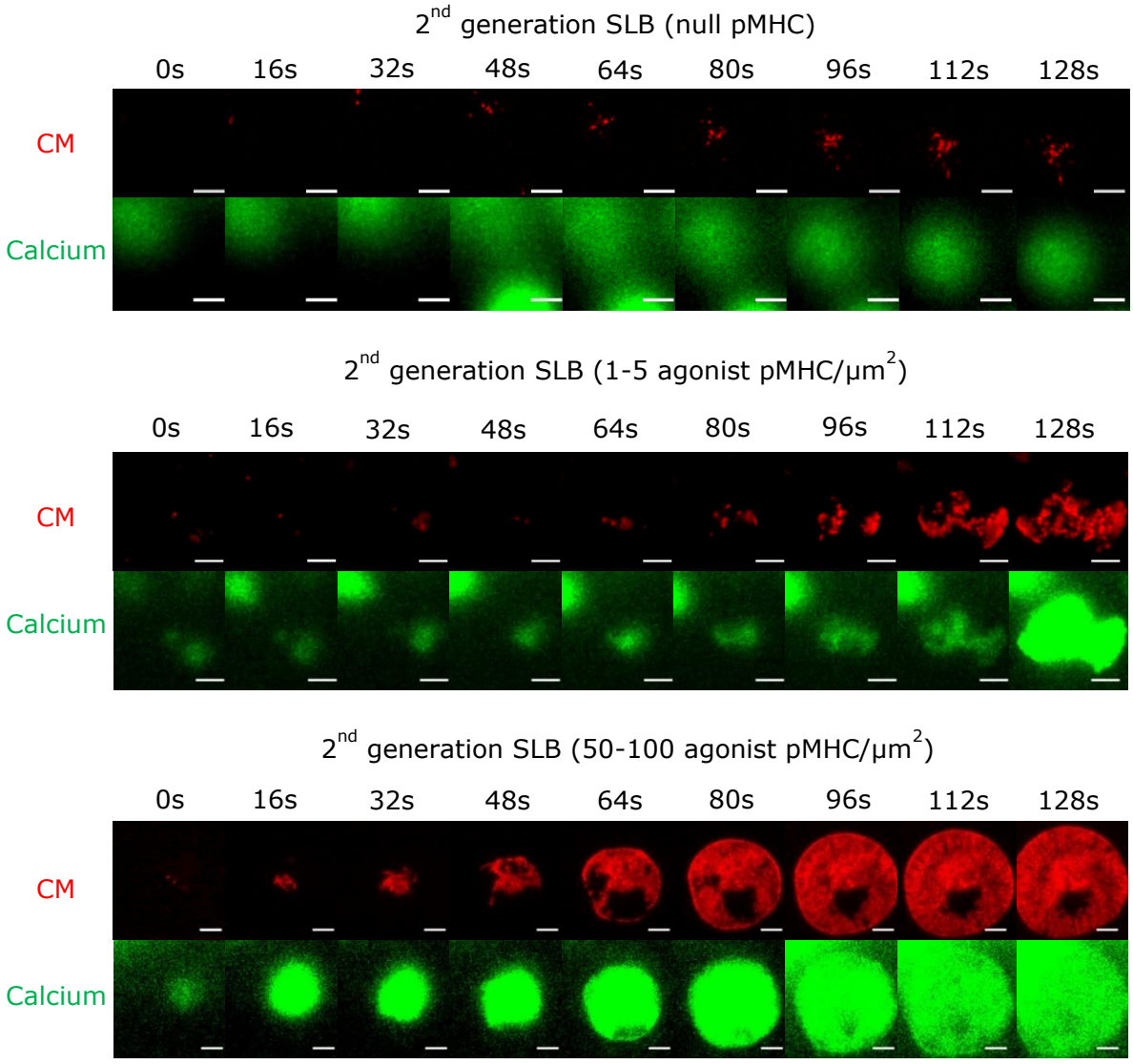

Figure 4.8. **Cells spend less time probing with small areas of cell membrane with increasing densities of agonist pMHC (9V).** J8-GECI-LFA-1 cells were imaged on 2nd generation SLBs with the indicated agonist pMHC density. Cells were imaged using the GECI (shown in green) and by labelling the cell membrane with CellMask™ Red (shown in red). Cells were imaged from when CellMask signal could first be seen under a cell. All scale bars are 5μm.

When analysing J8-GECI-LFA-1 cells on 1st generation SLBs presenting null pMHC, they would initially probe the surface using small and distinct areas of cell membrane like with cells on 2nd generation SLBs (**Figure 4.9A**). After ~5-minutes adhered to the surface (i.e. when the cell stopped moving), cells would begin to form more contiguous areas of CellMask presumably through interaction with ICAM-1 (**Figure 4.9B**). In contrast, cells on 2nd generation SLB continue to probe with small membrane areas (**Figure 4.9C**).

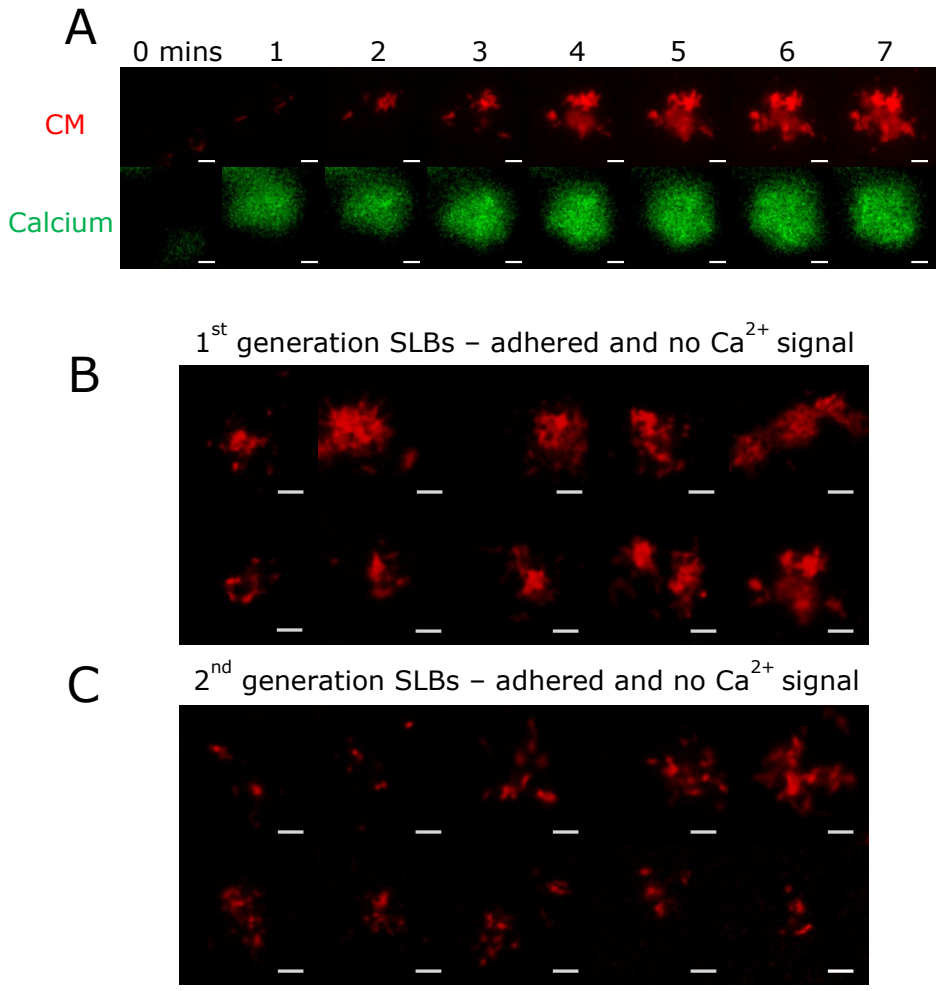

Figure 4.9. **Non-signaling J8-GECI-LFA-1 cells form more contiguous membrane areas on 1st generation SLBs**. (A) Time series of J8-GECI-LFA-1 cells interacting with a 1st generation SLB presenting null pMHC. Cells were tracked using the cell membrane labelled with CellMask Red ('CM,' shown in red) and GECI (shown in green). Images shown are from when the cell first adhered. Example of 10 cells taken 5-minute after adhering on 1st generation SLBs (B) or 2nd generation SLBs (C) presenting null pMHC. All scale bars are 5μm.

4.3.6. No distinct differences in synapse formation second generation SLBs

Next, cells were monitored for their ability to form immune synapses. This is characterised by a central area of pMHC/TCR accumulation (i.e. the cSMAC) surrounded by a ring of ICAM-1 accumulation (i.e. the pSMAC). This was tested by imaging cells on the same SLBs used for the calcium analysis in **Figures 4.3-4.6**. This was done immediately after the 10-minute video. This was possible as the SLBs used agonist pMHC-Alexa 647 and ICAM-1-Alexa 555. Shown in **Figure 4.10** are representative images from different agonist pMHC densities. On null pMHC, ICAM-1 accumulation was seen under 10-20% of cells (**Figure 4.10**). This occurred on both 1st and 2nd generation SLBs. At an agonist pMHC (9V) density of ~0.01 molecules/μm^2, similar results were seen. At ~0.1 molecules/μm^2 more prevalent ICAM-1 ring formations could now be seen on 1st generation SLBs. 2nd generation SLBs remained the same. At 10 or 100 molecules/μm^2, pMHC-Alexa 647 accumulation was clearly visible, and most cells (~60-70%) formed immune synapses. This was the case on both 1st and 2nd generation SLBs. This data shows that J8-GECI-LFA-1 cell line can form immune synapses, like primary T cells, and that synapse formation occurs on both 1st and 2nd generation SLBs. Altering the density of agonist pMHC appears to mainly effect the percentage of cells showing synapse formation.

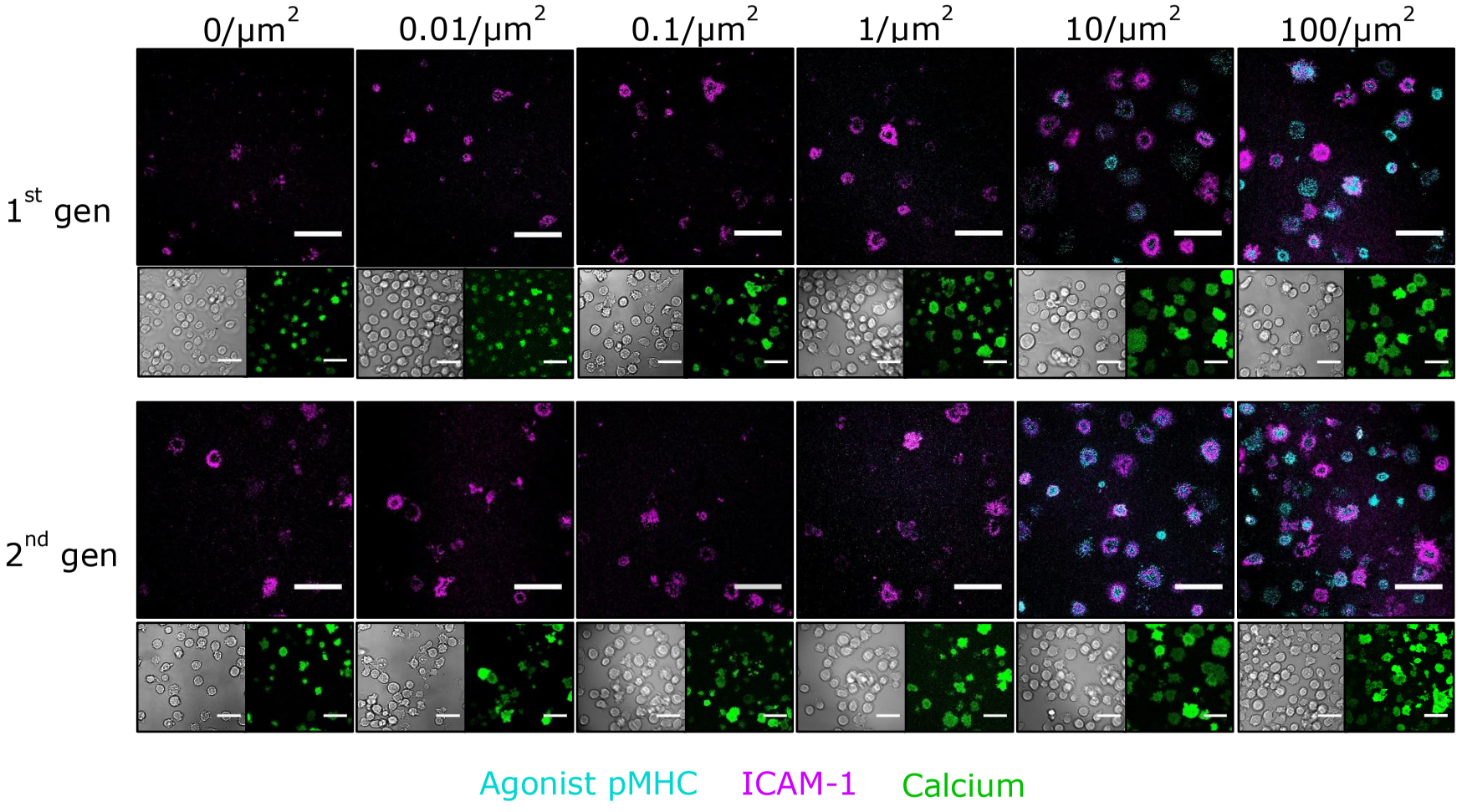
0/μm2
0.01/μm2
0.1/μm2
1/μm2
10/μm2
100/μm2
1st gen
2nd gen
Agonist pMHC
ICAM-1
Calcium

Figure 4.10. **Immune synapse formation on 1st and 2nd generation SLBs.** Immediately after the 10-minute video used for the Ca^{2+} signal analysis in **Figures 4.3-4.6**, the SLB and cells were imaged using a 63x magnification oil objective on the scanning confocal microscope. SLBs contained pMHC-Alexa 647 (shown in cyan) and ICAM-1-Alexa 555 (shown in magenta). Cells were imaged using brightfield illumination and their calcium signal (shown in green). Densities above images indicate number of agonist pMHC (9V) molecules/μm^2. Top row and bottom row are 1st and 2nd generation SLBs, respectively.

To observe the dynamics of synapse formation on 1st and 2nd generation SLBs, J8-GECI-LFA-1 cells were then imaged by TIRFM. High densities of agonist pMHC (50-100 molecules/μm^2) was used as pMHC accumulation was visible at this density and because it was not a limiting factor, ensuring most T-cells would activate. On 1st generation SLBs, J8-GECI-LFA-1 cells would stop on the surface, which coincided with pMHC and occasionally ICAM-1 accumulation. After a 30-60s delay a Ca^{2+} signal occurred (**Figure 4.11A**). After calcium release cells would form additional distinct zones of pMHC accumulation (or 'pMHC-TCR microclusters') surrounded by areas of ICAM-1 accumulation, all of which moved centripetally (**Figure 4.11A**). After 4-5-minutes, cells had formed a large central area of pMHC accumulation surrounded by a ring of ICAM-1 accumulation. Throughout the contact interface, areas of pMHC accumulation colocalised with 'holes' in ICAM-1 accumulation, indicative of ICAM-1 exclusion, highlighting how these proteins are pre-segregated into their own domains during synapse formation (**Figure 4.11B**). 10-minutes after adding cells to the SLB, most cells (~70-80% of cells) had formed immune synapses with a central area of pMHC accumulation surrounded by ICAM-1 (**Figure 4.11C**). Very similar results were found for cells on 2nd generation SLBs (**Figure 4.12A-C**). It appears that addition of CD58 and the APC glycocalyx did not alter the overall formation or appearance of the immune synapse in an easily discernible manner, at least when using high/saturating densities of agonist pMHC.

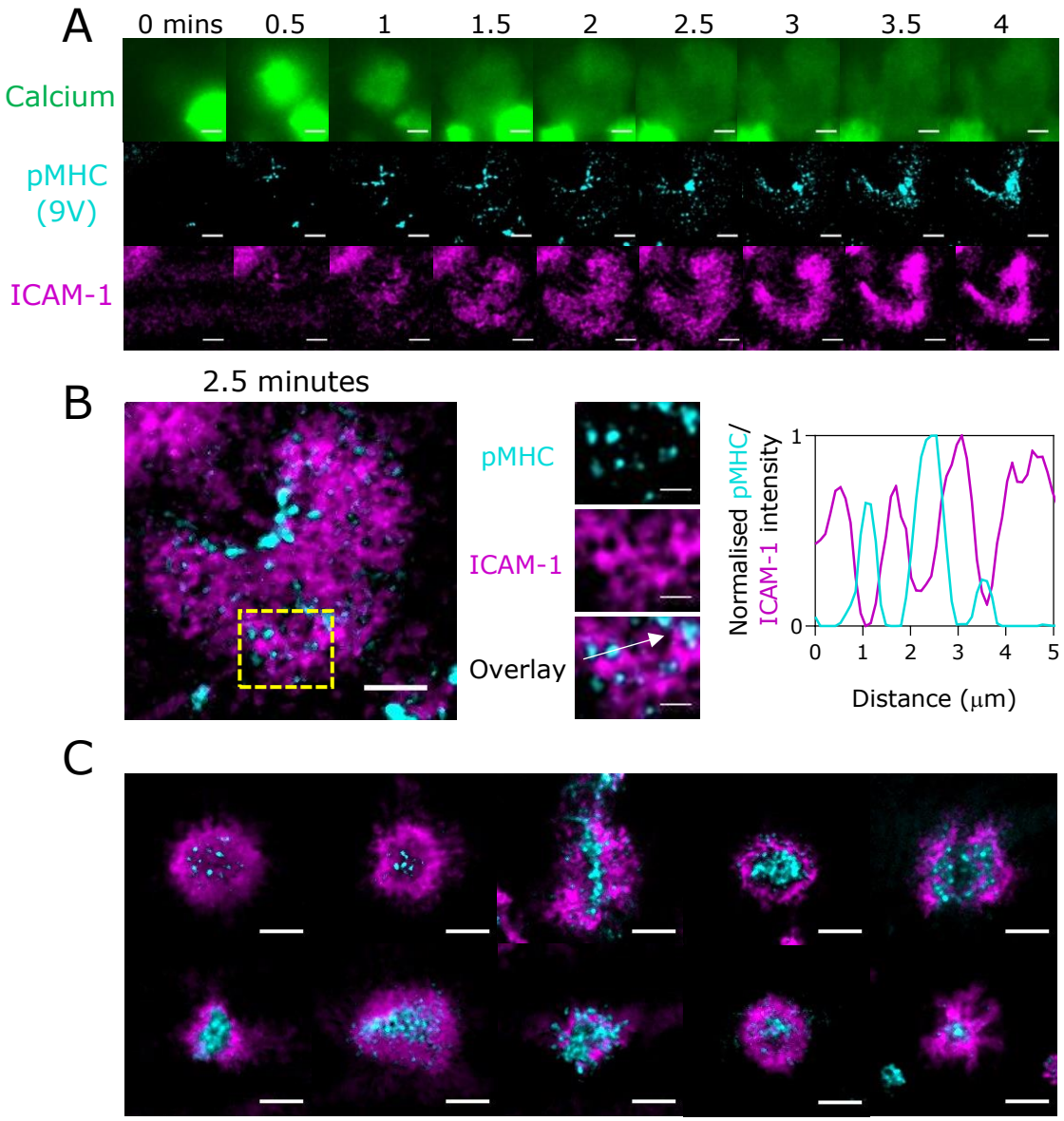

Figure 4.11. **pMHC and ICAM-1 exclusion/accumulation on 1st generation SLBs with high density of agonist pMHC (9V).** J8-GECI-LFA-1 were dropped on 1st generation SLBs containing high densities (50-100/μm^2) of agonist pMHC (9V). To visualise immune synapse formation, pMHC and ICAM-1 were labelled with Alexa 647 and 555, respectively. (A) Representative example of a cell forming a synapse over 4-minutes. Distinct areas of pMHC accumulation can be seen followed by calcium release. After calcium release, cells spread, and additional pMHC puncta and areas of ICAM-1 accumulation form. All proteins move centripetally over time. (B) Enlarged overlay of time point 2.5-minutes taken from (A). Middle is an inset taken from the yellow box in the left most image. Right plot: line intensity profile along and in direction of white arrow in inset overlay. Agonist pMHC (9V) accumulates in areas of ICAM-1 exclusion. (C) Examples of late-stage synapse formation (10-minutes after landing), showing the classical structure of the immune synapse; central agonist pMHC accumulation surrounded by a ring of ICAM-1. Scale bars are 5μm.

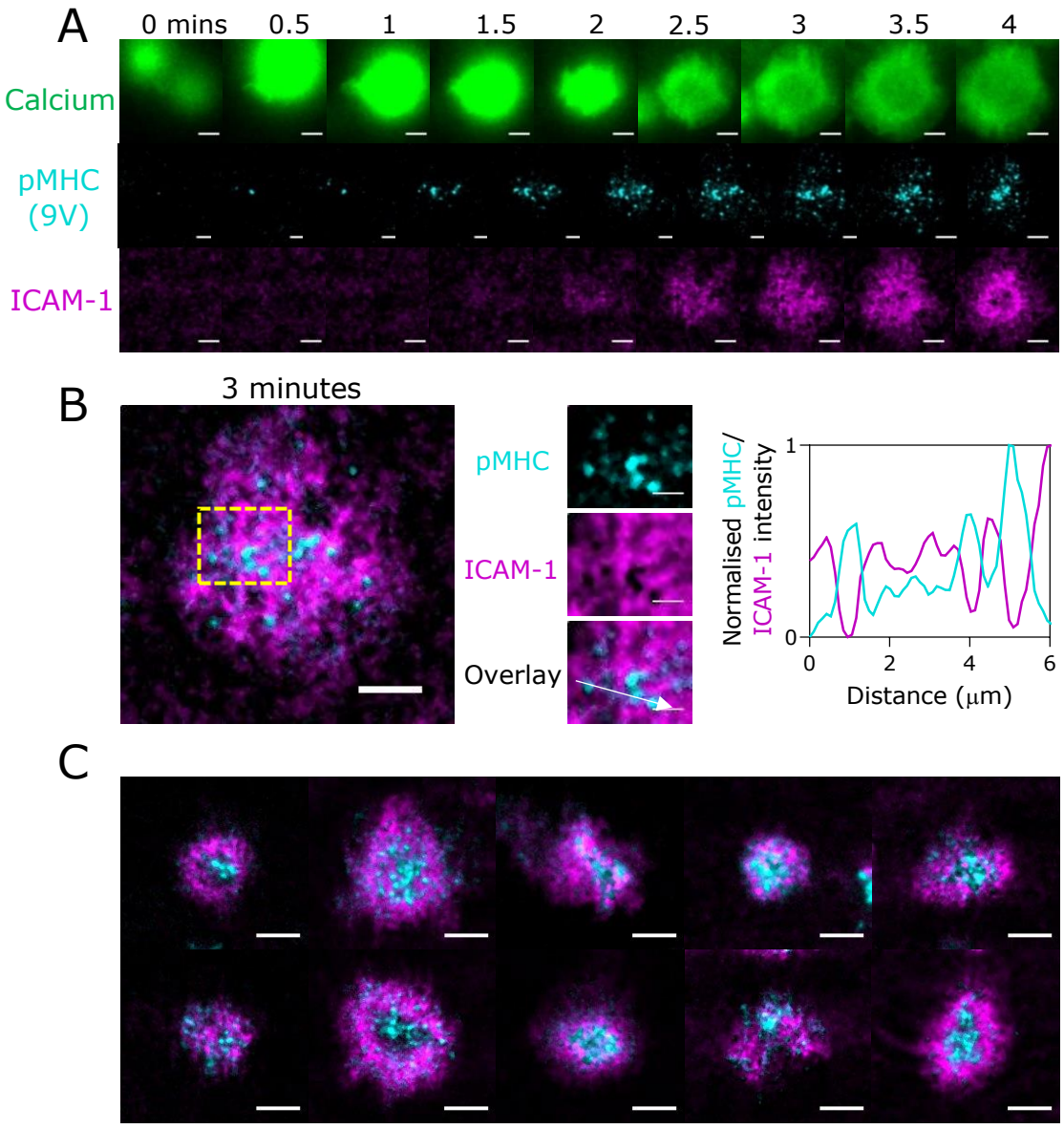

Figure 4.12. **pMHC and ICAM-1 exclusion/accumulation on 2nd generation SLBs (high density agonist pMHC).** J8-GECI-LFA-1 were dropped on 2nd generation SLBs containing high densities (50-100/μm²) of agonist pMHC (9V). To visualise immune synapse formation, pMHC and ICAM-1 were labelled with Alexa 647 and 555, respectively. (A) Representative example of a cell forming a synapse over 4-minutes. Distinct areas of pMHC accumulation can be seen followed by calcium release. After calcium release, cells spread, and additional pMHC puncta and areas of ICAM-1 accumulation form. All proteins move centripetally over time. (B) Enlarged overlay of time point 3-minutes taken from (A). Middle is an inset taken from the yellow box in the left most image. Right plot: line intensity profile along and in direction of white arrow in inset overlay. Agonist pMHC (9V) accumulates in areas of ICAM-1 exclusion. (C) Examples of late-stage synapse formation (10-minutes after landing), showing the classical structure of the immune synapse; central agonist pMHC accumulation surrounded by a ring of ICAM-1. Scale bars are 5μm.

4.4 Discussion

The results of this chapter characterises the behaviour of T cells on 1st and 2nd generation SLBs. Introduction of the APC glycocalyx and small adhesion protein CD58 led to several key differences. The first was delayed adhesion to the surface, likely from the extracellular domains of the glycocalyx (CD43 and CD45) forming a steric barrier to contact formation [114]. The second, was altered activation kinetics, whereby cells activate quicker but only once they have adhered to the surface. The third, was an enhancement in the duration of the Ca^{2+} signal. These two points are likely a result of adding CD58, which may enhance antigen scanning and stabilise pMHC-TCR engagement through forming comparable sized contacts to pMHC-TCR interactions [201]. The fourth difference was that prior to a Ca^{2+} signal, cells used small distinct areas of membrane (possibly microvilli, addressed further in **Chapter 5**) to probe the SLB surface, even when the cells had adhered (indicated by the cell becoming stationary). Although cells initially used small membrane points on 1st generation SLBs, they would form larger and more contiguous areas of membrane once adhered (and before a Ca^{2+} signal). This likely reflects a reduced capacity (or at least slowed kinetics) to adhere to ICAM-1 and spread out on 2nd generation SLBs, instead forcing the cell to maintain adhesion through small membrane points. Importantly, all these differences were only seen at low agonist pMHC densities (<1 molecules/μm^2). At high agonist pMHC densities (>10 molecules/μm^2) the surfaces became near indistinguishable in adhesion, activation kinetics and synapse formation, highlighting the importance of quantifying, and using, low agonist pMHC densities to test for surface specific effects.

4.4.1 Tuning the density of agonist pMHC

To modify the density of agonist pMHC (9V), null pMHC was exchanged out at a molar ratio. This technique has been applied successfully in previous studies [83], [327]. Maintaining a constant high total pMHC density accurately reflects the nature of T-cell interaction with APCs, where they are normally exposed to high densities of total pMHC but must scan for rare agonist antigens. Furthermore, as agonist pMHC was diluted 20-100x relative to null pMHC on the SLB, any unwarranted (and unlikely) aggregation of agonist pMHC would be with null pMHC, ensuring monomeric interaction with the TCR. More specific advantages to the system here is that it allows titration of agonist pMHC density within a linear regime without affecting other protein densities, given their competition for binding free NiNTA sites, as well as blocking free NiNTA sites.

In order to quantify agonist pMHC density, pFCS was used. Due to the unlikely event of very low densities of agonist pMHC entering the confocal volume during pFCS measurements, four-point concentration titrations were used to extrapolate densities <1 molecule/μm^2. This technique provided an accurate method to measure protein density given the relatively small variation for a given concentration of agonist pMHC 9V applied to SLBs produced on separate days (as was done here). Variation could lead to alterations in dose-response curves of activation but is largely mitigated by performing multiple repeats across many concentrations. Although there are many sources that add to variation, these can be largely addressed by: careful and stringent preparation of SLBs; using thawed, labelled proteins for short periods of time (< 2 weeks) to reduce fluorescence decay; and consistently performing calibrations of the microscope, such as

optimising the location of the confocal pinhole (regulates the shape of the point spread function), each experimental setup.

4.3.2 Adhesion on first generation SLBs

In **Chapter 3**, cells failed to adhere to the SLBs when using near-saturating densities of null pMHC. In this chapter, addition of ICAM-1 to high densities of null pMHC resulted in 80-90% of cells adhering to the surface, however, most cells did not show obvious areas of ICAM-1 accumulation. The lack of ICAM-1 accumulation is most likely a result of no/minimal 'inside-out' signaling from the TCR within this setup but this raises questions as to how T cells are adhering to first generation SLBs presenting only null pMHC if ICAM-1 is not being visually engaged. One possible explanation is that LFA-1 is engaging ICAM-1 whilst in a low-medium affinity conformation (perhaps established by using magnesium ions in the imaging media) but isn't detectable by simply imaging ICAM-1 accumulation, which may only be witnessed upon TCR/chemokine-derived 'inside-out' signaling [421], [422]. This could be tested simply by comparing time to adhesion and imaging ICAM-1 accumulation of cells interacting with first generation SLBs presenting null pMHC in the presence and absence of magnesium ions in both TCR^+ and TCR^- cell lines.

4.3.3 Activation kinetics on second generation SLBs

Despite T cells being less adherent overall on 2nd generation SLBs, they had a higher and faster baseline rate of activation than on 1st generation SLBs. One potential explanation

was because cells were quicker to respond once adhered on 2nd generation SLBs. The increased adhesion and signaling from (presumably) engaging CD58 outweighs the delayed adhesion and subsequent activation from the glycocalyx. However, this does not explain all characteristics of the dose-response curve. For example, why is it that ~2-3 molecules/μm^2 of agonist pMHC (9V) on 2nd generation SLBs (compared to ~0.01-0.1 molecules/μm^2 on 1st generation SLBs) are required before any changes in the occurrence or kinetics of T-cell activation are seen? A shift in the threshold implies cells have a difficulty finding or responding to low agonist pMHC densities, which is at odds with the observation that cells have a higher baseline rate of activation on 2nd generation SLBs. Perhaps there are a subset of cells best able to adhere to the surface. For example, cells in the top 25% in a distribution of CD2 (binds CD58) expression may be those showing a Ca^{2+} signal as they adhere quicker. Beyond the density of 2-3 molecules of agonist pMHC/μm^2, less adhesive cells may have more of a chance of responding to agonist pMHC. This could be examined by grouping cells into those that signal and those that don't and quantifying their time to adherence. Another possibility is that null pMHC may behave as a weak agonist, and its binding dominates until 2-3 molecules/μm^2 of agonist pMHC (9V) are present. The incorporation of auxiliary molecules (e.g. CD58) may enhance the probability of signaling to null pMHC, explaining the increase in the baseline amount of signaling seen on 2nd generation SLBs [416]. Modelling these results may help to provide the answer.

The overall difference in the activation curves between 1st and 2nd generation exhibit more subtle differences rather than orders of magnitude changes. This may be a result

of adding two opposing components in terms of their adhesive properties i.e. the small adhesion protein CD58, and the steric glycocalyx barrier. Furthermore, because two components were added the effect of each cannot be conclusively inferred from comparing 1st and 2nd generation SLBs. It would be beneficial to produce dose-response curves when adding/removing a single component at a time. For example, removing CD58 from 2nd generation SLBs may reduce the baseline level of activation and increase the density required for the half-maximal response as a result of the glycocalyx now dominating the adhesion-repulsion balance. This approach may also help to explain the cause of a higher baseline level of activation, and quicker time to respond on 2nd generation SLBs with low agonist pMHC densities.

4.3.4 Immune synapse formation

When comparing immune synapse formation on 1st and 2nd generation SLBs, no substantial differences were observed, implying that the more complex composition of 2nd generation SLBs does not impede or alter major reorganisation of pMHC/TCR and ICAM-1/LFA-1. Although high densities of agonist pMHC were used, it is unlikely that major differences in the overall structure of synapse formation will occur when comparing the SLBs at lower densities. In previous studies using 1st generation SLBs, commitment to synapse formation appears independent of agonist pMHC density (but not necessarily affinity), with as low as 0.2 molecules/μm^2 inducing the structure [83], [328]. However, agonist pMHC density does affect the percentage of cells forming synapses, the kinetics of synapse formation and its overall size [83], [85], [327], [328], results presented in this chapter). Given J8-GECI-LFA-1 cells showed more substantial

Ca^{2+} signaling on 2nd generation SLBs at low agonist pMHC density, and even on null pMHC, it is possible these metrics associated with synapse formation were enhanced relative to 1st generation SLBs. It would be beneficial to quantify such metrics to identify whether proteins other than pMHC and ICAM-1 govern the kinetics of immune synapse formation.

Chapter 5: Dynamic microvilli are essential for antigen scanning

5.1 Introduction

Efficient antigen scanning and discrimination underpin the initiation of the T cell adaptive immune response. Crucial to antigen scanning is forming close membrane contacts (~15nm across) with target cell or APCs. This enables the interaction of the TCR with foreign pMHC. To achieve these close contacts T cells must overcome the physical barrier comprising the large and heavily glycosylated protein glycocalyx that surrounds cells. This barrier can extend from 100-1000nm, dependent on cell type [329], [330]. T cells are known to spend 1-5 minutes scanning each APC, and because foreign pMHC is often in limited abundance, the question arises of how T cells can overcome the glycocalyx to efficiently identify rare antigen events in such short periods of time [61].

Scanning electron microscopy and 3D live fluorescence imaging have shown that T cells are coated in hundreds of dynamic actin-driven membrane protrusions, referred to as microvilli [122], [123]. These protrusions range from 100nm to several microns long and 100-500nm in diameter. Their dynamic nature is evidenced by their achieving 98% coverage of a T-cell surface in one minute, indicating their main purpose is to efficiently scan their 3D environment for antigen [122]. Their size and dynamic nature certainly make microvilli an attractive adaptation for overcoming the glycocalyx to achieve close contacts that permit TCR-pMHC binding [114], [121]. In support of microvilli as antigen

detectors, TCR, CD4, and Lck were found enriched at microvillus tips (relative to the cell body), and increased ZAP-70 recruitment was observed at microvilli contacts with anti-CD3 coated glass [123], [125], [126].

Previous attempts to visualise the molecular events at microvilli have employed 2D surfaces, due to the topological complexity of imaging cell-cell contacts. Cai et al. (2017) visualised the topology of contacts through a 'synaptic contact mapping (SCM)' technique involving T cells interacting with a 1st generation SLB system containing pMHC, ICAM-1 and quantum dots (QD; [122]). Using live imaging, the stability of membrane protrusions ('holes' in the QD signal) were found to be on average 540nm in diameter, comparable to microvilli diameter, and the holes correlated with TCR microcluster localisation and migration. However, this study focussed on analysing contacts minutes after cell landing, by which point the cells had already spread and formed synapses. The depth of these QD holes was ~50nm, much shallower than the length of microvilli. It is not clear whether these late stage contacts reflect the molecular composition of contacts made by microvilli. This is because cells undergo significant cytoskeletal rearrangements during synapse formation leading to protein reorganisation [266]. In addition, because they did not directly relate contacts to functional readouts of activation it remains unclear at which point the cell had first detected and responded productively to antigen. More recently, Razvag et al. (2019) attempted to address this. Using T cells on anti-CD3 coated glass in combination with several super-resolution imaging techniques, they showed robust ZAP-70 recruitment to initial and discrete areas of membrane contacting the glass [125]. However, due to the high affinity binding (2nM)

and potent crosslinking effects of immobile anti-CD3 antibody, whether productive signaling in response to bona fide ligand arises at initial microvilli contacts remains to be seen [331]. In addition, the influence of antigen density and affinity on T-cell surface microvilli contacts remains uncharacterised.

In this chapter, 2nd generation SLBs (pMHC, ICAM-1, CD58, CD43 and CD45) are used to address key aspects of T-cell microvillar contacts. The J8 cell line is first shown to be suitable to study microvillar biology. Next a novel approach to view microvillar contacts is developed. This is achieved by fluorescently labelling the SLB glycocalyx, which is excluded passively upon microvillar contact, represented by holes in the fluorescence signal. Using this approach, in combination with labelling the membrane and TCR, microvillar contacts are found to dominate the contact interface between T-cells and SLB. The formation of microvillar contacts are then related to T-cell activation by correlating their formation with calcium release across different agonist pMHC densities. Lastly, the importance of microvilli as efficient antigen scanning platforms is addressed.

5.2 Methods

Scanning electron microscopy (SEM)

13mm diameter glass slides were incubated with Poly-L-Lysine (PLL; 70-150kDa MW; Sigma) according to manufacturer's protocols. $1x10^6$ cells were gently placed on coated slides and left to settle for 20 minutes at room temperature. Cells were fixed in 4% PFA 0.25% glutaraldehyde in PBS overnight at 4˚C. Slides were rinsed in PBS and fixed using 1% OsO_4 incubated at room temperature for 30 minutes. Sample was washed in PBS and dehydrated using increasing concentrations of ethanol (50 to 100% in 10% increments) over an hour. Ethanol was removed and 0.5ml hexamethyldisilazane added for 3 minutes. This was removed and cells dried in a fume cupboard. Glass slides were mounted on carbon adhesive tape, sputter coated with gold, and viewed using a JEOL-6390 Scanning Electron Microscope.

Protein-topology mapping and microvilli quantification

0.5-$1x10^6$ J8s were labelled with anti-CD62L (L-selectin)-Alexa 647 at 4˚C for 1 hour. Cells were washed x2 in PBS, then fixed in 2% PFA and 0.25% glutaraldehyde for 20-minutes at room temperature. During this time cells were labelled with 1x CellMask™ Green Plasma Membrane Stain at room temperature. Cells were washed x2 in PBS and immediately placed on PLL-coated glass surfaces (previously washed with ethanol) for 10-minutes prior to imaging. Imaging was performed on an LSM 880 scanning confocal with AiryScan within 30-minutes of plating. Cells were specifically imaged from the midplane to the apical surface to ensure microvilli in contact with the PLL (basal planes)

were not included, as this could alter protein organisation even after fixation. Z-stacks were taken at 200nm slices every 2s and analysed in Fiji using the Z-projection (max intensity) feature. 15 frames were used per cell analysed. Microvilli diameter were quantified by manually choosing membrane protrusions with clear L-selectin enrichment, obtaining the cross-section line profile, and using the full width at half maximum (FWHM) of the increased signal as a measure of the diameter. 100s of FWHM were analysed automatically using a bespoke MATLAB® script.

CCZ mapping with CD45/CD43/cell membrane/TCR/Calcium

2nd generation SLBs were prepared as previously described in **Chapter 3**. In order to visualise contact topology, CD45RABC and CD43 were labelled separately with either Alexa-555 or -647 (Thermofisher), or both labelled with Alexa-555. Labelled proteins were tested on a nanodrop to ensure labelling efficiency >1 per molecule. All other proteins on the SLB remained unlabelled. SLBs were washed 10 times and resuspended in pre-warmed (37˚C) PBS + 2mM $MgS0_4$. To visualise membrane and/or TCR 0.5-1x10^6 J8-LFA-1 cells (with or without GECI) were labelled using 1xCellMask™ Red/Orange and/or 50ng/µl of UCHT-1 fab labelled with Alexa-488/TMR (Alexa-488 wasn't used on GECI containing cells due to spectral overlap) for 10-minutes in RPMI (no supplements) at 37˚C. Combinations of labelling used are shown in Table 5.1. Cells were then washed x2 and resuspended in pre-warmed (37˚C) PBS + 2mM $MgS0_4$. SLBs and membrane labelled cells were incubated at 37˚C for 5-minutes prior to being dropped gently onto the SLBs and immediately imaged by TIRF microscopy. A complete frame cycle was taken every 2s for 10-minutes as previously described in **Chapter 4**. Images were

processed using FIJI, with unequal TIRF field illumination of CD43 and CD45 corrected by partially removing background from the experimental video. This was done by averaging the background signal (z-projection), measuring the average intensity value, and subtracting 90% of that signal. This modified background (remaining 10%) was then removed from the experimental video. Contact analysis was performed using a bespoke MATLAB® script kindly written by Markus Koerbel (University of Cambridge, Klenerman Lab), described in **Section 2.7**

Label 1	Label 2	Label 3
TCR-Alexa 488	CD45-Alexa 555	CD43-Alexa 647
TCR-Alexa 488	CD45&CD43-Alexa 555	CellMask™ Red
GECI	CD45&CD43-Alexa 555	CellMask™ Red

Table 5.1. Labelling combination strategy.

Loss of antigen scanning and actin drug experiment

$1x10^6$ J8-GECI-LFA-1 cells were washed x1 in PBS and resuspended in either 10μM DMSO (control) 1μM latrunculin B, 10μM cytochalasin D or 100nM jasplakinolide diluted in RPMI (no supplements) for 1 hour at 37˚C with 5% $C0_2$. Cells were then fixed in PBS containing 2% PFA and 0.25% glutaraldehyde for 20-minutes at room temperature. During this period cells were also labelled with CellMask™ Red Plasma Membrane Stain. Cells were washed x2 in PBS and immediately placed on PLL-coated glass surfaces (previously washed with ethanol) for 10 minutes prior to imaging at room temeprature. Mage was performed as described for protein-topology mapping. For the triggering experiments, during drug incubation, SLBs were made containing either no glycocalyx (i.e. just pMHC and CD58) or with the glycocalyx (pMHC, CD58, CD45 and

CD43). pMHC-Alexa 647 and pFCS was used to ensure the density of agonist ligand remained constant across the surfaces. Each condition tested was staggered 30-minutes apart. Cells were then washed x2 and resuspended in pre-warmed (37°C) PBS + 2mM $MgS0_4$ with the same concentration of actin modifying drug. SLBs were washed x10 in pre-warmed (37°C) PBS + 2mM $MgS0_4$ with the same concentration of actin modifying drugs. Cells and SLB were incubated at 37°C for 5-minutes prior to use. The density of pMHC was quickly measured by pFCS and the cells then dropped onto the SLBs. Cells were imaged using a 780 LSM scanning confocal. Calcium release data was analysed using a bespoke MATALB® code (as used in **Chapter 3**).

5.3 Results

5.3.1 J8s can be used to study T-cell microvilli

Previous reports have shown that the T-cell surface is dominated by 'finger-like' membrane protrusions called microvilli. This was observed in both Jurkats and human primary cells [123], [126], [268]. To confirm this also for J8s, which had undergone extensive genetic modification, their morphology was imaged with scanning electron microscopy (SEM). J8s were found similar in morphology to the parental Jurkats (**Figure 5.1**). The diameter of microvilli was between 100-200nm. To confirm the protrusions seen from SEM were microvilli and ensure they were not an artefact of SEM processing, microvilli were imaged using confocal microscopy (**Figure 5.2**). As lymphocyte microvilli were previously found enriched with L-selectin, this could be used to further confirm that any observed membrane protrusions were microvilli [123], [332]. Using

only the images of the midplane from fixed J8s, L-selectin was found enriched on the membrane protrusions surrounding the cell (**Figure 5.2A**). The average diameter and predicted contact area of L-selectin enriched membrane protrusions was found to be 430nm, which corresponds to an average contact area of 0.15μm² at the tip (**Figure 5.2B&C**). As this average diameter is close to the diffraction limit of the confocal microscope (~250nm), the size of microvillar contact areas may be overestimated.

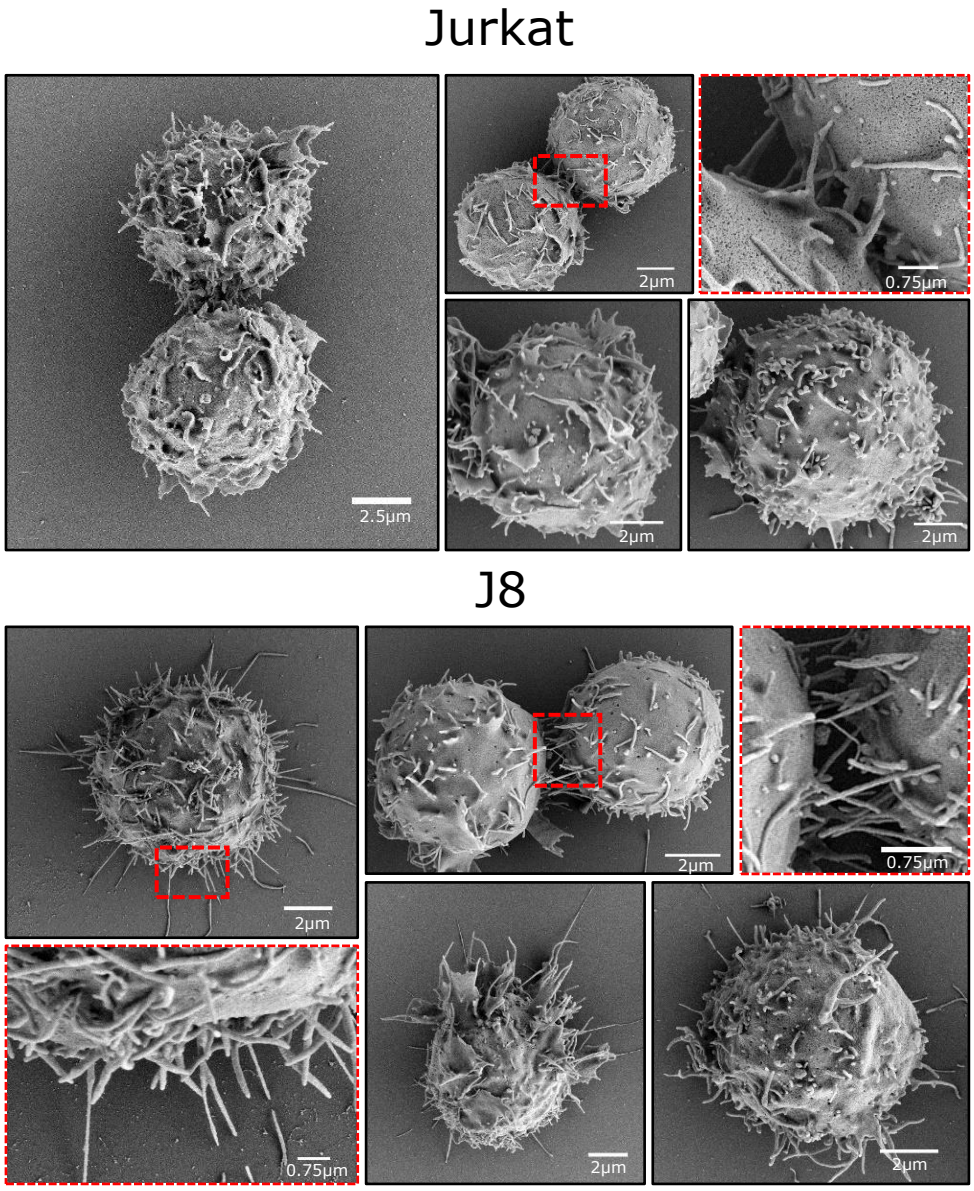

Figure 5.1. **Membrane topology of J8s (1).** (A&B) SEM images of (A) Jurkats or (B) J8s fixed on PLL-coated surfaces. Both Jurkats and J8s contain a mixture of single membrane protrusions of variable length but comparable diameter.

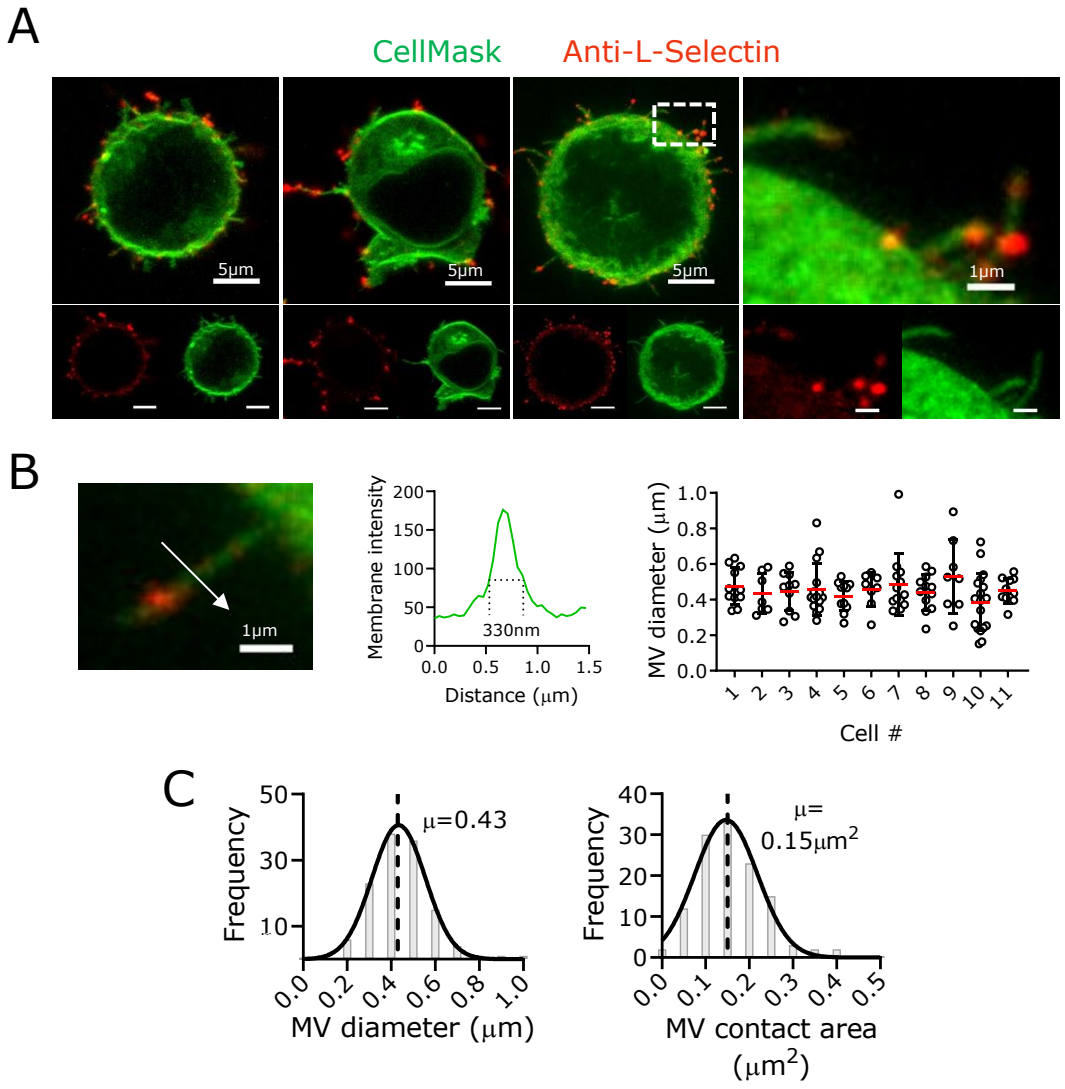

Figure 5.2. **Membrane topology of J8s (2).** (A) Three representative images of the Z-projected (max intensity) midplane of J8s labelled with CellMask™ Green (green) or anti-L-selectin (red). Right most image is an expanded image demarcated by the white box. L-selectin is clearly enriched at microvilli relative to the cell body. (B-D) Quantification of microvillus diameter and predicted contact area. (B) Left: example of a microvillus enriched in L-selectin. Middle: intensity profile along the direction of the white arrow. Right: width of microvillus are calculated from the FWHM of the intensity profile. Diameter of microvilli across cells. (C) Left: distribution of microvillus diameter from pooling all cells. The mean is 430nm. Right: Assuming only the tips make contacts, surface area of contacts were calculated using πr^2. The average contact area is predicted as 0.15µm^2. Images were taken from N=2 independent experiment.

5.3.2 Mapping contact topology using a model of the APC glycocalyx

In a previous study, Krummel and colleagues used SLBs functionalised with pMHC, ICAM-1 and QDs to observe contact topology [122]. Using TIRF to image the surface, 'holes; in the QD signal (decreased fluorescence) were found dependent on the size of the QDs. When testing 13nm vs 16nm QDs only the latter gave observable holes [122]. This supports the use of size-dependent redistribution of SLB components as an appropriate means to observe contact topology. Given pMHC-TCR is of similar dimensions to the 16nm QD, it would suggest small size differences will lead to segregation. However, since Cai et al. looked only at late contacts, the cells may have responded to antigen and undergone significant cytoskeletal rearrangements. As a result, the size of contacts may have grown or become more stable making them easier to observe. We speculated that we may better observe the initial microvillar contacts, prior to antigen detection, by using the same phenomenon of size-dependent protein exclusion using a larger and more physiologically relevant component; the APC glycocalyx [79], [116], [119], [333]–[335]. CD43 or CD45 (i.e. the APC glycocalyx) are reported to be significantly taller than pMHC or CD58 (or 16nm QDs), and have been shown to be excluded from the close membrane contacts formed when pMHC or CD58 bind their receptor [85], [116], [117], [141], [336]–[338].In our experimental setup, by labelling CD43 and/or CD45 on the SLB we should effectively see black holes in their fluorescence signal whenever a close contact formed by microvilli has been established (referred to as microvillar close contact zones (CCZs) from hereon**, Figure 5.3**).

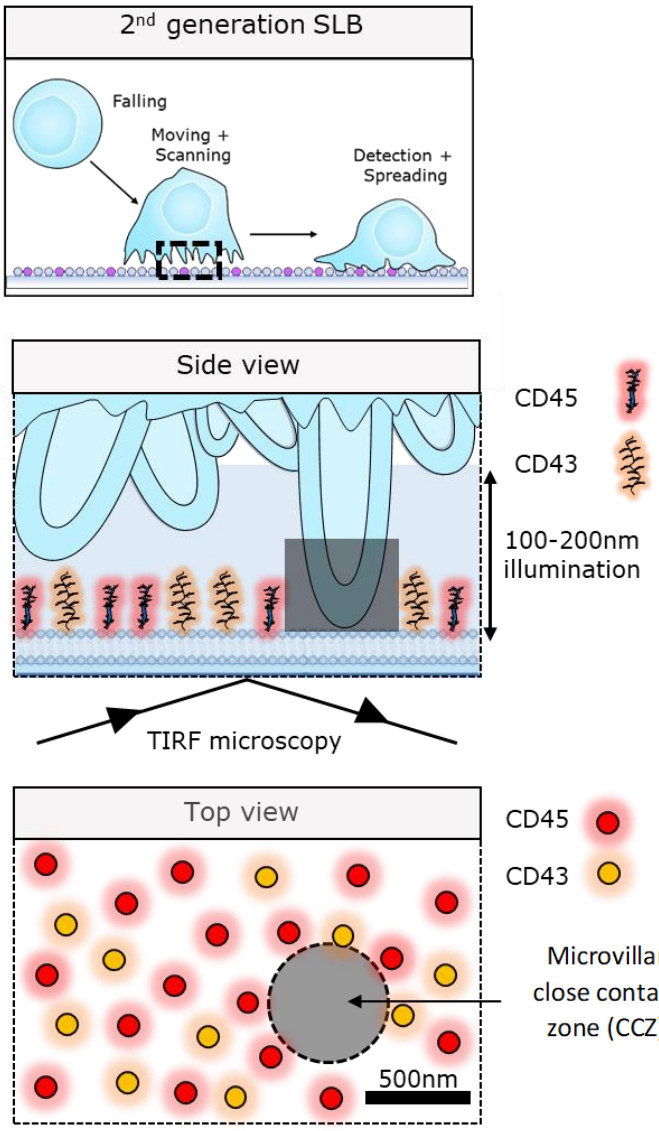

Figure 5.3. **Cartoon of microvillar close contact zone (CCZ) mapping.** Microvillar contacts can be observed by labelling the glycocalyx elements (e.g. CD43 and CD45) on 2nd generation SLBs (also contain CD58, ICAM-1, and pMHC (not shown)). As these proteins are known to be larger than pMHC-TCR and CD58-CD2 interaction, they will be passively excluded by microvilli during the formation of CCZs i.e. T cell-SLB contacts with a 15nm gap. As total internal reflection microscopy (TIRFM) only illuminates 100-200nm above the SLB surface, we can successfully image the contact interface. In TIRFM, microvillar CCZs will appear as small 100-500nm diameter black holes in the otherwise fluorescently homogenous SLB surface.

This was first tested by simultaneously imaging CD43 and CD45 on 2nd generation SLBs, and TCR on J8-LFA-1 cells (**Figure 5.4**). This would allow comparison between CD43 and CD45 exclusion for contact mapping, whilst showing that the TCR is present within close contacts. Lower densities of agonist pMHC (~1-5/μm^2) were used as high densities of pMHC would erroneously stabilise microvilli contacts by mimicking the activity of an adhesion protein. To confirm if we could see 'holes' in CD43 and CD45 signal, similar to holes in QD signal in Cai et al. (2017), early-late contacts (when cells had spread over the surface) were first analysed. J8s were dropped onto 2nd generation SLBs and immediately imaged every 2 seconds by TIRFM. Using the TCR fluorescence signal, cells were analysed from when they first stopped moving across the image field. From this point J8-LFA-1s showed several discrete zones of reduced CD43/CD45 fluorescent signal (i.e. CCZs) that visibly correlated with the TCR signal (**Figure 5.4A&B**). Kymographs showed a direct relation between TCR accumulation and CD43/CD45 exclusion over time indicating stabilisation of contacts (**Figure 5.4C**). Over 1-4 minutes cells would form more discrete zones of CD43/CD45 exclusion and distinct points of TCR fluorescence, which colocalised with these exclusion zones. This was indicative of a cell having activated and spread across the surface. Both the exclusion zones and TCR moved centripetally on the SLB (**Figure 5.4A-C**).

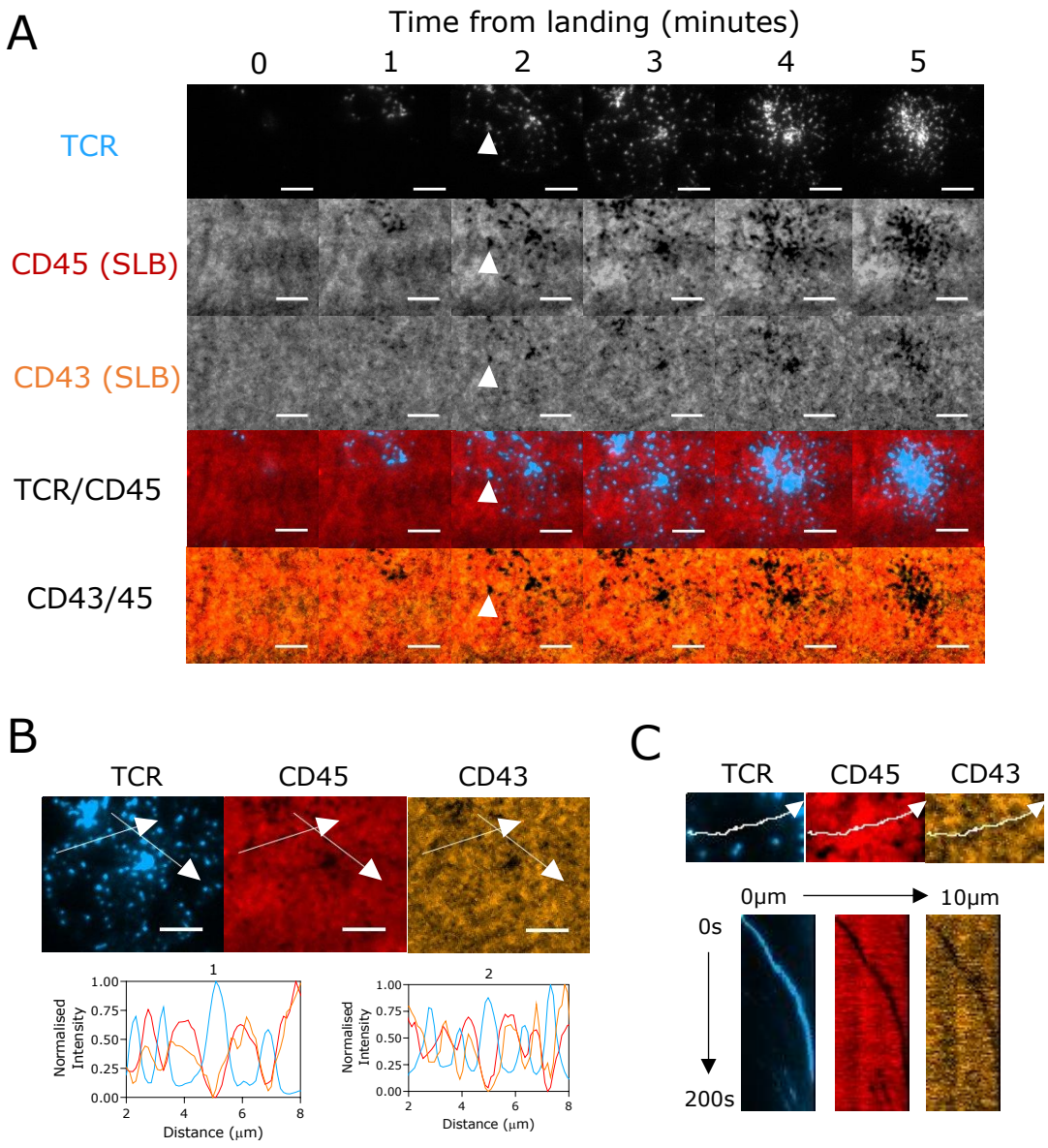

Figure 5.4. **Mapping CCZs with glycocalyx exclusion and TCR accumulation.** J8-LFA-1 cells were labelled with UCHT-1-Fab-Alexa 488 (to label the TCR) and gently deposited on 2nd generation SLBs with low densities of agonist pMHC (9V, 1-5μm^2). To identify CCZs, CD45 was labelled with Alexa-555 and CD43 with Alexa 647. (A) Representative panel of TCR signal (blue, first row), and exclusion of CD45 (red, second row) or CD43 (orange, middle row) over 5-minutes. CCZs are represented by black holes in both the CD45 and CD43 fluorescent signal (example at white arrow). Scale bar is 5μm. (B) Two intensity line profiles across several TCR accumulation spots show exclusion of CD45 and CD43 in areas of TCR accumulation on the SLB. Scale bar is 5μm. (C) A representative kymograph of CD45 and CD43 exclusion correlating with TCR accumulation. The contrast and brightness of the TCR, CD45 and CD43 signals were modified in some cases to make it easier to observe TCR within CD43/45 exclusion zones.

Cell spreading and centripetal migration of TCR signal into a central cluster is a well-documented behaviour after productive antigen detection and therefore cells could be manually categorised into 'activated' and 'non-activated' cells (**Figure 5.5**) [91], [339]. Videos were analysed using the 'contact analysis' code (described in **Section 2.7**). This analysis was done separately for CD45 (red) and CD43 (orange) to allow comparison of these proteins for observing microvillar CCZs (**Figure 5.5**). Focussing on CD45 exclusion (red lines), the number of microvillar CCZs grew substantially on cells that 'activated' compared to those that didn't with an average maximum of 60 CCZs vs. 10, respectively (**Figure 5.5A**). When tracking the average area of a microvillus CCZ from CD45 exclusion over time on activated cells they quickly increased upon first detection and plateaued between 0.15-0.17μm^2 (**Figure 5.5B**), consistent with a predicted microvillus contact area of 0.15μm^2 from **Figure 5.2**. This was similar for non-activated cells, suggesting growth and stabilisation of individual CCZs may be independent of TCR signaling. The total microvillar CCZ area on SLBs peaked at ~12μm^2. As Jurkats have a measured surface area between 364-670 μm^2, these cells only commit 1.8-3.3% of their total surface area to scanning for pMHC under low antigen conditions (**Figure 5.5C;** [340]). For cells that didn't activate, total CCZ area peaked at 4μm^2, which corresponds to 0.6-1.1% of their surface area. The last metric analysed was the extent of CD43/CD45 exclusion. This can provide an idea of contact 'tightness'. Exclusion values were calculated for each frame as $Exclusion = 1 - \frac{I_{inside}}{I_{outside}}$, with I_{inside} being pixel intensities inside the CCZ masks and $I_{outside}$ being the mean intensity of pixels at the edge of the cell membrane. These ratios are averaged across all CCZ pixel values then subtracted from 1. A value of 1 represents maximal exclusion, 0 is no exclusion, and values below

0 represent accumulation. Using this analysis, the average exclusion rapidly increased and plateaued comparably for activating and non-activating cells (both ~0.25-0.35).

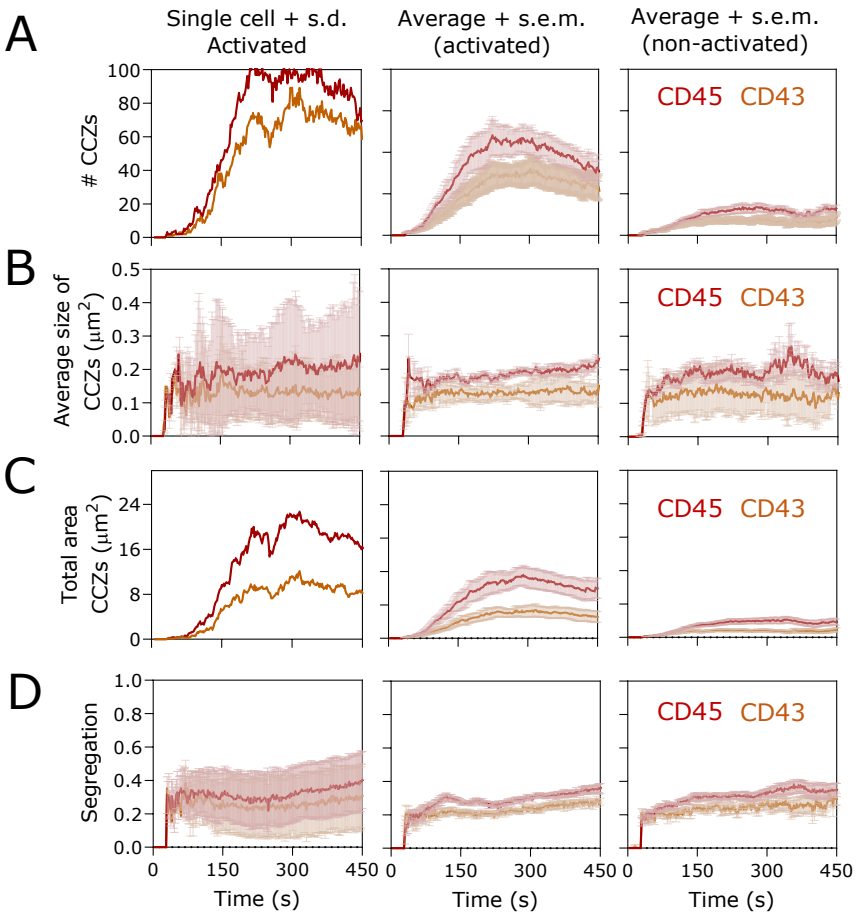

Figure 5.5. **'Contact analysis' of CD43 or CD45 CCZs**. Contact analysis of the cell in Figure 5.4 (left column) and the average of 'activating' (middle column) and non-activating (right column). Activating and non-activating cells were identified manually based on cells appearing to spread and show centripetal motion of TCR accumulation sites into a central cluster. The red line and orange lines are CCZs based on CD45 and CD43 segregation, respectively. All cells were aligned to when the number of CCZs detected first remained above 1 (set at 30s). # of CCZs (A), average size of CCZs (B), total area of CCZs (C) and extent segregation of CD43 or CD45 in their CCZs relative to their signal outside the CCZs in the entire field of view (D). How exclusion is calculated is described in the main text. 1 = maximum exclusion, 0 = no exclusion and < 0 = accumulation. (A-D)The second and third column show the average (± s.e.m.) from N=2 videos (n=7-10 cells for activated/non-activated).

CD45 and CD43 CCZs were also compared in **Figure 5.5**. Differences may reflect the rigidity and/or size of the molecules. Comparison helps identify if they could be labelled together to increase the signal/noise for detecting very early microvilli contacts. CCZs for CD43 (orange) and CD45 (red) were mostly overlapping, although visibly smaller for CD43 (**Figure 5.4**). Focussing on cells that activated, CD45 (red line) and CD43 (orange line) differed in average maximum number of contacts (60 vs. 40; **Figure 5.5A**), size of contacts (0.15-0.17 vs. 0.11-0.12; **Figure 5.5B**) and total area of CCZs (12μm^2 vs. 5μm^2; **Figure 5.5C**). The difference in average maximum exclusion between CD43 and CD45 was modest (0.3 vs. 0.36), with both values remaining stable over time (**Figure 5.5D**).

5.3.3 Three phases of close contact zone (CCZ) formation

After establishing an approach that could robustly detect contact topology, the next step was to identify when the first CCZs could be seen. At low densities of agonist pMHC (9V, ~1-5μm^2) cells took longer to adhere and were observed probing their surface prior to settling on the surface (presented in **Chapter 4**). This provides an opportunity to examine whether CCZ formation is seen before or after the cells had stopped moving and settled on the bilayer. In order to visualise initial contacts, the TCR, cell membrane, and the SLB glycocalyx (CD43 and CD45) were labelled. Three phases of cell activity occurred: (phase 1) scanning + moving (no CCZs), (phase 2) scanning + settled (CCZs first appear), and (phase 3) scanning + spreading (more and stable CCZs). Initially, small points of CellMask, presumably corresponding to microvillar tips, could be seen scanning across the surface 8-32s after cell moved into frame (phase 1, **Figure 5.6A**). No areas of glycocalyx exclusion, or CCZs, could be seen, although TCR and membrane tips

clearly co-localised. From 40-64s (phase 2), a slightly larger area of cell membrane and TCR signal settled and started to expand, presumably as a contact become more stabilised (**Figure 5.6B&C**). After this period (75-300s, phase 3) the cell began to spread on the surface, forming many visible CCZs that moved centripetally (**Figure 5.6D**).

To identify whether any transient but apparently 'invisible' close contacts formed during the 8-32s period of scanning, the glycocalyx signal was analysed using the contact analysis (**Figure 5.7**). During this period, no CCZs could be detected (**Figure 5.7A, first column**). As observed by eye, CCZs could be identified from 40-64s (**Figure 5.7A, second column**). During this period, the average segregation of CD43/45 increased from 0.03 to 0.07, indicating segregation, and the total number of contacts during this period went from 1-10, confirming this is when contacts first appeared. For the remaining time the extent of segregation, number of contacts, and average size of contacts increased (**Figure 5.7A, third column**). In order to allow comparisons between cells, the time taken for cells to adhere (i.e. drop below a threshold speed) was subtracted from the time CCZ first appeared. The time to adhere effectively represents the start of phase 2 in **Figure 5.6A**. The centroid of all the cell membrane signal was used to measure speed. Positive values indicate a cell had settled (i.e. speed dropped and stayed below the threshold value) prior to detection of CCZ. In a few cases CCZs were formed while cells were scanning on the move (i.e. during phase 1, shown as negative values in **Figure 5.7B**) but most cells would typically settle (phase 2) before CCZ were observed (**Figure 5.7B**). Overall, these results show three distinct phases of CCZ formation, with CCZs mostly detected when cells have slowed their movement and started to settle on the surface (phase 2).

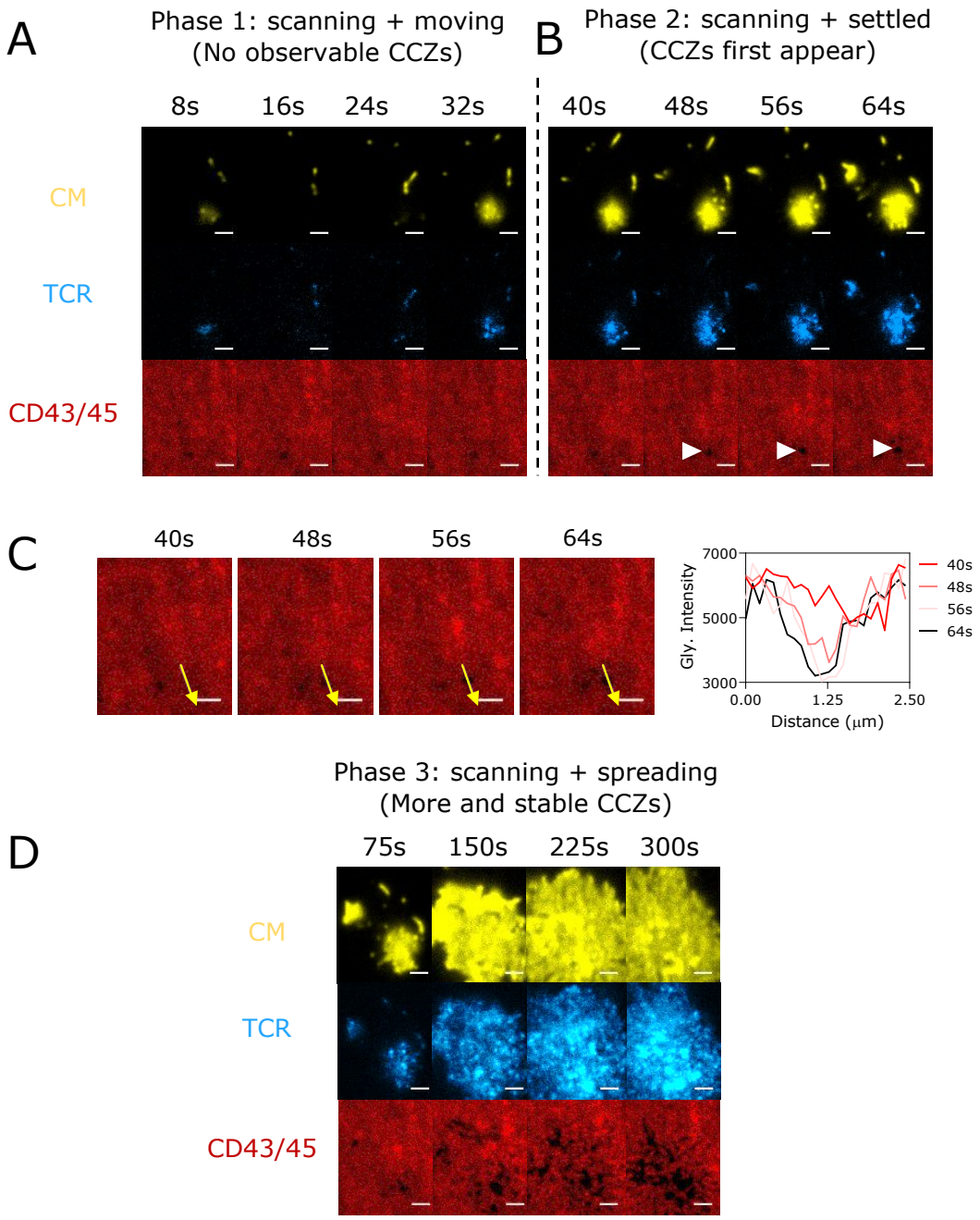

Figure 5.6. **Different stages of membrane contact scanning and CCZ formation**. J8-LFA-1 cells were labelled with UCHT-1-Fab-Alexa 488 and CellMask™ Red, to visualise the TCR (shown in blue) and cell membrane (CM, shown in yellow), respectively. They were then gently deposited on 2nd generation SLBs presenting 1-5μm² of agonist pMHC (9V). The glycocalyx (CD43 and CD45) on the SLBs was labelled with Alexa 555 (shown in red). TIRFM was used to image cells immediately upon addition to the surface. Images were taken every 2s. (A) Phase 1: scanning + moving (no close contacts). (B) Phase 2: scanning + settled (close contacts first appear). (C) Intensity line profile showing a visible CCZ. Line profiles were taken at the same location along, and in the direction, of the yellow arrow across several time points. Glycocalyx fluorescence intensity (Gly. Intensity) along the yellow arrows is shown in the plot to the right. (D) Phase 3: scanning + settled (contacts become stabilised). Scale bars are 2.5μm.

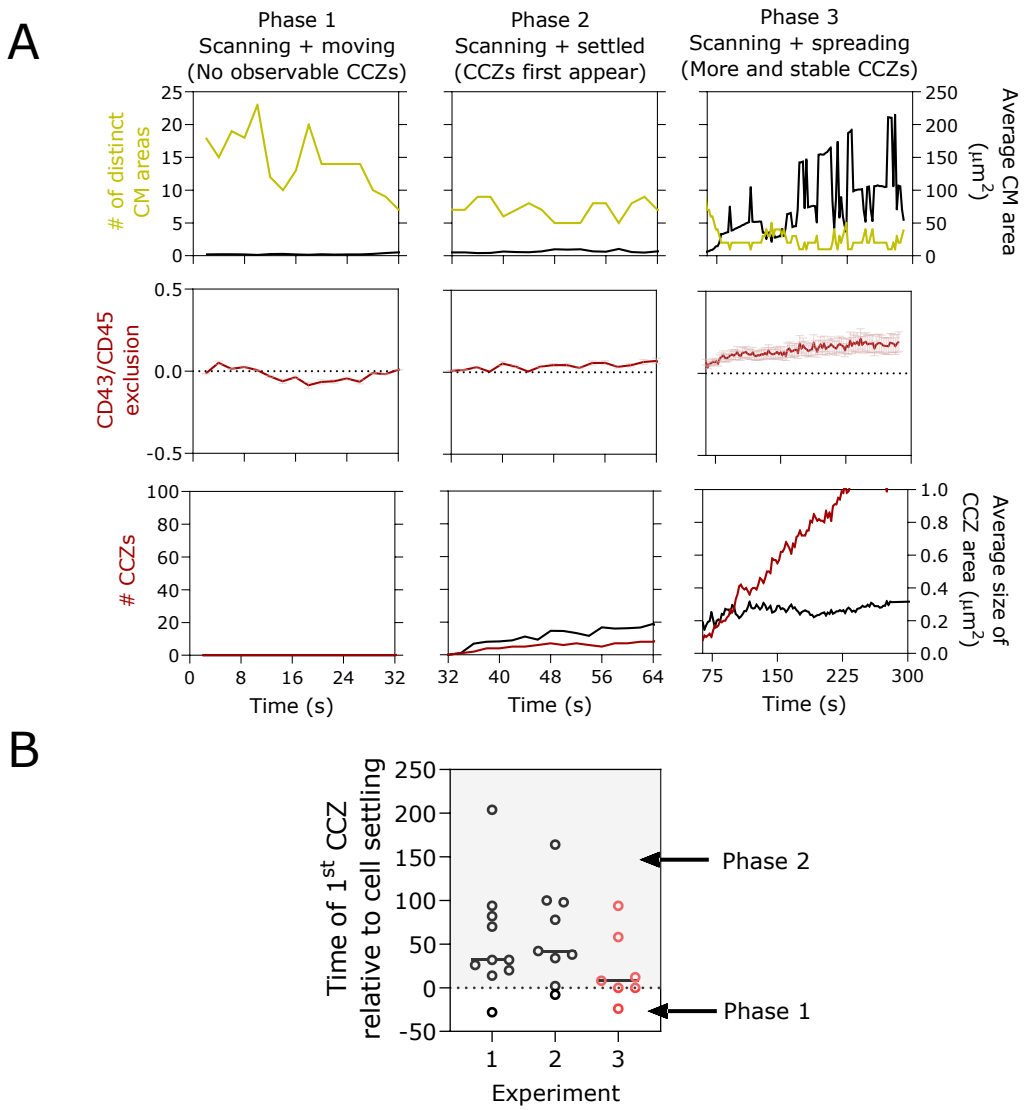

Figure 5.7. **Quantifying stages of membrane contact scanning and CCZ formation.** (A) Analysis of image shown in **Figure 5.6**. First column: phase 1 of CCZ formation. Quantification of cell membrane (CM) using CellMask fluorescence shows many distinct (yellow line) and small (black line) CM areas as they cell is moving over the surface (first row). No glycocalyx exclusion (red line middle row) or microvillar CCZs (red and black line bottom row) could be detected. Second column: phase 2. The distinct number of CM areas decreased, with each CM zone leftover increasing in area (top row). Glycocalyx exclusion (red line middle row) and CCZ formation (red and black line bottom row) can be detected from this phase. Third column: phase 3 whereby the cells now spread increasing CM area over the SLB surface, leading to many more CCZs being formed, with strong exclusion of the glycocalyx. (B) The time of first CCZ appearance was subtracted from the time a cells speed dropped and remained below 0.2μm/s (i.e. adhered, as seen in **Figure 4.2**). Positive values indicate a cell 'adhered' prior to CCZ detection. Experiment 3 (red) differed from 1 and 2 in that the UCHT-1 Fab-Alexa 488 signal was replaced with the GECI but still on the same SLB conditions.

5.3.4 T-cell signaling is initiated at microvillar CCZs

Detecting and examining the molecular events at initial microvillar contacts is important because it has recently been suggested that this is where the TCR discriminates between antigens [124]. Although likely, TCR triggering and T-cell signaling has not been shown with certainty to initiate at microvillar contacts [122], [125].This can be achieved by observing microvillar-induced CCZs in combination with calcium release in the J8-GECI-LFA-1 cells. In order to visualise signaling at initial close contacts, the cell membrane and the SLB glycocalyx (CD43 and CD45) were labelled. In the previous section, the first visible contacts could only be detected once the cell has settled (**Figure 5.6&5.7)**. However, we cannot rule out the possibility that cells may have already responded to antigen within close contacts not visible in our experiments. For this reason, this experiment was performed at high (50-100/μm^2), low (1-5/μm^2) and null (0/μm^2) densities of agonist pMHC (9V). High densities ensure that TCR-pMHC binding is not a limiting step, such that any close contacts, particularly those that may be invisible, will rapidly allow TCR-pMHC interaction and signaling. If signaling occurs prior to visible contact formation, then clearly 'invisible' contacts lead to TCR-pMHC engagement and exist long enough for productive signaling. However, if signaling occurs only after CCZs are visible, then we can detect the relevant and productive close contacts. Null pMHC addresses whether close contacts are visible, independent of agonist-driven TCR triggering. By comparing high, low and null conditions we can also examine how cells alter their behaviour in response to surface potency.

J8-GECI-LFA-1 cells were labelled with CellMask™ Red and dropped onto 2nd generation SLBs containing high (50-100/μm²; HD), low (1-5/μm²; LD) or no (0/μm²; Null) densities of agonist pMHC. To visualise CCZs the glycocalyx (CD43 and CD45) was labelled with Alexa-555. At HD, a cell formed at least one CCZ prior to the calcium release (**Figure 5.8A**). Calcium responses occurred at 42s (**Figure 5.8B, green dashed** line). Exclusion could be seen 12s before calcium release as was evident when manually producing line intensity profiles across the observable exclusion zone over time (**Figure 5.8C**). When submitting the video to the contact analysis (**Figure 5.5**) a single contact was identified by 26s (**Figure 5.8D '0-60s' graph**). The average exclusion value of the glycocalyx only stabilised above 0 at 30s (**Figure 5.8E red line '0-60s' graph)**. These data suggest that the CCZs form prior to calcium release. The signaling was productive, as after calcium release cells spread, forming a maximum of ~90 CCZs and larger contacts that became increasingly stable as seen by the increasing average segregation of the glycocalyx (**Figure 5.8D&E, '0-300s' graph**).

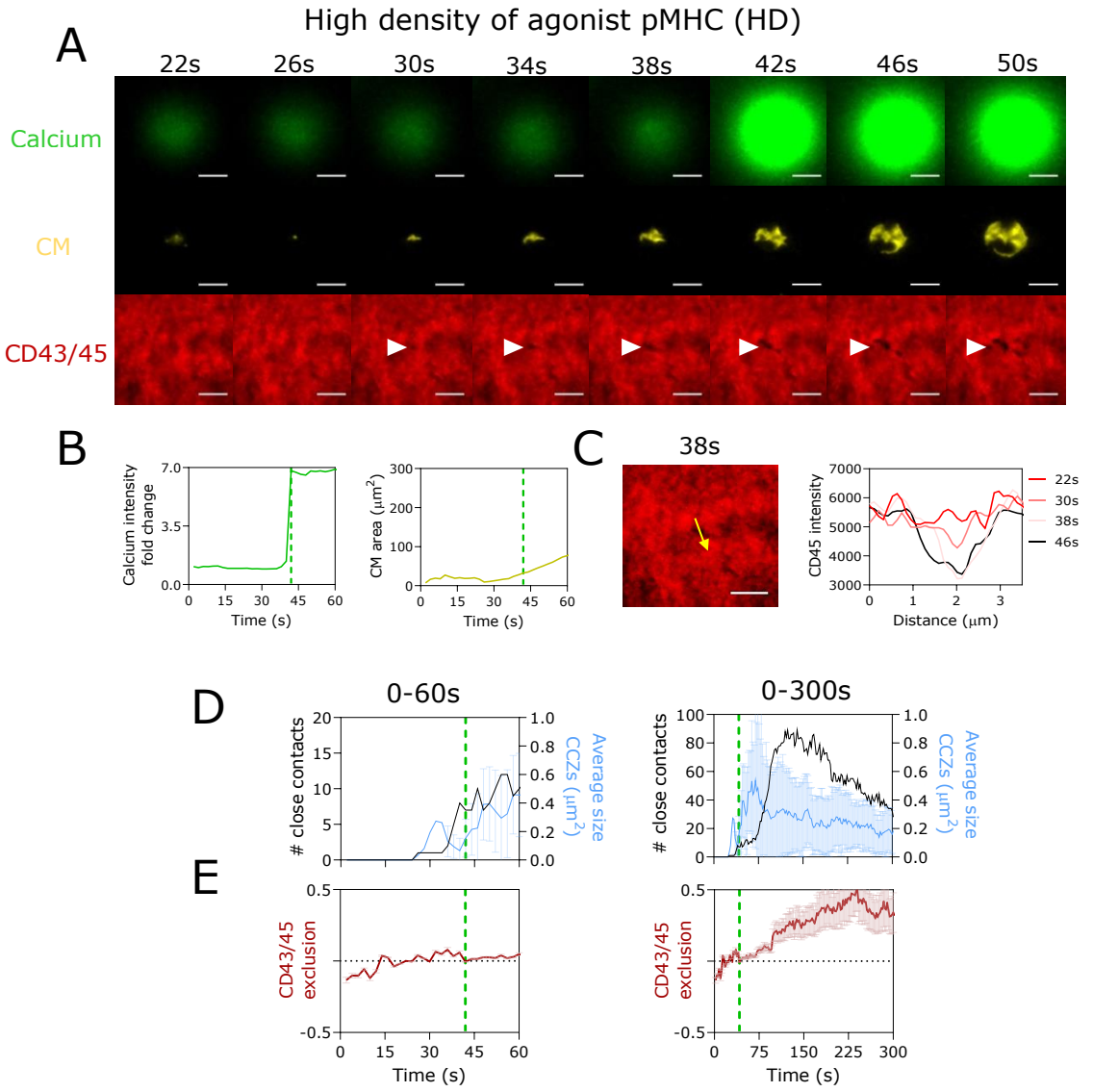

Figure 5.8. **Signaling is initiated at microvillar CCZs (high density agonist pMHC).** J8-GECI-LFA-1 cells (GECI shown in green) had their cell membrane (CM, shown in yellow) labelled with CellMask™ Red and were gently deposited on 2nd generation SLBs presenting 50-100µm² of agonist pMHC (9V). CD43 and CD45 were labelled with Alexa-555 to view CCZs (shown in red). (A) Panel showing calcium release (42s), increase in cell membrane (CM) area, and the first observable exclusion of CD43/45 at 30s. Scale bar is 5µm. (B) Left plot: normalised calcium signal. Calcium release occurs at 42s (green dashed line). Right plot: CM area over time. (C) Intensity line profile manually drawn across the visible CCZ at different time points. Exclusion can be seen at 30s. (D) Contact analysis output showing the first 60s (left) or 300s (right) of the cell's CCZ formation. The first CCZ appears at 26s. The number and average size of contacts rapidly increased after the predicted TCR triggering event (black line). The large increase in the number of CCZs over time is indicative of activation. (E) Extent of CD43/45 exclusion on the SLB for first 60s (left) or 300s (right).

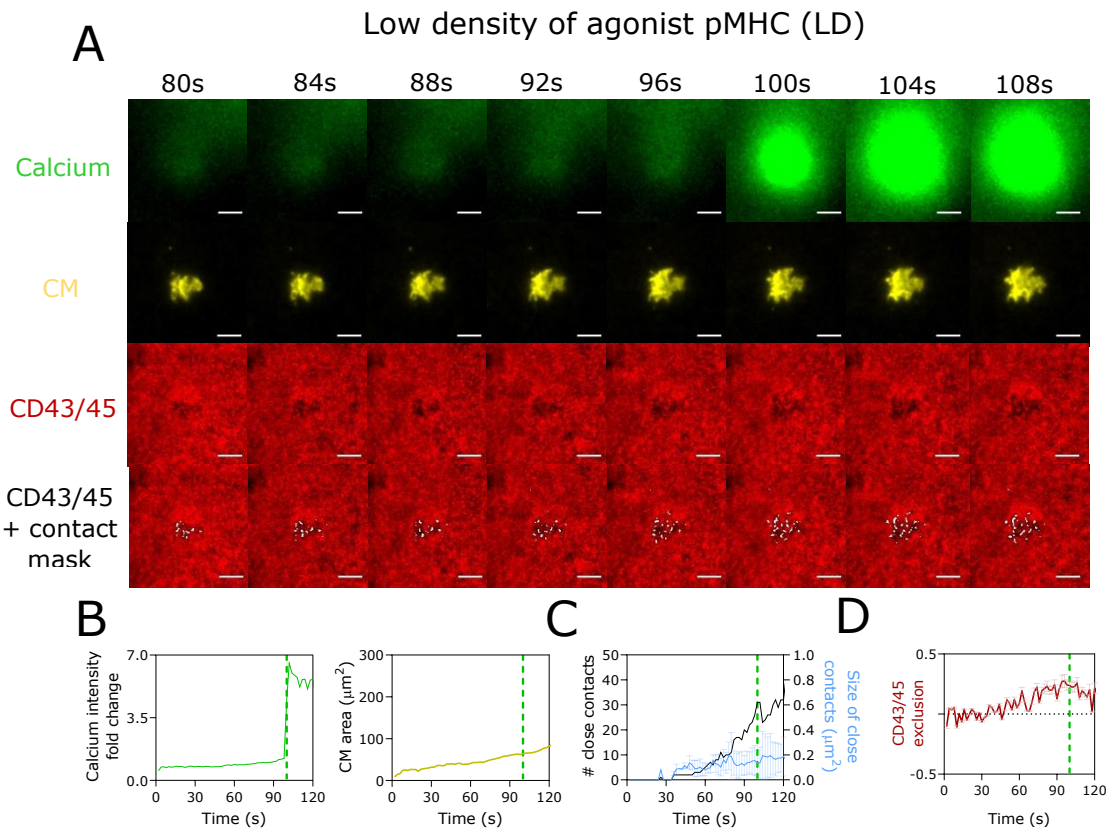

Figure 5.9. **Signaling is initiated at microvillar CCZs (low density agonist pMHC).** J8-GECI-LFA-1 cells (GECI shown in green) had their cell membrane (CM, shown in yellow) labelled with CellMask™ Red and were gently deposited on 2nd generation SLBs presenting 1-5µm² of agonist pMHC (9V). CD43 and CD45 were labelled with Alexa-555 to view CCZs (shown in red). (A) Panel showing calcium release (100s), increase in cell membrane (CM) area, and observable exclusion of CD43/45. The last row shows contact masks from the contact analysis (white segments). Scale bar is 5µm. (B) Left plot: normalised calcium signal. Calcium release occurs at 100s (green dashed line). Right plot: CM area over time. (C) Contact analysis output showing the first 120s of the cell's CCZ formation. The first CCZ appears at 30s. Calcium release occurs much later after many more contacts have formed (compared to high density agonist). (D) Extent of CD43/45 exclusion on the SLB. Exclusion occurs from 36s.

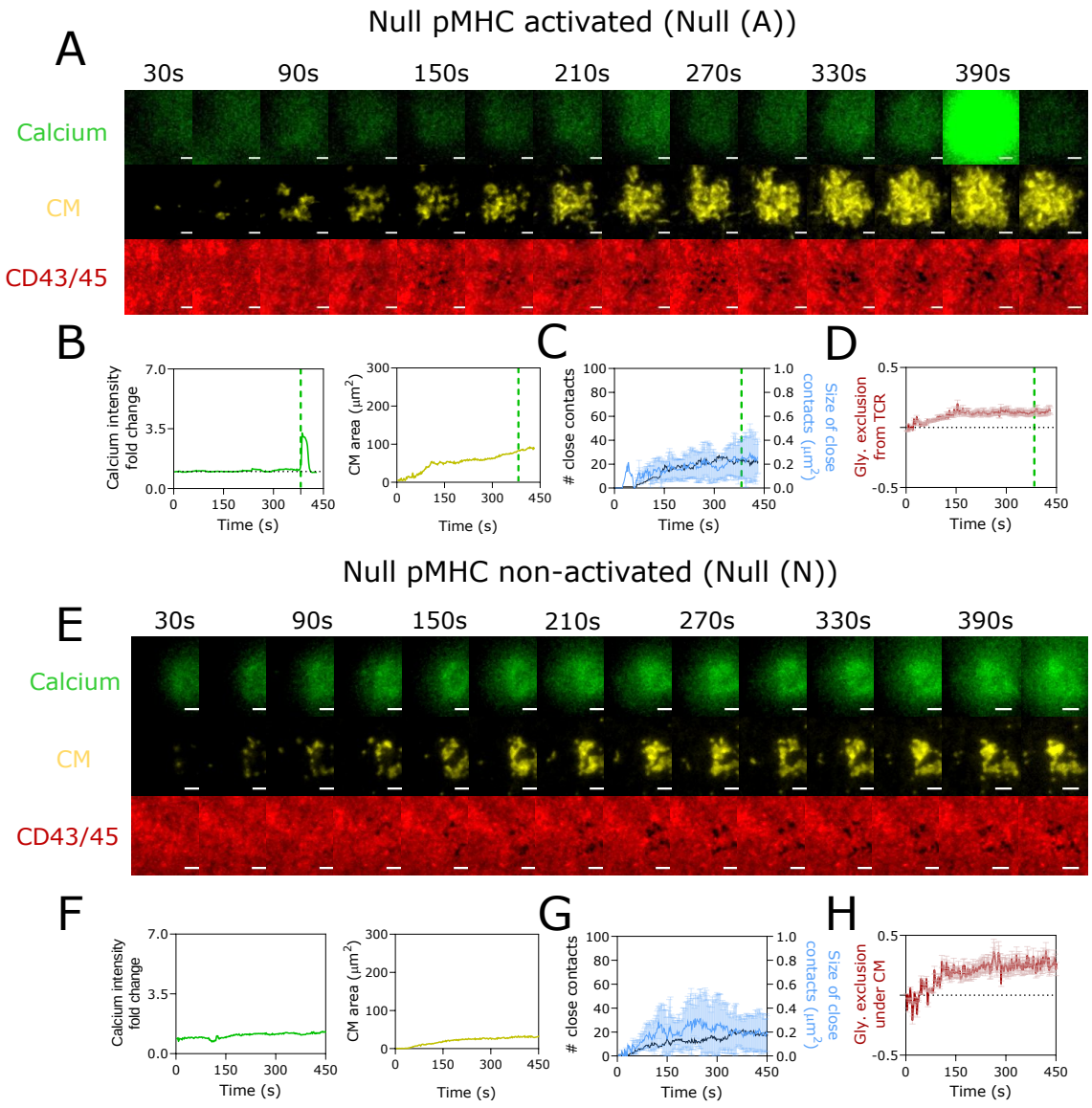

Figure 5.10. **Signaling is initiated at microvillar CCZs (null pMHC).** J8-GECI-LFA-1 cells (GECI shown in green) had their cell membrane (CM, shown in yellow) labelled with CellMask™ Red and were gently deposited on 2nd generation SLBs presenting null pMHC. CD43 and CD45 were labelled with Alexa-555 to view CCZs (shown in red). An example of a cell showing calcium release (A-D) and no calcium release (E-H) are shown. (A & E) Panel showing calcium signal, cell membrane (CM) area, and observable exclusion of CD43/45. Scale bar is 2.5μm. (B & F) Left plot: normalised calcium signal. Calcium release occurs at 384s. Right plot: CM area over time. (C & G) Contact analysis output showing CCZ formation over 450s. (D & H) Extent of CD43/45 exclusion on the SLB.

On LD and Null, signaling from microvilli CCZs was easier to observe as cells would typically form multiple contacts prior to signaling. On LD, calcium release occurred much later than under HD conditions, after the first CCZ and segregation of the glycocalyx could be seen (**Figure 5.9A-C**). On Null, activated (Null (A)) and non-activated (Null (N)) cells were analysed (**Figure 5.10**). Calcium response on Null is adhesion and TCR-dependent, and likely a result of CD58/CD2 interaction (addressed in **Chapter 7**). On Null, only 20-30% of cells respond (shown in **Chapter 4**) and for cells that showed calcium release (Null (A)), a calcium response took longer from first CCZ appearance, and qualitatively appeared somewhat weaker, consistent with the results in **Chapter 4** (**Figure 5.10A-D**). Null (N) cells would still form CCZs of comparable size despite not signaling (**Figure 5.10E-H**).

To quantify effects of the four conditions (HD, LD, Null (A) and Null (N)), the contact analysis was applied across multiple cells from 3-6 independent SLBs for each condition (**Figures 5.11-16**)[1]. First, the number of microvillar CCZs formed over time was analysed (**Figure 5.11A**). Cells were only included if they were completely in the imaging frame over the course of their spreading, and long enough to reach an observable plateau in their numbers of CCZs over time. This yielded 11-17 cells per condition. Timings were aligned so that the first and stable CCZ for each always appeared at 30s. Visibly, HD and LD had comparable rates of CCZ formation over time, with substantially fewer formed by Null (A) and even less by Null (N; **Figure 5.11A**). This was mirrored by the growth

[1] It should be noted that cells from two (out of four) videos for the LD condition were pooled from a condition where CD58 was labelled instead of the cell membrane.

of cell membrane area (**Figure 5.11B**). Quantification of the rate of CCZ formation from either first CCZ or after calcium release showed that cells that responded on LD and HD had significantly higher rates of CCZ formation than Null (A; both p = <0.001, **Figure 5.11C&D**). No difference was found between LD and HD (p = 0.870 for 0.916) for **Figure 5.11 C&D, respectively**). This suggests that upon detection of the first or a few antigens T cells strongly commit to further antigen scanning.

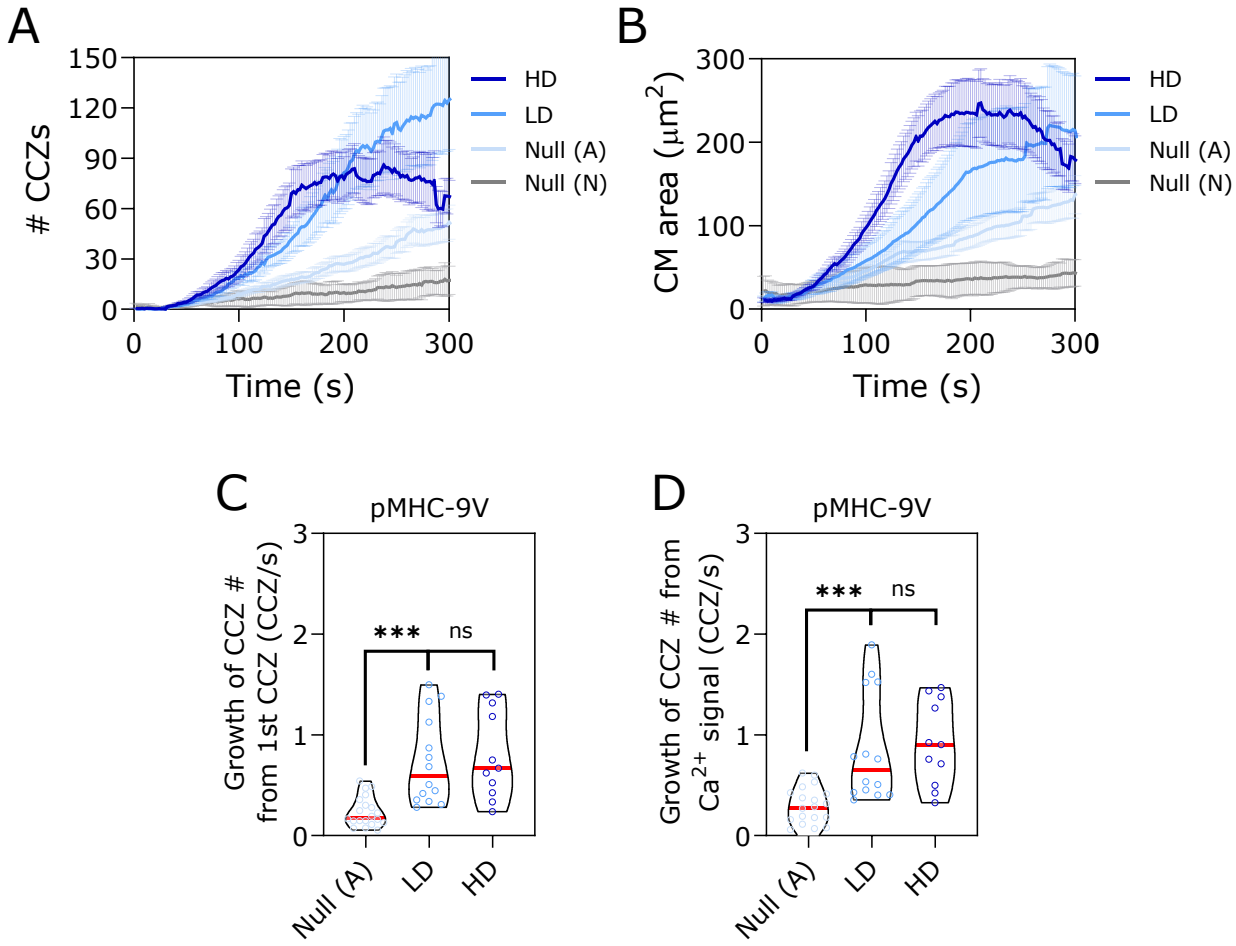

Figure 5.11. **Kinetics of CCZ formation and spreading with altered antigen density.** Average number (+ s.e.m.) of CCZs (A) or average total cell membrane (CM) area (B) formed over time. Cells were aligned so that the first stable CCZ was set at 30s. (C) Rate of CCZ formation from the 1st CCZ to the maximum number of CCZs. (D) Rate of CCZ formation from calcium release to the maximum number of CCZs. (C&D) Red line is the median. (A-D) N=3-6 separate SLBs (n=3-6 cells). Conditions were tested using one-way ANOVA with Tukey Multiple Comparison test. ***= p < 0.001, ns = p > 0.05. HD = high density (50-100μm²) agonist pMHC (9V), LD = low density (1-5μm²) agonist pMHC (9V), Null (A) = null density activated, and Null (N) = null density non-activated.

When analysing the calcium responses of these cells, Null (A) was found weakest (fold change of ~3) compared to LD (~4) and HD (~4.5; **Figure 5.12A**). The median integrated calcium was ~90, ~220 and ~300 for Null (A), LD and HD, respectively (**Figure 5.12B**). Only the Null (A) and HD calcium responses were significantly different (p = 0.017).

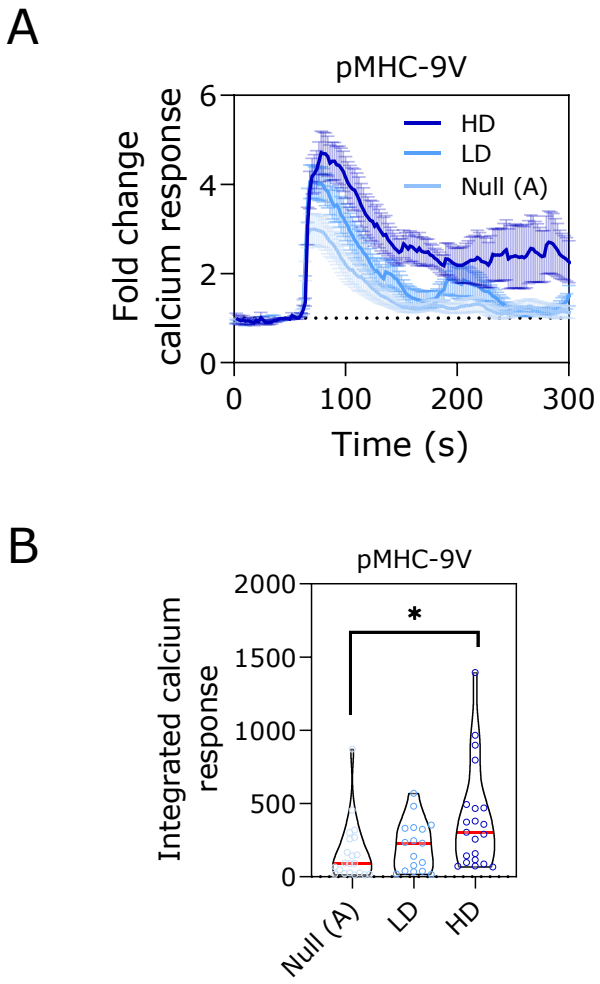

Figure 5.12. **Strength of calcium response with altered antigen density.** (A) Average calcium traces (+ s.e.m) over time. Cells were aligned so that Ca^{2+} signal occurred at 60s. N=3-6 separate SLBs (n=3-6 cells). (B) Integrated calcium values calculated from summing the area under each calcium curve. Red line is the median. Conditions were tested using one-way ANOVA with Tukey Multiple Comparison test. * = $p < 0.05$, ns = $p > 0.05$

Next, the relationship between CCZ formation and calcium release was analysed. Additional cells could be included for the following analyses as cells only needed to be present on the surface until they signalled rather than for long periods to analyse the CCZ formed over time. The median time to calcium release upon appearance of the first CCZ was 80s, 40s and 12s for Null (A), LD and HD, respectively (**Figure 5.13A**). Null (A) and LD were found significantly different ($p = 0.045$), whereas LD and HD were not ($p = 0.130$), despite the apparent differences. As cells took longer to signal on Null (A) and LD, they had formed more CCZs on average by the time calcium release occurred (both ~10 CCZs, Null (A) vs. LD, $p = 0.961$) than for HD (~10 vs.~ 3 CCZs, LD vs. HD, $p = 0.031$, **Figure 5.13B**). In accordance, the total CCZ area at calcium release was four-fold larger for Null (A) and LD (both 1.2-1.3μm^2, $p = 0.876$) than for HD (~0.3μm^2; LD vs. HD, $p = 0.039$, **Figure 5.13C**). No significant difference was found for the average area of CCZs at triggering between all samples, although HD did show a small decrease (~0.08 μm^2) relative to LD (~0.14μm^2; $p = 0.11$; **Figure 5.13D**). Cells on HD likely respond before CCZs grow to their maximal size, unlike on LD and Null (A).

Having previously measured the density of pMHC on the SLBs (**Figure 4.2**), this provided an opportunity to extrapolate the minimum number of pMHC available to a cell at the time of calcium release, and by inference the number of pMHC per microvillar CCZ (**Figure 5.14**). The minimum number of pMHC (also read 'instantaneous' number of pMHC detected) was extrapolated as estimating a more realistic total pMHC would require modelling the rate of pMHC 'trapping' by the TCR within microvillar contacts

over time. This metric requires knowledge of 2D K_{on}/K_{off} rates of TCR/pMHC at dynamic microvilli in the presence of auxiliary proteins like CD58, which is currently unknown.

By using the total area of CCZs at calcium release, cells on LD (assuming 2.5 molecules/μm^2 on average) were found to respond to a minimum of 0.1-15 pMHC across all CCZs, with a median total of 3 pMHC at point of calcium signaling (**Figure 5.14A**). In several cases the minimum number of pMHC was below 1, which may be because the cell is also capable of responding in the presence of null, a result of probabilistic encounters with antigen, or possibly an underestimated value as pMHC may have accumulated during the time CCZs were formed. As triggering on null pMHC showed overall slower rates of CCZ formation over time (**Figure 5.11A**), as well as weaker, albeit non-significant, calcium signals than cells with LD (**Figure 5.12B**), rate of CCZ formation was used in attempt to separate cells that had responded to agonist antigen (**Figure 5.14B**). This was done by choosing cells on the LD that had CCZ growth rates above the Null (A) conditions 90^{th} percentile for CCZ growth rate (Null 90^{th} percentile CCZ/s = 0.5932, **Figure 5.14B green dashed line**). 50% of cells that responded on LD were above the null conditions 90^{th} percentile. The median minimum number of antigens presented to these cells at calcium release was 3 (**Figure 5.14B**). Using total number of CCZs formed, and assuming each CCZ is of the same size, the minimum number of agonist pMHC per CCZ could be calculated for the stratified cells (**Figure 5.14C**). This led to a range between 0.2-0.4 agonist pMHC per microvillar CCZ at the point of Ca^{2+} signaling for each cell. In other words, a minimum of 20-40% of microvillar CCZs were likely in contact with an agonist pMHC at point of calcium release at this density. From the time

of first CCZ, all cells responded within 3-minutes (**Figure 5.13A**). Overall, these results show that T-cell signaling is initiated at microvilli contacts. Importantly, T cells are highly efficient and sensitive, using very small areas of membrane, and number of microvillar CCZs, to likely detect very low densities of antigen in small time periods.

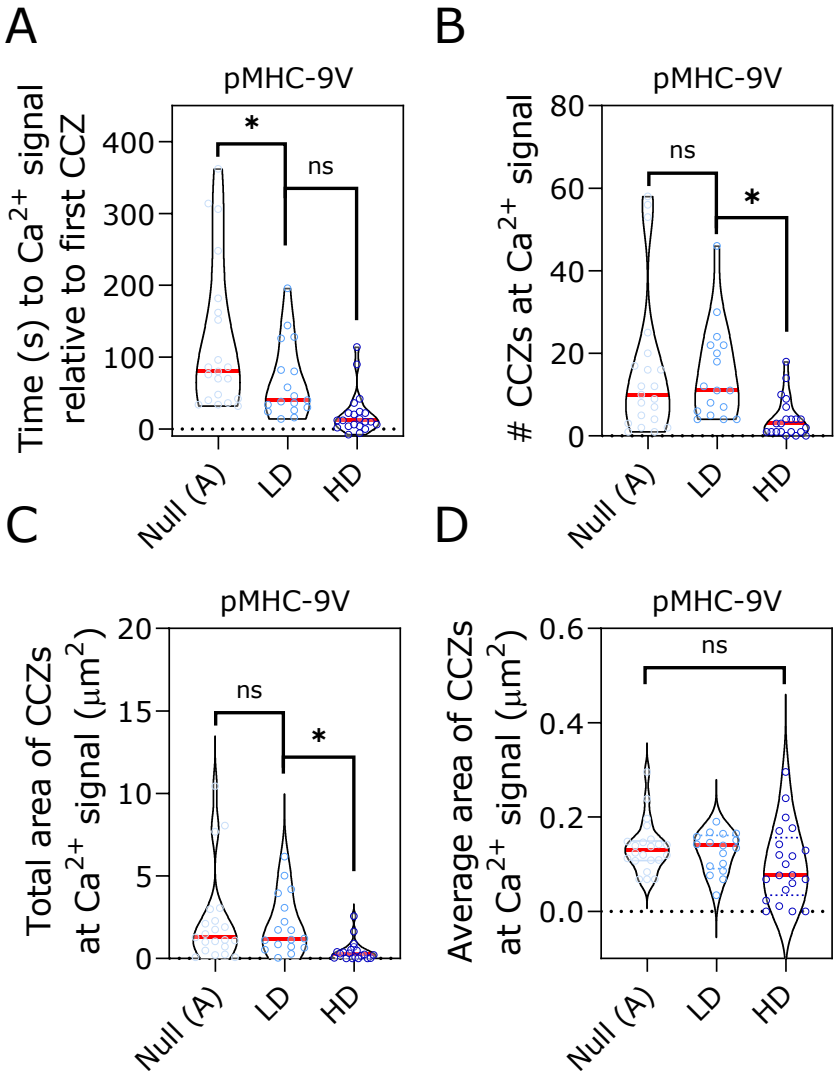

Figure 5.13. **The relation between CCZ formation and time to trigger.** (A) Time to Ca^{2+} signal relative to when the first CCZ appeared. (B) Number of CCZs at point of Ca^{2+} signal. (C) Total area of CCZs at point of Ca^{2+} signal (D) Average area of the CCZs at Ca^{2+} signal. (A-D) N=3-6 separate SLBs (n=3-6 cells). Red line is the median. Conditions were tested using one-way ANOVA with Tukey Multiple Comparison test. * = $p < 0.05$, ns = $p > 0.05$.

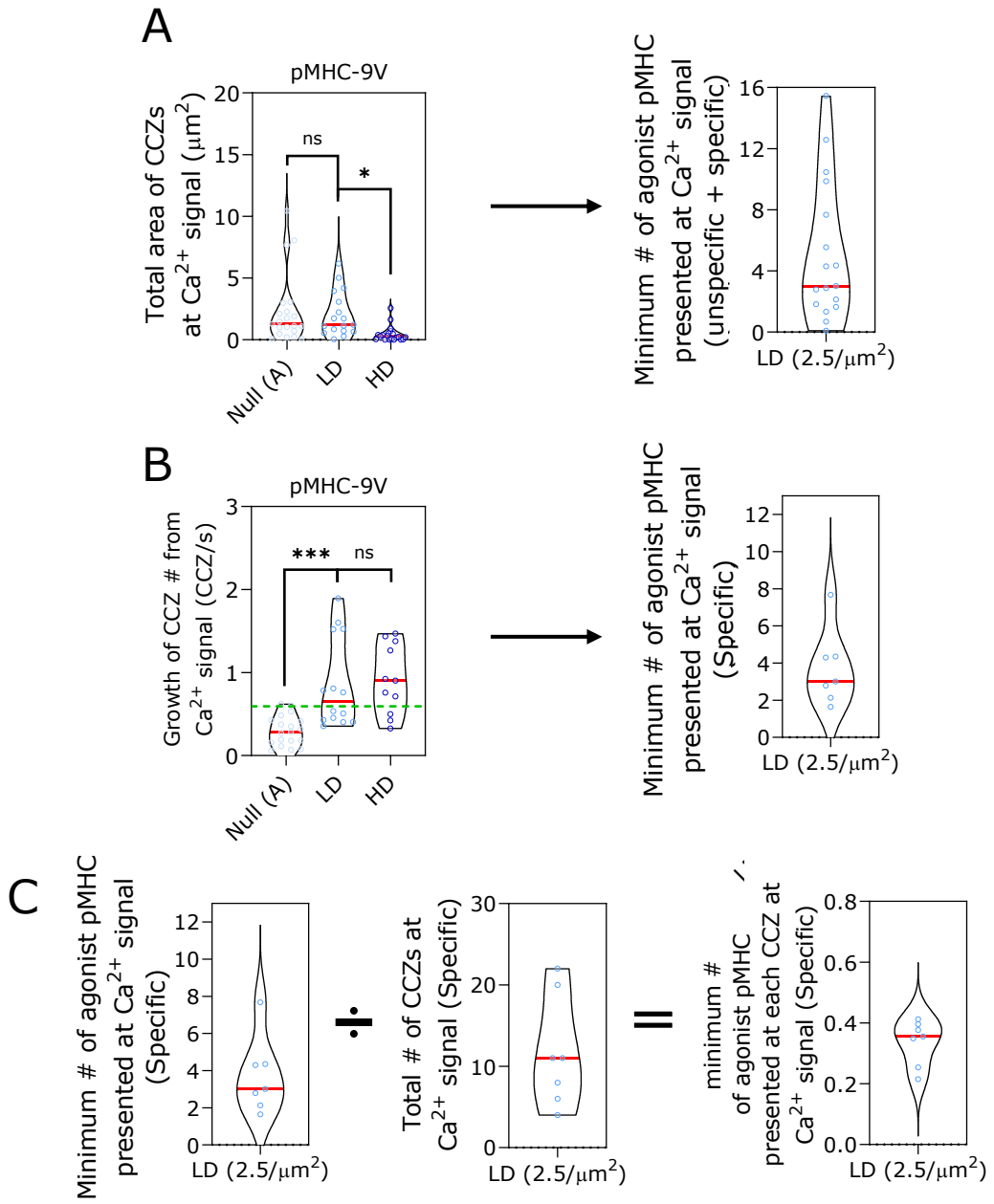

Figure 5.14. **T cells respond efficiently to low amounts of agonist pMHC.** (A) Left: the total area of CCZs quantified from multiplying the number of contacts by their size, taken from **Figure 5.14C**. Right: assuming the LD condition presented an average of 2.5 agonist pMHC (9V) per μm² the total number of agonist pMHC (9V) presented at triggering was quantified. However, because cells can trigger on both null and pMHC this incorporates both unspecific and antigen-dependent triggering. (B) Left: stratification of specific triggering based on rate of CCZ formation after triggering taken from **Figure 5.12C**. The 90th percentile of CCZ formation rate for Null (A) was used as threshold to identify antigen specific triggering (green dashed line). Right: stratification left 7 cells above the threshold ranging from 1.5-8 pMHC at point of triggering. Red line represent the median. (C) Calculating the number of agonist pMHC per CCZ for each cell using the total number of agonist pMHC presented for each cell divided by the total number of CCZs for that cell (assuming each CCZ is of the same size).

5.3.5 Dynamic microvilli increase the kinetics of antigen detection

Although T-cell signaling can be initiated from microvillar contacts, to what extent are microvilli necessary, and how do they impact the kinetics of antigen detection? In order to address this, microvilli and their behaviour were altered using actin-modifying drugs, and 100-1000s of modified cells were tested for calcium release on SLBs with and without a glycocalyx. From **Chapter 4** it is clear the glycocalyx reduces adhesion, preventing close contact formation. If microvilli could be removed and there was no difference between SLBs with and without a glycocalyx, this would show that microvilli are not required for antigen scanning. However, if this did affect antigen detection, clearly microvilli are necessary, presumably, in the first instance to overcome the glycocalyx barrier surrounding cells.

In order to alter microvilli, cells were either treated with latrunculin B (LatB), cytochalasin D (CytoD) or jasplakinolide (jasplak). LatB is a membrane permeable actin polymerisation inhibitor that forms a stoichiometric complex with monomeric G-actin. Their association prevents the formation of F-actin filaments, a major component of microvilli composition. CytoD also prevents the formation of actin filaments but operates through a different mechanism. CytoD binds filaments at the 'barbed-end' (fast growing end) blocking further filament assembly. This leads to depolymerisation from a net loss of actin monomers from the 'pointed-end' (slow growing end; [341]). Both LatB and CytoD treatment have been used to induce microvilli loss in T cells [122], [268], [342]. Jasplak has been shown to enhance nucleation and stabilisation of filaments. Although

the mechanism has not been characterised, jasplak likely operates in a similar manner to phalloidin with which it competitively inhibits. Phalloidin stabilises filaments by preventing monomer dissociation from both the barbed and pointed ends [343]. Jasplak was used instead of phalloidin as it has the advantage of being cell permeable. By stabilising filaments in cells using jasplak, microvillar structure may be preserved but they lose their dynamic nature. This would test whether the presence of microvilli alone is enough to bypass the glycocalyx, or whether they require dynamic cytoskeletal remodelling to create forces to push past the glycocalyx.

Cells treated with the actin-modifying drugs were first imaged to ensure they induced their intended effects; a loss of microvilli with LatB and CytoD and maintained presence of microvilli with jasplak (**Figure 5.15**). Drugs, or DMSO control, were diluted in RPMI and cells were treated for one hour to ensure the drugs had time to act. Cells were then washed, fixed for 20-minutes, and placed on PLL coated surfaces. Microvilli could be seen in the midplane of cells treated with DMSO alone. LatB and CytoD treatment resulted in a loss of microvilli, whereas Jasplak treated cells maintained their microvilli (**Figure 5.15**). Next, cells that were treated for 1 hour were dropped on to SLBs with or without a glycocalyx (**Figure 5.16A**). SLBs without a glycocalyx were used to ensure T-cell proximal signaling was not disrupted by drug treatment. High densities of agonist pMHC (50-100/μm^2) were used so that finding antigen was not a limiting factor. Combined, this approach ensures that any differences between no glycocalyx or glycocalyx-presenting SLBs was a result of a disrupted cytoskeleton and morphology. Cells showed maximal calcium response on no glycocalyx SLBs following each drug

treatment (**Figure 5.16B**). This result indicates that the actin cytoskeleton is not required for TCR triggering or the events that lead to calcium release in T cells. DMSO cells on the glycocalyx-presenting SLBs showed a small but significant decrease in proportion of responding cells compared to no glycocalyx SLBs, consistent with the reduced propensity for adhesion resulting from the glycocalyx barrier (**Figure 4.2**). LatB and CytoD cells showed a significant decrease on glycocalyx SLBs when compared to the DMSO control (**Figure 5.16B**). Importantly, jasplak cells also showed a similar drop in responding cells, suggesting the mere presence of microvilli is inefficient for bypassing the glycocalyx.

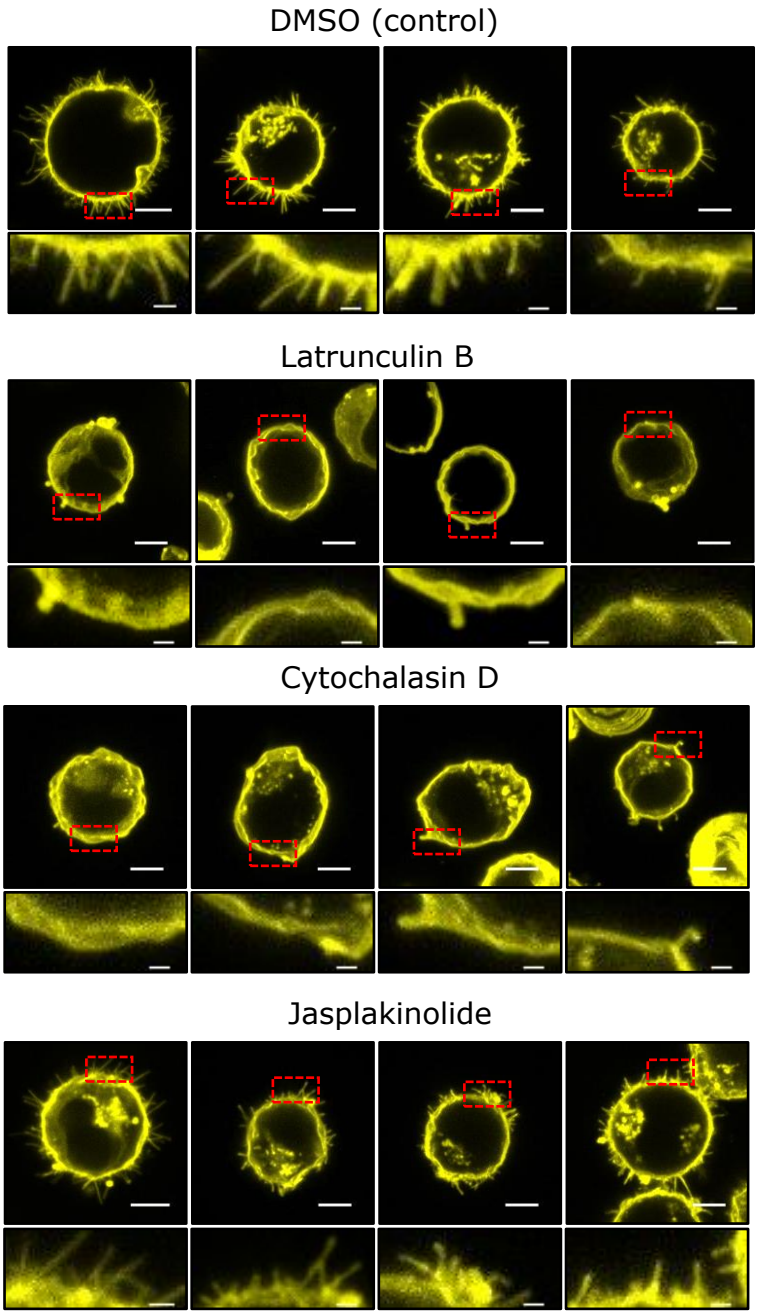

Figure 5.15. **Cell morphology after treatment with actin-modifying drugs.** J8-GECI-LFA-1 cells were placed in either 10μM DMSO (control; first row) 1μM latrunculin B (second row), 10μM cytochalasin D (third row) or 100nM jasplakinolide (fourth row) for one hour. Cells were then labelled with CellMask™ Red, fixed, placed on PLL-coated glass. Each image represents a max z-projection of 10x200nm z-stack frames starting just below the midplane of the cell. Representative images of N=3 independent experiments.

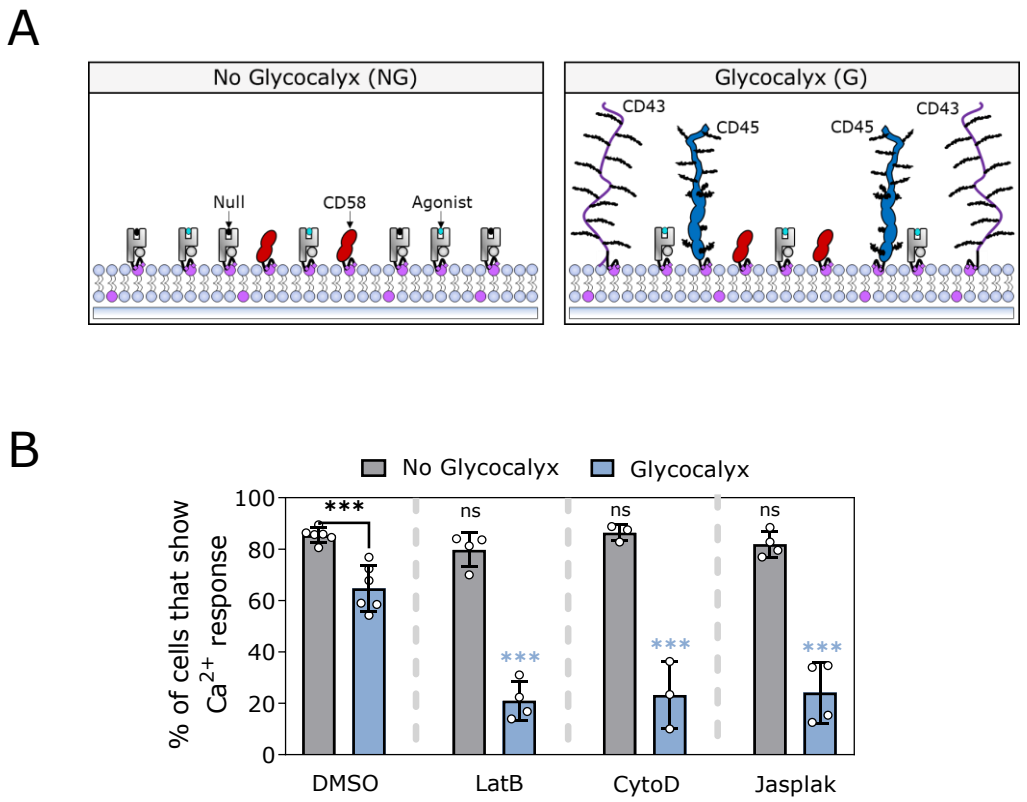

Figure 5.16. **Microvilli improve the rate of antigen detection in the presence of a glycocalyx**. (A) Cartoon representation of the no glycocalyx SLB (left, 'NG') or glycocalyx SLB (right, 'G'). The former contains only CD58 and agonist pMHC (9V). The latter contains CD58, CD43, CD45 and agonist pMHC (9V). Both contain 50-100μm^2 agonist pMHC (9V) to antigen encounter was not a limiting factor. (B) % of cells that show a calcium response (error bars are ± s.d.) on either NG (grey) or with G (blue) on different actin-modifying drugs. Cells were pre-treated for one hour with actin-filament disrupting drugs such as latrunculin B (LatB) and cytochalasin D (CytoD) or the 'actin-fixing' drug jasplakinolide (jasplak) and dropped on either NG or G. N=3-6 independent SLBs per condition (n=200-500 cells). For statistical testing, DMSO NG was compared against other NG conditions (shown as black ns), and DMSO G was compared against other G conditions (shown as blue ***). Only DMSO NG and G were compared (black line and ***). One-way ANOVA with Tukey Multiple Comparison test was used to test conditions. *** = $p < 0.001$, ns = $p > 0.05$.

5.4 Discussion

The results of this chapter confirm the importance of microvilli as the first structures involved in antigen engagement. By using the local exclusion of the SLB glycocalyx, the structures of microvilli contacts could be observed. Using this approach in combination with labelling the cell membrane with CellMask, the contours of the interface between T cell and SLB could be identified. Importantly, it was clear that microvillar CCZs dominated the interface, indicating cells do not form large flat contacts. Microvilli CCZs were observed prior to calcium release even at high (50-100/μm^2) densities of antigen, indicating they must be the sites of antigen detection and discrimination. Antigen recognition resulted in increased scanning efforts from the cell as they rapidly spread, resulting in additional microvillar CCZ. Lastly, microvilli were shown to substantially improve the efficiency of antigen detection, helping overcome the glycocalyx.

5.4.1 Microvilli on J8s

The J8 cell line had microvilli on their surface as seen in both SEM and confocal imaging. These were confirmed as microvilli by the enrichment of L-selectin on the membrane protrusions [123], [342]. When comparing to primary cells, J8s microvilli in SEM appeared less dense than in naïve, resting, and activated T cells [123], [126], [268]. It was recently calculated that Jurkats have half as many microvilli (2.5 vs. 4.5/μm^2; [126]). In terms of length, they were longer than naïve and resting cells, but comparable to activated T cells [123], [268]. The diameter of J8 microvilli (100-200nm) were more consistent with those in activated T cells (140-200nm) than resting (70-100nm; [123]).

Therefore, J8s may better reflect activated T cells. However, any differences could also be a result of variations in the extensive processing of the cells for SEM (i.e. different fixation protocols or dehydration steps for SEM processing), or because J8s are derived from a leukemic cell line, there may exist structural changes to the underlying actin cytoskeleton [266]. Despite this, J8s can evidently be used as model cells to study microvilli contacts.

Different diameter of microvilli are cited in the literature, ranging from 70-700nm, largely dependent on the technique used to quantify this (i.e. electron vs. fluorescence microscopy) [122]–[124], [126]. Here, SEM showed microvilli to be ~100-200nm, however confocal imaging showed a diameter of ~300-600nm. The finding that fluorescence imaging typically yields microvilli two-three-fold larger in diameter than SEM may result from the alcohol dehydration steps during SEM processing, which have previously been shown to significantly shrink samples [344]. Others have suggested they are diffraction limited structures, but even super resolution imaging has placed microvilli tip diameter between 200-650nm [122], [126]. As super resolution imaging doesn't require dehydration steps this may be more reflective of their true size.

5.4.2 Imaging microvilli CCZs by the exclusion of CD43 and CD45

In this chapter, areas of CD43 and/or CD45RABC exclusion on 2nd generation SLBs were used to identify microvilli CCZs in live cells. This method works by the passive exclusion

of large glycocoalyx proteins either because of their large and rigid nature, or due to lateral crowding from extensive receptor-ligand pairing [79], [116]. A key consideration is that microvilli are close in size to the diffraction limit, and as a result it may be that more transient or smaller contacts are not visible using this imaging technique. It would be useful to model the limitations of this approach, using both the size and extent of exclusion of CD43/45 to estimate microvillar contact sizes.

CD43 or CD45 based CCZs (i.e. areas of exclusion) exhibited a 20-40% reduction in fluorescence. This reflects the x-y diffraction limit from TIRF microscopy and the potential accommodation of CD43 and CD45 in the contacts. These values are consistent with a previous report observing reconstituted CD45RABC extracellular domain in a thermally equilibrated and reconstituted system [119]. Using a giant unilamellar vesicle functionalised with the extracellular domains of the TCR (200 molecules/μm^2) and CD45RABC (1000 molecules/μm^2), and SLB functionalised with pMHC (2.5μM K_d, 200 molecules/μm^2), Carbone et al., (2017) found that CD45RABC was only excluded 38% once adhesion had reached equilibrium (~30 minutes). This was done using a similar metric for exclusion i.e. 100*(1-(intensity in contact/intensity outside contact)). Therefore, the level of exclusion seen in this chapter provides a robust indicator of CCZs within seconds-minutes of cell contact. Interestingly, when analysing Jurkats attached to SLBs containing small adhesion molecules, similar exclusion values (25-41%) have been seen for non-binding receptors (e.g. CD4) smaller than the gap in the SLB/cell interface (<15nm), indicating lateral crowding may be a more dominant mechanism for exclusion, particularly in large adhesive contacts [416]. The relative contributions of sized based

exclusion and lateral crowding to CD43/45 exclusion in this chapter remain unclear, particularly as substantially smaller contacts were analysed compared to previous reports [416]. Quantifying the relative contributions of each mechanism at different adhesion regimes would be a valuable avenue of experimentation for the future.

Although both CD43 and CD45RABC can be used to identify CCZs, the number of CCZs identified, the total area of CCZs and the extent of exclusion over time was higher for CD45RABC than CD43. This difference is somewhat surprising as CD43 is thought to be a rigid molecule (owing to its extensive glycosylation and negative charge) and of similar dimensions to CD45RABC (~45 vs. 40nm), so one might expect it to exclude to the same extent [117]. It should be noted that in the only study to measure CD43 height to date, molecules with the "longest straight arms" were chosen for quantification, potentially neglecting more flexible and therefore "shorter" molecules [117]. If CD43 is less rigid than anticipated, it may allow more bent conformations of CD43 to exist, reducing overall exclusion relative to CD45RABC. However, another factor to consider is that protein conformations can be altered by lateral crowding effects, which can constrain protein degrees of freedom [113], [345]. It has been predicted that proteins may substantially extend at total physiological surface densities (>10,000/μm^2; [346]). As 3000-4000/μm^2 were used here, CD43 may not reach its full height. Additional testing of CD43 height and rigidity *in situ* is required, but as it is still capable of being passively excluded it must be substantially larger than the ~15nm gap between CD2-CD58 and TCR-pMHC, and therefore, can be used to map CCZs.

5.4.3 Dynamic microvilli are essential to efficient antigen scanning

T-cell microvilli require the dynamic growth and restructuring of actin filaments to efficiently scan for antigen as their loss or 'stabilisation' using actin-modifying drugs (LatB, CytoD and Jasplak) significantly reduced the proportion of cells that detected antigen in the presence of a glycocalyx. In contrast, most cells (~80%) responded in the absence of the SLB glycocalyx, consistent with previous reports showing T cells were capable of signaling when treated with latB and cytoD ([121], [124], [266]. This indicated that loss of dynamic morphological structures as the explanation for reduced signaling. Importantly, as 20-30% of drug-treated cells still signalled on glycocalyx containing SLBs, microvilli are not an absolute requirement for antigen detection, but rather a means to improve the rate of antigen detection. Tuning the balance between adhesion molecules and the glycocalyx (while keeping antigen density constant) on the SLB will alter the extent to which signaling is attenuated by actin-modifying drugs. While doing this, it would also be beneficial to study the kinetics of CCZ formation. A similar methodology was described in a more reductionist system, which showed that reconstitution of a single glycocalyx element (CD45R0, ~22nm) on one side of small-receptor-ligand functionalised giant unilamellar vesicle-SLB interface was enough to delay adhesion by 16-minutes [119]. As an alternative to drugs, genetic manipulation of morphology could be used, whereby overexpression of the N-terminal domain of ezrin, which links surface proteins to the actin cytoskeleton, can cause a loss of microvilli [126], [347].

Chapter 6 Adhesion proteins enhance antigen recognition at microvillar contacts

6.1 Introduction

The two most important adhesion proteins expressed on the surface of T cells are CD2 and LFA-1. CD2 is a small (~7nm) single-pass transmembrane protein that binds CD58 in humans with a relatively low affinity (3D K_d of 10-20μM, 2D K_d of 1-8 molecules/μm^2) [137]–[139], [348]. In mice CD2 predominantly binds CD48 (3D K_d of 90μM). In humans and mice, LFA-1 integrin is a CD11α/CD18 heterodimer that binds cellular adhesion molecules ICAM 1-5 and JAM 1-2, although the strongest-binding and best-characterised ligand is ICAM-1 [349]. LFA-1 differs from CD2 based on its size and its ability for conformation-based affinity regulation, whereupon signals derived from the TCR or chemokine signaling can change its height from <5nm to 20-25nm and affinity from 1mM to 100nM (i.e. 10,000x K_d change) [132], [133], [349], [350]. The findings that both CD2 and LFA-1 are conserved in T cells across species, and that their dominant ligands, CD58/CD48 and ICAM-1, are ubiquitously expressed on haemopoietic and non-haemopoietic cells, stress their importance in T-cell adhesion [351], [352].

CD2 and LFA-1 have both been implicated in enhancing T-cell activation through (at least in part) their adhesive capacity. In the case of CD2, calcium release, cytokine production and proliferation were enhanced in the presence of CD58/CD48 [353]–[359].

Also, transgenic expression of human CD58 in fibroblasts resulted in a 20-fold decrease in the effective antigen dose (EC50) to stimulate 50% maximal T-cell proliferation, and CD2 knockout murine T cells interacting with antigen-pulsed APCs produced a 3-10-fold decrease in activation across early signaling (calcium release), cytokine production and proliferation [142], [355], [357]. Similar findings have been obtained for LFA-1. For example, without LFA-1, cells required 10-100x more antigen to produce the same response, and antibodies against LFA-1 substantially blocked IL-2 production ([136], [142], [360]**.** Cooperative effects have been shown for CD2 and LFA-1, and in one case blocking the action of both reduced activation ~100-fold [142], [361]. Activation could be linked to adhesion based on a reduced ability to form conjugates with target cells when blocking CD2/CD58/CD48/LFA/ICAM-1 with antibodies in antigen-dependent and independent settings [142], [355], [361][362].

What is unclear about these proteins is how they contribute to antigen detection per se. Most *in vitro* imaging experiments on CD2-CD58 and LFA-1-ICAM-1 have relied on measurements made minutes after T cells have attached to the SLB and likely already identified antigen [92], [140], [141]. Both are known to form a significant component of the immune synapse [78]. As microvillus-based antigen scanning is a more recently emerging concept, the adhesion proteins are uncharacterised in this context [122]. The aims of this chapter were to observe how CD58 and ICAM-1 accumulate relative to microvillar CCZ formation and each other on 2nd generation SLBs, and whether incorporation of the APC glycocalyx into 2nd generation SLBs would phenocopy loss of adhesion molecule experiments. This would more specifically test whether the loss of

activation from reduced adhesion molecules and cell conjugation seen in previous studies was due to a reduced capacity to surmount the glycocalyx barrier.

6.2 Methods

TIRFM

2nd generation SLBs were prepared as previously described in **Section 2.7** and **Chapter 3**. In order to visualise contact topology CD45RABC and CD43 were both labelled with Alexa-555. CD58 and ICAM-1 were both labelled with Alexa-647 to image their reorganisation in relation to CD43/45 CCZs. ICAM-1 was also labelled with Alexa 555 to be imaged alongside CD58-Alexa 647 in one case. Low densities of agonist pMHC (9V, 1-5μm^2) were used, with concentration used determined by **Figure 4.1**. SLBs were washed 10x in pre-warmed (37˚C) PBS + 2mM $MgS0_4$, resuspended in the same, with the glass slides placed in pre-warmed (37˚C) metal chambers. J8-GECI-LFA-1 cells were washed x2 and resuspended in pre-warmed (37˚C) PBS + 2mM $MgS0_4$. SLBs and cells were incubated at 37˚C for five-minutes prior to being dropped gently onto the SLBs and imaged by TIRFM. A complete frame cycle was taken every 2s for 10-minutes as previously described in **Chapter 4**. Images were processed as described in **Section 2.7**. For ICAM-1 and CD58 the SLBs were imaged prior to use to gain the background signal. Background signal was averaged (z-projection) and removed from the experimental video. CD43/45 were processed as described in **Chapter 5**.

Label 1	Label 2	Label 3
GECI	CD45&CD43-Alexa 555	CD58-Alexa 647
GECI	CD45&CD43-Alexa 555	ICAM-1-Alexa 647
GECI	ICAM-1-Alexa 555	CD58-Alexa 647

Table 6.1. **Labelling combination strategy.**

Altering adhesion proteins on 2nd generation SLBs

In order to remove adhesion proteins from the composition of 2nd generation SLBs, the proteins were swapped out for near molar ratios of null pMHC. The final concentrations used can be found in **Table 6.2**. To ensure the SLBs remained comparable, pFCS was used to measure agonist pMHC (9V) density (labelled with Alexa 647).

	WT	ΔCD54	ΔCD58	ΔCD54/58	
Protein	Conc. (ng/μl)	Conc. (ng/μl)	Conc. (ng/μl)	Conc. (ng/μl)	Density (/μm^2)
Agonist pMHC (9V)	0.1	0.1	0.1	0.1	10-30
Null pMHC	9.9	11.15	10.95	12.2	>1700
ICAM-1	1.2	0	1.2	0	400-600 (or 0)
CD58	0.5	0.5	0	0	200-300 (or 0)
CD45	2.5	2.5	2.5	2.5	250-350
CD43	1.5	1.5	1.5	1.5	300-400

Table 6.2. **Concentrations for modified 2nd generation SLBs.**

Calcium assay

2nd generation SLBs were prepared with medium densities of agonist MHC (9V) labelled with Alexa-647 (10-30/μm^2) as described in **Chapters 2-**4. The rest of the proteins were unlabelled. For each individual SLB, 0.25-0.5x10^6 J8-GECI cells were washed x2 in pre-warmed (37°C) PBS + 2mM $MgS0_4$, resuspended in the same and incubated for a further

5 minutes at 37˚C. SLBs were also washed 10x in pre-warmed (37˚C) PBS + 2mM $MgS0_4$, resuspended in the same, with the glass slides placed in pre-warmed (37˚C) metal chambers. During the 5-minute incubation, pMHC-9V-Alexa 647 on SLBs was subject to 3x10s pFCS measurements using a 40x water objective (NA1.2; with 633nm laser at 1% laser power), to obtain density readouts of agonist pMHC (9V). The objective was changed to a 10x magnification, and cells were immediately dropped on the SLB and recorded at 1s intervals for 10-minutes (argon 488nm-laser at 10-20% power). pFCS and imaging were performed on the Zeiss LSM780 inverted confocal scanning microscope. Agonist pMHC density was obtained by fitting autocorrelation plots using both FoCuS point software and PyCorrfit [301], [302]. Cell displacement, time to adhesion, % signaling, and time to signaling were analysed using the bespoke MATLAB® script, as described in **Section 2.7**.

6.3 Results

6.3.1 CD58 and ICAM-1 accumulate prior to calcium release in spatially distinct zones

In order to test the role of adhesion proteins in antigen scanning, J8-LFA-GECI cells were imaged using TIRFM on 2nd generation SLBs. The GECI was used to relate CD58 or ICAM-1 accumulation to productive antigen detection. CD58 was examined first. Second generation SLBs were setup with CD58-Alexa 647, CD43/CD45-Alexa 555 to view CCZs (CCZ mapping from **Chapter 5**), and low densities of agonist pMHC (9V; 1-5 molecules/μm^2). Except for CD58 and CD43/45, all other proteins were unlabelled. J8-GECI-LFA-1 cells were dropped onto the SLB and immediately imaged. Upon landing, CD43/54 exclusion (i.e. CCZ formation), CD58 accumulation and calcium release could be seen (**Figure 6.1A**). Immediately after calcium release cells quickly spread, forming additional areas of CD58 accumulation and CCZs that moved centripetally, like the TCR, as noted in **Chapter 5** (**Figure 6.1A**). CD58 intensity anticorrelated with CD43/45, and most (if not all) CCZs colocalised with areas of CD58 accumulation (**Figure 6.1B**). CD58 and CCZs colocalised and visibly accumulated before calcium signaling (**Figure 6.1C**). Therefore, CCZs seen before signaling in **Chapter 5** most likely represent CD2-CD58-stabilised microvillar contacts. Considering the total surface area of CD58 accumulation at the Ca^{2+} signal was ~0.36μm^2, and with an assumed density of agonist pMHC at 2.5/μm^2 (based on measurements from **Chapter 4**), this means, on average, ~0.9 total pMHC were presented to this cell at the point of calcium release.

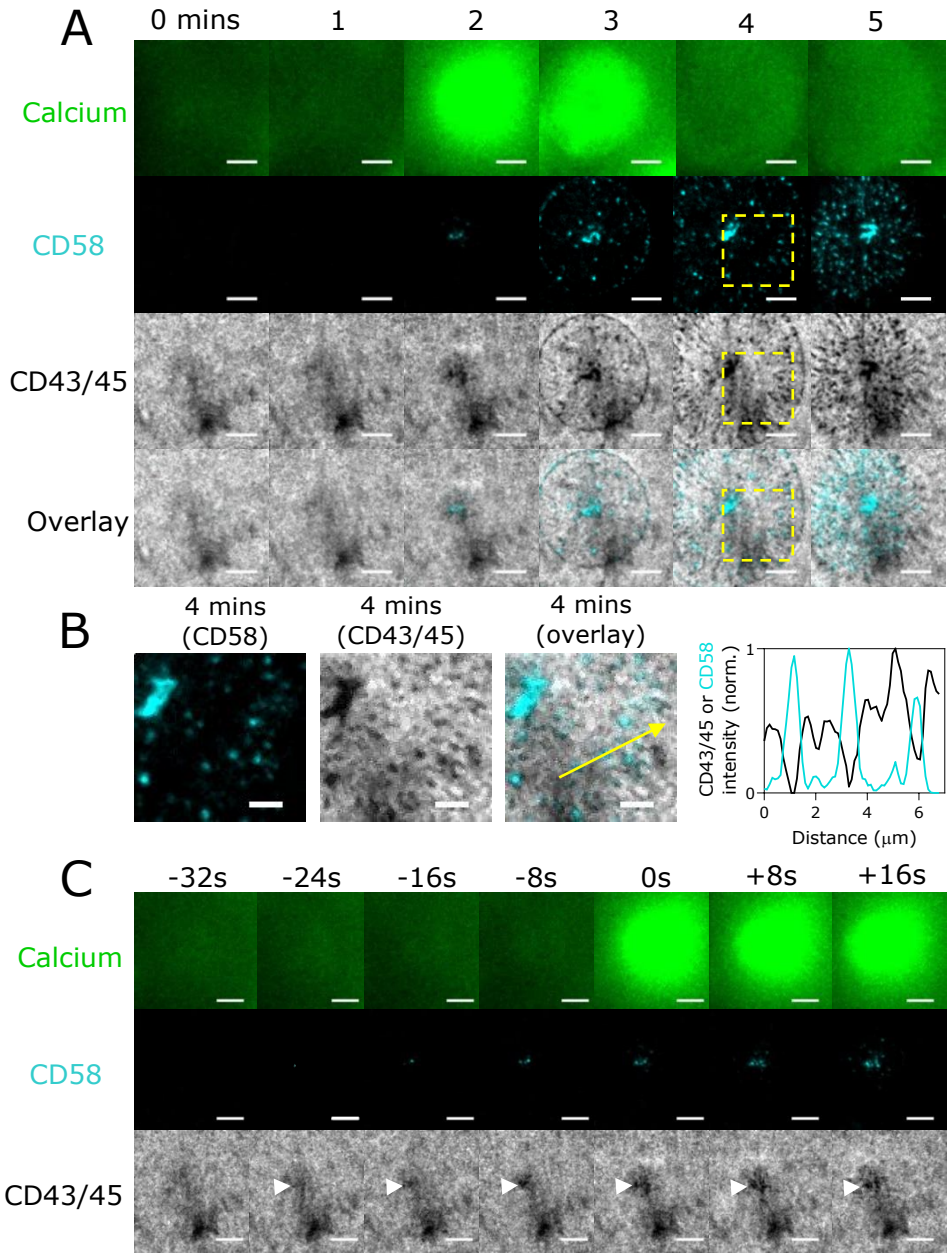

Figure 6.1. **CD58 accumulates at microvillar CCZs prior to signaling.** J8-GECI-LFA-1 cells were dropped on 2nd generation SLBs containing low density of agonist pMHC (9V, 1-5 molecules/μm²). CD58 was labelled with Alexa 647, and to view CCZs, CD43/45 both labelled with Alexa 555. (A) Image of calcium (green), CD58 accumulation (cyan), and CD43/45 (areas of exclusion = CCZs, grey) over the course of 5-minutes. Scale bar is 5μm. (B) Inset region designated by yellow box in (A). Right plot: min/max normalised intensity line profile along and in direction of yellow arrow in the image to the left. CD58 anticorrelates with CD43/45 intensity. Scale bar is 2.5μm. (C) Same cell in (A) but showing 32s prior and 16s after calcium release (0s). CD58 accumulation and CCZ formation (white arrows, bottom row) form prior to calcium release.

Next, ICAM-1 accumulation was examined alongside microvillar CCZ formation and calcium release. Over the first two-minutes preceding calcium signaling, ICAM-1 initially formed a small ring of accumulation around a CCZ (**Figure 6.2A**). After calcium release, the area of accumulation increased over time, with additional ICAM-1 rings forming. ICAM-1 rings have been shown surrounding 'TCR microclusters' on 1st generation SLBs [96]. ICAM-1 correlated with CD45/43 intensity (**Figure 6.2B**). Visibly, CD43/45 intensity decreased (manually quantified at ~10%) in the most intense areas of ICAM-1 accumulation, implying some degree of segregation, but not to the same extent as in CCZs (manually quantified as a ~40% decrease; **Figure 6.2B**). This highlights how the LFA-1-ICAM-1 complex and the glycocalyx, for the most part, colocalise within the same domains at the interface between T cell and SLB. Lastly, ICAM-1 rings formed around CCZs before calcium release, hinting at a role in stabilising initial microvillar contacts for antigen scanning (**Figure 6.2A&C**).

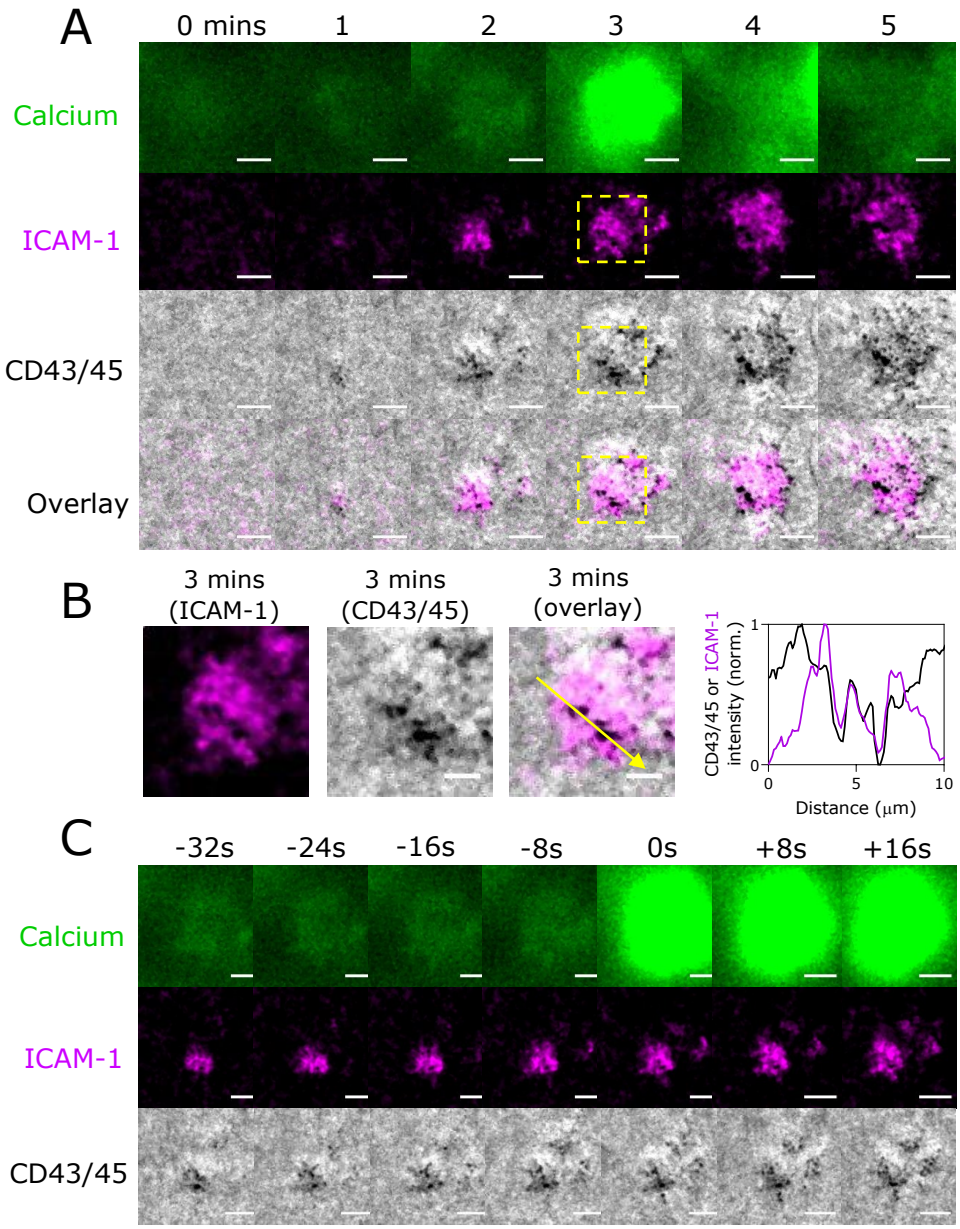

Figure 6.2. **ICAM-1 accumulates outside microvillar CCZs prior to signaling.** J8-GECI-LFA-1 cells were dropped on 2nd generation SLBs containing low density of agonist pMHC (9V, 1-5/μm²). ICAM-1 was labelled with Alexa 647, and to view CCZs, CD43/45 both labelled with Alexa 555. (A) Image of calcium (green), ICAM-1 accumulation (magenta), and CD43/45 exclusion based CCZs (grey) over the course of 5-minutes. Scale bar is 5μm. (B) Inset region designated by yellow box in (A). Right plot: min/max normalised intensity line profile along and in direction of yellow arrow in the image to the left. ICAM-1 correlates with CD43/45 intensity. Scale bar is 2.5μm. (C) Same cell in (A) but showing 32s prior and 16s after calcium release (0s). ICAM-1 accumulation and CCZ formation can be seen prior to calcium release.

6.3.2 CD58 accumulation/CCZ formation occurs before ICAM-1

CD58 colocalised with CCZs, whereas ICAM-1 formed rings of accumulation around CCZs. Both proteins appeared to accumulate prior to calcium release (**Figure 6.1&6.2**). This raised the question of whether ICAM-1/LFA-1 aided CD58/CD2 interaction (i.e. adhesion cascade based on receptor height), or vice versa. To test this, both were imaged simultaneously. CD58 and ICAM-1 formed spatially distinct zones with anticorrelated intensities (**Figure 6.3A&B**). At 40s before calcium release a single area of CD58 accumulation formed (**Figure 6.3C**). This was followed by a small region of ICAM-1 accumulation at the periphery of CD58 by 32s before calcium release (**Figure 6.3C**). Over time, ICAM-1 started to accumulate in a ring-like structure around the CD58 until calcium release (0s). The ring structure is clearly seen at the 1-minute mark in **Figure 6.3A**. To ensure that this cell was not an outlier, several cells were analysed, all of which indicated CD58 accumulation followed by ICAM-1 and then calcium (**Figure 6.4A**). In one case, several CD58 accumulation zones surrounded by ICAM-1 persisted in the absence of any observable calcium release for 330s and was mobile across the surface (**Figure 6.4B&C**). Since CCZs and CD58 colocalise, CCZs provided a proxy of CD58 accumulation allowing separate test under different labelling regimes (**Figure 6.5A&B**). Other experiments showing ICAM-1 and calcium, or CD58 and calcium were also analysed to provide additional support for their accumulation prior to calcium release (**Figure 6.5C&D**). The trends were consistent across all labelling conditions; CD58 accumulation/CCZ formation is followed by ICAM-1 accumulation, and then calcium release.

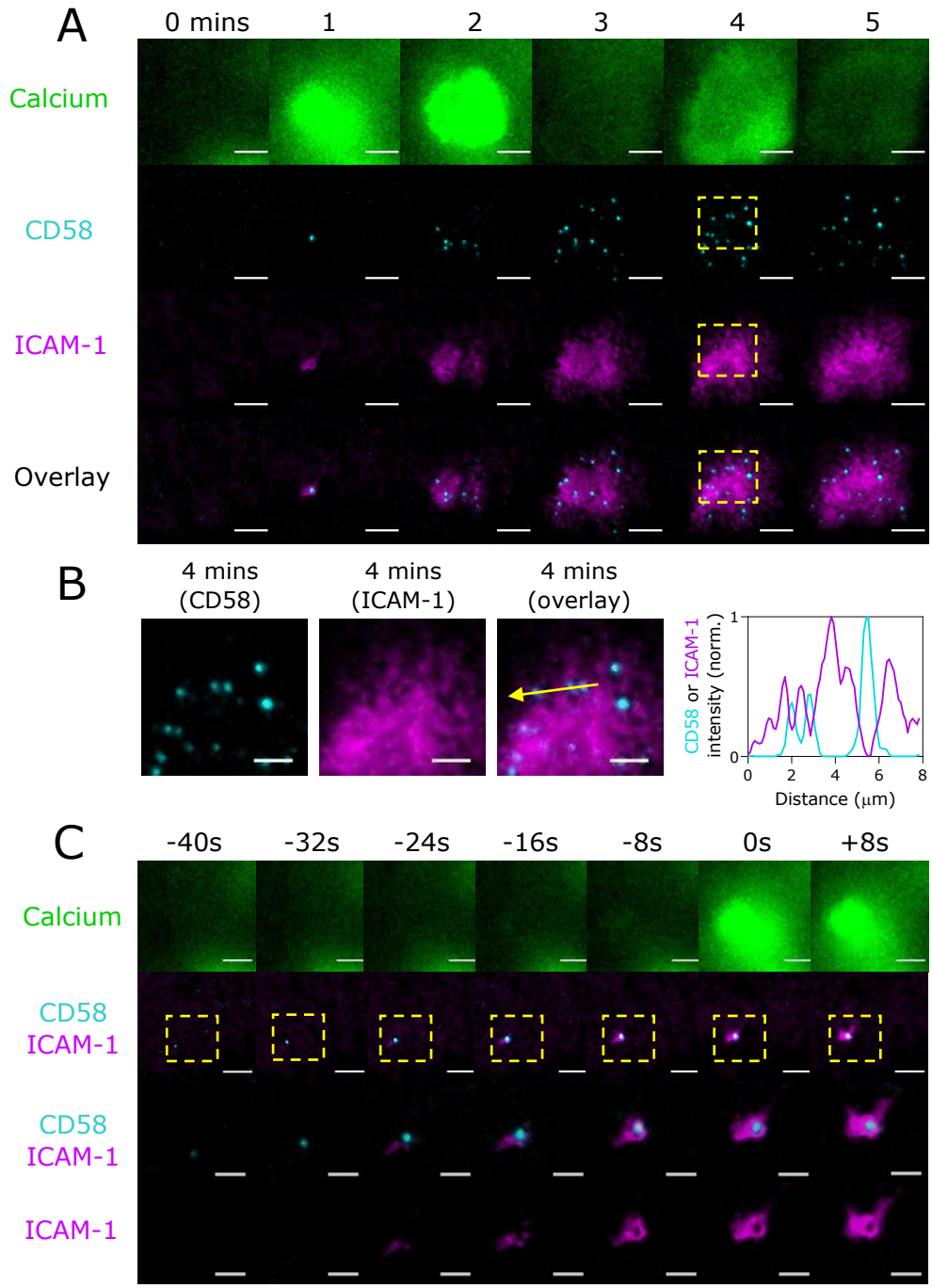

Figure 6.3. **CD58 and ICAM-1 accumulate in separate regions prior to signaling.** J8-GECI-LFA-1 cells were dropped on 2nd generation SLBs containing low density of agonist pMHC (9V, 1-5/μm²). CD58 was labelled with Alexa-647, and ICAM-1 was labelled with Alexa 555. (A) Image of calcium (green), ICAM-1 accumulation (magenta), and CD58 accumulation (cyan) over the course of 5-minutes. Scale bar is 5μm. (B) Inset region designated by yellow box in (A). Right plot: min/max normalised intensity line profile along and in direction of yellow arrow in the image to the left. ICAM-1 signal anticorrelates with CD58. Scale bar is 2.5μm. (C) Same cell in (A) but showing 40s prior, and 8s after, calcium release (0s). A ring of ICAM-1 accumulation can be seen forming around CD58 prior to calcium release. Row three and four are taken from the yellow inset in row two.

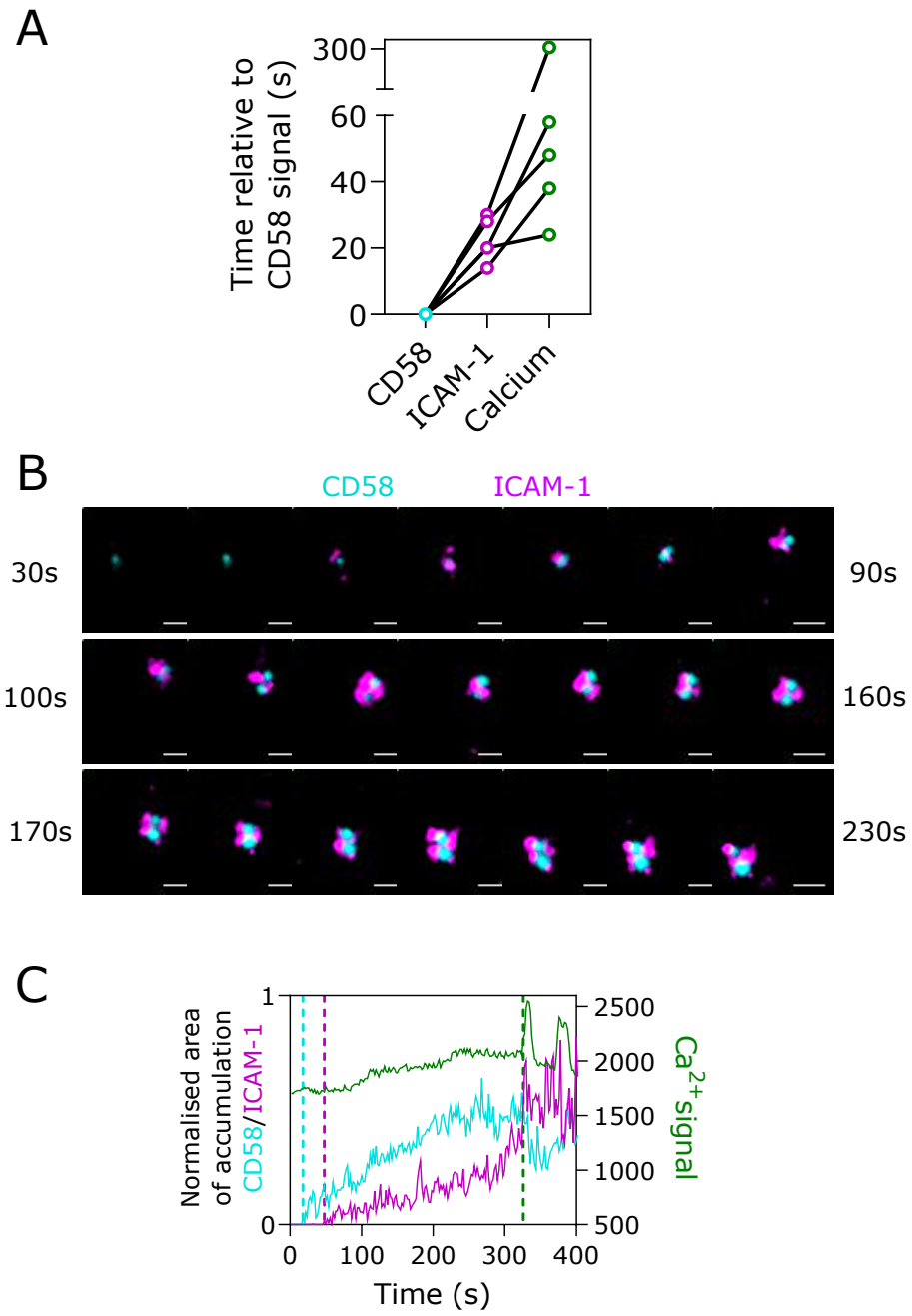

Figure 6.4. **CD58 and ICAM-1 accumulate prior to antigen detection.** (A) Quantification of CD58 accumulation relative to ICAM-1 and calcium release. CD58 accumulation was set at 0s for all cells. (B) Example of a cell that persistently accumulated CD58 surrounded by an ICAM-1 ring in the absence of signaling for 330s. Scale bar is 2.5µm. (C) Normalised intensity traces from (B).

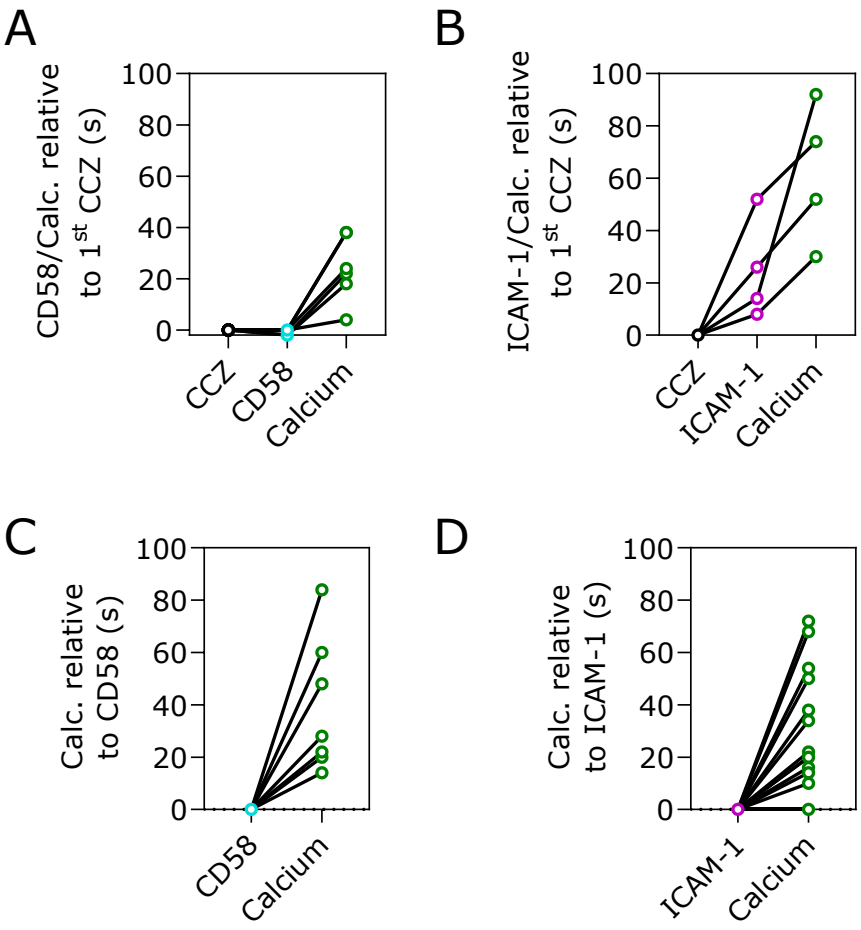

Figure 6.5. **CCZs formation, and CD58 and ICAM-1 accumulation are observed before calcium release.** (A) Time for (A) CD58 or (B) ICAM-1 accumulation and calcium release relative to formation of the first stable CCZ (set at 0s). Time for calcium release relative to (C) CD58 or (D) ICAM-1 accumulation. (A) Analysis of cells taken from **Figure 6.1**. Cells were labelled with GECI, SLB was labelled with CD43/45-Alexa 555, and CD58-Alexa 647. N=2 independent SLBs (n=6 cells total). (B) Analysis of cells taken from **Figure 6.2**. Cells were labelled with GECI, SLB was labelled with CD43/45-Alexa 555 and ICAM-1-Alexa 647. N=1 independent SLBs (n=4 cells). (C) Analysis of cells taken from **Figure 7.3** in **Chapter 7**. Cells were labelled with GECI and anti-gap8.3-Alexa 555, SLB was labelled with CD58-Alexa 647. N=3 independent SLBs (n=7 cells total). (D) Cells were labelled with GECI and CellMask™ Red, SLB was labelled with ICAM-1-Alexa 555. N=4 independent SLBs (n=13 cells total). (A-D) All are 2nd generation SLBs with low density agonist pMHC (9V, 1-5 molecules/μm^2).

6.3.3 CD58 and ICAM-1 both enhance antigen detection

Having found that CD58 and ICAM-1 accumulate prior to calcium release, these proteins were further tested for their capacity to aid antigen scanning. The two adhesion proteins were systematically removed from 2nd generation SLBs and J8-GECI-LFA-1 cells were tested for altered ability to detect antigen (given by calcium release; **Figure 6.6A**). To remove the adhesion proteins without changing remaining protein densities, they were exchanged at near-molar ratios with null pMHC. To ensure that the SLBs remained comparable, the density of agonist pMHC (9V)-Alexa 647 was measured by pFCS. All SLBs contained 10-30 molecules of agonist pMHC (9V)/μm^2, with no significant differences found (**Figure 6.6B**). As altering the concentration of even a single protein can alter the density of other proteins in a seemingly unpredictable manner, the fact that the different SLBs maintained a comparable density of agonist pMHC (9V) indicates the other proteins were also likely consistent. On 'wild type (WT)' conditions (i.e. 2nd generation SLBs), ~75% of cells responded in a 10-minute analysis (**Figure 6.6B&C**). Upon removing ICAM-1 (ΔCD54), a small but significant ($p = 0.042$) decrease to ~60% responding cells was seen. Removing CD58 had a larger effect, with ~40% of cells responding. The biggest effect came from removing both proteins (ΔCD54&58), which near abolished calcium release with only ~5% of cells now responding. Differences between SLBs were independent of measurement time (**Figure 6.6C**). Relative to WT, ΔCD54 created a ~1.25-fold decrease, ΔCD58 a ~1.75-fold decrease, and ΔCD54&58 a ~15-fold decrease in the fraction of cells that responded. This indicates that there may be synergy between CD2 and LFA-1, or at least a basic requirement for adhesion molecules to be present when it comes to productive antigen recognition.

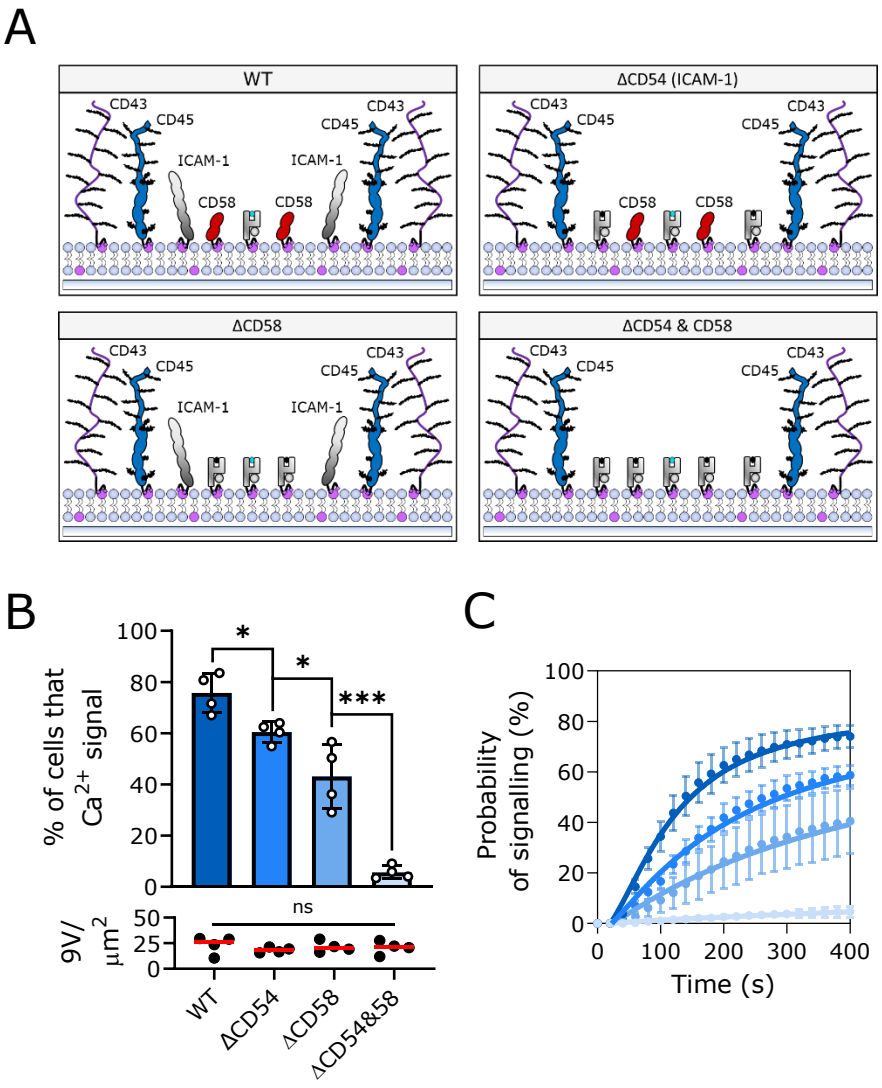

Figure 6.6. **CD58 and ICAM-1 cooperatively aid antigen detection.** (A) Cartoon representation of 2nd generation SLBs titrated for their adhesive property. In order to remove each adhesion protein, *ceteris paribus*, it was exchanged at a molar equivalence with null pMHC. Each SLB contained a range of 10-30 molecules of agonist pMHC (9V) per µm^2. (B) Percentage of cells that respond within a 10-minute video. To ensure each SLB showed comparable potency, pFCS of agonist pMHC (9V) was measured for every repeat (shown below graph). (C) The average (± s.d.) percentage of cells responding over a 10-minute video. Data points were fit using the [agonist] vs. response curve (four parameters, bottom constrained to 0). Percentage of cells responding and agonist pMHC (9V) density were tested using one-way ANOVA with Tukey Multiple Comparison test. ***= $p < 0.001$, * = $p<0.05$, ns = $p > 0.05$. No significant differences were found in the pMHC density across conditions. N=4 independent SLBs (n=300-500 cells).

To obtain an indication of whether the change in the percentage of responding cells was a result of adhesion, total displacement and time to adhesion were analysed. If cells take longer to adhere to the surface, the lower the likelihood of them signaling. First, displacement plots showed that cells had moved further over the SLB surface upon removal of adhesion molecules, with most displacement seen for the ΔCD54&58 SLB (**Figure 6.7A**). Quantification of displacement showed only a modest, non-significant difference between WT and ΔCD54 SLBs (median of 37 vs. 43μm, 1.16-fold increase, $p = 0.999$; **Figure 6.7B**). Compared to WT, ΔCD58 showed a larger, albeit non-significant, increase in displacement (median of 37 vs. 65μm, 1.75-fold increase, $p = 0.293$). A significant difference was found between WT and ΔCD54&58 (37 vs. 125μm, 3.4-fold increase, $p < 0.0001$). A similar trend was found when analysing the time taken for a cell to settle/adhere to the SLB (i.e. when a cell's velocity first dropped and stayed below 0.2μm/s; **Figure 6.7C**). Relative to WT, ΔCD54 took 1.5-fold longer to adhere on average (100 vs. 150s), ΔCD58 took 3-fold (100s vs. 300s), and ΔCD54&58 took 30-fold (100s vs. 3000s). Therefore, the cooperative decrease in responsiveness in **Figure 6.6B**, more than likely results from a cooperative decrease in adhesion.

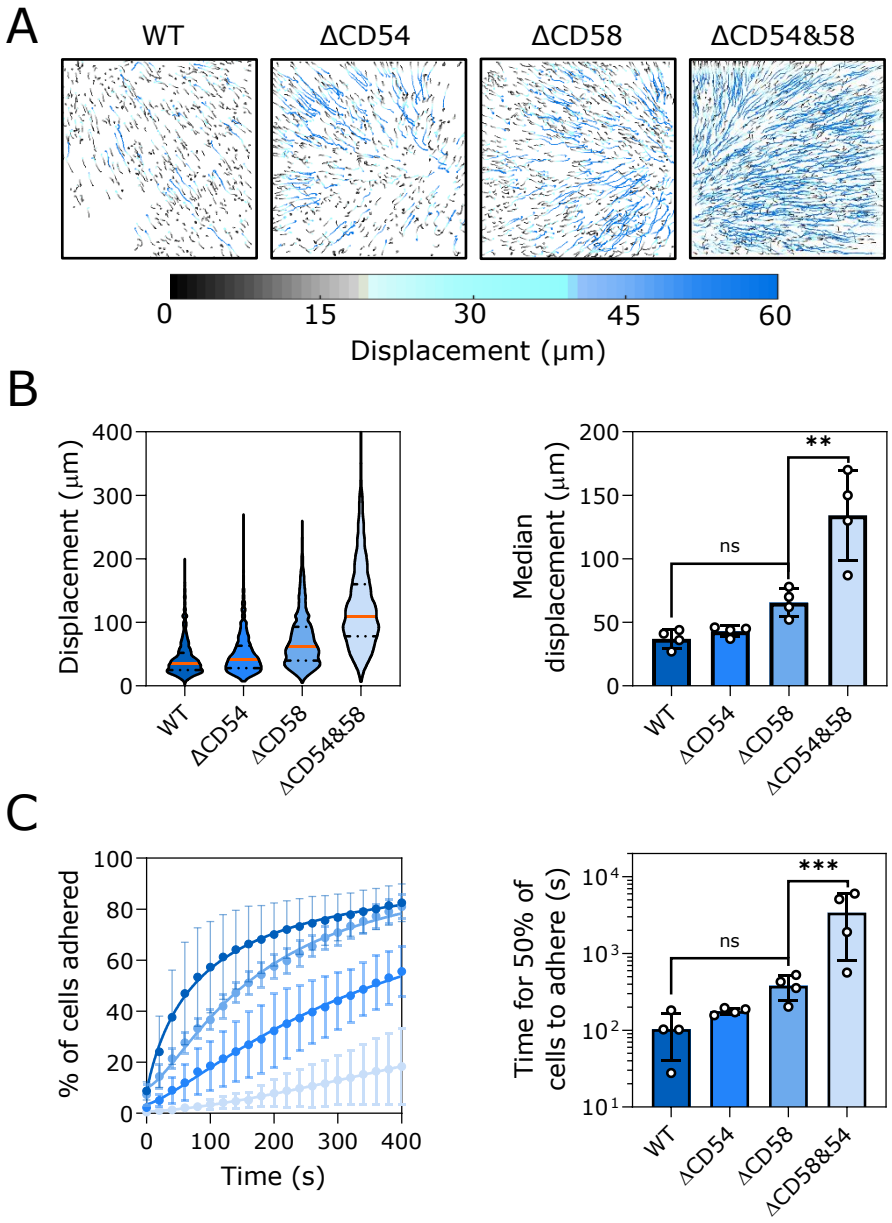

Figure 6.7. **CD58 and ICAM-1 show cooperative effects on adhesion.** (A) Representative displacement plots showing increased displacement of cells as adhesion proteins are removed from 2nd generation SLBs. Each dot/line represents a single cell that has the potential to go from black (0-15μm) to blue (45-60μm) in terms of their displacement. (B) Left plot: Representative violin plot of the displacement distribution from one experiment. Median given by orange line. Right: plots of the median displacement. (C) Left: average (± s.d.) cumulative distribution plots of percentage of cells adhered over time. Data points were fit using the [agonist] vs. response curve (four parameters, bottom and top constrained to 0 and 100, respectively). Right: time taken for 50% of cells to data, quantified using the EC50 of curves from left plot. (B&C) Conditions were tested using one-way ANOVA with Tukey Multiple Comparison test. ***= $p < 0.001$, **=$p < 0.01$, * =$p<0.05$, ns = $p > 0.05$. N=4 independent SLBs (n=300-500 cells).

To confirm changes in calcium release were a result of adhesion and not related to receptor signaling from CD2 and LFA-1, time to signaling was analysed. Two metrics were used: the first being the time to signal from when a cell first landed on the SLB ('track start'), and the second being from when a cell first settled/adhered ('settling') to the surface. These two metrics combined can be used to distinguish adhesion from receptor-specific signaling effects. If adhesion is playing a role, the signaling from track start should take longer with loss of adhesion molecules. If signals from the cytoplasmic domain of CD2 or LFA-1 are playing a role then the time to signaling from when a cell first settled may be altered with loss of adhesion molecules. The distributions for time to calcium release showed that only time from track start showed substantial differences, with minimal differences for time from when a cell settled (**Figure 6.8A&B**). To test for significance the median of each distribution across repeats was plotted, showing clearly two different trends across the two metrics (**Figure 6.8C**). The median time for calcium release ranged from 120s-250s (WT to ΔCD54&58) from track start or remained between 50-60s from time of settling across all conditions. Collectively, these results provide support for a cooperative role of CD2 and LFA-1 in antigen scanning, mediated through their adhesive properties. In their absence, the glycocalyx barrier appears to completely dominate the interaction, preventing CCZ formation and therefore antigen scanning.

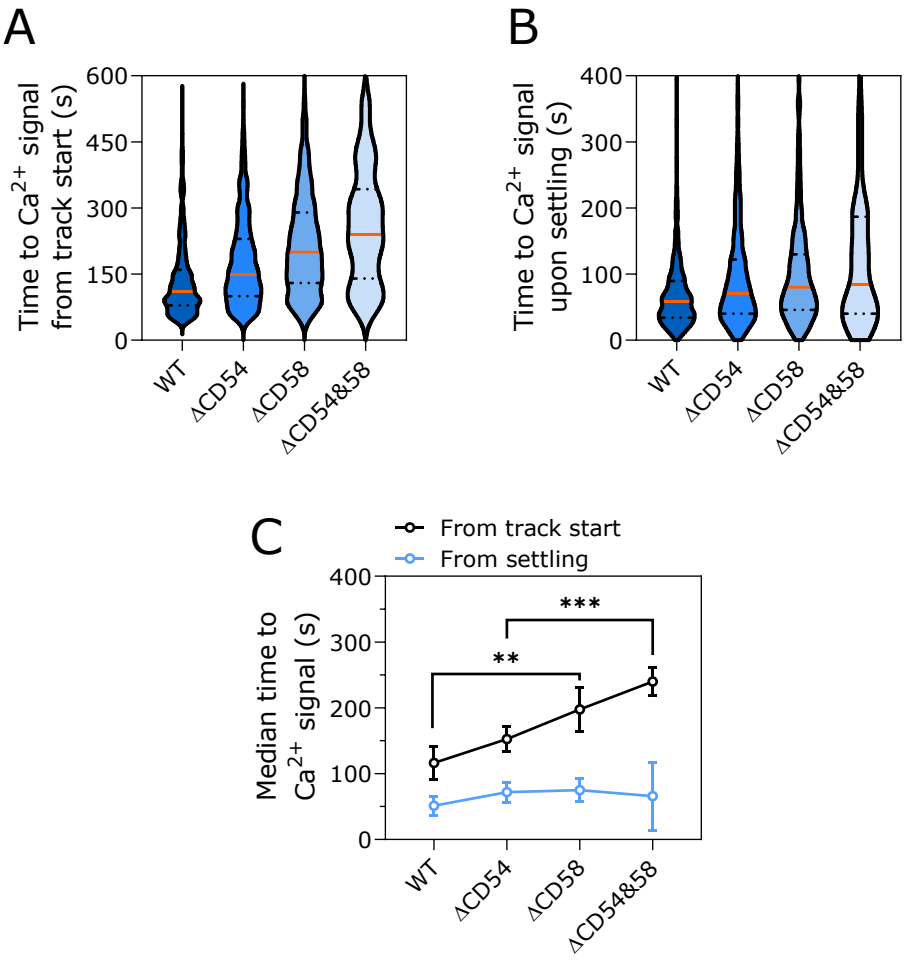

Figure 6.8. **Time to calcium release is only dependent on time taken to adhere to the SLB.** (A) Representative violin plot of the time to signal calculated from the track start of each cell to when the cell first showed calcium release (B) Representative violin plot of the time to signal calculated from the time from when each cell had settled (i.e. speed dropped and stayed below 0.2µm/s) to when the cell first showed calcium release. Cells that responded before settling on the surface (<15% of cells) were excluded from the analysis in both A&B. Median shown as orange line. (C) Plot showing the median across different conditions from the start of each track (black line) and once the cells had settled on the SLB (blue line). Conditions were tested using one-way ANOVA with Tukey Multiple Comparison test. ***= $p < 0.001$, **=$p < 0.01$, * =$p<0.05$, ns = $p > 0.05$. Significance was only between conditions when analysing from track start (black line). No significance was found between conditions once the cells had settled (blue line). A test of linearity was performed, which showed a linear increase in the median time to signal from track start with progressive loss of adhesion proteins ($R^2=0.80$, $p < 0.0001$), whereas no linear trend was found from cells settling ($R^2=0.06$, $p = 0.41$). N=4 independent SLBs (n=300-500 cells).

6.4 Discussion

Using TIRFM and calcium release analysis, this chapter examines the role of the small adhesion protein CD58 and larger integrin ICAM-1 (and by extension CD2 and LFA-1 on T cells) in antigen scanning. First to form are distinct and constrained areas of CD2-CD58 accumulation, which presumably represent attachment sites for the tips of MV. These coincide with areas of glycocalyx exclusion on the SLB. These contacts are subsequently stabilised by ICAM-1 accumulation. Given both accumulate before observable calcium release on low densities of agonist pMHC, they likely form an adhesive interface to support antigen detection rather than being a consequence of productive antigen recognition. In the presence of a glycocalyx, CD58 and ICAM-1 augment antigen detection predominantly through their adhesive properties, and loss of both results in a synergistic reduction in and almost complete loss of T cells that adhere and activate.

6.4.1 CD2: first at the 'APsCene'

Using TIRFM, it was clear that CD58 accumulated prior to ICAM-1. It is unlikely that low affinity ICAM-1/LFA-1 interaction occurred before CD58/CD2 as the experiments were performed in 2mM $MgS0_4$. Mg^{2+} ions form a coordination site in the binding domain of LFA-1 allowing a high affinity interaction with ICAM-1, independent of inside-out signaling [363], [364]. This choice of imaging medium would theoretically allow imaging of the earliest time point of ICAM-1-LFA-1 interaction. Unexpectedly, therefore, since CD58 accumulation was observed first even under these imaging

conditions, the data supports its role as the incipient adhesion protein involved in antigen scanning, at least in the context of 2nd generation SLBs.

6.4.2 LFA-1: second at the 'APsCene'

Observing ICAM-1 accumulation prior to a Ca^{2+} signal was surprising, as it implies ICAM-LFA-1 interaction supports antigen scanning even before productive antigen recognition rather than afterwards during immune synapse formation [78]. An obvious explanation may be supplementation of the imaging buffer with magnesium, but not calcium, inducing an artificially high affinity state for LFA-1. Extracellular calcium can have antagonistic effects on LFA-1 affinity for ICAM-1, particularly when both magnesium and calcium are used at physiological concentrations (both ~1mM; [363], [365]). However, this finding is controversial, as calcium at comparably high concentrations versus magnesium had no effect and was even synergistic when magnesium concentration was low [363], [366]–[370]. Furthermore, studies performed in complex media have shown that antigen-independent cell conjugation can be reduced by blocking LFA-1 or enhanced by transfection of ICAM-1 into target cells [361], [368], [371]. This would suggest ICAM-1 can bind independently of productive antigen recognition. Regardless, the influence of calcium could be tested in the future by imaging the GECI, CCZ formation/CD58 accumulation and labelled ICAM-1 in the presence and absence of calcium or magnesium or both in the imaging medium.

6.4.3 Altering the kinetics of antigen detection

By tuning the ratio of adhesive (CD58 and ICAM-1) to repulsive (i.e. the glycocalyx) proteins on the SLB, the kinetics of T-cell activation could be manipulated. A large loss of T-cell activation occurred in the combined absence of CD58 and ICAM-1, even with a moderate density of agonist pMHC (9V) capable of otherwise saturating responses on 1st and 2nd generation SLBs (**Chapter 4**). This is clearly attributable to a loss of adhesion to the surface imposed by the glycocalyx. By analysing the displacement, time to adhesion, and time to signaling, it seemed that differences in activation were a result of the adhesive extracellular component of CD2 and LFA-1 as opposed to their signaling through their cytoplasmic domains. However, as the influence of the cytoplasmic domain was not tested directly, this cannot be completely ruled out.

Chapter 7 Discriminatory signaling critically depends on size-constrained microvillar CCZs

7.1 Introduction

LFA-1 and CD2 were shown to have a role in stabilising contacts prior to productive antigen detection in the previous chapter. These proteins differed substantially in the geometry of accumulation. ICAM-1/LFA-1 complexes formed large blankets of engagement, with circular 'holes' at microvillar CCZs, whereas CD58-CD2 formed small, distinct, and circular puncta, colocalised with CCZs. The most obvious explanation for this striking difference may be due to the recent finding that CD2 is enriched at the microvillus tip, albeit this remains to be confirmed [126]. However, if found to be the case, what is the functional relevance of limiting the area of CD58-CD2 engagement to geometrically constrained microvillar contacts?

In a recent study, when using non-signaling adhesion pairs of similar affinity and size to CD58-CD2, but presumably higher density, T cells were shown to form large contacts (>1-micron diameter) on adhesion-molecule functionalised SLBs. Remarkably, most cells showed strong calcium responses, independent of any ligand for the TCR, and this correlated with large areas of CD45 exclusion [116]. In a follow-up study, this result could be mathematically explained by TCR dwell time within CD45 depleted regions [124]. Empirically parameterised modelling showed that in the absence of ligand,

doubling the diameter of CD45 exclusion zones from 400 to 800nm (sizes comparable to microvillar diameter) increased the probability of TCR triggering a thousand-fold [124]. This was due to increased dwell time of TCR within CD45 excluded regions of contact. This model could effectively predict potencies of well-characterised pMHC, implicating TCR diffusion (altered by pMHC affinity and density) and the CD45/Lck ratio (potentially fixed by the geometry of microvillar CCZs and coreceptor engagement) as the important parameters governing ligand discrimination.

In the results of this thesis so far, weak signaling (~20% of cells showing a Ca^{2+} signal) was initiated at small microvillar CCZs on 2nd generation SLBs presenting null pMHC (**Chapter 5**). Strong signaling (~80% of cells showing a Ca^{2+} signal) was dependent on the presence of agonist pMHC and occurred within similarly sized CCZs (**Chapter 5**). Clearly this shows that antigen discrimination is possible in small microvillar CCZs, which fits the predictions made by Fernandes et al. (2019, [124]). What remains now is to show whether antigen discrimination breaks down in the presence of large contacts. To this end, this chapter first shows that ligand-independent signaling on null pMHC is wholly TCR-dependent, and that CD45 exclusion on the T-cell membrane occurs at small microvillar CCZs. This is followed by a method to alter CCZ size through CD2 expression and lastly, evidence that antigen discrimination is only maintained in geometrically constrained microvillar CCZs.

7.2 Methods

Creating CD2-modified cell lines

To knockout CD2 in J8-GECI and J8^{TCR-}GECI cells, CRISPR-Cas9 guides were designed and selected for high specificity with minimal off targets using Benchling (hg38 reference genome) and CRISPOR. Oligos were then designed, annealed, and ligated into the LentiCRISPRv2 plasmid using the dual BsmBI sites, as previously described (addgene #52961; [298], [299]). Oligo sequences designed for direct annealing and ligation into LentiCRISPRv2 can be found in **Table 7.1**. Cells were transduced as in **Section 2.2**. Cells were sorted on the CD2^{-} population by FACS 7 days after transduction.

Knockout target	Exon	Sense	Guide sequence for cloning into LentiCRISPRv2
CD2	3	Forward	CACCGAGAGGGTCATCACACACAAG
		Reverse	AAACCTTGTGTGTGATGACCCTCTC
CD2	3	Forward	CACCGACAGCTGACAGGCTCGACAC
		Reverse	AAACGTGTCGAGCCTGTCAGCTGTC

Table 7.1. **CRISPR guides for CD2 gene knockout.** Forward and the corresponding reverse guide sequences were first annealed before ligation. Black sequences are the gRNA sequences whereas purple are base pairs added to allow for direct ligation of the annealed oligos into the BsmBI restriction digested plasmid.

To produce the J8-GECI-CD2WT^{High}, J8-GECI-CD2ΔINT^{High}, and J8^{TCR-}-GECI-CD2WT^{High} cell lines, J8-GECI-CD2KO or J8^{TCR-}-GECI-CD2KO cells were stably transduced with either wild-type CD2 (CD2WT) or CD2 with a cytoplasmic domain deletion leaving only 3aa of the intracellular domain (CD2ΔINT). Human codon optimised human CD2 with the endogenous signal peptide sequence (GeneArt Gene Synthesis ThermoFisher, UniProtKB P06729) was amplified using the primers given in **Table 7.2** and cloned in a

pHR backbone using BamHI and NotI restriction enzymes. Stable insertion of either CD2WT or CD2ΔINT into J8-GECI-CD2KO cells was performed as described in **Section 2.2**. J8-GECI-CD2KO cells were sorted for comparably high expression level of either $CD2WT^{High}$ or $CD2\Delta INT^{High}$ by FACS.

Primer name	Sense	Primer sequence for Gene string (5′ -3′)	Gene string
CD2WT	Forward	TAGTAGGGATCCGCCACCATGAGCTTCCCTTG	hCD2 (codon opt.)
CD2WT	Reverse	CTACTAGCGGCCGCTCAGTTGCTGCTAGGAGACAGGC	hCD2 (codon opt.)
CD2ΔINT	Forward	TAGTAGGGATCCGCCACCATGAGCTTCCCTTG	hCD2 (codon opt.)
CD2ΔINT	Reverse	CTACTAGCGGCCGCTCACTTCCGCTTGGTGATGTAGAAC	hCD2 (codon opt.)

Table 7.2. **Primer sequences for CD2 constructs.** Forward and the corresponding reverse primers for amplifying CD2WT or CD2ΔINT gene sequences from human codon optimised human CD2. Green and blue sequences indicate BamHI and NotI restriction enzyme sites, respectively. Orange sequence indicates sequence 'buffer' for restriction enzymes. Red sequence indicates stop codon.

TIRF imaging

2nd generation SLBs with null and low-density agonist pMHC (9V) were prepared as previously described in **Chapters 2-5**. CD58-Alexa 647 with no other proteins labelled. J8-GECI-LFA-1 cells were labelled with 10ng/μl anti-CD45-Alexa 555 10-minutes in RPMI (no supplements) at 37˚C. Cells were then washed x3 and resuspended in pre-warmed (37˚C) PBS + 2mM $MgS0_4$. SLBs and membrane labelled cells were incubated at 37˚C for 5-minutes prior to being allowed to settle onto the SLBs and imaged by TIRF

microscopy. GECI, anti-CD45-Alexa 555 and CD58-647 fluorescence intensity was measured every 2s for 10-20-minutes. Background intensity was removed from the CD58 signal by subtracting the z-projected average intensity of the SLB prior to adding cells to the SLB. Images were analysed using FIJI.

Calcium release experiment

Calcium release experiments were either performed on 2nd generation SLBs with low density of agonist pMHC (9V; described in **Chapter 4**) or 2nd generation SLBs without ICAM-1 but with null pMHC conditions (ΔCD54 SLB; described in **Chapter 6**). SLBs were produced as described in **Chapters 4 & 6**. SLBs and cells were washed in pre-warmed (37˚C) PBS + 2mM $MgS0_4$ and resuspended in the same. Cells were incubated a further 5-minutes at 37˚C before they gently deposited onto the SLB and GECI signal immediately imaged every 1s for 10-minutes. Videos were taken using the Zeiss LSM780 inverted confocal scanning microscope. Videos were analysed using the calcium tracking code described in **Section 2.7** and figures made in GraphPad Prism. In some cases, immediately after 10-minutes cells were imaged with brightfield and IRM to obtain contact information. Images were analysed using FIJI.

Contact imaging experiment

J8-GECI-CD2KO, J8-GECI-CD2WT^{High}, J8-GECI-CD2ΔINT^{High} and J8^{TCR-}-GECI-CD2WT^{High} cells were gently deposited onto 2nd generation SLBs without ICAM-1 (ΔCD54). CD45-Alexa-555 and CD58-Alexa-647 were used on the SLBs, whereas all other proteins were unstained. SLBs were produced as described in **Chapter 6**. Briefly, SLBs and cells were washed in pre-warmed (37˚C) PBS 2mM $MgS0_4$ and resuspended in the same. Cells were incubated for 5-minutes at 37˚C before adding to the SLB. During this period, CD58-Alexa 647 density was measured by 3x10s pFCS readings on a 40x water objective to ensure consistency across SLBs. pFCS data was analysed using FoCuS point and PyCorrfit [300], [301]. The 40x water objective was then exchanged for a 63x oil objective. Cells were added and gently deposited onto the SLB with the GECI, CD45-Alexa 555, CD58-Alexa 647, brightfield and IRM imaged every 10s for 15-minutes. This was all performed on the Zeiss LSM780 inverted confocal scanning microscope. Videos were analysed using FIJI. For quantification of CD58 contact area over time, background intensity was removed through a Z-projection average of the SLB before cells landed, CD58 signal manually thresholded using 'Otsu' approach, and area quantified using the 'analyse particles' feature of FIJI.

7.3 Results

7.3.1 Ca^{2+} signals on null pMHC is dependent on adhesion and the TCR

Calcium release in J8-GECI-LFA-1 cells correlated with the presence of microvillar CCZs in the absence of any agonist pMHC (**Chapter 5**). The fraction of cells that showed calcium release was ~20%. This may represent the basal amount of ligand-independent TCR triggering based on the size of CD58-CD2 engagement zones of cells interacting with 2nd generation SLBs presenting null pMHC. To begin to address the relationship between CCZ contact size and TCR triggering, this effect was first confirmed to be TCR-dependent. J8-GECI-LFA-1 (TCR^+) and $J8^{TCR-}$-GECI-LFA-1 (TCR^-) cells were examined on 2nd generation SLBs under null pMHC conditions. Consistent with the findings of **Chapter 4**, 20% of cells showed calcium release with the TCR^+ cells. No signaling was seen in the absence of the TCR, however (**Figure 7.1A**). To ensure that cells still adhered to the surface to the same degree the amount of displacement and time for 50% of cells to adhere was analysed (**Figure 7.1B**). No differences were found between TCR^+ and TCR^- cells in either metric. Lastly, after the 10-minute calcium release analysis, cells were immediately imaged using brightfield and IRM, which gives a more direct indicator of cell attachment and spreading. The median IRM contact area was similar with TCR^+ and TCR^- cells, i.e. 3 and 1.9μm^2, respectively (**Figure 7.1C**). However, there was a distinct population of TCR^+ cells that formed much larger contacts, indicative of cells spreading after signaling. This was identified by taking the TCR^+ cells with contact areas above the 95th percentile of TCR^- cells. The fraction of cells above this threshold was ~20%,

consistent with the number of cells that showed calcium responses. When removing the large-contact population from the TCR$^+$ cells, the median became near identical between TCR$^+$ and TCR$^-$ cells (both ~1.9µm^2; **Figure 7.1C**). Overall, this confirmed that both TCR$^+$ and TCR$^-$ cells adhered to the surface to a similar degree, but only TCR$^+$ cells showed calcium release and spreading, confirming TCR dependency on adhesion-dependent signaling in null pMHC conditions.

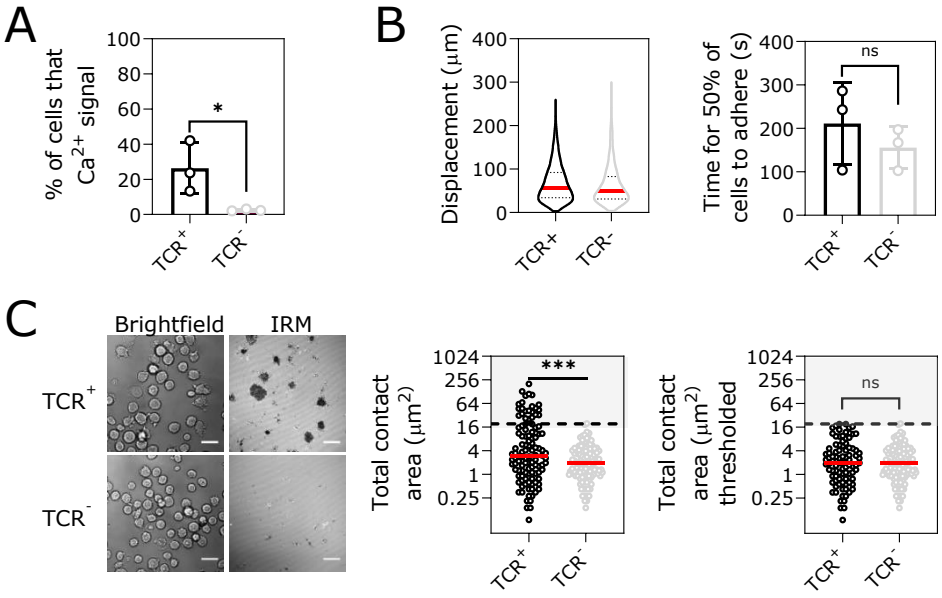

Figure 7.1. **Signaling on null pMHC is dependent on the TCR.** J8-GECI-LFA-1 (TCR$^+$) and J8^{TCR-}-GECI-LFA-1 (TCR$^-$) were gently deposited onto 2nd generation SLBs with null pMHC. (A) percentage of cells showing calcium release over a 10-minute video. Data shows N=3 independent SLBs per condition (n=200-500 cells). (B) Left plot: displacement of TCR$^+$ and TCR$^-$ cells. Median shown in red. Right plot: time for 50% of cells to settle/adhere to the surface. (C) Brightfield and IRM images taken immediately after the 10-minute video. Middle plot: quantification of IRM dark patch area per cell. This indicates where cells have adhered to the surface. Red line is the median. Black dashed line indicates the 95th percentile of IRM area for TCR$^-$ cells (~19µm^2). Values above this are taken to be cells that have activated and spread out. Right plot: same as middle plot but thresholded to remove TCR$^+$ cells above black dashed line. The median values are now the same for TCR$^+$ and TCR$^-$ cells. Data shown is all cells pooled from N=3 independent SLBs (n=114-121 cells total). Values above this in TCR$^+$ cells are likely those that have shown calcium response. (A-C) Cell lines were tested using Student's t-test. *** = $p < 0.001$, *= $p < 0.05$, ns = not significant = $p > 0.05$.

7.3.2 CD45 on T cells is excluded from areas of CD58 accumulation on the SLB

One explanation for how TCR triggering could occur at areas of CD58-CD2 engagement on null pMHC, is that it leads to the exclusion of CD45 on the T-cell surface [201]. CD45 exclusion will disrupt the kinase/phosphatase balance, in favour of the former within CCZs, with ligand-independent TCR triggering occurring in a manner dependent on CCZ diameter [124], [201], [203]. To test this, cell surface CD45 distribution was imaged at CD58/CD2 CCZs. J8-GECI-LFA-1 cells were labelled with anti-CD45-Alexa 555 (Gap8.3 antibody) and allowed to settle onto 2nd generation SLBs with Alexa 647 labelled CD58. Antibody was chosen because at 37˚C the Gap8.3 Fab K_{off} was too fast (not shown), leading to staining of CD45 on the SLB. Upon imaging of cells on null pMHC, areas of CD58 accumulation could be seen. These areas colocalised with areas of decreased Gap8.3 fluorescence intensity, indicating CD45 exclusion (**Figure 7.2**). In the example shown, the cell underwent calcium release with more clear areas of CD45 exclusion on the cell (**Figure 7.2**). As signaling was dependent on the TCR being present this means that CD45 exclusion and CD58/CD2 accumulation correlated with TCR triggering in the absence of ligand.

The same experiment was also performed on low densities of agonist pMHC (9V, 1-5/μm^2). Cells were imaged from when they first settled and started to exclude CD45 on the cell from areas of CD58 accumulation, as seen by intensity line profiles (**Figure 7.3A**). As this contact was observed 12 to 8s before calcium release, and the same contact persisted for at least 14s after calcium release, the exclusion of CD45 on the cell was likely

stable[2]. Examined at a much later time point after calcium release (186-192s) the cell had fully spread (indicative of productive signaling) and more clear areas of CD45 exclusion could be seen (**Figure 7.3B**). At the centre of the cell, areas of CD58 accumulation appeared larger, and this coincided with larger areas of CD45 exclusion (yellow inset). In the peripheral contact CD58 accumulation/CD45 exclusion was also seen, but to a lesser extent (green inset). Overall, these results indicate that CD45 is excluded from constrained zones of CD58-CD2 engagement, with the important finding that this can occur before TCR triggering.

[2] Exclusion was seen 12-8s before calcium release. The reason a range was given was because images were average z-projections across that period to increase signal/noise. Short time periods were chosen to reduce blur

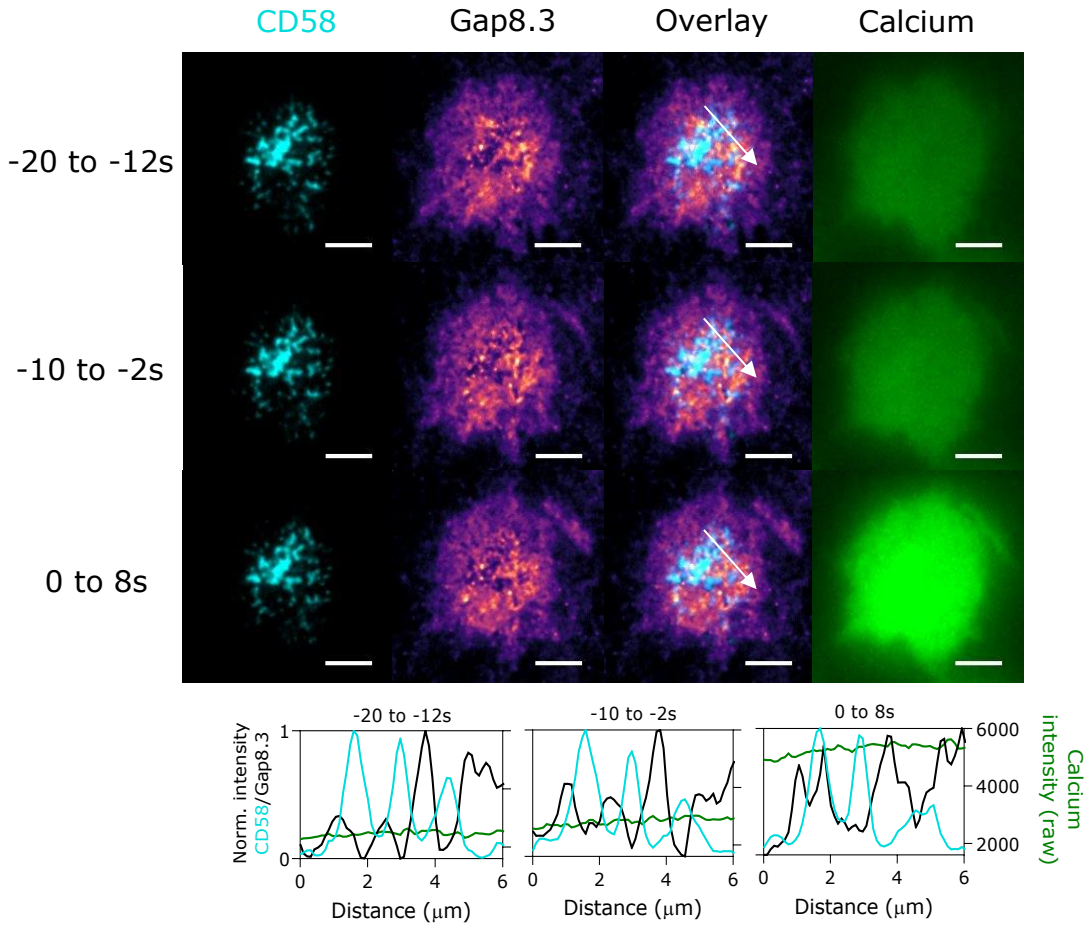

Figure 7.2. **Calcium release correlates with CD45 exclusion on the cell surface (null pMHC)**. J8-GECI-LFA-1 cells were labelled with Gap8.3 antibody-Alexa-555 (to detect CD45) and allowed to settle on 2nd generation SLBs with null pMHC and CD58 labelled with Alexa 647. The images here were of a cell taken ~10-minutes after dropping cells on the surface. (A) Z-projections (average) pooled from -20 to -12s, and -10 to -2s before calcium release, and 0-8s after calcium release. The plots at the bottom are line intensity profiles for mix/max normalised CD58 and Gap8.3 fluorescence intensity (left y-axis) along and in the direction of the white arrow shown in the overlay column. On the same plots the raw calcium intensity is shown (right y-axis) showing calcium release in the right most plot. In most cases CD58 anticorrelates with Gap8.3 signal. This shows that CD45 exclusion from CCZs (shown by CD58 accumulation) correlates with cell signaling.

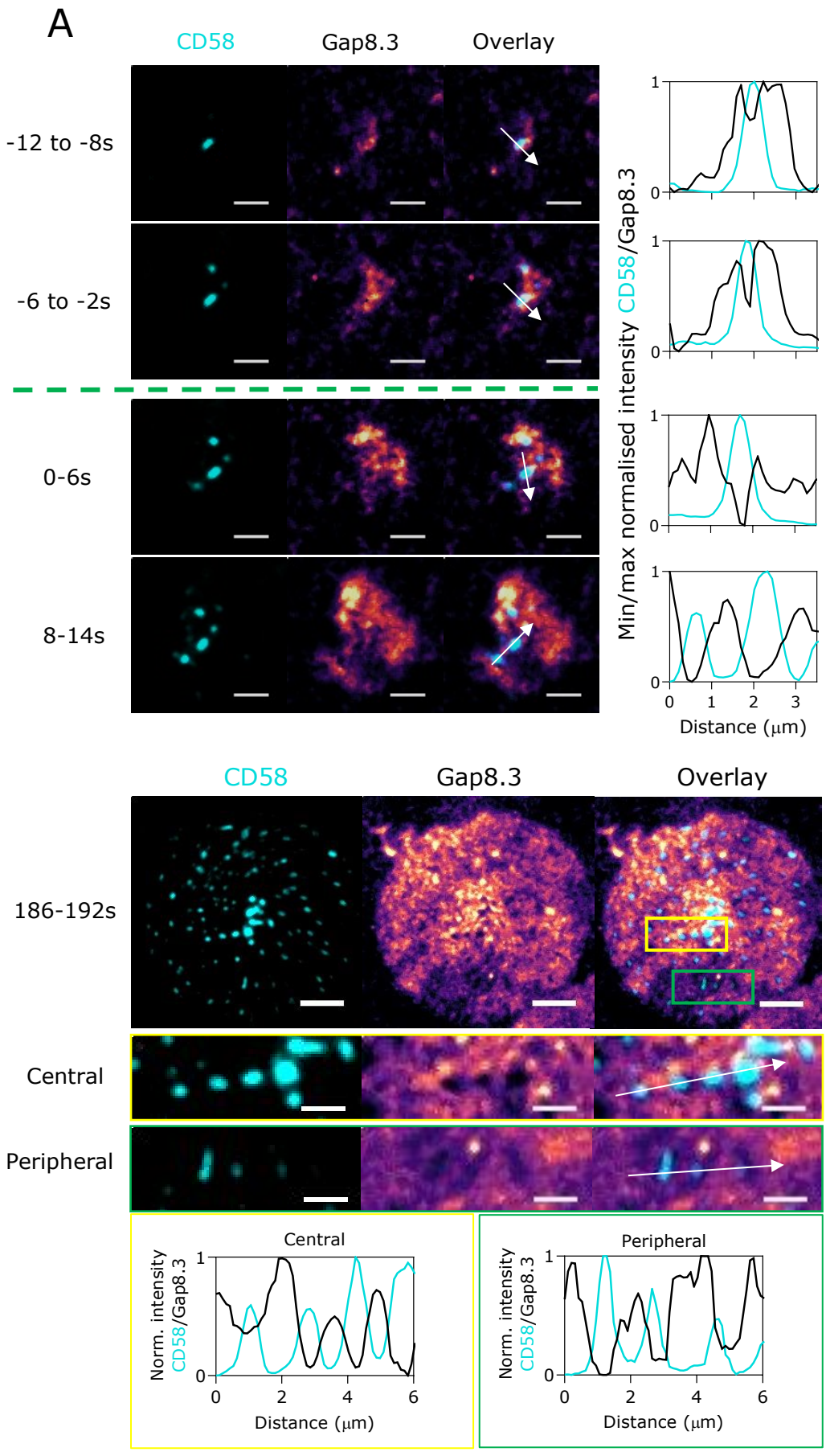
A
CD58
Gap8.3
Overlay
-12 to -8s
-6 to -2s
0-6s
8-14s
Min/max normalised intensity CD58/Gap8.3
Distance (μm)
186-192s
Central
Peripheral
Norm. intensity CD58/Gap8.3
Distance (μm)

Figure 7.3. **Calcium release correlates with CD45 exclusion on the cell surface (low density agonist pMHC)**. J8-GECI-LFA-1 cells were labelled with Gap8.3 antibody-Alexa-555 and gently deposited onto 2nd generation SLBs with low densities of agonist pMHC (9V, 1-5/μm^2) and CD58 labelled with Alexa 647. (A) Z-projections (average) pooled from -12 to -8s, and -6 to -2s before calcium release, and 0-6s and 8-14s after calcium release (separated by the green-dashed line). Z-projections were used to increase signal/noise. Plots to the right indicate line intensity profiles along and in direction of white arrow in overlay for that row. Segregation of CD45 on the J8s can be seen even from -12 to -8s. Line profiles only indicate segregation qualitatively but do not indicate the extent (manually quantified this ranged from ~10-30% decrease from other areas of Gap8.3 intensity). (B) Exclusion of CD45 at later stage synapses. Insets below indicate central (yellow box) or peripheral (green box) microvillar contacts/CD58 accumulation spots. Gap8.3/CD45 exclusion zones can be seen in both the centre and periphery of the contact interface, although visibly to a lesser extent in the periphery.

7.3.3 Large CD2-mediated CCZs increase the probability of TCR triggering in the absence of ligands

The CD45/Lck ratio is a key consideration for the quantitative model of signaling proposed by Fernandes et al. (2019). It was previously tested by expressing small amounts of truncated/short CD45 into T cells, which resulted in longer times to calcium release when using the non-signaling adhesion pair to induce ligand independent TCR triggering [124]. There are two factors to consider for how the TCR could signal in the context of more physiological CD58-CD2 mediated adhesion. The first is that CD58-CD2 engagement creates CCZs that lead to the exclusion of CD45 on T cells. This was previously shown for areas of CD58/small adhesion protein accumulation on SLBs [116], [124], [141]. The second is that the intracellular domain of CD2 may recruit kinases such as Lck and Fyn, with a later study showing a preference for Y505 de-phosphorylated Lck (open conformation Lck) relative to other states of Lck, thus increasing the pool of primed Lck within CCZs [92], [140], [141], [173]**.** Recruitment may occur via the SH3 domain of Lck to the proline rich segments of CD2 [173]. The proposal of Fernandes et al. (2019) can be tested in the more physiological setting of 2nd generation bilayers by forming large CD2-mediated CCZs in the presence and absence of the intracellular domain of CD2. It would be predicted that both result in calcium responses, based on CD45 exclusion, with additional and/or quicker signaling occurring in the presence of the intracellular domain potentially as a result of additional kinase recruitment i.e. increasing the Lck component of the CD45/Lck ratio.

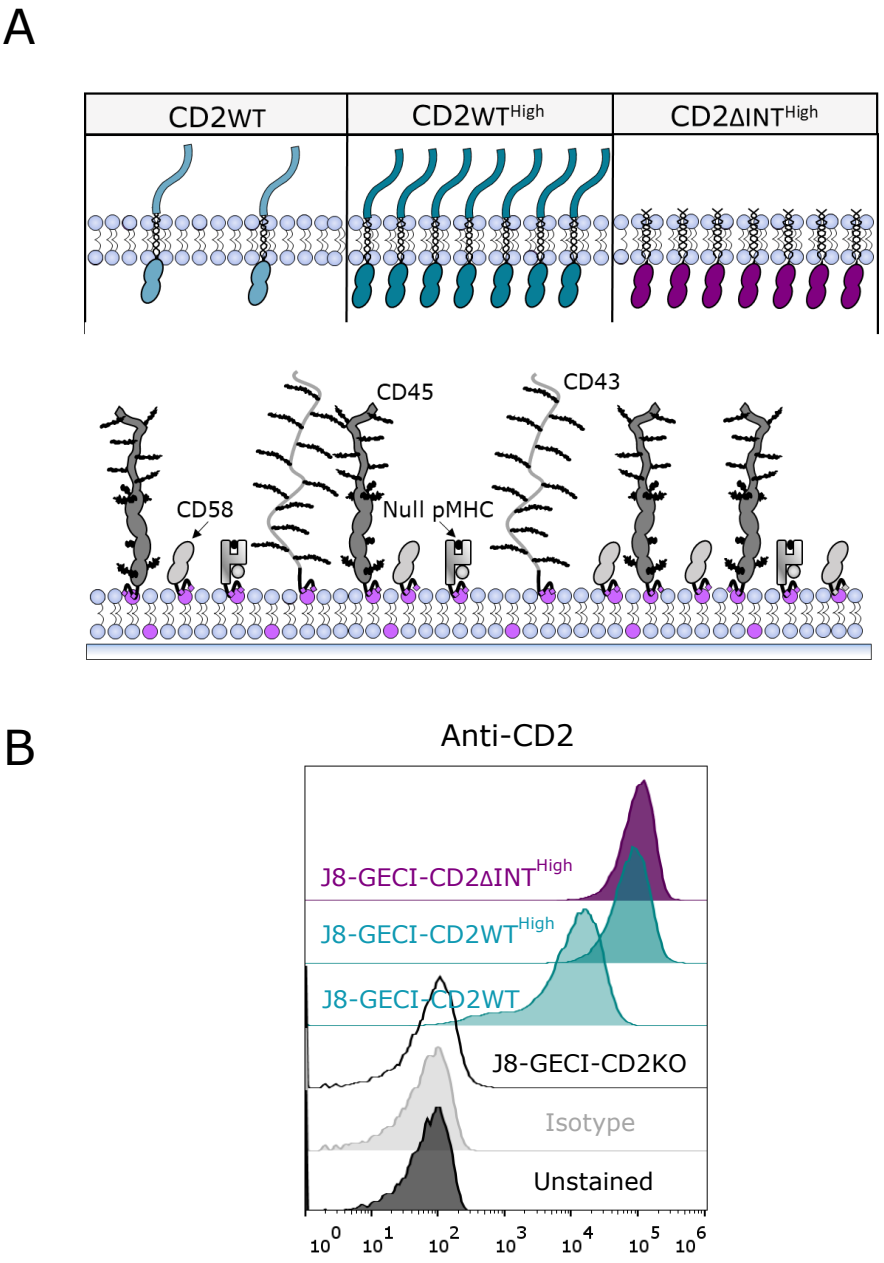

Figure 7.4. **Variant CD2 cell lines for altering contact size.** (A) Cartoon representation of the cell lines and experimental setup for the experiment. The SLB contained CD58, CD45, CD43 and null pMHC. ICAM-1 was not included to only address the adhesive role of CD58-CD2. (B) Flow diagrams showing J8-GECI-CD2KO cell line and introduction of the variant CD2 constructs at endogenous (CD2WT) or high expression (CD2WT^{High} and CD2ΔINT^{High}).

One approach to creating large CD2-mediated CCZs (and therefore areas of CD45 segregation) is to overexpress the adhesion protein. CD2 was first stably knocked out in J8-GECI cells using CRISPR-Cas9. Wild-type CD2 and CD2 with a truncated intracellular domain (i.e. only 3aa after the transmembrane region), were stably inserted and sorted for comparably high expression. These cell lines are referred to as CD2WT^{High} and CD2ΔINT^{High}, respectively (**Figure 7.4A&B**). Wild-type CD2 was also sorted to endogenous levels to ensure consistency when comparing cell lines (referred to as CD2WT). To address only the role of large CD2-mediated contacts on TCR triggering, 2nd generation SLBs with no ICAM-1 and only null pMHC conditions were tested (**Figure 7.4A**). The size of CCZs now made by each cell line was observed by using CD45 (on the SLB) labelled with Alexa-555 and CD58 labelled with Alexa-647. To obtain larger numbers of cells for more robust statistics scanning confocal microscopy with a lower magnification (63x) was used. Visibly, cells formed small, distinct areas of CD58 accumulation with CD2WT (**Figure 7.5**). As expected, CD2WT^{High} and CD2ΔINT^{High} cells formed larger areas of CD58 accumulation (**Figure 7.5**). In these cases, the CCZs grew to be ~3x larger in diameter on average across multiple cells than CD2WT (**Figure 7.6A**). Of note is that larger contacts did appear less circular, and therefore the contact size comparison only provides is a general idea of CCZ size rather than absolute difference. CD2WT^{High} and CD2ΔINT^{High} formed CCZs of comparable size indicating that contact formation was mediated by the extracellular domain only, as previously shown (**Figure 7.6A&B;** [140], [141]). Overall, this experiment indicated that higher expression of CD2 led to an increase in the size of CCZs.

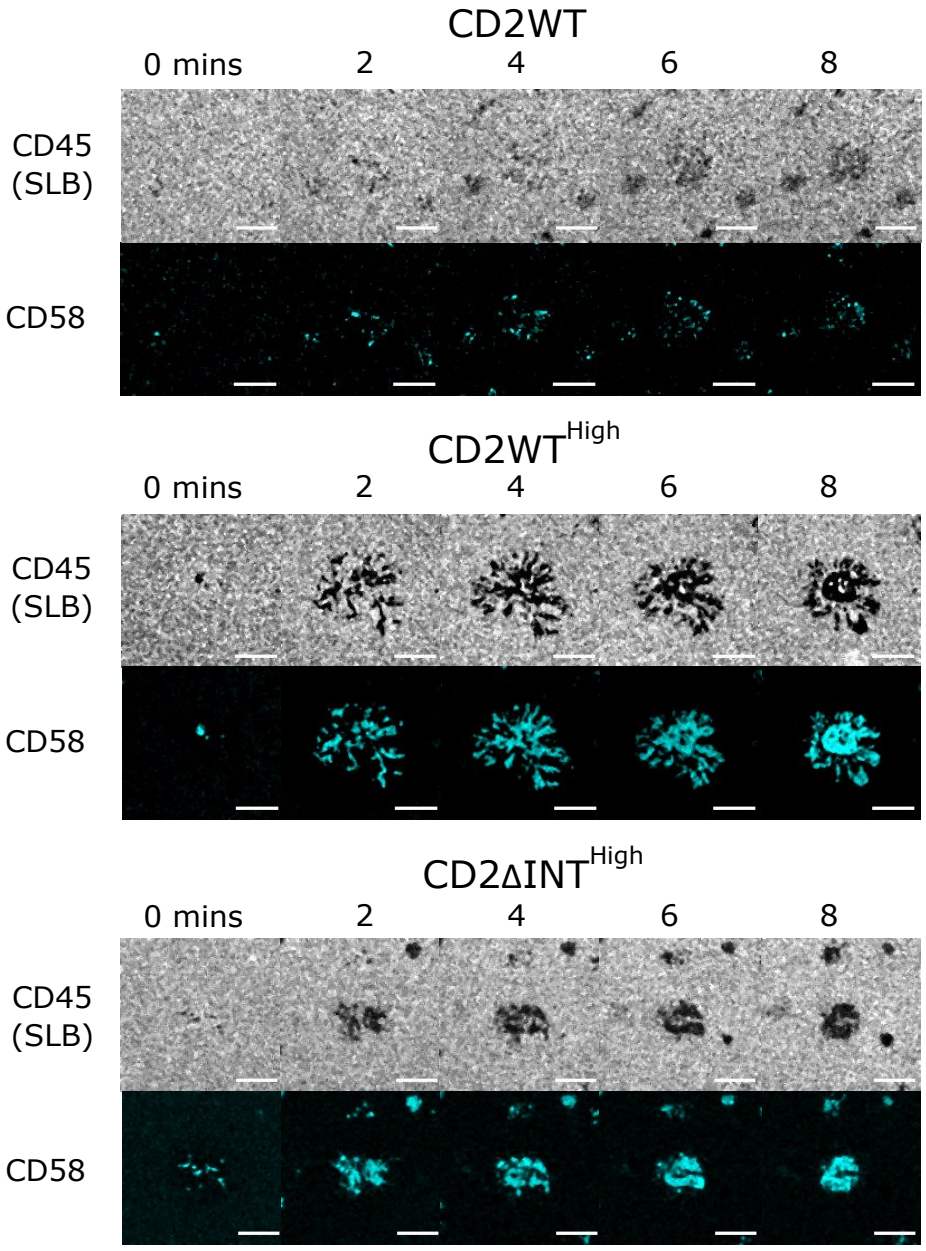

Figure 7.5. **CD2 expression alters close contact zone size (1)**. The indicated cells were allowed to settle on 2nd generation SLBs (ΔCD54) with null pMHC only. CD45-Alexa 555 (shown in grey) and CD58-Alexa 647 (shown in cyan) were used to view contacts. Scale bar is 5μm.

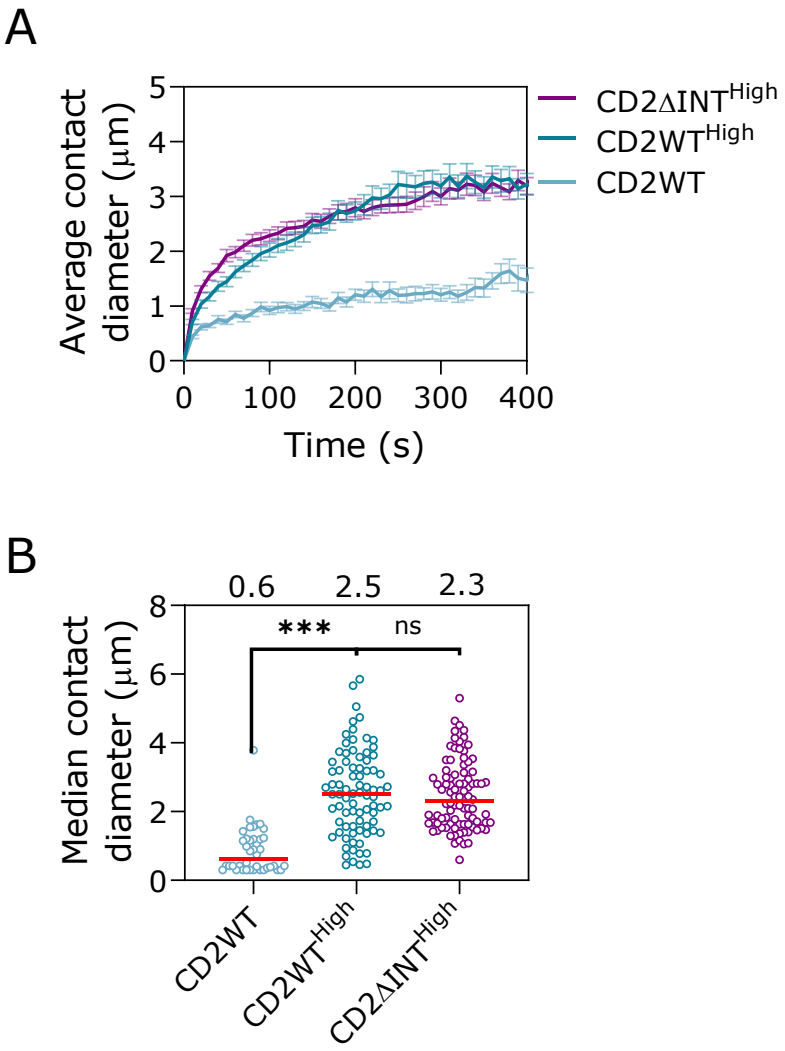

Figure 7.6. **CD2 expression alters close contact zone size (2).** Quantification of CD58-CD2 CCZs taken from the experiment in Figure 7.5. CD58 accumulation area was analysed using the contact analysis code in **Section 2.7**. (A) Average (± s.e.m.) contact diameter (μm) of cells over time. Lines represent the average across 42-90 cells taken from 3 independent SLBs for each cell line. Cells were aligned so that the 10s time point represents when CD58 accumulation first occurred. (B) Median CD58-CD2 CCZ diameter across the entire time tracking each cell. This metric was chosen as ~50% of values lie above and below it, thus providing a measurement of how big the CCZs are for at least half the time spent adhered to the SLB. Values above the graph represent the median of all data points (red line). Planned comparisons (CD2WT vs. $CD2WT^{High}$ and $CD2WT^{High}$ vs. $CD2\Delta INT^{High}$) were tested using Welch's t-test. ***= $p < 0.001$, ns = not significant = $p > 0.05$.

To relate these findings to TCR triggering, calcium release was analysed across hundreds of cells. CD2WT and CD2WT^{High} were found significantly different (20% vs. 70%, p=< 0.001, **Figure 7.7A**). CD2WT^{High} and CD2ΔINT^{High} were also found significantly different (70% vs. 40%, p=< 0.001, **Figure 7.7A**). The median time for 50% of cells to show calcium release was also analysed (**Figure 7.7B**). This was significantly different between CD2WT and CD2WT^{High} (~1200s vs. 150s, p=0.0467) and between CD2WT^{High} and CD2ΔINT^{High} (p=0.0023, **Figure 7.7B**). The differences between CD2WT and CD2WT^{High} could be a result of altered capacity to adhere to the surface (as opposed to their CCZ size), however, this was not significantly different (p= 0.2204; **Figure 7.7C&D**). When analysing only the cells that adhered/settled on the SLB, the probability of signaling showed dependence on time adhered, and the increase in probability was higher for CD2WT^{High} than CD2WT indicating that the difference in contact size was likely responsible for the difference in calcium release kinetics (**Figure 7.7E**). No significant difference in adherence occurred between CD2WT^{High} and CD2ΔINT^{High} (p=0.1087), indicating response kinetics were a result of CD2's intracellular domain, possibly through kinase recruitment (**Figure 7.7C&D**). This likely explains the weaker relationship between time adhered and probability of signaling for CD2ΔINT^{High} compared to CD2WT^{High} (**Figure 7.7E**).

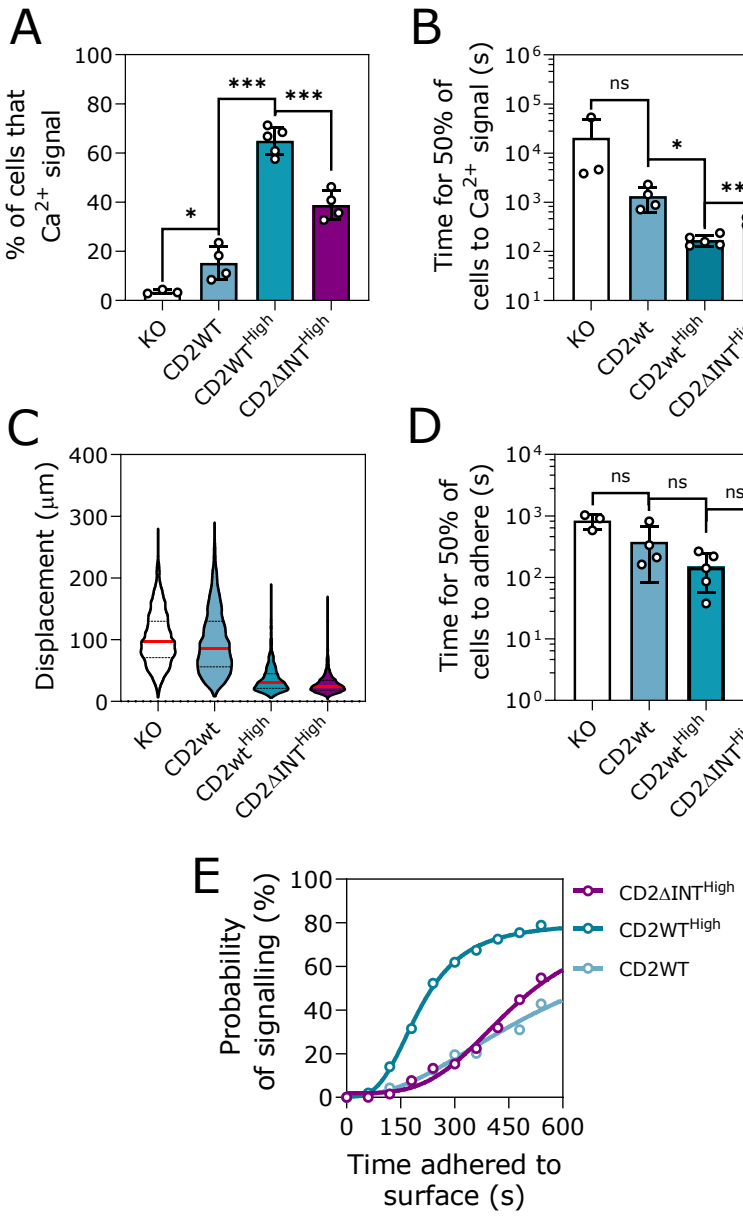

Figure 7.7. **Ligand independent TCR triggering positively correlates with CD2 expression.** Variant CD2 cell lines were gently deposited onto 2nd generation SLBs with null pMHC (and no CD54) and recorded for calcium release. (A) Percentage of cells showing calcium release over a 10-minute video. Planned comparisons (CD2KO vs. CD2WT, CD2WT vs. CD2WT^{High}, and CD2WT^{High} vs. CD2ΔINT^{High}) were testing using Student's t-test. ***= $p < 0.001$, * =$p<0.05$. (B) The median time taken for 50% of cells to show calcium release. (C) Representative violin plots for the displacement of cells. (D) Median time taken for 50% of cells to adhere to the surface. (B&D) Planned comparisons (CD2KO vs. CD2WT, CD2WT vs. CD2WT^{High}, and CD2WT^{High} vs. CD2ΔINT^{High}) were tested using Welch's unpaired t-test. ***= $p < 0.001$, **=$p <0.01$, * =$p<0.05$. (A, B,&D) N= 3-5 independent SLBs (n=200-500 cells). (E) Relation between the time adhered to the surface and the likelihood of signaling. For each cell line, all cells were pooled into 30s bins for time adhered to surface. The percentage of responding cells was then calculated for each bin. Data represents >600 cells pooled from across 3-5 independent SLBs per cell line tested.

Although controversial, CD2 engagement could induce calcium release de novo [372]–[374] To rule TCR-independent CD2-mediated signaling in or out, calcium release was tested for dependency on TCR in the CD2WT^{High} cell line when forming large CD58-CD2 mediated CCZs. J8^{TCR-}-GECI cells were transduced with wild-type CD2 and sorted to comparable levels as CD2WT^{High} (**Figure 7.8A**). With no TCR, no calcium release was seen (**Figure 7.8B**). The rate of adhesion to the surface, and metrics associated with CCZ formation over time remained comparable between the TCR^{+} and TCR^{-} cell line, indicating that the presence of the TCR was the necessary component to induce calcium release (**Figure 7.8B&C**).

Lastly, the ability to alter contact sizes was used to show that size constrained microvillar contacts ensure discriminatory signaling (**Figure 7.9**). CD2WT vs. CD2WT^{High} cells gently deposited onto 2nd generation SLBs on either null pMHC or medium density agonist pMHC (9V, 10-30/μm^2) conditions. CD2WT, which forms size-constrained contacts, showed a large increase in the proportion of signaling cells with the addition of agonist pMHC (20% to 80% responding cells, p=<0.001). In contrast, CD2WT^{High}, which forms ~3-4x larger contacts on average, showed no significant difference between null pMHC or agonist pMHC conditions (both 75-80% responding cells, p=0.2759). Clearly, CD58-CD2 mediated CCZs must be constrained in size to ensure discriminatory signaling.

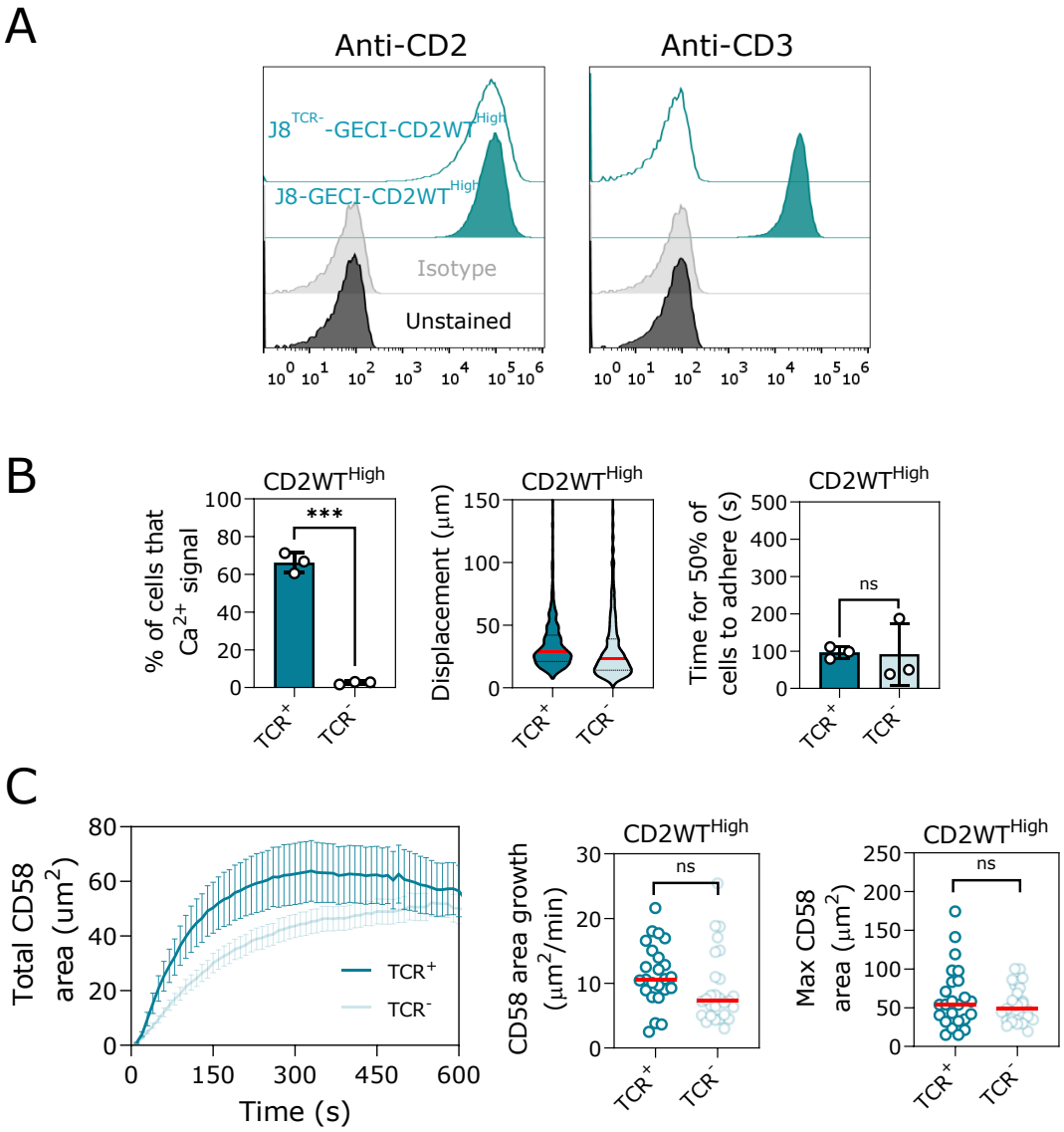

Figure 7.8. **Ligand independent signaling through CD2 is TCR dependent.** (A) Flow cytometry plots showing comparably high expression of CD2 (left plot) or lack of CD3 (right plot) in the J8^{TCR-}GECI (TCR^{-}) cell line compared to J8-GECI (TCR^{+}). (B&C) Both TCR^{+} and TCR^{-} cell lines were gently deposited onto 2nd generation SLBs (ΔCD54) with null pMHC only. CD45 and CD58 were labelled with Alexa 55 and Alexa 647, respectively. (B) Calcium release assay. Percentage of cells showing calcium release (left plot), displacement (middle plot) and time for 50% of cells to adhere (right plot). Per cell line, N=3 independent SLBs (n=200-500 cells). (C) Using the same experimental setup as **Figure 7.5**, the total area (left plot), growth rate (middle plot) and maximum CD58 accumulation area were quantified. Data shows 24-27 cells taken from 2-independent SLBs per cell line. (B&C) Cell lines were tested using Student's t-test. ***= $p < 0.001$, ns = not significant = $p > 0.05$.

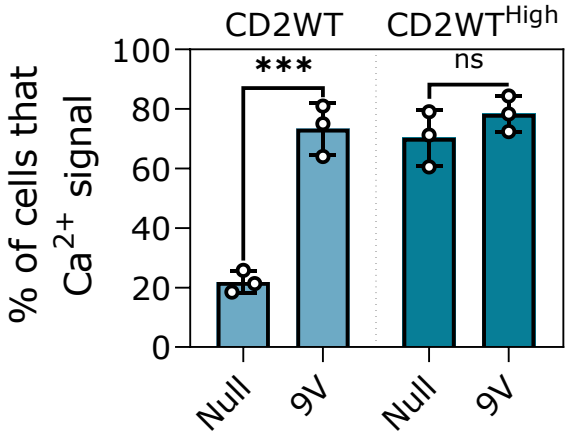

Figure 7.9. **Size constrained CD58-CD2 mediated CCZs are essential for discriminatory signaling.** J8-GECI-CD2WT or J8-GECI-CD2WT^{High} cells gently deposited onto 2nd generation SLBs (with no ICAM-1) containing either just null pMHC or agonist pMHC at 10-30 molecules/μm^2. Shown is the percentage of cells responding within a 10-minute video. CD2WT Null and 9V and CD2WT^{High} Null and 9V were tested using Student's t-test. ***= $p < 0.001$, ns = not significant = $p > 0.05$.

7.4 Discussion

The results presented in this chapter builds upon the data in **Chapters 5 & 6**. It shows that the mechanism of TCR triggering and antigen discrimination is linked to size constrained, CD58-CD2-mediated CCZs formed when the tips of microvilli first contact the 2nd generation SLB to scan for antigen. These results validate key predictions of the KS model [124], [203]. For example, CD45 on the cell surface was observed segregating from CD58-CD2 CCZs in the presence and absence of agonist pMHC, and in both cases occurred prior to calcium release (a proxy for TCR triggering). The probability of TCR triggering could be increased by boosting the expression of CD2, which increased the CCZ diameter, and by inference the diameter of CD45 segregation zones. The CD45/Lck

ratio was further modified by removing the cytoplasmic domain of CD2, likely reducing kinase recruitment to CCZs, resulting in an overall reduction in TCR triggering probability within a given time period. Lastly, to link these results and the previous chapters together, size-constrained microvillar CCZs were necessary for discriminatory signaling.

7.4.1 CD45 segregation from CD58-CD2-mediated CCZs

Although CD45 is easily observed to exclude passively from the 2D SLB, it is substantially more difficult to view on the 3D T-cell membrane using TIRFM. In order to view CD45 exclusion on the T-cell surface at initial microvillar CCZs (prior to calcium release) the average fluorescence signal had to be taken by combining the images of several time points, providing a slow temporal resolution of 8s. CD45 exclusion could not be observed when taking the raw images at 2s intervals. However, given CD45 does exclude on the SLB (and CD58 accumulates in these areas of exclusion) it can be surmised that CD45 is excluding on the T-cell surface, despite the difficulties of imaging at this time scale.

As contacts are dynamic, the size and extent of CD45 exclusion may be distorted by averaging over large timescales. It may be beneficial to increase the frequency of images (i.e. every 0.25s) and average these across 1s intervals to provide better temporal resolution, although this runs the risk of bleaching samples. Difficulties in viewing CD45 segregation may be because the TIRFM excitation field extends 100-200nm causing

excitation of CD45 molecules along the z-plane of the MV, reducing the overall appearance of exclusion at microvillar tips. Although more recent advances in super resolution imaging could overcome this, particularly techniques that have improved resolution in the axial plane to below 200nm, they require fixed cells and thus functional readouts of activation cannot be concurrently performed alongside studies of nanoscale protein reorganisation [123], [126]. At the very least, the data here shows that CD45 segregation can be observed before productive antigen recognition (given by calcium release), however, no conclusions can be made about the extent. Quantifying the extent is important as it provides a parameter that can feed into mathematical models. Such models are essential for providing mechanistic understanding of TCR triggering and antigen discrimination [124].

Given the difficulty of observing CD45 exclusion at initial microvillar contacts, even in the presence of CD58, which likely enhances segregation, it seems unlikely that exclusion would be seen with 1st generation SLBs using low densities of agonist pMHC or null pMHC. In accordance, CD45 exclusion from areas of TCR signal was not observed on ICAM-1 only SLBs, even once the cell had settled across the surface [230]. In contrast, CD45 exclusion will likely be seen from high densities of pMHC on 1st generation SLBs, albeit less than if CD58 was also present, as this causes strong signaling leading cells to spread across the surface resulting in shortened microvilli (~50nm in length), and because it enhances CD45 segregation through artificially stabilising microvillar contacts via the TCR acting as an adhesion molecule [122].

7.4.2 Phosphatase exclusion can explain TCR triggering at CD58-CD2-mediated CCZs

Decreasing CD45 density (and therefore the CD45/Lck ratio) from large areas of CD2 engagement on the T-cell surface can lead to TCR triggering [116], [124]. This was confirmed by cells forming large CCZs through overexpression of a mutant CD2 lacking the intracellular domain, as described in this chapter. However, increased CCZ size was only correlated with increased TCR triggering across experiments. To provide a direct relationship between CCZ size and TCR triggering, cells need to be monitored for calcium release, CD58 accumulation and CD45 exclusion (on the cell) concurrently. Using the natural variation among cells, the probability of triggering from the average size of contacts of individual cells could be used to directly relate the size of CCZs to the probability of TCR triggering. This could be done for both CD2WT and CD2ΔINT cell lines. Due to time constraints, CD2ΔINT at wildtype expression levels of CD2 was not established but would be useful to compare to the CD2ΔINT^{High} cell line to show the effect of altered contact size alone on TCR triggering. It is likely that minimal TCR triggering will occur with CD2ΔINT, although this remains to be seen.

Chapter 8 General discussion

How T cells scan the APC membrane for antigen, and how the TCR discriminates foreign antigen from self are key questions for immunologists. Although the relevant molecular components involved in activation, and how they reorganise during this process, are well established, the events that occur in initial contacts, where antigen is first detected and discrimination occurs, remain poorly characterised. Recently, dynamic, actin-rich membrane structures referred to as microvilli, have been posited as membrane platforms for efficient scanning of antigen and even antigen discrimination [122], [124]. However, neither of these putative functions of T-cell microvilli have been explicitly and/or empirically tested. It is also not known how key surface molecules are organised relative to microvillar contacts, especially prior to antigen recognition. The current glass and SLB systems for studying T-cell contacts are less than ideal to address this. The results of this thesis introduce a novel cell line and more physiological SLB system to visualise the key molecular events that occur at microvillar contacts. The system is also used to test the functional importance of microvillar contacts in antigen detection and discrimination.

8.1 A new model system to study T-cell biology

1st generation SLBs (pMHC and ICAM-1) are a powerful tool to study the spatiotemporal organisation of proteins at the T-cell surface, particularly during synapse formation. However, as discussed in **Section 1.5.3**, a novel SLB system with increased complexity

was required for more faithfully studying the early events in T cell contact with APCs. In **Chapter 3**, alongside the J8 cell line, 2nd generation SLBs were established and optimised to create a better model surface to study T cells. This system newly incorporated the APC glycocalyx and small adhesion molecule CD58. The physiological relevance of the 2nd generation SLB (pMHC, ICAM-1, CD58, CD43 and CD45) was exemplified throughout this thesis by its ability to build upon key findings obtained previously in purely cellular settings. Examples are discussed below.

(1) As presented in **Chapter 4**, cells were substantially more mobile and less adhesive to 2nd generation SLBs when compared to 1st generation SLBs. This provides additional support for the anti-adhesive, cell-repulsing effects of the glycocoalyx, indicated from previous cell conjugation experiments [291], [293], [294], [375].

(2) In the last sections of **Chapter 5**, the importance of T-cell membrane topology in efficient antigen scanning was established. T-cell microvilli require the dynamic growth and restructuring of actin filaments to efficiently scan for antigen as their loss or 'stabilisation' using actin-modifying drugs (LatB, CytoD and Jasplak) significantly reduced the proportion of cells that detected antigen in the presence of a glycocalyx. In contrast, most cells (~80%) responded in the absence of the SLB glycocalyx, supporting loss of dynamic morphological structures as the explanation for reduced signaling. This result is consistent with a previous report analysing calcium responses in human primary $CD4^+$ memory T cells treated with latrunculin A and dropped onto a monolayer of antigen-pulsed endothelial cells [121]. The drug-treated cells failed to show calcium responses when contacting endothelial cells but were still able to respond to anti-CD3/CD28 (albeit more weakly). Sage et al. (2012) speculated that drug-induced loss of

invadosome-like protrusions (ILPs; similar to microvilli, see **Section 1.3.2**) was responsible. The results described in **Chapter 5** validate this speculation and build upon this by showing that the glycocalyx elements were responsible for a lack of signaling when membrane topology is lost.

(3) By altering the adhesion-repulsion balance of 2nd generation SLBs in **Chapter 6**, a near-complete loss of adhesion and T-cell activation occurred upon the combined removal of CD58 and ICAM-1 from 2nd generation SLBs, even when a moderate density of agonist pMHC (9V) was presented. This is consistent with previous reports showing minimal conjugation and activation of T cells when they interact with antigen-pulsed target cells in the absence of CD2 or LFA-1 (or their ligands; [142], [361], [371], [376]. Furthermore, the cooperative loss of activation from removing both CD58 and ICAM-1 from the SLBs in **Chapter 6** was previously observed using murine T cells, where CD2 and LFA-1 were shown to have additive/cooperative effects, albeit on later markers of activation (e.g. T-cell proliferation measured via thymidine uptake) i.e. 3-10-fold reduction in activation with a loss of CD2, ~10-fold for a loss of LFA-1, and ~100-fold for the loss of both CD2 and LFA-1 [142]. Loss of adhesion, rather than costimulation, was evoked to explain the loss of activation, due to a reduction in conjugation. This is mirrored by the results of **Chapter 6**.

8.2 Three phases to contact on second generation SLBs

As first mentioned in **Chapter 5**, the sequence of events that occur as T cells interact with 2nd generation SLBs is best described in three key phases of contact. Phase 1 is when T cells are mobile and probe the surface using small and distinct regions of membrane. Phase 2 is when cells have settled or adhered to the surface and it is at this point when microvillar CCZs are first typically seen. During this phase additional CCZs are formed at a slow rate. Phase 3 is for cells that exhibit a Ca^{2+} signal, resulting in cell spreading and an increased rate of CCZ formation. The events observed in **Chapters 4-7** of thesis are discussed in the context of these three phases.

8.2.1 Phase 1: mobile cells use microvilli to probe their environment

By labelling the cell membrane, the J8-GECI-LFA-1 cell line moving over 2nd generation SLBs were observed interacting with the surface with small (~0.5μm in diameter) and distinct membrane regions. Similar structures and have previously been noted with Jurkats and human primary $CD4^+$ T cells interacting with pMHC or antibody-coated glass by using IRM and/or by TIRFM of the fluorescently labelled cell membrane [90], [125], [263], [266], [339], [377]. As the J8-GECI-LFA-1 cells clearly exhibited L-selectin enriched membrane protrusions (**Chapter 5**), and given their size, these were likely microvilli probing the surface. The word probing is used here as these microvillar contacts showed oscillatory behaviour, moving in and out of the TIRFM field. As this

occurred while cells were mobile (shown in **Chapter 4**), and rarely coincided with 'holes' in the glycocalyx layer of the SLB (indicative of microvillar CCZs, shown in **Chapter 5**) these are unlikely to be stable or signaling-influenced sites of membrane contact. That these microvillar probes disappear from the field of view may reflect recent findings using advanced 3D super resolution imaging techniques (i.e. LLSM) that they can spontaneously reabsorb and project from the membrane [122]. It would be interesting to quantify the 'dwell-time' of the membrane puncta within the TIRF field as it may provide an alternative means to parametrise microvilli remodelling rates, rather than using more-challenging live 3D-imaging and data analysis techniques [122]. This system could conceivably be used to test whether cells 'sense' the stiffness of their surface, represented by changes in the dwell-time. Altering stiffness could be achieved by changing glycocalyx composition, or by creating SLBs on stiffness-tuneable surfaces such as PDMS.

8.2.2 Phase 2: microvillar contacts are stabilised by CD2 and LFA-1

The next phase of contact is characterised by adherence to the surface, coinciding with the appearance of small (~0.5μm in diameter), distinct and more stable 'holes' in the homogeneous glycocalyx layer on the SLB. Given that the size of these holes are comparable with the dimensions of microvilli, and they coincide with distinct areas of the cell membrane when imaging 2nd generation SLBs, they likely represent more stabilised microvillar contacts (also referred as microvillar close contact zones (CCZs)). More intense areas of TCR fluorescence were seen at microvillar CCZs, indicating these

are the location of antigen sensing, as others have indicated [122], [123]. Using TIRFM to observe CD58, ICAM-1 and calcium release, results presented in **Chapter 6** identified distinct and constrained areas of CD2-CD58 accumulation that colocalise with microvillar CCZs on the SLB. These contacts are subsequently stabilised by a surrounding region and occasionally a ring of ICAM-1 accumulation. ICAM-1 was excluded from the central region of CD58 accumulation/microvillar CCZs. Given both accumulate before observable calcium release on low densities of agonist pMHC, they likely form an adhesive interface to support antigen detection rather than being a consequence of productive antigen recognition (detected as calcium release).

Stability of microvillar CCZs

As the concept of microvilli as antigen-sensing platforms has only recently started to develop, few analyses exist examining the factors that influence the stability of microvillar CCZs or contact dwell time [122], [123]. However, from the studies that do exist, it seems that important factors on the APC side may include the overall adhesion-repulsion balance of the surface and binding kinetics of pMHC that is presented. For example, Brodovitch et al. (2013) quantified the initial membrane probing dynamics in primary T cells over the first minute of interaction with an antibody-coated glass surface [377]. They noted that on a non-adhesive surface (anti-IgG1), these membrane 'contacts' lasted ~9s on average, whereas on a non-stimulatory but adhesive surface (anti-HLA) they lasted ~28s.

In another study, Krummel and colleagues, quantified microvillar contact persistence time using 1st generation SLBs further functionalised with QDs [122]. Using TIRFM, CCZs were represented by holes in QD fluorescence. By labelling the TCR, CCZs made with the surface were separated into 'TCR^{+}' and 'TCR^{-}' contacts based on a threshold set by the background fluorescence of the entire imaging field. On agonist pMHC, TCR^{+} and TCR^{-} contacts showed a median persistence of ~11s and ~4s, respectively. On weak agonist pMHC and null pMHC, only TCR^{-} contacts occurred and both had a persistence of ~4s. Interestingly, increased persistence was dependent on TCR occupancy, rather than on TCR-mediated signals, as contacts were stabilised with agonist pMHC in a signaling-independent manner, shown by specifically blocking ZAP-70 activity or using the kinase inhibitor PP2. Of note, Cai et al., (2017) only focussed on contacts within the synapse, and therefore may not reflect initial microvillar contacts prior to stimulation. In addition, as they were using 1st generation SLBs, there may have been an artificial dependence of contact stability on antigen density. High densities of agonist pMHC could in effect mimic the role of the abundant small adhesion protein CD58, which binds CD2 with comparable affinity to agonist pMHC (10-20 μM vs. 1-100μM; [137]–[139], [348], [248]). Lower, and perhaps more physiological densities, would be unlikely to stabilise contacts in a signaling-independent manner. As pMHC density was not characterised in Cai et al. (2017) this is purely speculative.

Upon adhesion of J8 cells to 2nd generation SLBs, the average degree of segregation of CD43 and CD54 from CCZs, and average size of CCZs rapidly increased, indicating that CCZs stabilised. For clarity, stabilisation refers to individual CCZs forming, and

remaining on the SLB surface over time. A more direct metric would be building a distribution of times that CCZ can be tracked for, before disappearing from the SLB (i.e. 'dwell time;' this is currently a work in progress), however, stability can be inferred from the rapid increase in segregation and contact size. The results presented in **Chapter 5**, show modest differences in the stability of CCZs with different densities of agonist pMHC over time. On 2nd generation SLBs, microvillar stabilisation is unlikely to be TCR signaling-induced because non-signaling cells on null pMHC formed CCZs with modest differences compared to SLBs presenting high densities of agonist pMHC. However, in contrast to Cai et al. (2017) this was not a result of TCR occupancy, but more likely the CD2-CD58 interaction in 2nd generation SLBs. More extensive characterisation of how antigen density, affinity, and other receptor-ligand pairs alter microvilli contact stability pre- and post-signaling would be an interesting subject for future work.

CD58/CD2

CD2 is known to enhance T-cell activation through both its adhesive and costimulatory properties [353]–[359]. Imaging experiments involving CD58/CD2 have predominantly focused on early to late stage synapse formation (i.e. imaging cells ~1 to 60-minutes after interaction with their target surface) of T cells with anti-TCR-coated glass, CD58-funtionalised SLBs or target cells [83], [92], [140], [141], [156], [378]. These studies have collectively described the localisation of CD2 during synapse formation, but little is known how this protein operates in the initial interactions prior to antigen recognition. The results of this thesis addresses this gap in our knowledge by showing that CD58/CD2 operates, and likely stabilises, initial microvillar contacts to promote antigen

scanning. Their role as an adhesive interface that aids antigen scanning is supported by their accumulation prior to calcium release on 2nd generation SLBs presenting either null pMHC or agonist (and null) pMHC, and through the loss of adhesion and subsequent activation resulting from their removal from the SLB surface, presented in **Chapter 6**.

There are several lines of evidence that argue in favour of CD58/CD2 as a prominent component for antigen scanning in human T cells. For example, CD58/CD2 engagement has comparable dimensions to pMHC/TCR and was recently found enriched at the microvillus tip [126], [201], [379]. In support of the former point, 2-minutes after association with the SLB, CD2 was shown to colocalise with the TCR when using CD58-functionalised SLB surfaces [141].. The same finding is presented in **Chapters 5 and 6** of this thesis, whereby TCR (on the cell) and CD58 (on the SLB) accumulation was colocalised exclusively within microvilli CCZs (albeit in different experiments), indicating TCR and CD2 are topologically constrained to the same regions. In contrast, another key adhesion protein, ICAM-1, was excluded from areas of pMHC (and by inference TCR) accumulation (**Chapter 4**), and from microvillar CCZs (**Chapter 6**). CD58 is also ubiquitously expressed in most tissues. It is found on all cells of haemopoietic origins, endothelial cells, epithelial cells, and fibroblastic cells [331], [352], [357],[380]. This protein may therefore provide a general mechanism to aid antigen scanning and activation across the whole body, albeit to differing degrees dependent on cell type and disease state of that cell [381].

Although homologs of CD58/CD2 exist in sheep, pigs, chickens, ducks and zebrafish, the use of the CD58/CD2 pair specifically in T-cell microvillar-based antigen scanning, however, is not an entirely conserved feature across vertebrates, although it may be partially compensated by other proteins of similar characteristics [382], [383]. For example, mice/rats lack a CD58 homolog, with the major ligand for CD2 in mice/rats being CD48. Interestingly, CD48 exhibits 5-10-fold lower 3D affinity and 40-50-fold lower 2D affinity for mouse/rat CD2, than human CD58 for human CD2, which likely explains the subtle defects in T-cell development and activation to viral challenge seen in CD2-deficient mice [384]. Subsequent *in vitro* experiments showed CD48/CD2 could enhance activation, but only under conditions of low antigen presentation [142]. Although CD2/CD58 are not always conserved, it appears there is a general need for small adhesion protein interaction, presumably to form CCZs.

ICAM-1/LFA-1

The function of LFA-1 has mostly been attributed to T-cell homing to the LN, and activation through stabilising large contact interfaces between cells [78], [135]. LFA-1 has been shown to provide increased adhesion, allowing for more efficient TCR-pMHC engagement, and supposedly co-stimulatory signals to T cells, lowering the threshold for activation [136], [142], [360]. Like CD2, most imaging experiments have focused on ICAM-1/LFA-1 during the formation of the immune synapse [83], [84], [86], [91], [93], [96], [141], [283], [322], [385] The role of ICAM-1/LFA-1 in initial antigen scanning is less clear. The ICAM-1/LFA-1 complex is much larger (30-40nm) than the pMHC/TCR complex (~15nm) and was shown to accumulate in areas spatially segregated from TCR

and CD58/CD2 accumulation, albeit during synapse formation [92], [96], [97], [140], [141]. At the very least, this indicates it cannot be directly promoting pMHC/TCR engagement from within close contact zones. Furthermore, LFA-1 in TK-1 (a $CD8^+$ mouse leukemic T-cell line) was found predominantly at the cell body compared to the microvilli when using gold-labelled antibodies and scanning electron microscopy [288]. Similar results were obtained when transfecting LFA-1 into the K562 cell line, and when examining LFA-1 in neutrophils [386], [387]. If microvilli are the first point of contacts on APCs, logically LFA-1 presence away from microvilli would argue against a dominant role in antigen scanning.

In experiments presented in **Chapter 5**, ICAM-1 accumulated a median of ~30s prior to calcium release. During this period, accumulation was found surrounding/excluded from microvillar CCZs and areas of CD58 accumulation, and typically occurred after the appearance of both. Although ICAM-1/LFA-1 are not involved in the initial microvillar CCZs, they appear to stabilise the surrounding area of a CCZ to produce an adhesive interface that likely increases contact dwell time or microvillar antigen scanning efforts. The ring-like ICAM-1 structures seen on the SLBs in **Chapter 6,** resembles those seen in later synapse formation on 1st generation SLBs [96]. They also resemble the ILP contacts made by primary T cells interacting with antigen-pulsed endothelial cells, which formed rings of ICAM-1 accumulation prior to calcium release [121].

One possible reason for observing ICAM-1 accumulation after CD58 accumulation but prior to a Ca^{2+} signal on 2nd generation SLBs is that CD2-mediated signaling occurred. CD2 signaling pathways were shown to have considerable overlap with the TCR, with CD2 signaling largely dependent on the TCR being present, suggesting it triggers the TCR, although how it achieves this is unclear (discussed in **Section 8.3**; [141], [388]). Perhaps CD2 engagement evokes ligand-independent triggering from the TCR, producing 'weaker signals,' which are enough to induce the activity of more immediate components downstream in the CD2/TCR-signaling pathway (e.g. a conformational change in LFA-1 to a higher affinity state) but rarely leads to full activation. In support, TCR-dependent calcium release has been observed on T cells interacting with CD58-functionalised SLBs [141]. The benefit of doing this is that it may promote a more transient localised adhesive interface to modestly increase scanning efforts in the presence of a weak signal. Only strong signals may induce a full commitment to scan in the direction of the original signaling contact (indicated by cell spreading and synapse formation). This would involve ICAM-1/LFA-1 promoting more intense, localised areas of microvillar scanning, but not being directly involved in microvillar contacts themselves.

The need for CD2-mediated signaling, however, is not a strict requirement for increased ICAM-1 engagement as previous reports have indicated ICAM-1 accumulation on SLB surfaces presenting either only ICAM-1 or null pMHC and ICAM-1 [378], [389]. Furthermore, using 1st generation SLBs, Hashimoto-Tane et al. (2016) found (although not explicitly shown) that ICAM-1/LFA-1-mediated adhesion rings formed in the

absence of agonist antigen (and absence of TCR microclusters), albeit at a significantly slower rate and lower density than with agonist [97]. As these studies did not directly image early markers of T-cell activation alongside antigen-independent ICAM-1 accumulation, TCR signaling may still have occurred. Support for this can be found in experiments shown in **Chapter 4**, where ~12% cells exhibited 'weaker' calcium signals (based on duration of response) on 1st generation SLBs presenting null pMHC. This correlated with a small fraction of cells showing small areas of ICAM-1 accumulation. A more direct test would be to identify whether ICAM-1 accumulates in the absence of TCR signals using a TCR knockout cell line.

8.2.3 Phase 3: Activation and cell spreading is initiated from microvillar CCZs

To transition from phase 2 to phase 3 was critically dependent on T-cell activation. T-cell activation, indicated by calcium release, occurred at CD58 enriched microvillar CCZs on 2nd generation SLBs. The time spent in phase 2 depended on the density of agonist antigen presented, as cells on low densities of agonist pMHC (1-5 molecules/μm^2) took twice as long and formed three times more microvillar CCZs before calcium release occurred compared to cells on high densities of agonist pMHC (50-100 molecules/μm^2). Cells that didn't activate remained in phase 2, slowly making additional CCZs up to a limit of 10-20 over the course of 10-minutes. Phase 3 was characterised by an increased rate of cell spreading (indicated by a wider area of CellMask fluorescence) and microvillar CCZ formation. During spreading, additional regions of TCR and CD58 accumulation appeared, both colocalised within microvillar CCZs, and eventually began

to migrate centripetally. ICAM-1 accumulation also became more widespread, remaining excluded from microvillar CCZs, instead accumulating in the space between them. After 5-minutes a mature immune synapse formed, with a central area of pMHC/TCR and CD58/CD2, and peripheral area of ICAM-1/LFA-1 accumulation.

Calcium release correlates with the presence of microvillar CCZs

TCR triggering and T-cell activation have previously been shown to occur at small initial contacts. For example, TCR and ZAP-70 were found colocalised at initial close contacts, of T cells interacting with anti-CD3-coated glass surfaces [90], [125]. Contacts were observed using IRM or TIRFM of the fluorescently labelled cell membrane. Calcium release was also seen from small contacts in IRM [90]. However, the high affinity and crosslinking nature of antibodies strongly suggests, but does not prove, that microvilli are the sites of initial antigen recognition. The results of **Chapter 5** confirm microvilli contacts are indeed the site of antigen recognition by directly showing that T-cell signaling, subsequent cell spreading, and synapse formation is mediated by microvilli CCZs in the presence of very low amounts of bona fide TCR ligand.

Remarkably, using 2nd generation SLBs at low antigen densities (1-5/μm^2, assumed 2.5/μm^2 on average), antigen-specific calcium release (and subsequent rapid cell spreading) occurred when less than 0.25% (~10 CCZs = ~1.5μm^2 total CCZ area) of the total surface area of the T-cell membrane was in close contact with the surface. It was estimated that 0.2-0.4 agonist pMHC per microvillar CCZ, or in other words, only ~20-

40% of CCZs, experienced a single agonist pMHC at point of calcium release under these conditions. In addition, calcium release occurred within 3-minutes of attachment to the SLB. These findings simultaneously highlight the sensitivity and efficiency of antigen recognition by T cells. Given the low fraction of microvillar CCZs that had probabilistically encountered an agonist pMHC in this setup, it seems more likely that each microvillar CCZ was acting independent of the other to achieve an early state of activation (i.e. calcium release and cell spreading) in the cell. This is because it is hard to see how membrane proximal TCR signals could be integrated across spatially segregated zones. One downstream component of TCR signaling, LAT, has been posited as a hub for integration of spatiotemporal correlated pMHC/TCR signals, however, LAT itself appears to accumulate in spatially segregated zones, colocalized to small membrane contacts with anti-CD3-coated glass, and more recently, found to have a preferred localisation for microvilli [126], [247]. Perhaps molecules further downstream could be integrated across multiple CCZ prior to early activation, although it is currently unclear how. It may be that cells that responded were those which had two or more microvilli in very close proximity, or those that experienced the coalescing of microvillar CCZs, although this seemed rare prior to calcium release and spreading. Further quantification of CCZ dynamics for cells that do and do not calcium release may provide clarity on the matter.

It is possible, however, that signals may still be integrated (or even required) across microvillar CCZs to achieve later stages of activation (i.e. sustained calcium and effector functions). For example, by imaging $CD4^+$ mouse T cells on 1st generation SLBs, Lin et al.

(2019), found that for weak agonist pMHC presented at low densities, pMHC/TCR binding events could be spatiotemporally integrated to achieve NFAT translocation (requires sustained calcium signals) provided they were within 2μm and 30s of each other [247]. In a separate study using $CD8^+$ mouse T cells also interacting with 1st generation SLBs, microvillar CCZs were found at a constant density of 1.5/μm^2, which would allow for spatially separated pMHC/TCR engagement within this 2μm range [122]. Furthermore, if we assume that TCR microclusters represent sites of microvillar CCZs, as this thesis and others have indicated, more central TCR microclusters/CCZs, which have been established for longer periods, are known to be no longer associated with active kinase activity [122], [123], [268]. Only new peripheral TCR microclusters/CCZs maintain this capacity, indicating sustained signaling, and therefore activation must be temporally integrated across multiple microvillar CCZs [85], [86].

A relationship between signal strength, cell spreading and CCZ formation

Provided a cell showed a calcium response, they would enter phase 3, characterised by an increased rate of cell spreading and CCZ formation. Interestingly, cells that non-specifically signalled on null pMHC (which was adhesion and TCR-dependent) showed a reduced rate of CCZ formation relative to high densities of agonist pMHC. This coincided with a weaker calcium response (measured from the integrated calcium increase). This may reflect a relationship between antigen scanning dynamics and ligand independent vs. dependent TCR signaling or ligand potency. A similar finding was made by Brodovitch et al. (2015), who noticed a correlation between surface potency and rate of cell spreading, measured using 1G4-specific Jurkat ($CD8^-$) interacting with glass

surfaces coated in pMHC of differing binding kinetics and density [339]. Combined with the data in **Chapter 5**, this may indicate that strong/antigen-dependent signals fully commit a T cell to redirect its scanning activity in the direction of the original signal. Weaker/antigen-independent signals only transiently increase scanning activity such that a T cell remains efficient scanning across many DCs. These may also be the source of 'tonic signals,' which are essential for T-cell survival and prevent them from entering a hyporesponsiveness state [390].[156], [391]

Microvillar-based receptor/ligand reorganisation at the immune synapse

It was clear that activated T cells that spread across 2nd generation SLBs, observed by labelling the cell membrane, did not form a completely flat interface with the SLB. Instead, the interface between T cell and SLB was dominated by microvillar CCZs, with a maximum of 3.3% of the total surface area forming contacts sufficiently close to allow pMHC/TCR engagement. Distinct and small areas of heightened TCR fluorescence (perhaps corresponding to TCR microclusters) and pMHC accumulation, also correlated with CCZs and would move centripetally within the CCZs (**Chapter 5**). This was also seen in [122]**.** The centripetal migration of pMHC/TCR microclusters is known to be a result of underlying actin cytoskeleton [83], [85], [91], [392]–[394]. TCR microclusters have been hypothesised to directly associate with actin through transient slippage events [322], [394]. This drives TCR microclusters towards the centre of the synapse, however, it is currently unclear how (if at all) they form. As TCR fluorescence colocalised exclusively with microvillar CCZs throughout synapse formation (presented in **Chapter 5**), it is tempting to speculate that actin-rich microvilli are platforms to organise proteins

without a need for direct association receptors/ligands with centripetal actin flow. Effectively, as the cell's cytoskeleton and lamellipodia retract, microvilli, and by extension all small receptor/ligand interactions that occur at microvillar CCZs, will be dragged centripetally to the centre of the cell. If true, proteins that are missing their cytoplasmic domain, and therefore cannot associate with actin, but are still found colocalised with TCR microclusters, would be expected to centripetally migrate with TCR microclusters. A good candidate to test this may be CD28, as T cells expressing a mutated version of CD28 missing the entire cytoplasmic domain still formed distinct points of accumulation that colocalised with TCR microclusters on SLBs presenting pMHC, ICAM-1 and CD80 [93]**.** Of note, 'microvillar-based protein reorganisation' may only be true for the early synapse structure, but not for mature synapses or even all proteins, as a recent and thorough analysis of CD2, which is initially colocalised with the TCR in microvillar CCZs at least for the first ~5-minutes, was found to form a distinct "corolla"-like structure in the dSMAC of late synapses (> 10-minutes; [156]).

8.2.1 Monofocal vs. multifocal immune synapses

Formation of the mature immune synapse has been extensively characterised using T and B cells, cytotoxic T cells and target cells, or T cells and 1st generation SLBs [80], [84] [395][396] (see **Section 1.5.3**). However, instead of forming a singular adhesive interface, DCs, arguably the most potent activators of the T-cell response, are known to predominantly form multifocal synapses with T cells [101], [397]. The reasons for this difference are currently unknown, although the glycocalyx has been posited to form a barrier to large contact interfaces [398]. However, cells on 2nd generation SLBs, which

incorporate the APC glycocalyx, were indistinguishable from those on 1st generation SLBs, when forming immune synapses, albeit at high antigen densities. This indicates, at the very least, that the steric barrier created by the glycocalyx on SLBs is not responsible for differential synapse formation. It is possible, however, that linkage of glycocalyx proteins to the underlying cytoskeleton could prevent large adhesive interfaces, although this remains to be tested. Another factor that may be key is the topology of DC, which are covered in microvilli and ruffles [399]. This may lead to topologically constrained contacts between T cells and DCs, giving rise to multifocal contacts.

8.3 TCR triggering and discriminatory signaling at microvillar CCZs

The KS model has posited that sized-constrained regions of CD45 exclusion on the T-cell membrane are key to achieving antigen discrimination [124]. The results presented throughout this thesis provide strong support for the KS model. For example, the results in **Chapter 5** showed that on 2nd generation SLBs, ligand-dependent TCR triggering (using calcium release as a proxy) correlated with the appearance of size-constrained microvillar CCZs. Using low densities of agonist pMHC, activating and non-activating cells formed microvillar CCZs that were comparably constrained in size, even across early stages of the immune synapse, highlighting the constrained geometry of these contacts. In experiments described in **Chapters 6 and 7**, also on 2nd generation SLBs presenting either null pMHC or low densities of agonist pMHC, the small adhesion

molecule CD58 accumulated exclusively within microvillar CCZs and coincided with areas of CD45 exclusion on the T-cell membrane. Lastly in **Chapter 7**, by altering the size of CCZs through altering CD58/CD2 adhesion, and by inference CD45 exclusion on the T-cell membrane, a loss of antigen discrimination occurred.

8.3.1 CD45 exclusion from microvillar CCZs

Using non-specific adhesive surfaces, anti-TCR coated glass, CD58-functionalised SLBs, 1st generation SLBs, and GUV-based systems, CD45 exclusion has previously been shown to occur at TCR microclusters and/or areas of CD58/adhesion molecule accumulation [85], [92], [318], [400], [401], [116], [119], [124], [125], [141], [230], [231], [278]. Similar results have been found for B cells, NK cells, mast cells, and macrophages [334], [335], [402], [403]. Although in most of these studies signal-induced reorganisation of CD45 cannot be ruled out, segregation is likely a passive process that occurs before signaling, dependent on protein dimensions and lateral crowding of proteins. In support of this, CD45 on the T-cell membrane was shown to passively exclude from large regions of tightly adhesive surfaces prior to T-cell signaling [116], [124]. The results of **Chapter 7** build upon these findings by showing that CD45 segregation can be seen prior to calcium release at initial microvillar CCZs mediated by CD58-CD2 interaction on 2nd generation SLBs. This occurred in the absence and presence of agonist pMHC. After calcium release, once the cell had spread, CD45 exclusion on the T-cell membrane from areas of CD58/CD2 engagement became more pronounced, as has been shown previously with T cells interacting on CD58-functionalsied SLBs [141]. A recent report

did not observe CD45 segregation at areas of TCR accumulation, particularly in the periphery of cells that had spread out (presumably after antigen detection; [122]). This is likely explained by both the absence of small adhesion proteins which likely enhances CD45 segregation and issues of axial resolution resulting from uneven membrane topology,

8.3.2 Antigen discrimination is dependent on size-constrained CCZs

Over expression of wild-type CD2 resulted in a high probability of TCR triggering in the absence of agonist pMHC (~75% of cells showed a response). At least half of this signaling could be attributed to passive formation of large areas of CD58 accumulation, and by inference, CD45 exclusion on the T-cell surface, since 40% of cells were triggered when they over-expressed a mutant CD2 lacking the intracellular domain. Importantly, these results support the claim that that there is not a strict requirement for ligand interaction to trigger the TCR, arguing against ligand specific models of TCR triggering (e.g. conformational change or aggregation), and provide experimental validation for the KS model [116], [124], [203].

A key prediction of the KS model is that decreasing the CD45/Lck ratio should lead to shorter time and/or greater probability of a TCR trigger occurring. As discussed, decreasing CD45 density (and therefore the CD45/Lck ratio) from large areas of small adhesion molecule engagement alone is enough to drive TCR triggering (results of this

thesis; [116], [124]). Interestingly, this effect could be supplemented through the intracellular domain of CD2. In **Chapter 7**, Lck/Fyn recruitment to the intracellular domain was evoked to explain the enhancement in TCR triggering. This could decrease the CD45/Lck ratio further by increasing the pool of kinase within CD58/CD2 contacts. This is mainly supported by the observation of a constitutively 'open' conformation of Lck and auto-phosphorylated Src kinase colocalising in regions of CD58 accumulation but only when the intracellular domain of CD2 was present [141]. Although likely, as kinases were not imaged in the present study, other explanations cannot be ruled out. For example, direct association of CD2 with CD3 has been reported [404]. This could effectively hold the TCR within CD58/CD2 mediated CD45 exclusion zones, increasing the probability of TCR triggering without necessarily altering the CD45/Lck ratio. However, it is currently unclear how direct association occurs. In future experiments it would interesting to address direct association of Lck/Fyn and/or TCR with CD2 using biophysical approaches such as pFCS, scanning FCS, FRET-FLIM or dual single particle tracking in combination with cell lines expressing versions of these proteins mutated at predicted interaction sites.

The last experiment presented in the thesis highlights how the constrained nature of microvillar CCZs is critical to T cells ability to discriminate antigens. In the absence of agonist pMHC, size constrained CD58-CD2 mediated CCZs only resulted in ~20% of cells showing a calcium response. By increasing the average CCZ 'diameter' at least three-fold this resulted in 70% of cells being triggered. This high level of TCR triggering could only be achieved in size constrained contacts in the presence of relatively high

densities (10-30μm^2) of strong agonist pMHC (7.2μM K_d), highlighting the importance of constraining CCZ size in order to obtain specific antigen responses.

8.3.3 Ligand-independent TCR triggering at small microvillar CCZs

The triggering of 20% of cells at constrained contacts in the absence of TCR ligands would represent a high 'false-positive' rate for T cells. Several factors may be responsible. First, the rigidity of the underlying glass support may exaggerate CD45 exclusion from areas of CD58-CD2 interaction. APC membranes are ~10^5-10^6 less stiff than the glass surface, and have their own topology, as opposed to being flat [272]. Analysing TCR triggering on 2nd generation SLBs built on PDMS surfaces of differing stiffness could be used to address this question [277]. Second, the probability of calcium release may be tuned by additional components not included in 2nd generation SLBs, such as the balancing signals of inhibitory and costimulatory receptors. For example, PD-1 ligand transduced into a monolayer of APCs substantially delayed calcium release kinetics in T cells, indicating these proteins function early [157]. Incorporating additional components into 2nd generation SLBs may reduce this triggering. Third, it may be that this "background" is close to being physiological and represents a 'tonic' form of signaling that prevents T cells from entering a state of hyporesponsiveness [390]. This could be predominantly dependent on self-pMHC in vivo and may be a result of weak engagement of null pMHC on 2nd generation SLBs. An MHC-independent contribution has been also been noted for tonic signaling, which may be TCR signaling mediated through CD2 engagement [49], [141]. In experiments presented in **Chapter 5**, calcium

release under null pMHC conditions appeared 'weaker' and cells that responded showed less of a commitment to form additional microvillar CCZs after signaling, further supporting a sub-activation threshold/tonic-like response.

8.3.4 Are constrained CCZs a conserved feature of immune signaling?

It is possible that the need for constrained CCZs is a conserved feature of immune signaling, but perhaps restricted to non-catalytic tyrosine phosphorylated receptors (NTRs). These represent a large family, which have no intrinsic catalytic activity themselves, and instead serve as platforms for the initiation of downstream signaling pathways by extrinsic kinases. They are characterised by containing the conserved ITAM/ITIM motifs, with their signaling likely modulated by the balance between Src family kinases and (receptor) protein tyrosine phosphate (PTP) activity locally [405]. NTRs include the TCR, BCR, Fc receptor family, KIR family SLAM family, C-type lectin domain and SIGLEC family. CD45 (a receptor PTP) alone has been implicated in not only T-cell signaling (as indicated in this thesis), but also B-cell signaling (acting on the BCR), mast cell signaling (actin on FcεRI), and macrophage phagocytosis (acting on FcγR and Dectin-1), dependent on its exclusion from close membrane contacts where their signaling receptors are engaged [79], [124], [203], [335], [402], [403], [406]. As a result, it is possible that constrained CCZs affect the signaling capabilities of these receptors, and that affinities are "optimised" to give effective signaling in small contacts. One receptor of interest would be FcγRIII (CD16) on NK cells. This is because ζ chain dimers can associate with the receptor, largely mimicking the signaling domains of the TCR, and

because NK cells have highly comparable morphology to T cells, surrounded by microvilli [407]. Interestingly, CD2-mediated signals in NK cells (one of the few cell types that express CD2) were dependent on CD16/ζζ complexes, like the dependency of TCR for CD2-mediated signaling in T cells [408]–[410]. This indicates there may be a conserved sensitivity to CD2-mediated CCZ size between T cells and NK cells. 2nd generation SLBs are well placed to address this using IgG instead of agonist pMHC.

8.4 Concluding remarks

The work described in this thesis provides an account of the early events in T-cell activation, focused on the relationship between surface topology, antigen detection and discrimination. As well as the key molecular events in initial contacts, it highlights the sensitivity, the efficiency and how quickly T cells can recognise their antigens, critically depending on the formation of dynamic microvilli. Furthermore, the mechanism of TCR triggering and antigen discrimination were found to be intimately tied to the geometry of microvillar CCZs, as predicted by the KS model. These insights were only possible using a more physiological surface to study the nature of T-cell contacts, highlighting the value of more complex, but still reductionist, models to comprehend key processes in immune cell activation. Until actual cell-cell contacts can be imaged with sufficient spatio-temporal resolution, owing to their special advantages for fluorescence imaging we can expect 3rd, 4th … Nth generation SLBs, incorporating yet other factors such as physiological surface stiffness, e.g. with PDMS, and/or costimulatory/inhibitory receptors, to continue giving crucial insights into the mechanisms of T-cell activation.

Appendix A

Testing immune synapse formation in the J8 and J8-GECI cell line

J8-GECI cells were imaged 10-minutes after being placed on 1st generation SLBs presenting high densities of agonist pMHC (50-100 molecules/μm^2). In order to observe immune synapse formation agonist pMHC (9V) and ICAM-1 were labelled with Alexa-555 and Alexa-647, respectively (**Appendix A Figure 1A**). J8-GECI cells bound pMHC (confirming it was functional) but produced 'holes' in the ICAM-1 signal (i.e. local exclusion) instead of accumulation at what were presumed to be regions of contact (**Appendix A Figure 1B**). To ameliorate this the same experiment was attempted in PBS containing magnesium sulphate ($MgS0_4$) at 2mM (physiological range in serum is 0.5-2mM), as the binding pocket of LFA-1 (the receptor for ICAM-1) is known to coordinate a magnesium ion, substantially increasing the affinity for ICAM-1 [370]. Once again, no ICAM-1 accumulation occurred (**Appendix A Figure 1B**).

Reconstituting LFA-1 to physiological levels to observe ICAM-1 accumulation

To understand if this was a problem with the ICAM-1 or cell line, primary T cells isolated from human PBMCs were tested on 1st gen SLBs (**Appendix A Figure 2**). To bypass the need for antigen specificity, pMHC was substituted with a 'pan-specific' UCHT-1 Fab, with the C-terminus of the heavy chain component fused to HaloTag-H6-linker-H6 (referred to as UCHT-1-Halo Fab from hereon; **Appendix A Figure 2A**). This attaches to the SLB and binds to the extracellular regions of CD3ε of the TCR-CD3 complex, such that each TCR binds two UCHT-1-Halo Fabs. As the extracellular region of CD3ε has a

short extracellular domain, the HaloTag domain (~4nm) was added to the Fab (~7nm) to maintain more comparable dimensions to the pMHC-TCR interaction (~13-15nm). Primary T cells bound the UCHT-1-Halo Fab and strong ICAM-1 accumulation in PBS + $MgS0_4$ (but not PBS) was observed, confirming that ICAM-1 was functional and required $MgS0_4$ (**Appendix A Figure 2B**). As the SLB system was functional, the cell line required optimising.

Although the J8-GECI cells were LFA-1 positive their expression was compared against primary T cells. The expression of LFA-1 in primary T cells was expressed by two populations, small and large cells, likely reflecting naïve vs. activated resting/memory T cells, respectively (**Appendix A Figure 2C**). It is well known that activated T cells are known to upregulate LFA-1 and undergo blasting whereby cells double in size and at least quadruple in surface area [411], [412]. Compared to J8-GECIs, small primary T-cells exhibited a four-fold increase in the median fluorescence intensity, whereas large cells gave a 10x increase, indicating LFA-1 expression on the J8 cells required boosting (**Appendix A Figure 2C**). J8-GECIs (as well as J8s, $J8^{TCR-}$ and $J8^{TCR-}$-GECI, not shown) were stably transduced with both chains of LFA-1 (CD11α and CD18) and sorted for primary T-cell levels of expression (large cells; **Appendix A Figure 2C**). This was done for several reasons: (1) pre-activation of T cells prior to study on 1st generation SLBs is typically performed, and activation is known to upregulate LFA-1 expression [83], [85], [283], [411], [413], [86], [89], [91], [96], [97], [247], [281], [282]. Therefore, high expression is consistent with the current literature, allowing fairer comparisons with previous studies. (2) The diameter of Jurkats is closer to activated primary T cells despite Jurkats having

lower LFA-1 expression [414], [415]. This means that the expression levels of LFA-1 must be matched to the similar surface area of activated primary cells. (3) Increasing the LFA-1 levels gives the best chance of visualising synapse formation. Accordingly, when testing J8-GECI-LFA-1-boosted cells on 1st gen SLBs with either UCHT-1-Halo Fab or agonist pMHC (9V), ICAM-1 was found to accumulate and the cells formed classical immune synapses (i.e. pMHC at the centre surrounded by a ring of ICAM-1; **Appendix A Figure 2D**). ICAM-1 accumulation was only visible in PBS + $MgS0_4$ (not PBS), highlighting the need for magnesium ions to be present in the imaging buffer (**Appendix A Figure 2D**).

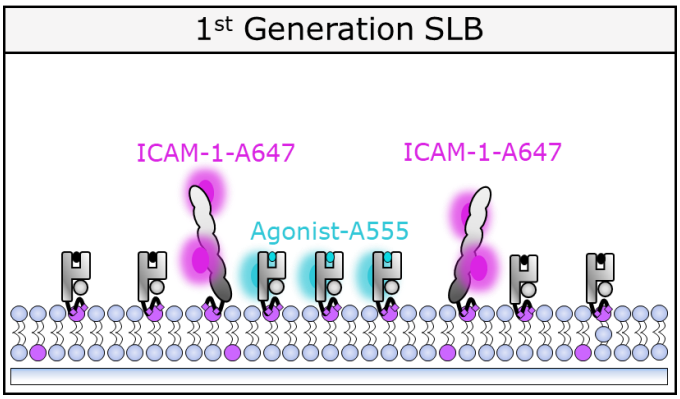

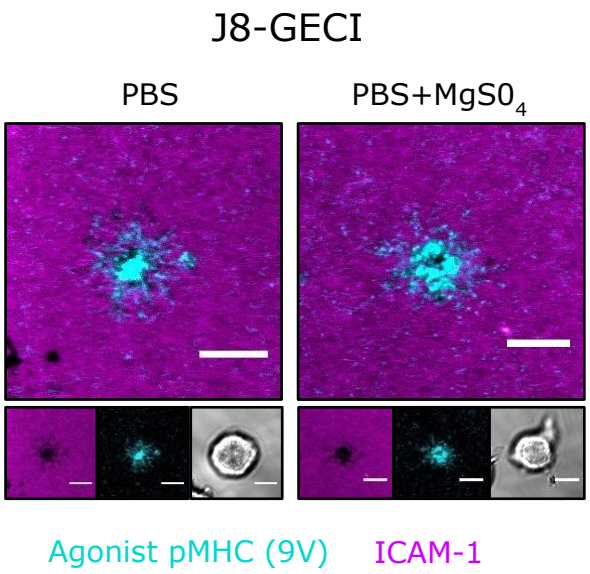

Appendix A Figure 1. **No ICAM-1 accumulation by J8-GECI cells.** (A) Cartoon representation of 1st generation SLB with Alexa-647 labelled ICAM-1 (ICAM-1-A647) and Alexa-555 labelled agonist pMHC (9V; Agonist-A555). (B) Example of J8-GECI cells on 1st generation SLBs either in PBS (left) or PBS + $MgS0_4$ (right). Despite pMHC binding, immune synapse formation does not occur in either media.

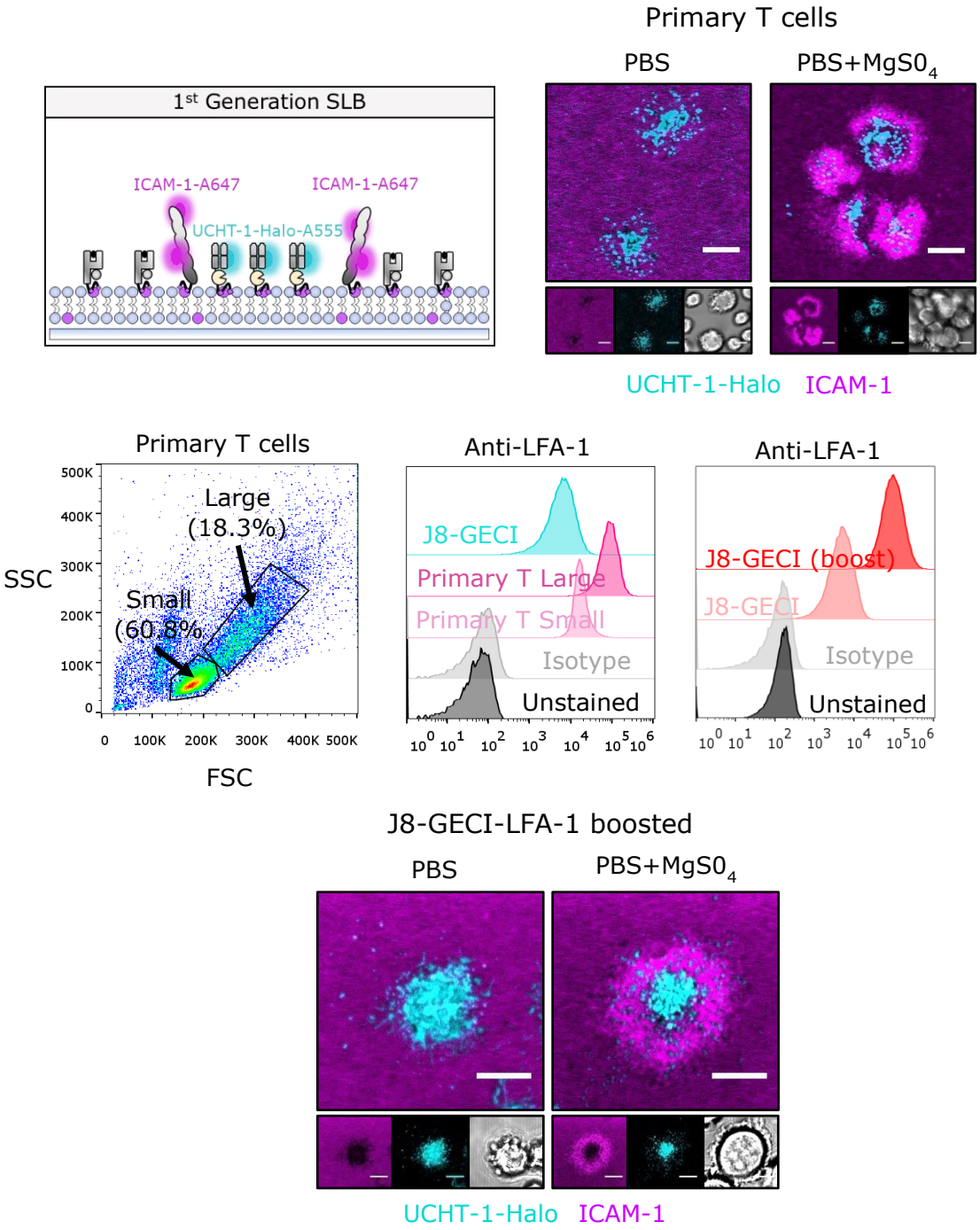

Appendix A Figure 2. **ICAM-1 accumulation requires physiological expression of ICAM-1 and magnesium ions.** (A) Cartoon representation of 1st generation SLB with Alexa-647 labelled ICAM-1 (ICAM-1-A647) and Alexa-555 labelled UCHT-1-Halo Fab. (B) PBMC-derived T cells forming immune synapses (central accumulation of UCHT-Halo-His and peripheral ring of accumulation of ICAM-1) only in the presence of MgS0$_4$. (C) Matching the expression levels of LFA-1 in J8-GECI cells to PBMC-derived primary T cells. (D) J8-GECI-LFA-1 boosted cells now form immune synapses in the presence of MgS0$_4$.

Bibliography

[1] W. B. Whitman, D. C. Coleman, and W. J. Wiebe, "Prokaryotes: The unseen majority," *Proceedings of the National Academy of Sciences of the United States of America*, vol. 95, no. 12. Proc Natl Acad Sci U S A, pp. 6578–6583, 09-Jun-1998.

[2] Y. M. Bar-On, R. Phillips, and R. Milo, "The biomass distribution on Earth," *Proc. Natl. Acad. Sci. U. S. A.*, vol. 115, no. 25, pp. 6506–6511, Jun. 2018.

[3] W. A. M. Loenen, D. T. F. Dryden, E. A. Raleigh, G. G. Wilson, and N. E. Murrayy, "Highlights of the DNA cutters: A short history of the restriction enzymes," *Nucleic Acids Res.*, vol. 42, no. 1, pp. 3–19, Jan. 2014.

[4] E. V. Koonin and K. S. Makarova, "Origins and evolution of CRISPR-Cas systems," *Philosophical Transactions of the Royal Society B: Biological Sciences*, vol. 374, no. 1772. Royal Society Publishing, 13-May-2019.

[5] R. Jack, L. Du Pasquier, R. Jack, and L. Du Pasquier, "From Unicellular to Metazoan Immunity," in *Evolutionary Concepts in Immunology*, Springer International Publishing, 2019, pp. 17–32.

[6] B. Weiss, R. Ebel, M. Elbrächter, M. Kirchner, and P. Proksch, "Defense metabolites from the marine sponge Verongia aerophoba," *Biochem. Syst. Ecol.*, vol. 24, no. 1, pp. 1–7, Jan. 1996.

[7] M. Srivastava *et al.*, "The Amphimedon queenslandica genome and the evolution of animal complexity," *Nature*, vol. 466, no. 7307, pp. 720–726, Aug. 2010.

[8] S. B. Helber, D. J. J. Hoeijmakers, C. A. Muhando, S. Rohde, and P. J. Schupp, "Sponge chemical defenses are a possible mechanism for increasing sponge abundance on reefs in Zanzibar," *PLoS One*, vol. 13, no. 6, Jun. 2018.

[9] M. E. Kotas and R. Medzhitov, "Homeostasis, Inflammation, and Disease Susceptibility," *Cell*, vol. 160, no. 5. Cell Press, pp. 816–827, 26-Feb-2015.

[10] M. Milinski, "The Major Histocompatibility Complex, Sexual Selection, and Mate Choice," *Annu. Rev. Ecol. Evol. Syst.*, vol. 37, no. 1, pp. 159–186, Dec. 2006.

[11] C. A. Janeway, "Approaching the asymptote? Evolution and revolution in immunology," in *Cold Spring Harbor Symposia on Quantitative Biology*, 1989, vol. 54, no. 1, pp. 1–13.

[12] Y. Xing and K. A. Hogquist, "T-Cell tolerance: Central and peripheral," *Cold Spring Harb. Perspect. Biol.*, vol. 4, no. 6, pp. 1–15, Jun. 2012.

[13] L. Wang, F. S. Wang, and M. E. Gershwin, "Human autoimmune diseases: A comprehensive update," *Journal of Internal Medicine*, vol. 278, no. 4. Blackwell Publishing Ltd, pp. 369–395, 01-Oct-2015.

[14] D. B. Mills, "The origin of phagocytosis in Earth history," *Interface Focus*, vol. 10, no. 4, p. 20200019, Aug. 2020.

[15] M. G. Netea *et al.*, "A guiding map for inflammation," *Nature Immunology*, vol. 18, no. 8. Nature Publishing Group, pp. 826–831, 19-Jul-2017.

[16] R. Medzhitov, P. Preston-Hurlburt, and C. A. Janeway, "A human homologue of the Drosophila toll protein signals activation of adaptive immunity," *Nature*, vol. 388, no. 6640, pp. 394–397, 1997.

[17] J. C. Kagan and G. M. Barton, "Emerging principles governing signal transduction by Pattern-Recognition receptors," *Cold Spring Harb. Perspect. Biol.*, vol. 7, no. 3, p. 2020, Mar. 2015.

[18] T. Boehm, M. Hirano, S. J. Holland, S. Das, M. Schorpp, and M. D. Cooper, "Evolution of Alternative Adaptive Immune Systems in Vertebrates," *Annu. Rev. Immunol.*, vol. 36, no. 1, pp. 19–42, Apr. 2018.

[19] Z. Pamcer, C. T. Amemiya, G. R. A. Ehrhardt, J. Coitlin, G. L. Gartland, and M. D. Cooper, "Somatic diversification of variable lymphocyte receptors in the agnathan sea lamprey," *Nature*, vol. 430, no. 6996, pp. 174–180, Jul. 2004.

[20] M. F. Flajnik, "A cold-blooded view of adaptive immunity," *Nat. Rev. Immunol.*, vol. 18, no. 7, pp. 438–453, Jul. 2018.

[21] M. F. Flajnik and M. Kasahara, "Origin and evolution of the adaptive immune system: Genetic events and selective pressures," *Nature Reviews Genetics*, vol. 11, no. 1. NIH Public Access, pp. 47–59, Jan-2010.

[22] M. Wieczorek *et al.*, "Major histocompatibility complex (MHC) class I and MHC class II proteins: Conformational plasticity in antigen presentation," *Frontiers in Immunology*, vol. 8, no. MAR. Frontiers Research Foundation, p. 1, 17-Mar-2017.

[23] K. Muegge, M. P. Vila, and S. K. Durum, "Interleukin-7: A cofactor for V(D)J rearrangement of the T cell receptor β gene," *Science (80-.).*, vol. 261, no. 5117, pp. 93–95, Jul. 1993.

[24] D. Jung, C. Giallourakis, R. Mostoslavsky, and F. W. Alt, "Mechanism and control of V(D)J recombination at the immunoglobulin heavy chain locus," *Annual Review of Immunology*, vol. 24. Annu Rev Immunol, pp. 541–570, 2006.

[25] A. Murugan, T. Mora, A. M. Walczak, and C. G. Callan, "Statistical inference of the generation probability of T-cell receptors from sequence repertoires," vol. 2, 2012.

[26] M. K. Jenkins, H. H. Chu, J. B. McLachlan, and J. J. Moon, "On the composition of the preimmune repertoire of T cells specific for peptide-major histocompatibility complex ligands," *Annual Review of Immunology*, vol. 28. Annual Reviews , pp. 275–294, 23-Apr-2010.

[27] D. Mason, "A very high level of crossreactivity is an essential feature of the T- cell receptor," *Immunol. Today*, vol. 19, no. 9, pp. 395–404, Sep. 1998.

[28] J. Nikolich-Žugich, M. K. Slifka, and I. Messaoudi, "The many important facets of T-cell repertoire diversity," *Nature Reviews Immunology*, vol. 4, no. 2. Nature Publishing Group, pp. 123–132, 2004.

[29] T. P. Arstila, A. Casrouge, V. Baron, J. Even, J. Kanellopoulos, and P. Kourilsky, "A direct estimate of the human αβ T cell receptor diversity," *Science (80-.).*, vol. 286, no. 5441, pp. 958–961, Oct. 1999.

[30] Q. Qi *et al.*, "Diversity and clonal selection in the human T-cell repertoire," *Proc. Natl. Acad. Sci. U. S. A.*, vol. 111, no. 36, pp. 13139–13144, Sep. 2014.

[31] E. Muraille, "Generation of Individual Diversity: A Too Neglected Fundamental Property of Adaptive Immune System," *Front. Immunol.*, vol. 5, no. MAY, p. 208, May 2014.

[32] L. Wooldridge *et al.*, "A single autoimmune T cell receptor recognizes more than a million different peptides," *J. Biol. Chem.*, vol. 287, no. 2, pp. 1168–1177, Jan. 2012.

[33] M. E. Birnbaum *et al.*, "Deconstructing the peptide-MHC specificity of t cell recognition," *Cell*, vol. 157, no. 5, pp. 1073–1087, May 2014.

[34] K. L. Rock, E. Reits, and J. Neefjes, "Present Yourself! By MHC Class I and MHC Class II Molecules," *Trends in Immunology*, vol. 37, no. 11. Elsevier Ltd, pp. 724–737, 01-Nov-2016.

[35] L. C. Anton and J. W. Yewdell, "Translating DRiPs: MHC class I immunosurveillance of pathogens and tumors," *J. Leukoc. Biol.*, vol. 95, no. 4, pp. 551–562, Apr. 2014.

[36] D. Bourdetsky, C. E. H. Schmelzer, and A. Admon, "The nature and extent of contributions by defective ribosome products to the HLA peptidome," *Proc. Natl. Acad. Sci. U. S. A.*, vol. 111, no. 16, pp. E1591–E1599, Apr. 2014.

[37] M. Raghavan, N. Del Cid, S. M. Rizvi, and L. R. Peters, "MHC class I assembly: out and about," *Trends in Immunology*, vol. 29, no. 9. NIH Public Access, pp. 436–443, Sep-2008.

[38] T. ten Broeke, R. Wubbolts, and W. Stoorvogel, "MHC class II antigen presentation by dendritic cells regulated through endosomal sorting," *Cold Spring Harb. Perspect. Biol.*, vol. 5, no. 12, Dec. 2013.

[39] M. Embgenbroich and S. Burgdorf, "Current concepts of antigen cross-presentation," *Frontiers in Immunology*, vol. 9, no. JUL. Frontiers Media S.A., p. 1643, 16-Jul-2018.

[40] K. S. Kobayashi and P. J. Van Den Elsen, "NLRC5: A key regulator of MHC class I-dependent immune responses," *Nature Reviews Immunology*, vol. 12, no. 12. Nature Publishing Group, pp. 813–820, 23-Dec-2012.

[41] L. Klein, B. Kyewski, P. M. Allen, and K. A. Hogquist, "Positive and negative selection of the T cell repertoire: What thymocytes see (and don't see)," *Nature Reviews Immunology*, vol. 14, no. 6. Nature Publishing Group, pp. 377–391, 2014.

[42] N. L. La Gruta, S. Gras, S. R. Daley, P. G. Thomas, and J. Rossjohn, "Understanding the drivers of MHC restriction of T cell receptors," 2018. *Nat. Rev. Immunol.* vol. 18, no. 7, pp. 467-478, 2018.

[43] M. S. Anderson *et al.*, "Projection of an immunological self shadow within the thymus by the aire protein," *Science (80-.).*, vol. 298, no. 5597, pp. 1395–1401, Nov. 2002.

[44] E. S. Venanzi, R. Melamed, D. Mathis, and C. Benoist, "The variable immunological self: Genetic variation and nongenetic noise in Aire-regulated transcription," *Proc. Natl. Acad. Sci. U. S. A.*, vol. 105, no. 41, pp. 15860–15865, Oct. 2008.

[45] R. Perniola, "Twenty years of AIRE," *Frontiers in Immunology*, vol. 9, no. FEB. Frontiers Media S.A., p. 1, 12-Feb-2018.

[46] K. Shortman, D. Vremec, and M. Egerton, "The kinetics of T cell antigen receptor expression by subgroups of CD4+8+ thymocytes: Delineation of CD4+8+32+ thymocytes as post-selection intermediates leading to mature T cells," *J. Exp. Med.*, vol. 173, no. 2, pp. 323–332, 1991.

[47] M. Huesmann, B. Scott, P. Kisielow, and H. von Boehmer, "Kinetics and efficacy of

positive selection in the thymus of normal and T cell receptor transgenic mice," *Cell*, vol. 66, no. 3, pp. 533–540, Aug. 1991.

[48] C. D. Surh and J. Sprent, "T-cell apoptosis detected in situ during positive and negative selection in the thymus," *Nature*, vol. 372, no. 6501, pp. 100–103, 1994.

[49] K. Hochweller, G. H. Wabnitz, Y. Samstag, J. Suffner, G. J. Hämmerling, and N. Garbi, "Dendritic cells control T cell tonic signaling required for responsiveness to foreign antigen," *Proc. Natl. Acad. Sci. U. S. A.*, vol. 107, no. 13, pp. 5931–5936, Mar. 2010.

[50] D. R. Forsdyke, "Further implications of a theory of immunity," *J. Theor. Biol.*, vol. 52, no. 1, pp. 187–198, Jul. 1975.

[51] M. Krogsgaard, Q. J. Li, C. Sumen, J. B. Huppa, M. Huse, and M. M. Davis, "Agonist/endogenous peptide-MHC heterodimers drive T cell activation and sensitivity," *Nature*, vol. 434, no. 7030, pp. 238–243, Mar. 2005.

[52] J. N. Mandl, J. P. Monteiro, N. Vrisekoop, and R. N. Germain, "T Cell-Positive Selection Uses Self-Ligand Binding Strength to Optimize Repertoire Recognition of Foreign Antigens," *Immunity*, vol. 38, no. 2, pp. 263–274, Feb. 2013.

[53] I. Štefanoví, J. R. Dorfman, and R. N. Germain, "Self-recognition promotes the foreign antigen sensitivity of naive T lymphocytes," *Nature*, vol. 420, no. 6914, pp. 429–434, Nov. 2002.

[54] C. D. Surh and J. Sprent, "Homeostasis of Naive and Memory T Cells," *Immunity*, vol. 29, no. 6. Cell Press, pp. 848–862, 19-Dec-2008.

[55] M. Matloubian *et al.*, "Lymphocyte egress from thymus and peripheral lymphoid organs is dependent on S1P receptor 1," *Nature*, vol. 427, no. 6972, pp. 355–360, Jan. 2004.

[56] P. J. Fink, "The Biology of Recent Thymic Emigrants," *Annu. Rev. Immunol.*, vol. 31, no. 1, pp. 31–50, Mar. 2013.

[57] M. E. Smith and W. L. Ford, "The recirculating lymphocyte pool of the rat: A systematic description of the migratory behaviour of recirculating lymphocytes," *Immunology*, vol. 49, no. 1, pp. 83–94, 1983.

[58] L. M. Bradley, S. R. Watson, and S. L. Swain, "Entry of naive CD4 T cells into peripheral lymph nodes requires I-selectin," *J. Exp. Med.*, vol. 180, no. 6, pp. 2401–2406, Dec. 1994.

[59] M. Bajénoff *et al.*, "Stromal Cell Networks Regulate Lymphocyte Entry, Migration, and Territoriality in Lymph Nodes," *Immunity*, vol. 25, no. 6, pp. 989–1001, Dec. 2006.

[60] R. T. Boscacci *et al.*, "Comprehensive analysis of lymph node stroma-expressed Ig superfamily members reveals redundant and nonredundant roles for ICAM-1, ICAM-2, and VCAM-1 in lymphocyte homing," *Blood*, vol. 116, no. 6, pp. 915–925, Aug. 2010.

[61] J. N. Mandl *et al.*, "Quantification of lymph node transit times reveals differences in antigen surveillance strategies of naïve CD4+ and CD8+ T cells," *Proc. Natl. Acad. Sci. U. S. A.*, vol. 109, no. 44, pp. 18036–18041, Oct. 2012.

[62] G. Lythe, R. E. Callard, R. L. Hoare, and C. Molina-París, "How many TCR clonotypes does a body maintain?," *J. Theor. Biol.*, vol. 389, pp. 214–224, Jan. 2016.

[63] S. E. Acton *et al.*, "Dendritic cells control fibroblastic reticular network tension and lymph node expansion," *Nature*, vol. 514, no. 7253, pp. 498–502, Oct. 2014.

[64] T. Katakai, T. Hara, M. Sugai, H. Gonda, and A. Shimizu, "Lymph node fibroblastic reticular cells construct the stromal reticulum via contact with lymphocytes," *J. Exp. Med.*, vol. 200, no. 6, pp. 783–795, Sep. 2004.

[65] A. L. Fletcher, S. E. Acton, and K. Knoblich, "Lymph node fibroblastic reticular cells in health and disease," *Nature Reviews Immunology*, vol. 15, no. 6. Nature Publishing Group, pp. 350–361, 27-Jun-2015.

[66] M. J. Miller, A. S. Hejazi, S. H. Wei, M. D. Cahalan, and I. Parker, "T cell repertoire scanning is promoted by dynamic dendritic cell behavior and random T cell motility in the lymph node," *Proc. Natl. Acad. Sci. U. S. A.*, vol. 101, no. 4, pp. 998–1003, Jan. 2004.

[67] P. Bousso and E. Robey, "Dynamics of CD8+ T cell priming by dendritic cells in intact lymph nodes," *Nat. Immunol.*, vol. 4, no. 6, pp. 579–585, May 2003.

[68] T. R. Mempel, T. Junt, and U. H. von Andrian, "Rulers over Randomness: Stroma Cells Guide Lymphocyte Migration in Lymph Nodes," *Immunity*, vol. 25, no. 6. Immunity, pp. 867–869, Dec-2006.

[69] M. Bajénoff *et al.*, "Stromal Cell Networks Regulate Lymphocyte Entry, Migration, and Territoriality in Lymph Nodes," *Immunity*, vol. 25, no. 6, pp. 989–1001, Dec. 2006.

[70] M. F. Krummel, F. Bartumeus, and A. Gérard, "T cell migration, search strategies and mechanisms," *Nature Reviews Immunology*, vol. 16, no. 3. Nature Publishing Group, pp. 193–201, 01-Mar-2016.

[71] H. D. Moreau *et al.*, "Signal strength regulates antigen-mediated T-cell deceleration by distinct mechanisms to promote local exploration or arrest," *Proc. Natl. Acad. Sci. U. S. A.*, vol. 112, no. 39, pp. 12151–12156, Sep. 2015.

[72] P. A. Thill, A. Weiss, and A. K. Chakraborty, " Phosphorylation of a Tyrosine Residue on Zap70 by Lck and Its Subsequent Binding via an SH2 Domain May Be a Key Gatekeeper of T Cell Receptor Signaling In Vivo ," *Mol. Cell. Biol.*, vol. 36, no. 18, pp. 2396–2402, Sep. 2016.

[73] A. Liaunardy-Jopeace, B. L. Murton, M. Mahesh, J. W. Chin, and J. R. James, "Encoding optical control in LCK kinase to quantitatively investigate its activity in live cells," *Nat. Struct. Mol. Biol.*, vol. 24, no. 12, pp. 1155–1163, 2017.

[74] M. Huse *et al.*, "Spatial and Temporal Dynamics of T Cell Receptor Signaling with a Photoactivatable Agonist," *Immunity*, vol. 27, no. 1, pp. 76–88, Jul. 2007.

[75] M. D. Cahalan and K. G. Chandy, "The functional network of ion channels in T lymphocytes," *Immunological Reviews*, vol. 231, no. 1. NIH Public Access, pp. 59–87, Sep-2009.

[76] N. Joseph, B. Reicher, and M. Barda-Saad, "The calcium feedback loop and T cell activation: How cytoskeleton networks control intracellular calcium flux," *Biochimica et Biophysica Acta - Biomembranes*, vol. 1838, no. 2. Biochim Biophys Acta, pp. 557–568, Feb-2014.

[77] J. R. James and R. D. Vale, "Biophysical mechanism of T-cell receptor triggering in a reconstituted system," *Nature*, vol. 487, no. 7405, pp. 64–69, Jun. 2012.

[78] M. L. Dustin, "The immunological synapse," *Cancer immunology research*, vol. 2, no. 11. NIH Public Access, pp. 1023–1033, 01-Nov-2014.

[79] E. M. Schmid *et al.*, "Size-dependent protein segregation at membrane interfaces," *Nat. Phys.*, vol. 12, no. 7, pp. 704–711, Jun. 2016.

[80] C. R. F. Monks, B. A. Freiberg, H. Kupfer, N. Sciaky, and A. Kupfer, "Three-dimensional segregation of supramolecular activation clusters in T cells," *Nature*, vol. 395, no. 6697, pp. 82–86, Sep. 1998.

[81] B. A. Freiberg *et al.*, "Staging and resetting T cell activation in SMACs," *Nat. Immunol.*, vol. 3, no. 10, pp. 911–917, 2002.

[82] G. Gaud, R. Lesourne, and P. E. Love, "Regulatory mechanisms in T cell receptor signalling," *Nature Reviews Immunology*, vol. 18, no. 8. Nature Publishing Group, pp. 485–497, 01-Aug-2018.

[83] A. Grakoui *et al.*, "The immunological synapse: A molecular machine controlling T cell activation," *Science (80-.).*, vol. 285, no. 5425, pp. 221–227, Jul. 1999.

[84] K. H. Lee, A. D. Holdorf, M. L. Dustin, A. C. Chan, P. M. Allen, and A. S. Shaw, "T cell receptor signaling precedes immunological synapse formation," *Science (80-.).*, vol. 295, no. 5559, pp. 1539–1542, Feb. 2002.

[85] R. Varma, G. Campi, T. Yokosuka, T. Saito, and M. L. Dustin, "T Cell Receptor-Proximal Signals Are Sustained in Peripheral Microclusters and Terminated in the Central Supramolecular Activation Cluster," *Immunity*, vol. 25, no. 1, pp. 117–127, Jul. 2006.

[86] T. Yokosuka *et al.*, "Newly generated T cell receptor microclusters initiate and sustain T cell activation by recruitment of Zap70 and SLP-76," *Nat. Immunol.*, vol. 6, no. 12, pp. 1253–1262, Dec. 2005.

[87] S. Čemerski *et al.*, "The Balance between T Cell Receptor Signaling and Degradation at the Center of the Immunological Synapse Is Determined by Antigen Quality," *Immunity*, vol. 29, no. 3, pp. 414–422, Sep. 2008.

[88] K. Choudhuri *et al.*, "Polarized release of T-cell-receptor-enriched microvesicles at the immunological synapse," *Nature*, vol. 507, no. 7490, pp. 118–123, Feb. 2014.

[89] Bálint *et al.*, "Supramolecular attack particles are autonomous killing entities released from cytotoxic T cells," *Science (80-.).*, vol. 368, no. 6493, pp. 897–901, May 2020.

[90] S. C. Bunnell *et al.*, "T cell receptor ligation induces the formation of dynamically regulated signaling assemblies," *J. Cell Biol.*, vol. 158, no. 7, pp. 1263–1275, Sep. 2002.

[91] G. Campi, R. Varma, and M. L. Dustin, "Actin and agonist MHC-peptide complex-dependent T cell receptor microclusters as scaffolds for signaling," *J. Exp. Med.*, vol. 202, no. 8, pp. 1031–1036, Oct. 2005.

[92] A. D. Douglass and R. D. Vale, "Single-molecule microscopy reveals plasma membrane microdomains created by protein-protein networks that exclude or trap signaling molecules in T cells," *Cell*, vol. 121, no. 6, pp. 937–950, Jun. 2005.

[93] T. Yokosuka *et al.*, "Spatiotemporal Regulation of T Cell Costimulation by TCR-CD28 Microclusters and Protein Kinase C θ Translocation," *Immunity*, vol. 29, no. 4, pp. 589–601, Oct. 2008.

[94] A. Hashimoto-Tane *et al.*, "Dynein-Driven Transport of T Cell Receptor Microclusters Regulates Immune Synapse Formation and T Cell Activation," *Immunity*, vol. 34, no. 6, pp. 919–931, Jun. 2011.

[95] A. Hashimoto-Tane and T. Saito, "Dynamic regulation of TCR-microclusters and the microsynapse for T cell activation," *Frontiers in Immunology*, vol. 7, no. JUN. Frontiers Research Foundation, p. 1, 28-Jun-2016.

[96] N. C. Hartman, J. A. Nye, and J. T. Groves, "Cluster size regulates protein sorting in the immunological synapse," *Proc. Natl. Acad. Sci. U. S. A.*, vol. 106, no. 31, pp. 12729–12734, Aug. 2009.

[97] A. Hashimoto-Tane *et al.*, "Micro-adhesion rings surrounding TCR microclusters are essential for T cell activation," *J. Exp. Med.*, vol. 213, no. 8, pp. 1609–1625, Jul. 2016.

[98] M. Gunzer *et al.*, "Antigen presentation in extracellular matrix: Interactions of T cells with dendritic cells are dynamic, short lived, and sequential," *Immunity*, vol. 13, no. 3, pp. 323–332, Sep. 2000.

[99] M. L. Dustin, "T-cell activation through immunological synapses and kinapses," *Immunological Reviews*, vol. 221, no. 1. Immunol Rev, pp. 77–89, Feb-2008.

[100] P. Bousso, "T-cell activation by dendritic cells in the lymph node: Lessons from the movies," *Nature Reviews Immunology*, vol. 8, no. 9. Nat Rev Immunol, pp. 675–684, Sep-2008.

[101] C. Brossard *et al.*, "Multifocal structure of the T cell - Dendritic cell synapse," *Eur. J. Immunol.*, vol. 35, no. 6, pp. 1741–1753, Jun. 2005.

[102] F. Tamzalit *et al.*, "Interfacial actin protrusions mechanically enhance killing by cytotoxic T cells," *Sci. Immunol.*, vol. 4, no. 33, p. 5445, Mar. 2019.

[103] F. Marangoni *et al.*, "The Transcription Factor NFAT Exhibits Signal Memory during Serial T Cell Interactions with Antigen-Presenting Cells," *Immunity*, vol. 38, no. 2, pp. 237–249, Feb. 2013.

[104] V. Mayya *et al.*, "Durable Interactions of T Cells with T Cell Receptor Stimuli in the Absence of a Stable Immunological Synapse," *Cell Rep.*, vol. 22, no. 2, pp. 340–349, 2018.

[105] G. Suzuki, Y. Kawase, S. Koyasu, I. Yahara, Y. Kobayashi, and R. H. Schwartz, "Antigen-induced suppression of the proliferative response of T cell clones.," *J. Immunol.*, vol. 140, no. 5, 1988.

[106] M. K. Jenkins, C. A. Chen, G. Jung, D. L. Mueller, and R. H. Schwartz, "Inhibition of antigen-specific proliferation of type 1 murine T cell clones after stimulation with immobilized anti-CD3 monoclonal antibody.," *J. Immunol.*, vol. 144, no. 1, 1990.

[107] F. A. Harding, J. G. McArthur, J. A. Gross, D. H. Raulet, and J. P. Allison, "CD28-mediated signalling co-stimulates murine T cells and prevents induction of anergy in T-cell clones," *Nature*, vol. 356, no. 6370, pp. 607–609, 1992.

[108] C. G. Vinuesa, M. A. Linterman, D. Yu, and I. C. M. Maclennan, "Follicular Helper T Cells," *Annu. Rev. Immunol.*, vol. 34, pp. 335–368, May 2016.

[109] N. Zhang and M. J. Bevan, "CD8+ T Cells: Foot Soldiers of the Immune System," *Immunity*, vol. 35, no. 2. Elsevier, pp. 161–168, 26-Aug-2011.

[110] V. P. Badovinac, J. S. Haring, and J. T. Harty, "Initial T Cell Receptor Transgenic Cell Precursor Frequency Dictates Critical Aspects of the CD8+ T Cell Response to Infection," *Immunity*, vol. 26, no. 6, pp. 827–841, Jun. 2007.

[111] N. Manjunath, R. S. Johnson, D. E. Staunton, R. Pasqualini, and B. Ardman, "Targeted

disruption of CD43 gene enhances T lymphocyte adhesion.," *J. Immunol.*, vol. 151, no. 3, 1993.

[112] N. Manjunath, M. Correa, M. Ardman, and B. Ardman, "Negative regulation of T-cell adhesion and activation by CD43," *Nature*, vol. 377, no. 6549. Nature Publishing Group, pp. 535–538, 12-Oct-1995.

[113] A. R. Carolyn Shurer, J. Chin-Hun Kuo, L. Moné Roberts, G. W. Feigenson, H. L. Reesink, and M. J. Paszek, "Physical Principles of Membrane Shape Regulation by the Glycocalyx Correspondence," *Cell*, vol. 177, 2019.

[114] J. Pettmann, A. M. Santos, O. Dushek, and S. J. Davis, "Membrane ultrastructure and T cell activation," *Frontiers in Immunology*, vol. 9, no. SEP. Frontiers Media S.A., p. 2152, 25-Sep-2018.

[115] A. . Williams, A.F. & Barclay, *Handbook of Experimental Immunology*. Blackwell Scientific Publications, 1986.

[116] V. T. Chang *et al.*, "Initiation of T cell signaling by CD45 segregation at 'close contacts,'" *Nat. Immunol.*, vol. 17, no. 5, pp. 574–582, May 2016.

[117] J. G. Cyster, D. M. Shotton, and A. F. Williams, "The dimensions of the T lymphocyte glycoprotein leukosialin and identification of linear protein epitopes that can be modified by glycosylation.," *EMBO J.*, vol. 10, no. 4, pp. 893–902, Apr. 1991.

[118] J. Newby and J. Allard, "First-Passage Time to Clear the Way for Receptor-Ligand Binding in a Crowded Environment," *Phys. Rev. Lett.*, vol. 116, no. 12, p. 128101, Mar. 2016.

[119] C. B. Carbone *et al.*, "In vitro reconstitution of T cell receptor-mediated segregation of the CD45 phosphatase," *Proc. Natl. Acad. Sci. U. S. A.*, vol. 114, no. 44, pp. E9338–E9345, Oct. 2017.

[120] C. V. Carman *et al.*, "Transcellular Diapedesis Is Initiated by Invasive Podosomes," *Immunity*, vol. 26, no. 6, pp. 784–797, Jun. 2007.

[121] P. T. Sage *et al.*, "Antigen Recognition Is Facilitated by Invadosome-like Protrusions Formed by Memory/Effector T Cells," *J. Immunol.*, vol. 188, no. 8, pp. 3686–3699, Apr. 2012.

[122] E. Cai *et al.*, "Visualizing dynamic microvillar search and stabilization during ligand detection by T cells," *Science (80-.).*, vol. 356, no. 6338, May 2017.

[123] Y. Jung *et al.*, "Three-dimensional localization of T-cell receptors in relation to microvilli using a combination of superresolution microscopies," *Proc. Natl. Acad. Sci. U. S. A.*, vol. 113, no. 40, pp. E5916–E5924, Oct. 2016.

[124] R. A. Fernandes *et al.*, "A cell topography-based mechanism for ligand discrimination by the T cell receptor," *Proc. Natl. Acad. Sci. U. S. A.*, vol. 116, no. 28, pp. 14002–14010, Jul. 2019.

[125] Y. Razvag, Y. Neve-Oz, J. Sajman, O. Yakovian, M. Reches, and S. Correspondence, "T Cell Activation through Isolated Tight Contacts," *Cell Rep.*, vol. 29, pp. 3506–3521, 2019.

[126] S. Ghosh, V. Di Bartolo, R. Alon, A. Alcover, and G. Haran, "ERM-Dependent Assembly of T Cell Receptor Signaling and Co-stimulatory Molecules on Microvilli prior to Activation," *Cell Rep.*, vol. 30, pp. 3434–3447, 2020.

[127] M. J. Mitchell and M. R. King, "Physical biology in cancer. 3. The role of cell glycocalyx in vascular transport of circulating tumor cells," *Am. J. Physiol. - Cell Physiol.*, vol. 306, no. 2, Jan. 2014.

[128] T. A. Springer, "Traffic signals for lymphocyte recirculation and leukocyte emigration: The multistep paradigm," *Cell*, vol. 76, no. 2. Elsevier, pp. 301–314, 28-Jan-1994.

[129] G. Ostermann, K. S. C. Weber, A. Zernecke, A. Schröder, and C. Weber, "JAM-I is a ligand of the β2 integrin LFA-I involved in transendothelial migration of leukocytes," *Nat. Immunol.*, vol. 3, no. 2, pp. 151–158, Jan. 2002.

[130] T. Katakai, K. Habiro, and T. Kinashi, "Dendritic Cells Regulate High-Speed Interstitial T Cell Migration in the Lymph Node via LFA-1/ICAM-1," *J. Immunol.*, vol. 191, no. 3, pp. 1188–1199, Aug. 2013.

[131] G. Constantin *et al.*, "Chemokines trigger immediate β2 integrin affinity and mobility changes: Differential regulation and roles in lymphocyte arrest under flow," *Immunity*, vol. 13, no. 6, pp. 759–769, Dec. 2000.

[132] J. Takagi, B. M. Petre, T. Walz, and T. A. Springer, "Global conformational earrangements in integrin extracellular domains in outside-in and inside-out signaling," *Cell*, vol. 110, no. 5, pp. 599–611, Sep. 2002.

[133] M. Shimaoka *et al.*, "AL-57, a ligand-mimetic antibody to integrin LFA-1, reveals chemokine-induced affinity up-regulation in lymphocytes," *Proc. Natl. Acad. Sci. U. S. A.*, vol. 103, no. 38, pp. 13991–13996, Sep. 2006.

[134] E. J. Park *et al.*, "Distinct roles for LFA-1 affinity regulation during T-cell adhesion, diapedesis, and interstitial migration in lymph nodes," *Blood*, vol. 115, no. 8, pp. 1572–1581, Feb. 2010.

[135] B. L. Walling and M. Kim, "LFA-1 in T cell migration and differentiation," *Frontiers in Immunology*, vol. 9, no. MAY. Frontiers Media S.A., p. 952, 03-May-2018.

[136] M. F. Bachmann *et al.*, "Distinct roles for LFA-1 and CD28 during activation of naive T cells: Adhesion versus costimulation," *Immunity*, vol. 7, no. 4, pp. 549–557, 1997.

[137] P. A. van der Merwe *et al.*, "Human Cell-Adhesion Molecule CD2 Binds CD58 (LFA-3) with a Very Low Affinity and an Extremely Fast Dissociation Rate but Does Not Bind CD48 or CD59," *Biochemistry*, vol. 33, no. 33, pp. 10149–10160, Aug. 1994.

[138] M. L. Dustin, S. K. Bromley, Z. Kan, D. A. Peterson, and E. R. Unanue, "Antigen receptor engagement delivers a stop signal to migrating T lymphocytes," *Proc. Natl. Acad. Sci. U. S. A.*, vol. 94, no. 8, pp. 3909–3913, Apr. 1997.

[139] D. M. Zhu, M. L. Dustin, C. W. Cairo, H. S. Thatte, and D. E. Golan, "Mechanisms of Cellular Avidity Regulation in CD2-CD58-Mediated T Cell Adhesion.," *ACS Chem. Biol.*, vol. 1, no. 10, pp. 649–658, 2006.

[140] M. L. Dustin *et al.*, "A novel adaptor protein orchestrates receptor patterning and cytoskeletal polarity in T-cell contacts," *Cell*, vol. 94, no. 5, pp. 667–677, Sep. 1998.

[141] Y. Kaizuka, A. D. Douglass, S. Vardhana, M. L. Dustin, and R. D. Vale, "The coreceptor CD2 uses plasma membrane microdomains to transduce signals in T cells," *J. Cell Biol.*, vol. 185, no. 3, pp. 521–534, May 2009.

[142] M. F. Bachmann, M. Barner, and M. Kopf, "CD2 sets quantitative thresholds in T cell

activation," *J. Exp. Med.*, vol. 190, no. 10, pp. 1383–1391, Nov. 1999.

[143] C. N. Magee, O. Boenisch, and N. Najafian, "The role of costimulatory molecules in directing the functional differentiation of alloreactive T helper cells," *American Journal of Transplantation*, vol. 12, no. 10. NIH Public Access, pp. 2588–2600, Oct-2012.

[144] A. Larbi and T. Fulop, "From 'truly naïve' to 'exhausted senescent' T cells: When markers predict functionality," *Cytometry Part A*, vol. 85, no. 1. John Wiley & Sons, Ltd, pp. 25–35, 01-Jan-2014.

[145] N. Watanabe *et al.*, "BTLA is a lymphocyte inhibitory receptor with similarities to CTLA-4 and PD-1," *Nat. Immunol.*, vol. 4, no. 7, pp. 670–679, Jul. 2003.

[146] L. Derré *et al.*, "BTLA mediates inhibition of human tumor-specific CD8+ T cells that can be partially reversed by vaccination," *J. Clin. Invest.*, vol. 120, no. 1, pp. 157–167, Jan. 2010.

[147] L. Baitsch *et al.*, "Exhaustion of tumor-specific CD8+ T cells in metastases from melanoma patients," *J. Clin. Invest.*, vol. 121, no. 6, pp. 2350–2360, Jun. 2011.

[148] A. Legat, D. E. Speiser, H. Pircher, D. Zehn, and S. A. Fuertes Marraco, "Inhibitory receptor expression depends more dominantly on differentiation and activation than 'exhaustion' of human CD8 T cells," *Front. Immunol.*, vol. 4, no. DEC, 2013.

[149] M. A. ElTanbouly, E. Schaafsma, R. J. Noelle, and J. L. Lines, "VISTA: Coming of age as a multi-lineage immune checkpoint," *Clin. Exp. Immunol.*, vol. 200, no. 2, pp. 120–130, May 2020.

[150] G. G. Chiang and B. M. Sefton, "Specific Dephosphorylation of the Lck Tyrosine Protein Kinase at Tyr-394 by the SHP-1 Protein-tyrosine Phosphatase," *J. Biol. Chem.*, vol. 276, no. 25, pp. 23173–23178, Jun. 2001.

[151] D. R. Plas *et al.*, "Direct regulation of ZAP-70 by SHP-1 in T cell antigen receptor signaling," *Science (80-.).*, vol. 272, no. 5265, pp. 1173–1176, May 1996.

[152] E. Hui *et al.*, "T cell costimulatory receptor CD28 is a primary target for PD-1-mediated inhibition," *Science (80-.).*, vol. 355, no. 6332, pp. 1428–1433, Mar. 2017.

[153] R. J. Lebbink *et al.*, "Collagens are functional, high affinity ligands for the inhibitory immune receptor LAIR-1," *J. Exp. Med.*, vol. 203, no. 6, pp. 1419–1425, Jun. 2006.

[154] M. L. del Rio, C. L. Lucas, L. Buhler, G. Rayat, and J. I. Rodriguez-Barbosa, "HVEM/LIGHT/BTLA/CD160 cosignaling pathways as targets for immune regulation," *J. Leukoc. Biol.*, vol. 87, no. 2, pp. 223–235, Feb. 2010.

[155] L. Chen and D. B. Flies, "Molecular mechanisms of T cell co-stimulation and co-inhibition," *Nature Reviews Immunology*, vol. 13, no. 4. NIH Public Access, pp. 227–242, Apr-2013.

[156] P. Demetriou *et al.*, "A dynamic CD2-rich compartment at the outer edge of the immunological synapse boosts and integrates signals," *Nat. Immunol.*, vol. 21, no. 10, pp. 1232–1243, Oct. 2020.

[157] F. Wei *et al.*, "Strength of PD-1 signaling differentially affects T-cell effector functions," *Proc. Natl. Acad. Sci. U. S. A.*, vol. 110, no. 27, pp. E2480–E2489, Jul. 2013.

[158] H. Schneider *et al.*, "Reversal of the TCR stop signal by CTLA-4," *Science (80-.).*, vol. 313, no. 5795, pp. 1972–1975, Sep. 2006.

[159] D. Dong *et al.*, "Structural basis of assembly of the human T cell receptor–CD3 complex," *Nature*, vol. 573, no. 7775, pp. 546–552, Sep. 2019.

[160] B. F. Lillemeier, M. A. Mörtelmaier, M. B. Forstner, J. B. Huppa, J. T. Groves, and M. M. Davis, "TCR and Lat are expressed on separate protein islands on T cell membranes and concatenate during activation," *Nat. Immunol.*, vol. 11, no. 1, pp. 90–96, Jan. 2010.

[161] W. W. A. Schamel *et al.*, "Coexistence of multivalent and monovalent TCRs explains high sensitivity and wide range of response," *J. Exp. Med.*, vol. 202, no. 4, pp. 493–503, Aug. 2005.

[162] P. D. Dunne *et al.*, "DySCo: Quantitating associations of membrane proteins using two-color single-molecule tracking," *Biophys. J.*, vol. 97, no. 4, pp. L5–L7, Aug. 2009.

[163] J. R. James *et al.*, "The T cell receptor triggering apparatus is composed of monovalent or monomeric proteins," *J. Biol. Chem.*, vol. 286, no. 37, pp. 31993–32001, Sep. 2011.

[164] E. Molnár, S. Deswal, and W. W. A. Schamel, "Pre-clustered TCR complexes," *FEBS Lett.*, vol. 584, no. 24, pp. 4832–4837, Dec. 2010.

[165] S. V. Pageon *et al.*, "Functional role of T-cell receptor nanoclusters in signal initiation and antigen discrimination," *Proc. Natl. Acad. Sci. U. S. A.*, vol. 113, no. 37, pp. E5454–E5463, Sep. 2016.

[166] B. Rossboth *et al.*, "TCRs are randomly distributed on the plasma membrane of resting antigen-experienced T cells," *Nat. Immunol.*, vol. 19, no. 8, pp. 821–827, Aug. 2018.

[167] M. Brameshuber *et al.*, "Monomeric TCRs drive T cell antigen recognition article," *Nat. Immunol.*, vol. 19, no. 5, pp. 487–496, May 2018.

[168] P. Annibale, S. Vanni, M. Scarselli, U. Rothlisberger, and A. Radenovic, "Quantitative Photo Activated Localization Microscopy: Unraveling the Effects of Photoblinking," *PLoS One*, vol. 6, no. 7, p. e22678, Jul. 2011.

[169] D. R. Whelan and T. D. M. Bell, "Image artifacts in single molecule localization microscopy: Why optimization of sample preparation protocols matters," *Sci. Rep.*, vol. 5, 2015.

[170] A. Burgert, S. Letschert, S. Doose, and M. Sauer, "Artifacts in single-molecule localization microscopy," *Histochem. Cell Biol.*, vol. 144, no. 2, pp. 123–131, Aug. 2015.

[171] M. J. J. E. Bijlmakers, M. Isobe-Nakamura, L. J. Ruddock, and M. Marsh, "Intrinsic signals in the unique domain target p56(lck) to the plasma membrane independently of CD4," *J. Cell Biol.*, vol. 137, no. 5, pp. 1029–1040, Jun. 1997.

[172] P. W. Kim, Z. Y. J. Sun, S. C. Blacklow, G. Wagner, and M. J. Eck, "A zinc clasp structure tethers Lck to T cell coreceptors CD4 and CD8," *Science (80-.).*, vol. 301, no. 5640, pp. 1725–1728, Sep. 2003.

[173] G. M. Bell, J. Fargnoli, J. B. Bolen, L. Kish, and J. B. Imboden, "The SH3 domain of p56lck binds to proline-rich sequences in the cytoplasmic domain of CD2," *J. Exp. Med.*, vol. 183, no. 1, pp. 169–178, Jan. 1996.

[174] T. Vang *et al.*, "Activation of the COOH-terminal Src kinase (Csk) by cAMP-dependent protein kinase inhibits signaling through the T cell receptor," *J. Exp. Med.*, vol. 193, no. 4, pp. 497–507, Feb. 2001.

[175] K. Nika, L. Tautz, Y. Arimura, T. Vang, S. Williams, and T. Mustelin, "A weak Lck tail

bite is necessary for lck function in T cell antigen receptor signaling," *J. Biol. Chem.*, vol. 282, no. 49, pp. 36000–36009, Dec. 2007.

[176] W. Xu, A. Doshi, M. Lei, M. J. Eck, and S. C. Harrison, "Crystal structures of c-Src reveal features of its autoinhibitory mechanism," *Mol. Cell*, vol. 3, no. 5, pp. 629–638, 1999.

[177] H. Yamaguchi and W. A. Hendrickson, "Structural basis for activation of human lymphocyte kinase Lck upon tyrosine phosphorylation," *Nature*, vol. 384, no. 6608, p. 484, Dec. 1996.

[178] L. McNeill *et al.*, "The Differential Regulation of Lck Kinase Phosphorylation Sites by CD45 Is Critical for T Cell Receptor Signaling Responses," *Immunity*, vol. 27, no. 3, pp. 425–437, Sep. 2007.

[179] I. Štefanová, B. Hemmer, M. Vergelli, R. Martin, W. E. Biddison, and R. N. Germain, "TCR ligand discrimination is enforced by competing ERK positive and SHP-I negative feedback pathways," *Nat. Immunol.*, vol. 4, no. 3, pp. 248–254, Mar. 2003.

[180] K. Nika *et al.*, "Constitutively active lck kinase in T cells drives antigen receptor signal transduction," *Immunity*, vol. 32, no. 6, pp. 766–777, Jun. 2010.

[181] J. Casas *et al.*, "Ligand-engaged TCR is triggered by Lck not associated with CD8 coreceptor," *Nat. Commun.*, vol. 5, 2014.

[182] Q. Wei *et al.*, "Lck bound to coreceptor is less active than free Lck," *Proc. Natl. Acad. Sci. U. S. A.*, vol. 117, no. 27, pp. 15809–15817, Jul. 2020.

[183] R. M. Locksley, S. L. Reiner, F. Hatam, D. R. Littman, and N. Killeen, "Helper T cells without CD4: Control of leishmaniasis in CD4-deficient mice," *Science (80-.).*, vol. 261, no. 5127, pp. 1448–1451, 1993.

[184] M. W. Schilham *et al.*, "Alloreactive cytotoxic T cells can develop and function in mice lacking both CD4 and CD8," *Eur. J. Immunol.*, vol. 23, no. 6, pp. 1299–1304, 1993.

[185] F. Van Laethem *et al.*, "Deletion of CD4 and CD8 Coreceptors Permits Generation of αβT Cells that Recognize Antigens Independently of the MHC," *Immunity*, vol. 27, no. 5, pp. 735–750, Nov. 2007.

[186] P. Jönsson *et al.*, "Remarkably low affinity of CD4/peptide-major histocompatibility complex class II protein interactions," *Proc. Natl. Acad. Sci. U. S. A.*, vol. 113, no. 20, pp. 5682–5687, May 2016.

[187] J. R. Wyer *et al.*, "T cell receptor and coreceptor CD8αα bind peptide-MHC independently and with distinct kinetics," *Immunity*, vol. 10, no. 2, pp. 219–225, 1999.

[188] A. J. Leishman *et al.*, "T cell responses modulated through interaction between CD8αα and the nonclassical MHC class I molecule, TL," *Science (80-.).*, vol. 294, no. 5548, pp. 1936–1939, Nov. 2001.

[189] Y. Yin, X. X. Wang, and R. A. Mariuzza, "Crystal structure of a complete ternary complex of T-cell receptor, peptide-MHC, and CD4," *Proc. Natl. Acad. Sci. U. S. A.*, vol. 109, no. 14, pp. 5405–5410, Apr. 2012.

[190] H. Xu and D. R. Littman, "A kinase-independent function of Lck in potentiating antigen-specific T cell activation," *Cell*, vol. 74, no. 4, pp. 633–643, Aug. 1993.

[191] P. A. van der Merwe and S. P. Cordoba, "Late Arrival: Recruiting Coreceptors to the T Cell Receptor Complex," *Immunity*, vol. 34, no. 1. Immunity, pp. 1–3, 28-Jan-2011.

[192] A. H. Courtney *et al.*, "CD45 functions as a signaling gatekeeper in T cells," *Sci. Signal.*, vol. 12, no. 604, p. 8151, Oct. 2019.

[193] A. Musumeci, K. Lutz, E. Winheim, and A. B. Krug, "What makes a PDC: Recent advances in understanding plasmacytoid DC development and heterogeneity," *Frontiers in Immunology*, vol. 10, no. MAY. Frontiers Media S.A., p. 1222, 29-May-2019.

[194] S. J. Rodig, A. Shahsafaei, B. Li, and D. M. Dorfman, "The CD45 isoform B220 identifies select subsets of human B cells and B-cell lymphoproliferative disorders," *Hum. Pathol.*, vol. 36, no. 1, pp. 51–57, 2005.

[195] E. Z. Tchilian and P. C. L. Beverley, "Altered CD45 expression and disease," *Trends in Immunology*, vol. 27, no. 3. Elsevier Ltd, pp. 146–153, 01-Mar-2006.

[196] J. T. Pingel and M. L. Thomas, "Evidence that the leukocyte-common antigen is required for antigen-induced T lymphocyte proliferation," *Cell*, vol. 58, no. 6, pp. 1055–1065, Sep. 1989.

[197] K. F. Byth *et al.*, "CD45-null transgenic mice reveal a positive regulatory role for CD45 in early thymocyte development, in the selection of CD4+CD8+ thymocytes, and in B cell maturation," *J. Exp. Med.*, vol. 183, no. 4, pp. 1707–1718, Apr. 1996.

[198] E. Hui and R. D. Vale, "In vitro membrane reconstitution of the T-cell receptor proximal signaling network," *Nat. Struct. Mol. Biol.*, vol. 21, no. 2, pp. 133–142, Feb. 2014.

[199] S. C. Jameson and M. J. Bevan, "T Cell Receptor Antagonists and Partial Agonists," 1995.

[200] C. A. Janeway, "Ligands for the T-cell receptor: hard times for avidity models," *Immunol. Today*, vol. 16, no. 5, pp. 223–225, Jan. 1995.

[201] S. J. Davis and P. A. Van Der Merwe, "The structure and ligand interactions of CD2: Implications for T-cell function," *Immunology Today*, vol. 17, no. 4. Elsevier Ltd, pp. 177–187, 01-Apr-1996.

[202] P. A. Van Der Merwe, S. J. Davis, A. S. Shaw, and M. L. Dustin, "Cytoskeletal polarization and redistribution of cell-surface molecules during T cell antigen recognition," *Semin. Immunol.*, vol. 12, no. 1, pp. 5–21, 2000.

[203] S. J. Davis and P. A. van der Merwe, "The kinetic-segregation model: TCR triggering and beyond," *Nature Immunology*, vol. 7, no. 8. Nat Immunol, pp. 803–809, Aug-2006.

[204] J. B. Reiser *et al.*, "CDR3 loop flexibility contributes to the degeneracy of TCR recognition," *Nat. Immunol.*, vol. 4, no. 3, pp. 241–247, Mar. 2003.

[205] W. F. Hawse *et al.*, "TCR Scanning of Peptide/MHC through Complementary Matching of Receptor and Ligand Molecular Flexibility," *J. Immunol.*, vol. 192, no. 6, pp. 2885–2891, Mar. 2014.

[206] M. Krogsgaard *et al.*, "Evidence that Structural Rearrangements and/or Flexibility during TCR Binding Can Contribute to T Cell Activation," *Mol. Cell*, vol. 12, no. 6, pp. 1367–1378, 2003.

[207] K. C. Garcia *et al.*, "Structural basis of plasticity in T cell receptor recognition of a self peptide-MHC antigen," *Science (80-.).*, vol. 279, no. 5354, pp. 1166–1172, Feb. 1998.

[208] C. J. Holland *et al.*, "In Silico and structural analyses demonstrate that intrinsic protein motions guide T cell receptor complementarity determining region loop flexibility," *Front. Immunol.*, vol. 9, no. APR, p. 11, Apr. 2018.

[209] R. A. Fernandes *et al.*, "T cell receptors are structures capable of initiating signaling in the absence of large conformational rearrangements," *J. Biol. Chem.*, vol. 287, no. 16, pp. 13324–13335, Apr. 2012.

[210] W. F. Hawse *et al.*, "Cutting Edge: Evidence for a Dynamically Driven T Cell Signaling Mechanism," *J. Immunol.*, vol. 188, no. 12, pp. 5819–5823, Jun. 2012.

[211] T. Beddoe *et al.*, "Antigen Ligation Triggers a Conformational Change within the Constant Domain of the αβ T Cell Receptor," *Immunity*, vol. 30, no. 6, pp. 777–788, Jun. 2009.

[212] S. Rangarajan *et al.*, "Peptide–MHC (pMHC) binding to a human antiviral T cell receptor induces long-range allosteric communication between pMHC- and CD3-binding sites," *J. Biol. Chem.*, vol. 293, no. 41, pp. 15991–16005, Oct. 2018.

[213] M. S. Kuhns *et al.*, "Evidence for a functional sidedness to the αβTCR," *Proc. Natl. Acad. Sci. U. S. A.*, vol. 107, no. 11, pp. 5094–5099, Mar. 2010.

[214] D. Gil, W. W. A. Schamel, M. Montoya, F. Sánchez-Madrid, and B. Alarcón, "Recruitment of Nck by CD3ε reveals a ligand-induced conformational change essential for T cell receptor signaling and synapse formation," *Cell*, vol. 109, no. 7, pp. 901–912, Jun. 2002.

[215] C. Xu *et al.*, "Regulation of T Cell Receptor Activation by Dynamic Membrane Binding of the CD3ε Cytoplasmic Tyrosine-Based Motif," *Cell*, vol. 135, no. 4, pp. 702–713, Nov. 2008.

[216] D. Aivazian and L. J. Stern, "Phosphorylation of T cell receptor ζ is regulated by a lipid dependent folding transition," *Nat. Struct. Biol.*, vol. 7, no. 11, pp. 1023–1026, 2000.

[217] H. Zhang, S. P. Cordoba, O. Dushek, and P. A. Van Der Merwe, "Basic residues in the T-cell receptor ζ cytoplasmic domain mediate membrane association and modulate signaling," *Proc. Natl. Acad. Sci. U. S. A.*, vol. 108, no. 48, pp. 19323–19328, Nov. 2011.

[218] M. S. Kuhns and M. M. Davis, "The Safety on the TCR Trigger," *Cell*, vol. 135, no. 4. Cell, pp. 594–596, 14-Nov-2008.

[219] R. A. Fernandes, C. Yu, A. M. Carmo, E. J. Evans, P. Anton van der Merwe, and S. J. Davis, "What Controls T Cell Receptor Phosphorylation?," *Cell*, vol. 142, no. 5. Elsevier, pp. 668–669, 03-Sep-2010.

[220] G. J. Zlabinger *et al.*, "Cytokine release and dynamics of leukocyte populations after CD3/TCR monoclonal antibody treatment," *J. Clin. Immunol.*, vol. 12, no. 3, pp. 170–177, May 1992.

[221] J. P. Abastado, Y. C. Lone, A. Casrouge, G. Boulot, and P. Kourilsky, "Dimerization of soluble major histocompatibility complex-peptide complexes is sufficient for activation of T cell hybridoma and induction of unresponsiveness," *J. Exp. Med.*, vol. 182, no. 2, pp. 439–447, Aug. 1995.

[222] J. D. Stone and L. J. Stern, "CD8 T Cells, Like CD4 T Cells, Are Triggered by Multivalent Engagement of TCRs by MHC-Peptide Ligands but Not by Monovalent Engagement," *J. Immunol.*, vol. 176, no. 3, pp. 1498–1505, Feb. 2006.

[223] K. Matsui, J. J. Boniface, P. A. Reay, H. Schild, B. Fazekas De St Groth, and M. M. Davis, "Low affinity interaction of peptide-MHC complexes with T cell receptors," *Science (80-.).*, vol. 254, no. 5039, pp. 1788–1791, 1991.

[224] M. Krogsgaard and M. M. Davis, "How T cells 'see' antigen," *Nature Immunology*, vol. 6, no. 3. Nat Immunol, pp. 239–245, 2005.

[225] Z. Ma, K. A. Sharp, P. A. Janmey, and T. H. Finkel, "Surface-Anchored Monomeric Agonist pMHCs Alone Trigger TCR with High Sensitivity," *PLoS Biol.*, vol. 6, no. 2, p. e43, Feb. 2008.

[226] M. Krogsgaard, J. Juang, and M. M. Davis, "A role for 'self' in T-cell activation," *Seminars in Immunology*, vol. 19, no. 4. NIH Public Access, pp. 236–244, Aug-2007.

[227] J. Delon *et al.*, "CD8 expression allows T cell signaling by monomeric peptide-MHC complexes," *Immunity*, vol. 9, no. 4, pp. 467–473, Oct. 1998.

[228] D. J. Irvine, M. A. Purbhoo, M. Krogsgaard, and M. M. Davis, "Direct observation of ligand recognition by T cells," *Nature*, vol. 419, no. 6909, pp. 845–849, Oct. 2002.

[229] J. Huang *et al.*, "A Single peptide-major histocompatibility complex ligand triggers digital cytokine secretion in CD4+ T Cells," *Immunity*, vol. 39, no. 5, pp. 846–857, Nov. 2013.

[230] T. J. Crites *et al.*, "TCR Microclusters Pre-Exist and Contain Molecules Necessary for TCR Signal Transduction," *J. Immunol.*, vol. 193, no. 1, pp. 56–67, Jul. 2014.

[231] Y. Razvag, Y. Neve-Oz, J. Sajman, M. Reches, and E. Sherman, "Nanoscale kinetic segregation of TCR and CD45 in engaged microvilli facilitates early T cell activation," *Nat. Commun.*, vol. 9, no. 1, pp. 1–17, Dec. 2018.

[232] C. Irles, A. Symons, F. Michel, T. R. Bakker, P. A. van der Merwe, and O. Acuto, "CD45 ectodomain controls interaction with GEMs and Lck activity for optimal TCR signaling," *Nat. Immunol.*, vol. 4, no. 2, pp. 189–197, Feb. 2003.

[233] K. Choudhuri, D. Wiseman, M. H. Brown, K. Gould, and P. A. Van Der Merwe, "T-cell receptor triggering is critically dependent on the dimensions of its peptide-MHC ligand," *Nature*, vol. 436, no. 7050, pp. 578–582, Jul. 2005.

[234] S. P. Cordoba *et al.*, "The large ectodomains of CD45 and CD148 regulate their segregation from and inhibition of ligated T-cell receptor," *Blood*, vol. 121, no. 21, pp. 4295–4302, May 2013.

[235] J. J. O'Shea, D. W. Mcvicar, T. L. Bailey, C. Burns, and M. J. Smyth, "Activation of human peripheral blood T lymphocytes by pharmacological induction of protein-tyrosine phosphorylation," *Proc. Natl. Acad. Sci. U. S. A.*, vol. 89, no. 21, pp. 10306–10310, 1992.

[236] P. A. Van Der Merwe and O. Dushek, "Mechanisms for T cell receptor triggering," *Nature Reviews Immunology*, vol. 11, no. 1. Nat Rev Immunol, pp. 47–55, Jan-2011.

[237] J. R. James, "Tuning ITAM multiplicity on T cell receptors can control potency and selectivity to ligand density," *Sci. Signal.*, vol. 11, no. 531, p. 1088, May 2018.

[238] G. P. O'Donoghue, R. M. Pielak, A. A. Smoligovets, J. J. Lin, and J. T. Groves, "Direct single molecule measurement of TCR triggering by agonist pMHC in living primary T cells," *Elife*, vol. 2013, no. 2, Jul. 2013.

[239] S. Valitutti, S. Miller, M. Cella, E. Padovan, and A. Lanzavecchia, "Serial triggering of many T-cell receptors by a few peptide-MHC complexes," *Nature*, vol. 375, no. 6527. Nature Publishing Group, pp. 148–151, 11-May-1995.

[240] J. Huang *et al.*, "The kinetics of two-dimensional TCR and pMHC interactions determine

T-cell responsiveness," *Nature*, vol. 464, no. 7290, pp. 932–936, Apr. 2010.

[241] J. B. Huppa *et al.*, "TCR-peptide-MHC interactions in situ show accelerated kinetics and increased affinity," *Nature*, vol. 463, no. 7283, pp. 963–967, Feb. 2010.

[242] R. M. Pielak *et al.*, "Early T cell receptor signals globally modulate ligand: receptor affinities during antigen discrimination."

[243] C. Wofsy, D. Coombs, and B. Goldstein, "Calculations show substantial serial engagement of T cell receptors," *Biophys. J.*, vol. 80, no. 2, pp. 606–612, 2001.

[244] O. Dushek and D. Coombs, "Analysis of serial engagement and peptide-MHC transport in T cell receptor microclusters," *Biophys. J.*, vol. 94, no. 9, pp. 3447–3460, May 2008.

[245] S. F. Friend, F. Deason-Towne, L. K. Peterson, A. J. Berger, and L. L. Dragone, "Regulation of T cell receptor complex-mediated signaling by ubiquitin and ubiquitin-like modifications," *American Journal of Clinical and Experimental Immunology*, vol. 3, no. 3. E-Century Publishing Corporation, pp. 107–123, 2014.

[246] M. Lever *et al.*, "Architecture of a minimal signaling pathway explains the T-cell response to a 1 million-fold variation in antigen affinity and dose," *Proc. Natl. Acad. Sci. U. S. A.*, vol. 113, no. 43, pp. E6630–E6638, Oct. 2016.

[247] J. J. Y. Lin, S. T. Low-Nam, K. N. Alfieri, D. B. McAffee, N. C. Fay, and J. T. Groves, "Mapping the stochastic sequence of individual ligand-receptor binding events to cellular activation: T cells act on the rare events," *Sci. Signal.*, vol. 12, no. 564, Jan. 2019.

[248] T. Sasada, Y. Ghendler, J. huai Wang, and E. L. Reinherz, "Thymic selection is influenced by subtle structural variation involving the p4 residue of an MHC class I-bound peptide," *Eur. J. Immunol.*, vol. 30, no. 5, pp. 1281–1289, 2000.

[249] K. Matsui, J. J. Boniface, P. Steffner, P. A. Reay, and M. M. Davis, "Kinetics of T-cell receptor binding to peptide/I-E(k) complexes: Correlation of the dissociation rate with T-cell responsiveness," *Proc. Natl. Acad. Sci. U. S. A.*, vol. 91, no. 26, pp. 12862–12866, Dec. 1994.

[250] E. N. Kersh, A. S. Shaw, and P. M. Allen, "Fidelity of T cell activation through multistep T cell receptor ζ phosphorylation," *Science (80-.).*, vol. 281, no. 5376, pp. 572–575, Jul. 1998.

[251] J. J. Hopefield, "Kinetic proofreading: a new mechanism for reducing errors in biosynthetic processes requiring high specificity," *Proc. Natl. Acad. Sci. U. S. A.*, vol. 71, no. 10, pp. 4135–4139, 1974.

[252] T. W. Mckeithan, "Kinetic proofreading in T-cell receptor signal transduction," *Proc. Natl. Acad. Sci. U. S. A.*, vol. 92, no. 11, pp. 5042–5046, May 1995.

[253] L. J. Carreño, S. M. Bueno, P. Bull, S. G. Nathenson, and A. M. Kalergis, "The half-life of the T-cell receptor/peptide?major histocompatibility complex interaction can modulate T-cell activation in response to bacterial challenge," *Immunology*, vol. 121, no. 2, pp. 227–237, Jun. 2007.

[254] A. H. Kalergis *et al.*, "Efficient T cell activation requires an optimal dwell-time of interaction between the TCR and the pMHC complex," *Nat. Immunol.*, vol. 2, no. 3, pp. 229–234, Mar. 2001.

[255] S. Qi, M. Krogsgaard, M. M. Davis, and A. K. Chakraborty, "Molecular flexibility can

influence the stimulatory ability of receptor-ligand interactions at cell-cell junctions," *Proc. Natl. Acad. Sci. U. S. A.*, vol. 103, no. 12, pp. 4416–4421, Mar. 2006.

[256] O. S. Yousefi *et al.*, "Optogenetic control shows that kinetic proofreading regulates the activity of the t cell receptor," *Elife*, vol. 8, Apr. 2019.

[257] D. K. Tischer and O. D. Weiner, "Light-based tuning of ligand half-life supports kinetic proofreading model of T cell signaling," *Elife*, vol. 8, 2019.

[258] C. C. Govern, M. K. Paczosa, A. K. Chakraborty, and E. S. Huseby, "Fast on-rates allow short dwell time ligands to activate T cells," *Proc. Natl. Acad. Sci. U. S. A.*, vol. 107, no. 19, pp. 8724–8729, May 2010.

[259] J. D. Stone, A. S. Chervin, and D. M. Kranz, "T-cell receptor binding affinities and kinetics: impact on T-cell activity and specificity," *Immunology*, vol. 126, no. 2. Immunology, pp. 165–176, Feb-2009.

[260] J. M. Boulter, N. Schmitz, A. K. Sewell, A. J. Godkin, M. F. Bachmann, and A. M. Gallimore, "Potent T cell agonism mediated by a very rapid TCR/pMHG interaction," *Eur. J. Immunol.*, vol. 37, no. 3, pp. 798–806, Mar. 2007.

[261] M. Aleksic *et al.*, "Article Dependence of T Cell Antigen Recognition on T Cell Receptor-Peptide MHC Confinement Time," *Immunity*, vol. 32, pp. 163–174.

[262] P. François, G. Voisinne, E. D. Siggia, G. Altan-Bonnet, and M. Vergassola, "Phenotypic model for early T-cell activation displaying sensitivity, specificity, and antagonism," *Proc. Natl. Acad. Sci. U. S. A.*, vol. 110, no. 10, p. E888, Mar. 2013.

[263] S. C. Bunnell, V. Kapoor, R. P. Trible, W. Zhang, and L. E. Samelson, "Dynamic actin polymerization drives T cell receptor-induced spreading: A role for the signal transduction adaptor LAT," *Immunity*, vol. 14, no. 3, pp. 315–329, 2001.

[264] I. A. Yudushkin and R. D. Vale, "Imaging T-cell receptor activation reveals accumulation of tyrosine-phosphorylated CD3ζ in the endosomal compartment," *Proc. Natl. Acad. Sci. U. S. A.*, vol. 107, no. 51, pp. 22128–22133, Dec. 2010.

[265] Y. Ma *et al.*, "An intermolecular FRET sensor detects the dynamics of T cell receptor clustering," *Nat. Commun.*, vol. 8, no. 1, pp. 1–11, Apr. 2017.

[266] M. Fritzsche *et al.*, "Cytoskeletal actin dynamics shape a ramifying actin network underpinning immunological synapse formation," *Sci. Adv.*, vol. 3, no. 6, p. e1603032, Jun. 2017.

[267] K. I. Jankowska *et al.*, "Integrins modulate T cell receptor signaling by constraining actin flow at the immunological synapse," *Front. Immunol.*, vol. 9, no. JAN, Jan. 2018.

[268] H. R. Kim *et al.*, "T cell microvilli constitute immunological synaptosomes that carry messages to antigen-presenting cells," *Nat. Commun.*, vol. 9, no. 1, pp. 1–19, Dec. 2018.

[269] D. K. Sasmal *et al.*, "TCR–pMHC bond conformation controls TCR ligand discrimination," *Cell. Mol. Immunol.*, vol. 17, no. 3, pp. 203–217, Mar. 2020.

[270] H. Colin-York *et al.*, "Cytoskeletal Control of Antigen-Dependent T Cell Activation," *Cell Rep.*, vol. 26, no. 12, pp. 3369-3379.e5, Mar. 2019.

[271] J. Yi, L. Balagopalan, T. Nguyen, K. M. McIntire, and L. E. Samelson, "TCR microclusters form spatially segregated domains and sequentially assemble in calcium-dependent kinetic steps," *Nat. Commun.*, vol. 10, no. 1, Dec. 2019.

[272] P. A. Janmey, D. A. Fletcher, and C. A. Reinhart-King, "Stiffness Sensing by Cells," *Physiological reviews*, vol. 100, no. 2. NLM (Medline), pp. 695–724, 01-Apr-2020.

[273] M. Saitakis *et al.*, "Different TCR-induced T lymphocyte responses are potentiated by stiffness with variable sensitivityDifferent TCR-induced T lymphocyte responses are potentiated by stiffness with variable sensitivity," *Elife*, vol. 6, Jun. 2017.

[274] A. Wahl *et al.*, "Biphasic mechanosensitivity of T cell receptor-mediated spreading of lymphocytes," *Proc. Natl. Acad. Sci. U. S. A.*, vol. 116, no. 13, pp. 5908–5913, Mar. 2019.

[275] E. Tabdanov *et al.*, "Micropatterning of TCR and LFA-1 ligands reveals complementary effects on cytoskeleton mechanics in T cells," *Integr. Biol. (United Kingdom)*, vol. 7, no. 10, pp. 1272–1284, Oct. 2015.

[276] J. A. Nye and J. T. Groves, "Kinetic Control of Histidine-Tagged Protein Surface Density on Supported Lipid Bilayers," 2008.

[277] K. M. R. Faysal, J. S. Park, J. Nguyen, L. Garcia, and A. B. Subramaniam, "Lipid bilayers are long-lived on solvent cleaned plasma-oxidized poly(dimethyl) siloxane (ox-PDMS)," *PLoS One*, vol. 12, no. 1, Jan. 2017.

[278] E. Jenkins *et al.*, "Reconstitution of immune cell interactions in free-standing membranes," *J. Cell Sci.*, vol. 132, no. 4, Feb. 2019.

[279] A. S. Cheung, D. K. Y. Zhang, S. T. Koshy, and D. J. Mooney, "Scaffolds that mimic antigen-presenting cells enable ex vivo expansion of primary T cells," *Nat. Biotechnol.*, vol. 36, no. 2, pp. 160–169, Feb. 2018.

[280] T. Funatsu, Y. Harada, M. Tokunaga, K. Saito, and T. Yanagida, "Imaging of single fluorescent molecules and individual ATP turnovers by single myosin molecules in aqueous solution," *Nature*, vol. 374, no. 6522, pp. 555–559, 1995.

[281] A. A. Smoligovets, A. W. Smith, H. J. Wu, R. S. Petit, and J. T. Groves, "Characterization of dynamic actin associations with T-cell receptor microclusters in primary T cells," *J. Cell Sci.*, vol. 125, no. 3, pp. 735–742, Feb. 2012.

[282] T. Ilani, G. Vasiliver-Shamis, S. Vardhana, A. Bretscher, and M. L. Dustin, "T cell antigen receptor signaling and immunological synapse stability require myosin IIA," *Nat. Immunol.*, vol. 10, no. 5, pp. 531–539, 2009.

[283] S. Kumari *et al.*, "Actin foci facilitate activation of the phospholipase C-γ in primary T lymphocytes via the WASP pathway," *Elife*, vol. 2015, no. 4, pp. 1–31, 2015.

[284] D. Thumkeo *et al.*, "MDia1/3-dependent actin polymerization spatiotemporally controls LAT phosphorylation by Zap70 at the immune synapse," *Sci. Adv.*, vol. 6, no. 1, p. eaay2432, Jan. 2020.

[285] S. Kumari *et al.*, "Cytoskeletal tension actively sustains the migratory T-cell synaptic contact," *EMBO J.*, vol. 39, no. 5, Mar. 2020.

[286] J. J. Lin *et al.*, "Membrane Association Transforms an Inert Anti-TCRβ Fab' Ligand into a Potent T Cell Receptor Agonist," *Biophys. J.*, vol. 118, no. 12, pp. 2879–2893, Jun. 2020.

[287] L. V. Sibener *et al.*, "Isolation of a Structural Mechanism for Uncoupling T Cell Receptor Signaling from Peptide-MHC Binding," *Cell*, vol. 174, no. 3, pp. 672-687.e27, Jul. 2018.

[288] C. Berlin *et al.*, "a4 Integrins Mediate Lymphocyte Attachment and Rolling under Physiologic Flow," 1995.

[289] T. A. Springer and M. L. Dustin, "Integrin inside-out signaling and the immunological synapse," *Current Opinion in Cell Biology*, vol. 24, no. 1. Curr Opin Cell Biol, pp. 107–115, Feb-2012.

[290] P. J. Thul *et al.*, "A subcellular map of the human proteome," *Science (80-.).*, vol. 356, no. 6340, May 2017.

[291] S. Weinbaum, J. M. Tarbell, and E. R. Damiano, "The structure and function of the endothelial glycocalyx layer," *Annual Review of Biomedical Engineering*, vol. 9. Annu Rev Biomed Eng, pp. 121–167, 2007.

[292] L. Möckl, "The Emerging Role of the Mammalian Glycocalyx in Functional Membrane Organization and Immune System Regulation," *Frontiers in Cell and Developmental Biology*, vol. 8. Frontiers Media S.A., 15-Apr-2020.

[293] M. C. Clark and L. G. Baum, "T cells modulate glycans on CD43 and CD45 during development and activation, signal regulation, and survival," *Annals of the New York Academy of Sciences*, vol. 1253, no. 1. Blackwell Publishing Inc., pp. 58–67, 2012.

[294] W. R. A. Brown, A. N. Barclay, C. A. Sunderland, and A. F. Williams, "Identification of a glycophorin-like molecule at the cell surface of rat thymocytes," *Nature*, vol. 289, no. 5797, pp. 456–460, 1981.

[295] E. Remold-O'donnell, D. M. Kenney, R. Parkman, L. Cairns, B. Savage, and F. S. Rosen, "Characterization of a human lymphocyte surface sialoglycoprotein that is defective in wiskott-aldrich syndrome," *J. Exp. Med.*, vol. 159, no. 6, pp. 1705–1723, Jun. 1984.

[296] B. Ardman, M. A. Sikorski, and D. E. Staunton, "CD43 interferes with T-lymphocyte adhesion," *Proc. Natl. Acad. Sci. U. S. A.*, vol. 89, no. 11, pp. 5001–5005, 1992.

[297] B. M. Stockton, G. Cheng, N. Manjunath, B. Ardman, and U. H. von Andrian, "Negative Regulation of T Cell Homing by CD43," *Immunity*, vol. 8, no. 3, pp. 373–381, Mar. 1998.

[298] N. E. Sanjana, O. Shalem, and F. Zhang, "Improved vectors and genome-wide libraries for CRISPR screening," *Nature Methods*, vol. 11, no. 8. Nature Publishing Group, pp. 783–784, 30-Jul-2014.

[299] O. Shalem *et al.*, "Genome-scale CRISPR-Cas9 knockout screening in human cells," *Science (80-.).*, vol. 343, no. 6166, pp. 84–87, Jan. 2014.

[300] V. A. Barr and S. C. Bunnell, "Interference reflection microscopy," *Current Protocols in Cell Biology*, vol. CHAPTER, no. SUPPL.45. NIH Public Access, p. Unit, 2009.

[301] P. Müller, P. Schwille, and T. Weidemann, "PyCorrFit-generic data evaluation for fluorescence correlation spectroscopy," *Bioinformatics*, vol. 30, no. 17, pp. 2532–2533, Sep. 2014.

[302] D. Waithe, M. P. Clausen, E. Sezgin, and C. Eggeling, "FoCuS-point: Software for STED fluorescence correlation and time-gated single photon counting," *Bioinformatics*, vol. 32, no. 6, pp. 958–960, Mar. 2016.

[303] E. Remold-O'Donnell, C. Zimmerman, D. Kenney, and F. Rosen, "Expression on blood cells of sialophorin, the surface glycoprotein that is defective in Wiskott-Aldrich syndrome," *Blood*, vol. 70, no. 1, pp. 104–109, Jul. 1987.

[304] M. Maio and L. Del Vecchio, "Expression and functional role of CD54/intercellular adhesion molecule-1 (ICAM-1) on human blood cells," *Leuk. Lymphoma*, vol. 8, no. 1–2,

pp. 23–33, 1992.

[305] I. S. Trowbridge and M. L. Thomas, "CD45: An emerging role as a protein tyrosine phosphatase required for lymphocyte activation and development," *Annual Review of Immunology*, vol. 12. Annual Reviews Inc., pp. 85–116, 1994.

[306] K. A. Roebuck and A. Finnegan, "Regulation of intercellular adhesion molecule-1 (CD54) gene expression," *Journal of Leukocyte Biology*, vol. 66, no. 6. Federation of American Societies for Experimental Biology, pp. 876–888, 1999.

[307] R. T. Abraham and A. Weiss, "Jurkat T cells and development of the T-cell receptor signalling paradigm," *Nature Reviews Immunology*, vol. 4, no. 4. Nature Publishing Group, pp. 301–308, 2004.

[308] R. R. Bartelt, N. Cruz-Orcutt, M. Collins, and J. C. D. Houtman, "Comparison of T cell receptor-induced proximal signaling and downstream functions in immortalized and primary T cells," *PLoS One*, vol. 4, no. 5, May 2009.

[309] H. Dumortier *et al.*, " Antigen Presentation by an Immature Myeloid Dendritic Cell Line Does Not Cause CTL Deletion In Vivo, but Generates CD8 + Central Memory-Like T Cells That Can Be Rescued for Full Effector Function ," *J. Immunol.*, vol. 175, no. 2, pp. 855–863, Jul. 2005.

[310] J. R. Wiśniewski, M. Y. Hein, J. Cox, and M. Mann, "A 'proteomic ruler' for protein copy number and concentration estimation without spike-in standards," *Mol. Cell. Proteomics*, vol. 13, no. 12, pp. 3497–3506, Dec. 2014.

[311] J. L. Chen *et al.*, "Structural and kinetic basis for heightened immunogenicity of T cell vaccines," *J. Exp. Med.*, vol. 201, no. 8, pp. 1243–1255, Apr. 2005.

[312] D. R. Littman, Y. Thomas, P. J. Maddon, L. Chess, and R. Axel, "The isolation and sequence of the gene encoding T8: A molecule defining functional classes of T lymphocytes," *Cell*, vol. 40, no. 2, pp. 237–246, Feb. 1985.

[313] O. Perwitasari *et al.*, "Targeting organic anion transporter 3 with probenecid as a novel anti-influenza A virus strategy," *Antimicrob. Agents Chemother.*, vol. 57, no. 1, pp. 475–483, Jan. 2013.

[314] H. Dana *et al.*, "High-performance calcium sensors for imaging activity in neuronal populations and microcompartments," *Nat. Methods*, vol. 16, no. 7, pp. 649–657, Jul. 2019.

[315] X. Shi *et al.*, "Ca 2+ regulates T-cell receptor activation by modulating the charge property of lipids," *Nature*, vol. 493, no. 7430, pp. 111–115, Jan. 2013.

[316] F. Khan, M. He, and M. J. Taussig, "Double-hexahistidine tag with high-affinity binding for protein immobilization, purification, and detection on Ni-nitrilotriacetic acid surfaces," *Anal. Chem.*, vol. 78, no. 9, pp. 3072–3079, May 2006.

[317] A. M. Santos *et al.*, "Capturing resting T cells: The perils of PLL correspondence," *Nature Immunology*, vol. 19, no. 3. Nature Publishing Group, pp. 203–205, 01-Mar-2018.

[318] A. Ponjavic *et al.*, "Single-Molecule Light-Sheet Imaging of Suspended T Cells," *Biophys. J.*, vol. 114, no. 9, pp. 2200–2211, May 2018.

[319] N. Kučerka, Y. Liu, N. Chu, H. I. Petrache, S. Tristram-Nagle, and J. F. Nagle, "Structure of fully hydrated fluid phase DMPC and DLPC lipid bilayers using x-ray scattering from oriented multilamellar arrays and from unilamellar vesicles," *Biophys. J.*, vol. 88, no. 4,

pp. 2626–2637, 2005.

[320] M. Hubo, B. Trinschek, F. Kryczanowsky, A. Tuettenberg, K. Steinbrink, and H. Jonuleit, "Costimulatory molecules on immunogenic versus tolerogenic human dendritic cells," *Front. Immunol.*, vol. 4, no. APR, p. 82, Apr. 2013.

[321] L. Gioia, A. Siddique, S. R. Head, D. R. Salomon, and A. I. Su, "A genome-wide survey of mutations in the Jurkat cell line," *BMC Genomics*, vol. 19, no. 1, p. 334, May 2018.

[322] Y. Kaizuka, A. D. Douglass, R. Varma, M. L. Dustin, and R. D. Vale, "Mechanisms for segregating T cell receptor and adhesion molecules during immunological synapse formation in Jurkat T cells," *Proc. Natl. Acad. Sci. U. S. A.*, vol. 104, no. 51, pp. 20296–20301, Dec. 2007.

[323] P. Beemiller, J. Jacobelli, and M. F. Krummel, "Integration of the movement of signaling microclusters with cellular motility in immunological synapses," *Nat. Immunol.*, vol. 13, no. 8, pp. 787–795, Aug. 2012.

[324] A. K. Rudd, J. M. Valls Cuevas, and N. K. Devaraj, "SNAP-tag-reactive lipid anchors enable targeted and spatiotemporally controlled localization of proteins to phospholipid membranes," *J. Am. Chem. Soc.*, vol. 137, no. 15, pp. 4884–4887, Apr. 2015.

[325] U. O'doherty *et al.*, "Dendritic cells freshly isolated from human blood express CD4 and mature into typical immtmostimulatory dendritic cells after culture in monocyte-conditioned medium," *J. Exp. Med.*, vol. 178, no. 3, pp. 1067–1078, Sep. 1993.

[326] E. Fanales-Belasio, G. Zambruno, A. Cavani, and G. Girolomoni, "Antibodies against sialophorin (CD43) enhance the capacity of dendritic cells to cluster and activate T lymphocytes.," *J. Immunol.*, vol. 159, no. 5, 1997.

[327] B. N. Manz, B. L. Jackson, R. S. Petit, M. L. Dustin, and J. Groves, "T-cell triggering thresholds are modulated by the number of antigen within individual T-cell receptor clusters," *Proc. Natl. Acad. Sci. U. S. A.*, vol. 108, no. 22, pp. 9089–9094, May 2011.

[328] A. D. Schubert *et al.*, "Self-reactive human CD4 T cell clones form unusual immunological synapses," *J. Exp. Med.*, vol. 209, no. 2, pp. 335–352, Feb. 2012.

[329] G. I. Bell, M. Dembo, and P. Bongrand, "Cell adhesion. Competition between nonspecific repulsion and specific bonding," *Biophys. J.*, vol. 45, no. 6, pp. 1051–1064, 1984.

[330] T. A. Springer, "Adhesion receptors of the immune system," *Nature*, vol. 346, no. 6283. Nature, pp. 425–434, 1990.

[331] Q. Li *et al.*, "Chemically Self-Assembled Antibody Nanorings (CSANs): Design and Characterization of an Anti-CD3 IgM Biomimetic."

[332] S. R. Hasslen, U. H. von Andrian, E. C. Butcher, R. D. Nelson, and S. L. Erlandsen, "Spatial distribution of L-selectin (CD62L) on human lymphocytes and transfected murine L1-2 cells," *Histochem. J.*, vol. 27, no. 7, pp. 547–554, 1995.

[333] N. J. Burroughs, K. Köhler, V. Miloserdov, M. L. Dustin, P. A. van der Merwe, and D. M. Davis, "Boltzmann energy-based image analysis demonstrates that extracellular domain size differences explain protein segregation at immune synapses," *PLoS Comput. Biol.*, vol. 7, no. 8, p. 1002076, Aug. 2011.

[334] M. H. Bakalar, A. M. Joffe, E. M. Schmid, S. Son, M. Podolski, and D. A. F. Correspondence, "Size-Dependent Segregation Controls Macrophage Phagocytosis of

Antibody-Opsonized Targets," *Cell*, vol. 174, pp. 131-142.e13, 2018.

[335] J. H. Felce *et al.*, "CD45 exclusion– and cross-linking–based receptor signaling together broaden FceRI reactivity," *Sci. Signal.*, vol. 11, no. 561, Dec. 2018.

[336] G. R. Woollett, A. N. Barclay, M. Puklavec, and A. F. Williams, "Molecular and antigenic heterogeneity of the rat leukocyte-common antigen from thymocytes and T and B lymphocytes," *Eur. J. Immunol.*, vol. 15, no. 2, pp. 168–173, 1985.

[337] A. N. Barclay and M. N. McCall, "Structure and function of the leucocyte common antigen CD45; From alloantigen to mapping of restricted epitopes using recombinant soluble CD45 isoforms," in *Biochemical Society Transactions*, 1992, vol. 20, no. 1, pp. 161–164.

[338] V. Junghans, A. M. Santos, Y. Lui, S. J. Davis, and P. Jönsson, "Dimensions and Interactions of Large T-Cell Surface Proteins," *Frontiers in immunology*, vol. 9. NLM (Medline), p. 2215, 2018.

[339] A. Brodovitch, E. Shenderov, V. Cerundolo, P. Bongrand, A. Pierres, and P. A. van der Merwe, "T lymphocytes need less than 3 min to discriminate between peptide MHCs with similar TCR-binding parameters," *Eur. J. Immunol.*, vol. 45, no. 6, pp. 1635–1642, Jun. 2015.

[340] Y. Feng *et al.*, "Polarization imaging and classification of Jurkat T and Ramos B cells using a flow cytometer," *Cytom. Part A*, vol. 85, no. 11, pp. 986–986, Nov. 2014.

[341] C. Rotsch and M. Radmacher, "Drug-induced changes of cytoskeletal structure and mechanics in fibroblasts: An atomic force microscopy study," *Biophys. J.*, vol. 78, no. 1, pp. 520–535, Jan. 2000.

[342] U. H. Von Andrian, S. R. Hasslen, R. D. Nelson, S. L. Erlandsen, and E. C. Butchert, "A Central Role for Microvillous Receptor Presentation in Leukocyte Adhesion under Flow," 1995.

[343] J. A. Cooper, "Effects of cytochalasin and phalloidin on actin.," *The Journal of cell biology*, vol. 105, no. 4. J Cell Biol, pp. 1473–1478, 1987.

[344] Y. Zhang *et al.*, "Quantitating morphological changes in biological samples during scanning electron microscopy sample preparation with correlative super-resolution microscopy," *PLoS One*, vol. 12, no. 5, May 2017.

[345] J. C. Stachowiak *et al.*, "Membrane bending by protein-protein crowding," *Nat. Cell Biol.*, vol. 14, no. 9, pp. 944–949, Sep. 2012.

[346] S. Son *et al.*, "Molecular height measurement by cell surface optical profilometry (CSOP)," *Proc. Natl. Acad. Sci. U. S. A.*, vol. 117, no. 25, pp. 14209–14219, Jun. 2020.

[347] M. J. Brown *et al.*, "Chemokine stimulation of human peripheral blood T lymphocytes induces rapid dephosphorylation of ERM proteins, which facilitates loss of microvilli and polarization," *Blood*, vol. 102, no. 12, pp. 3890–3899, Dec. 2003.

[348] S. J. Davis *et al.*, "Ligand binding by the immunoglobulin superfamily recognition molecule CD2 is glycosylation-independent," *J. Biol. Chem.*, vol. 270, no. 1, pp. 369–375, Jan. 1995.

[349] M. Shimaoka *et al.*, "Reversibly locking a protein fold in an active conformation with a disulfide bond: Integrin αL I domains with high affinity and antagonist activity in vivo,"

Proc. Natl. Acad. Sci. U. S. A., vol. 98, no. 11, pp. 6009–6014, May 2001.

[350] M. Shimaoka *et al.*, "Structures of the αL I domain and its complex with ICAM-1 reveal a shape-shifting pathway for integrin regulation," *Cell*, vol. 112, no. 1. Cell Press, pp. 99–111, 10-Jan-2003.

[351] T. N. Ramos, D. C. Bullard, and S. R. Barnum, "ICAM-1: Isoforms and Phenotypes," *J. Immunol.*, vol. 192, no. 10, pp. 4469–4474, May 2014.

[352] C. Binder *et al.*, "CD2 Immunobiology," *Frontiers in Immunology*, vol. 11. Frontiers Media S.A., p. 1090, 09-Jun-2020.

[353] P. Moingeon, H. C. Chang, B. P. Wallner, C. Stebbins, A. Z. Frey, and E. L. Reinherz, "CD2-mediated adhesion facilitates T lymphocyte antigen recognition function," *Nature*, vol. 339, no. 6222, pp. 312–314, 1989.

[354] S. C. Meuer *et al.*, "An alternative pathway of T-cell activation: A functional role for the 50 kd T11 sheep erythrocyte receptor protein," *Cell*, vol. 36, no. 4, pp. 897–906, 1984.

[355] S. Koyasu *et al.*, "Role of interaction of CD2 molecules with lymphocyte function-associated antigen 3 in T-cell recognition of nominal antigen," 1990.

[356] C. C. W. Hughes, C. O. S. Savage, and J. S. Pober, "Endothelial cells augment T cell interleukin 2 production by a contact-dependent mechanism involving CD2/LFA-3 interaction," *J. Exp. Med.*, vol. 171, no. 5, pp. 1453–1467, May 1990.

[357] T. Sasada and E. L. Reinherz, "A Critical Role for CD2 in Both Thymic Selection Events and Mature T Cell Function 1," 2001.

[358] R. Zaru, T. O. Cameron, L. J. Stern, S. Müller, and S. Valitutti, "Cutting Edge: TCR Engagement and Triggering in the Absence of Large-Scale Molecular Segregation at the T Cell-APC Contact Site 1," 2002.

[359] N. Espagnolle *et al.*, "CD2 and TCR synergize for the activation of phospholipase Cγ1/calcium pathway at the immunological synapse," *Int. Immunol.*, vol. 19, no. 3, pp. 239–248, Mar. 2007.

[360] Y. Wang *et al.*, "LFA-1 affinity regulation is necessary for the activation and proliferation of naive T cells," *J. Biol. Chem.*, vol. 284, no. 19, pp. 12645–12653, May 2009.

[361] S. Shaw, G. E. Ginther Luce, R. Quinones, R. E. Gress, T. A. Springer, and M. E. Sanders, "Two antigen-independent adhesion pathways used by human cytotoxic T-cell clones," *Nature*, vol. 323, no. 6085, pp. 262–264, 1986.

[362] H. Spits *et al.*, "Alloantigen recognition is preceded by nonspecific adhesion of cytotoxic T cells and target cells," *Science (80-.).*, vol. 232, no. 4748, pp. 403–405, 1986.

[363] M. P. Stewart, C. Cabanas, and N. Hogg, "T cell adhesion to intercellular adhesion molecule-1 (ICAM-1) is controlled by cell spreading and the activation of integrin LFA-1.," *J. Immunol.*, vol. 156, no. 5, 1996.

[364] H. Zhang, J. H. Liu, W. Yang, T. Springer, M. Shimaoka, and J. H. Wang, "Structural basis of activation-dependent binding of ligand-mimetic antibody AL-57 to integrin LFA-1," *Proc. Natl. Acad. Sci. U. S. A.*, vol. 106, no. 43, pp. 18345–18350, Oct. 2009.

[365] I. Dransfield, C. Cabanas, A. Craig, and N. Hogg, "Divalent Cation Regulation of the Function of the Leukocyte Integrin LFA1."

[366] R. Rothlein, M. L. Dustin, S. D. Marlin, and T. A. Springer, "A human intercellular adhesion molecule (ICAM-1) distinct from LFA-1.," *J. Immunol.*, vol. 137, no. 4, 1986.

[367] S. D. Marlin and T. A. Springer, "Purified intercellular adhesion molecule-1 (ICAM-1) is a ligand for lymphocyte function-associated antigen 1 (LFA-1)," *Cell*, vol. 51, no. 5, pp. 813–819, Dec. 1987.

[368] M. W. Makgoba *et al.*, "ICAM-1 a ligand for LFA-1-dependent adhesion of B, T and myeloid cells," *Nature*, vol. 331, no. 6151, pp. 86–88, 1988.

[369] Y. Van Kooyk, P. Weder, K. Heije, and C. G. Figdor, "Extracellular Ca2+ modulates leukocyte function-associated antigen-1 cell surface distribution on T lymphocytes and consequently affects cell adhesion," *J. Cell Biol.*, vol. 124, no. 6, pp. 1061–1070, 1994.

[370] M. E. Labadia, D. D. Jeanfavre, G. O. Caviness, and M. M. Morelock, "Molecular Regulation of the Interaction Between Leukocyte Function-Associated Antigen-1 and Soluble ICAM-1 by Divalent Metal Cations," *J. Immunol.*, vol. 161, no. 2, 1998.

[371] A. G. Wingren *et al.*, "T cell activation pathways: B7, LFA-3, and ICAM-1 shape unique T cell profiles," *Critical Reviews in Immunology*, vol. 15, no. 3–4. pp. 235–253, 01-Jan-1995.

[372] A. Moretta, A. Poggi, D. Olive, C. Bottino, C. Fortis, and G. Pantaleo, "Selection and characterization of T-cell variants lacking molecules involved in T-cell activation (T3 T-cell receptor, T44, and T11): Analysis of the functional relationship among different pathways of activation," *Proc. Natl. Acad. Sci. U. S. A.*, vol. 84, no. 6, pp. 1654–1658, 1987.

[373] A. D. Beyers, A. N. Barclay, D. A. Law, Q. He, and A. F. Williams, "Activation of T Lymphocytes via Monoclonal Antibodies against Rat Cell Surface Antigens with Particular Reference to CD2 Antigen," *Immunol. Rev.*, vol. 111, no. 1, pp. 59–77, 1989.

[374] H. Ohno, C. Ushiyama, M. Taniguchi, R. N. Germain, and T. Saito, "CD2 can mediate TCR/CD3-independent T cell activation.," *J. Immunol.*, vol. 146, no. 11, 1991.

[375] J. R. Ostberg, R. K. Barth, and J. G. Frelinger, "The Roman god Janus: A paradigm for the function of CD43," *Immunol. Today*, vol. 19, no. 12, pp. 546–550, Dec. 1998.

[376] A. M. Krensky, F. Sanchez-Madrid, E. Robbins, J. A. Nagy, T. A. Springer, and S. J. Burakoff, "The functional significance, distribution, and structure of LFA-1, LFA-2, and LFA-3: cell surface antigens associated with CTL-target interactions.," *J. Immunol.*, vol. 131, no. 2, 1983.

[377] A. Brodovitch, P. Bongrand, and A. Pierres, "T Lymphocytes Sense Antigens within Seconds and Make a Decision within One Minute," *J. Immunol.*, vol. 191, no. 5, pp. 2064–2071, Sep. 2013.

[378] N. Anikeeva, K. Somersalo, T. N. Sims, V. K. Thomas, M. L. Dustin, and Y. Sykulev, "Distinct role of lymphocyte function-associated antigen-1 in mediating effective cytolytic activity by cytotoxic T lymphocytes," *Proc. Natl. Acad. Sci. U. S. A.*, vol. 102, no. 18, pp. 6437–6442, May 2005.

[379] P. Anton van der Merwe, P. N. McNamee, E. A. Davies, A. N. Barclay, and S. J. Davis, "Topology of the CD2-CD48 cell-adhesion molecule complex: implications for antigen recognition by T cells," *Curr. Biol.*, vol. 5, no. 1, pp. 74–84, Jan. 1995.

[380] P. E. Framson, D. H. Cho, L. Y. Lee, and R. M. Hershberg, "Polarized expression and function of the costimulatory molecule CD58 on human intestinal epithelial cells," *Gastroenterology*, vol. 116, no. 5, pp. 1054–1062, May 1999.

[381] E. C. Y. Wang *et al.*, "Suppression of costimulation by human cytomegalovirus promotes evasion of cellular immune defenses," *Proc. Natl. Acad. Sci. U. S. A.*, vol. 115, no. 19, pp. 4998–5003, May 2018.

[382] E. J. Evans *et al.*, "Crystal structure and binding properties of the CD2 and CD244 (2B4)-binding protein, CD48," *J. Biol. Chem.*, vol. 281, no. 39, pp. 29309–29320, Sep. 2006.

[383] T. Shao *et al.*, "Costimulatory function of Cd58/Cd2 interaction in adaptive humoral immunity in a zebrafish model," *Front. Immunol.*, vol. 9, no. MAY, p. 31, May 2018.

[384] N. Killeen, S. G. Stuart, and D. R. Littman, "Development and function of T cells in mice with a disrupted CD2 gene.," *EMBO J.*, vol. 11, no. 12, pp. 4329–4336, Dec. 1992.

[385] J. Tong *et al.*, "CD43 Regulation of T Cell Activation Is Not through Steric Inhibition of T Cell-APC Interactions but through an Intracellular Mechanism," *J. Exp. Med.*, vol. 199, no. 9, pp. 1277–1283, May 2004.

[386] F. M. Pavalko, D. M. Walker, L. Graham, M. Goheen, C. M. Doerschuk, and G. S. Kansas, "The cytoplasmic domain of L-selectin interacts with cytoskeletal proteins via α-actinin: Receptor positioning in microvilli does not require interaction with α-actinin," *J. Cell Biol.*, vol. 129, no. 4, pp. 1155–1164, 1995.

[387] S. A. Hocdé, O. Hyrien, and R. E. Waugh, "Cell adhesion molecule distribution relative to neutrophil surface topography assessed by TIRFM," *Biophys. J.*, vol. 97, no. 1, pp. 379–387, 2009.

[388] V. Zurli *et al.*, "Phosphoproteomics of CD2 signaling reveals AMPK-dependent regulation of lytic granule polarization in cytotoxic T cells," *Sci. Signal.*, vol. 13, no. 631, p. 1965, May 2020.

[389] K. Somersalo *et al.*, "Cytotoxic T lymphocytes form an antigen-independent ring junction," *J. Clin. Invest.*, vol. 113, no. 1, pp. 49–57, Jan. 2004.

[390] D. R. Myers, J. Zikherman, and J. P. Roose, "Tonic Signals: Why Do Lymphocytes Bother?," *Trends in Immunology*, vol. 38, no. 11. Elsevier Ltd, pp. 844–857, 01-Nov-2017.

[391] G. A. Azar, F. Lemaître, E. A. Robey, and P. Bousso, "Subcellular dynamics of T cell immunological synapses and kinapses in lymph nodes," *Proc. Natl. Acad. Sci. U. S. A.*, vol. 107, no. 8, pp. 3675–3680, Feb. 2010.

[392] C. Wülfing and M. M. Davis, "A receptor/cytoskeletal movement triggered by costimulation during T cell activation," *Science (80-.).*, vol. 282, no. 5397, pp. 2266–2269, Dec. 1998.

[393] I. Tskvitaria-Fuller, A. L. Rozelle, H. L. Yin, and C. Wülfing, "Regulation of Sustained Actin Dynamics by the TCR and Costimulation as a Mechanism of Receptor Localization," *J. Immunol.*, vol. 171, no. 5, pp. 2287–2295, Sep. 2003.

[394] A. L. DeMond, K. D. Mossman, T. Starr, M. L. Dustin, and J. T. Groves, "T cell receptor microcluster transport through molecular mazes reveals mechanism of translocation," *Biophys. J.*, vol. 94, no. 8, pp. 3286–3292, Apr. 2008.

[395] D. R. Fooksman *et al.*, "Functional anatomy of T cell activation and synapse formation," *Annual Review of Immunology*, vol. 28. NIH Public Access, pp. 79–105, 23-Apr-2010.

[396] A. T. Ritter, Y. Asano, J. Lippincott-Schwartz, and G. M. Griffiths Correspondence, "Actin Depletion Initiates Events Leading to Granule Secretion at the Immunological

Synapse," *Immunity*, vol. 42, pp. 864–876, 2015.

[397] S.-Y. Tseng, J. C. Waite, M. Liu, S. Vardhana, and M. L. Dustin, "T Cell-Dendritic Cell Immunological Synapses Contain TCR-dependent CD28-CD80 Clusters That Recruit Protein Kinase Cθ," *J. Immunol.*, vol. 181, no. 7, pp. 4852–4863, Oct. 2008.

[398] M. F. Krummel and M. D. Cahalan, "The Immunological Synapse: a Dynamic Platform for Local Signaling."

[399] P. J. Fisher, P. A. Bulur, S. Vuk-Pavlovic, F. G. Prendergast, and A. B. Dietz, "Dendritic cell microvilli: A novel membrane structure associated with the multifocal synapse and T-cell clustering," *Blood*, vol. 112, no. 13, pp. 5037–5045, Dec. 2008.

[400] M. A. Al-Aghbar, Y. S. Chu, B. M. Chen, and S. R. Roffler, "High-affinity ligands can trigger T cell receptor signaling without CD45 segregation," *Front. Immunol.*, vol. 9, no. APR, p. 1, Apr. 2018.

[401] S. Coelho *et al.*, "Ultraprecise single-molecule localization microscopy enables in situ distance measurements in intact cells," *Sci. Adv.*, vol. 6, no. 16, p. eaay8271, Apr. 2020.

[402] D. Depoil *et al.*, "CD19 is essential for B cell activation by promoting B cell receptor-antigen microcluster formation in response to membrane-bound ligand," *Nat. Immunol.*, vol. 9, no. 1, pp. 63–72, Jan. 2008.

[403] S. A. Freeman *et al.*, "Integrins Form an Expanding Diffusional Barrier that Coordinates Phagocytosis," *Cell*, vol. 164, no. 1–2, pp. 128–140, Jan. 2016.

[404] M. H. Brown, D. A. Cantrell, G. Brattsand, M. J. Crumpton, and M. Gullberg, "The CD2 antigen associates with the T-cell antigen receptor CD3 antigen complex on the surface of human T lymphocytes," *Nature*, vol. 339, no. 6225, pp. 551–553, 1989.

[405] O. Dushek, J. Goyette, and P. A. van der Merwe, "Non-catalytic tyrosine-phosphorylated receptors," *Immunol. Rev.*, vol. 250, no. 1, pp. 258–276, Nov. 2012.

[406] H. S. Goodridge *et al.*, "Activation of the innate immune receptor Dectin-1 upon formation of a ˜Phagocytic synapse-™," *Nature*, vol. 472, no. 7344, pp. 471–475, Apr. 2011.

[407] L. L. Lanier, G. Yu, and J. H. Phillips, "Co-association of CD3ζ with a receptor (CD16) for IgG Fc on human natural killer cells," *Nature*, vol. 342, no. 6251, pp. 803–805, 1989.

[408] P. Anderson, M. Caligiuri, C. O'Brien, T. Manley, J. Ritz, and S. F. Schlossman, "Fc gamma receptor type III (CD16) is included in the zeta NK receptor complex expressed by human natural killer cells," *Proc. Natl. Acad. Sci.*, vol. 87, no. 6, 1990.

[409] P. Moingeon *et al.*, "CD3ζ dependence of the CD2 pathway of activation in T lymphocytes and natural killer cells," *Proc. Natl. Acad. Sci. U. S. A.*, vol. 89, no. 4, pp. 1492–1496, Feb. 1992.

[410] L. K. Bockenstedt, M. A. Goldsmith, M. Dustin, D. Olive, T. A. Springer, and A. Weiss, "The CD2 ligand LFA-3 activates T cells but depends on the expression and function of the antigen receptor.," *J. Immunol.*, vol. 141, no. 6, 1988.

[411] M. E. Sanders *et al.*, "Human memory T lymphocytes express increased levels of three cell adhesion molecules (LFA-3, CD2, and LFA-1) and three other molecules (UCHL1, CDw29, and Pgp-1) and have enhanced IFN-gamma production.," *J. Immunol.*, vol. 140, no. 5, 1988.

[412] R. Obst, “The timing of T cell priming and cycling,” *Frontiers in Immunology*, vol. 6, no. NOV. Frontiers Research Foundation, p. 1, 2015.

[413] C.-J. Hsu *et al.*, “Ligand Mobility Modulates Immunological Synapse Formation and T Cell Activation,” *PLoS One*, vol. 7, no. 2, p. e32398, Feb. 2012.

[414] M. J. Rosenbluth, W. A. Lam, and D. A. Fletcher, “Force microscopy of nonadherent cells: A comparison of leukemia cell deformability,” *Biophys. J.*, vol. 90, no. 8, pp. 2994–3003, 2006.

[415] J. N. Gibson, P. Beesetty, C. Sulentic, and J. A. Kozak, “Rapid quantification of mitogen-induced blastogenesis in T lymphocytes for identifying immunomodulatory drugs,” *J. Vis. Exp.*, vol. 2016, no. 118, p. 55212, Dec. 2016.

[416] V. Junghans, M. Chouliara, A. M. Santos, D. Hatherley, J. Petersen, T. Dam, L. Svensson, J. Rossjohn, S. J. Davis, P. Jonsson, "Effects of a local auxiliary protein on the two-dimensional affinity of a TCR-peptide MHC interaction," *J. Cell Sci.,* vol. 133, no. 15, jcs245985, 2020.

[417] H. Cai, J. Muller, D. Depoil, V. Mayya, M. P. Sheetz, M. L. Dustin, S. J. Wind, "Full control of ligand positioning reveals spatial thresholds for T cell receptor triggering," *Nature nanotechnology*,vol. 13, no. 7, pp. 610-617, 2018.

[418] M. Taylor, K. husain, Z. J. Gartner, S. Mayor, R. D. Vale, "A DNA-Based T Cell Receptor Reveals a Role for Receptor Clustering in Ligand Discrimination," *Cell*, vol. 169, no. 1, pp. 108-119.e20, 2017.

[419] C. S. Delaveris, E. R. Webster, S. M. Banik, S. G. Boxer, C. R. Bertozzi, "Membrane-tethered mucin-like polypeptides sterically inhibit binding and slow fusion kinetics of influenza A virus," *Proc. Natl. Acad. Sci. U.S.A.,* vol. 117, no. 23, pp. 12643-12650, 2020.

[420] M. D. Vahey, D. A. Fletcher, "Influenza A virus surface proteins are organized to help penetrate host mucus," *eLife*, vol. 8. pp. e43764, 2019.

[421] M. L. Dustin, T. A. Springer, "T-cell receptor cross-linking transiently stimulates adhesiveness through LFA-1," *Nature*, vol. 341, no. 6243, pp. 619-24, 1989.

[422] M. P. Stewart, A. McDowall, N. Hogg, "LFA-1-mediated Adhesion Is Regulated by Cytoskeletal Restraint and by a Ca^{2+}- dependent Protease, Calpain," *The Journal of cell biology*,vol. 140, no. 3, pp. 699-707, 1998.

[423] W-L. Lo, N. H. Shah, N. Ahsan, V. Horkova, O. Stepanek, A. R. Salomon, J. Kuriyan, A. Weiss, "Lck promotes Zap70-dependent LAT phosphorylation by bridging Zap70 to LAT," *Nat. Immunol*., vol. 19, no. 7, pp. 733-741, 2018.

[424] T. Yokosuka, M. Takamatsu, W. Koboyashi-Imanishi, A. Hashimoto-Tane, M. Azuma, T. Saito, "Programmed cell death 1 forms negative costimulatory microclusters that directly inhibit T cell receptor signaing by recruiting phosphatase SHP2," *J. Exp. Med.* vol. 209, no. 6, pp. 1201-17, 2012.

[425] A. K. Sewell, "Why must T cells be cross-reactive?" *Nat. Rev. Imunol.* vol. 12, no. 9, pp. 669-77, 2012.

[426] T. Lammermann, B. Bader, S. Monkley, T. Worbs, R. Wdlich-Soldner, K. Hirsch, M. Keller, R. Forster, D. Critchley, R. Fassler, M. Sixt, "Rapid leukocyte migration by integrin-independent flowing and squeezing," *Nature*, vol. 453, no. 7191, pp. 51-55, 2008.

[427] K. Kohler, S. Xiong, J. Brzostek, M. Mehrabi, P. Eissmann, A. Harrison, S. Cordoba, S. Oddos, V. Miloserdov, K. Gould, N. Burroughs, P. Merwe, D. Davis, " Matched sizes of activating and inhibitory receptor/ligand pairs are required for optimal signal integration by human natural killer cells," *PLOS One*, vol. 5, no. 11, e15374, 2010.

[428] M. Sieh, J. B. Bolen, A. Weiss, "CD45 specifically modulates binding of Lck to a phosphopeptide encompassing the negative regulatory tyrosine of Lck," *EMBO J.*, vol. 12, no. 1, pp. 315-321, 1993.